# Manipulation of the mutual synchronisation in a pair of spin-torque oscillators

Xavier Du Hamel de Milly

université PARIS-SACLAY

NNT: 2017SACLS442


# Manipulation de la synchronisation mutuelle dans une paire d'oscillateurs à transfert de spin

THÈSE DE DOCTORAT DE L'UNIVERSITÉ PARIS-SACLAY
préparée à l'Université Paris-Sud

École doctorale n° 564: Physique en Île-de-France (PIF)
Spécialité: Physique

Thèse présentée et soutenue à Gif-sur-Yvette, le 29 novembre 2017, par

**Xavier du Hamel de Milly**

Service de Physique de l'État Condensé, CEA Saclay

devant le jury composé de :

| | |
|---|---|
| Mme Ursula Ebels<br>Directeur de recherche, Spintec Grenoble | Président et rapporteur |
| M. Stéphane Mangin<br>Professeur, Université de Lorraine | Rapporteur |
| M. Nicolas Bizière<br>Chargé de recherche, CEMES Toulouse | Examinateur |
| M. Vincent Cros<br>Directeur de recherche, CNRS/Thales | Examinateur |
| M. Joo-Von Kim<br>Chargé de recherche, C2N | Examinateur |
| M. Grégoire de Loubens<br>CR1, CEA/SPEC | Directeur de thèse |

Thèse de doctorat

# Contents

# Remerciements

Une thèse est faite d'un ensemble de petits détails, et le tout est évalué par un manuscrit et une soutenance qui ne laissent pas forcément tous ces détails transparaître. C'est pourquoi j'aimerais en dire un peu plus ici, et je resterai toujours en-deçà de ce qu'il faudrait.

En premier lieu j'aimerais remercier les membres du jury: merci à Ursula Ebels pour avoir présidé et rapporté ma thèse, à Stéphane Mangin pour l'avoir rapportée, à Nicolas Bizière, Vincent Cros et Joo-Von Kim d'avoir accepté d'assister à ma soutenance, et à Grégoire de Loubens de m'avoir suivi pendant ces trois années.

Bien entendu le LNO tient une place prépondérante. En premier lieu Grégoire, qui a toujours su rester disponible, et qui m'a laissé développer cet aspect de simulations et m'a fait confiance quand je me suis embarqué dans l'exploration de la théorie des bifurcations, un aspect que je ne me serais jamais attendu à rencontrer dans un laboratoire d'expérimentateurs. Je tiens à remercier en particulier Claude, qui m'a permis de travailler sur cet aspect capteurs, quand il m'a paru nécessaire d'apporter un aspect appliqué dans une thèse d'intérêt très fondamental. Il y a également ceux avec qui j'ai pu travailler directement, Yi et Vladimir. Et le reste de l'équipe, Olivier, Myriam, Michel, Jean-Yves, Aurélie, Jean-Baptiste, Gwen, Dorothée, Anne, Greg et Gérald, Élodie, Vincent, qui a été mon excellent co-bureau pendant 3 ans, Nathan, les stagiaires pour certains devenus thésards, les apprentis, et les postdocs de passage, sans oublier la team Crivasense. Puis au sein du SPEC j'ai trouvé le soutien également de François Daviaud, et Corinne notre secrétaire préférée. Et ce sans oublier les théoriciens et tous ceux que j'avais l'habitude de voir aux heures de repas.

Je n'oublie pas toutes nos collaborations, notamment les chercheurs et thésards de l'UMΦ, qui nous ont permis de travailler sur ces échantillons, et avec qui nous avons eu des échanges réguliers sur la physique des oscillateurs à transfert de spin. Et je n'oublie pas les moments mémorables lors de conférences à travers l'Europe. Je tiens à mentionner tout particulièrement Vasyl Tyberkevych de d'Oakland University, avec qui j'ai pu avoir plusieurs échanges sur des aspects plus théoriques, et qui nous aiguillés vers la bonne explication pour des résultats parmi les plus intéressants de la thèse. Merci également à Francesco Andriulli qui m'a aidé dès l'école d'ingénieur à entrer dans ce cursus nanotechnologies. Et une mention spéciale à Jorge Cham, qui m'a aidé à relativiser sur la condition de thésard.

Bien sûr, la vie de thésard ne s'arrête pas dès que l'on passe la porte du labo, je pense également à ma famille et mes amis, qui m'ont soutenu malgré cette drôle d'idée de faire une thèse. Oui, mes spin précessent toujours, même si ils ont parfois des trajectoires étranges! Et comme la postérité le fait dire à Mike Barfield: "La théorie du chaos a été inventée par les scientifiques qui paniquaient à l'idée que le public commençaient à comprendre les anciennes.".

# Object of the thesis

The field of spintronics was born in the seventies, but the present boom happened with the GMR effect first reported in 1988, which enabled highly sensitive local magnetic field sensors. This was particularly illustrated in GMR read heads for HDD, with industrial applications no later than 1996, which lead to an increase in the storage density in HDD by several orders of magnitude. This was by the time when the complementary effect of GMR, the spin tranfer torque (STT), was theoretically predicted. The magnetoresistivity allows to electrically measure the orientation of the magnetisation of a magnetic layer which is modified by an external perturbation, by comparison with a reference layer. The STT gives the possibility to electrically modify this relative orientation by acting against the damping. In Spin Torque Nano Oscillators (STNOs) it fully compensates the damping, leading to self-sustained precessions of the magnetisation, which are then converted into voltage oscillations via the magnetoresistive effects, as first reported in 2003. In an MRAM it destabilises the magnetisation of one layer up to to the point where the magnetisation is reversed. Today GMR- and TMR-based sensors are well-established in industry, while STT-based applications remain mostly prospective, although a few applications have already found their way to industry with MRAMs. This thesis also presents these two aspects, an applicative aspect with the development of a GMR sensor, and a more prospective aspect with the study of mutually coupled STNOs, which might help for the development of STNO-based radiofrequency devices, and are from a fundamental point of view a platform to study experimentally highly nonlinear oscillators, which are seldom in nature.

The first part of this work focuses on the GMR effect and aims to produce a standardised, reproducible, GMR position sensor, which will be derived in a pressure sensor. These sensors find application in automotive environments, where a pressure sensor will measure oil pressure.

The second part of the work presented in this thesis provides material in the framework of the MEMOS ANR project, which aims at developping a hardware adapted to associative memories. STNOs are a material of choice for this particular application as nonlinear electronic oscillators. There now exists a wide variety of literature on the subject.

Namely STNOs have been the focus of intense studies due to possible applications in the field of microwave device as tunable, radiation hard, CMOS compatible devices, with frequencies ranging from hundreds of MHz to several tens of GHz, putting them on the roadmap of microwave devices. Most obviously here is not the place to provide an exhaustive review on STNOs, but we will rather focus on matters directly related to the experimental work presented in this thesis. A lot of effort has been done by the magnetism community to improve the performances of these oscillators in the perspective of their potential application as RF devices. Notably their output power and linewidth still lag behind that of the current technologies, due to their nano size which limit the output power and make them sensitive to thermal noise due to the small oscillating volume. However even though spin torque oscillators do not meet the requirements for applications, a plethora of prototypes has been demonstrated, for the generation and the detection of microwave signals. Among the strategies that have been developped to improve the microwave characteristics are the choice of materials and the type of oscillating mode, the synchronisation to a stable reference signal, and the mutual synchronisation of several STNOs, which stabilises them by increasing the oscillating volume. Namely due to nonlinearities, spin torque oscillators excel at synchronising, with synchronisation

bandwidths sometimes ten times larger than in the linear case. This latter strategy will be studied in this thesis. Over more than a decade, it has been demonstrated that two STNOs could mutually synchronise via spin wave coupling, electrical coupling, or dipolar coupling. It took more years to synchronise more than two oscillators, and now the limit has been pushed to nine. This allows us to start thinking of more complex devices.

In a second place nonlinear oscillators have required the development of a specific mathematical treatment to model the synchronisation phenomena. Although biological oscillators may display a very complex behaviour, highly nonlinear oscillators are seldom in physics. Hence despite several existing theoretical models for such oscillators, we benefit from little experimental results on revealing the implications of nonlinearities in such systems. The qualitative changes open the way to new types of devices, notably associative memories. The domain of neural networks is blossoming at the present time, but these are software-based applications of the mathematical models. As the synchronisation of several oscillators has been realised, the next step will be to explore the possibilities of more complex devices, notably bioinspired computing architectures which rely on the synchronisation states of nonlinear auto-oscillators. However the current hardware computing architectures which are based on binary information bits and separate storage and processing units, are not well-adapted to reproduce the plastic, adaptable, power-efficient, highly interconnected structure of the brain. Spin torque oscillators offer nanosized nonlinear oscillators, with large coupling capacities, what makes them good candidates for such applications.

In this thesis we find interest in technologies based on the same GMR structure, but at several stages of industrial development. First we will study the case of a GMR sensor, where the technological solutions are well assessed but still leave room for innovation. Here the physics is well-understood, and the challenges rather concern the design of the device for a specific situation. Then we move on to STNOs, which are at earlier stages of the technological development, and although the fundamental principles of these devices have already been well-studied, they still do not pass farther than the prototype stage. We focus on the strategy of mutual synchronisation, which should improve the performances of microwave devices and open the way to more complex structures, but although the fundamental process has been demonstrated all the implications are still not perfectly understood. In this perspective we will study the minimal nonlinear oscillator network constituted by a pair of mutually coupled STNOs. The originality of this work is the introduction of a microwave antenna to generate a microwave field and act as a third "ideal" oscillator, to explore the rich dynamics of this system, which find both of fundamental and applicative interests.

In this manuscript, part I presents general aspects of spintronics. The first chapter introduces the basic concepts of spintronics, and describes the fundamental physical effects of magnetoresistivity, spin transfer torque and the equation of magnetisation dynamics at play in this thesis. Chapter two presents a quick overview of existing spintronic technologies as an illustration of the implications of the preceding chapter, to contextualise the work presented in parts II and III. The aim is to provide a general overview of the field of spintronics, by covering mature technologies based on the GMR and TMR effects, to more prospective technologies involving the converse effect that is the STT with STNOs.

Part II is the applicative part and covers passive spintronics devices, that is, sensors. Chapter three describes the realisation of a specific example of magnetic proximity sensor,

which uses a GMR as an RF detector, and is derived as a pressure sensor. We present the background and issues for the design of the sensor, the mechanical considerations for the membrane subjected to pressure, the sensor design, numerical simulations and the experimental measurements.

Part III is the fundamental part and considers an active spintronic device that is the spin torque oscillator. Chapter four introduces the concepts of nonlinear auto-oscillators preliminary to the description of spin torque oscillators, and the model. In chapter five we review the state-of-the-art of STNOs and their applications. We summarise the recent results on STNOs, focusing in particular on vortex-based STNOs, and provide analytical results for the description of the effects of the bias conditions on the vortex state, and the gyrotropic mode of the vortex described by the Thiele equation, which underlies the physical results presented. In particular we outline the effect of dipolar interaction between neighbouring magnetic vortices.

In chapter six the experimental setup and the samples are presented. They consist in various geometries of single STNOs and pairs of STNOs. In chapter seven the experimental results are introduced. First we take advantage of the techniques of spectrum analyser measurements and voltage-FMR to characterise single STNOs and pairs of mutually coupled STNOs. Then we present original results on the pairs of coupled STNOs, involving the microwave antenna. In a situation where the two STNOs are not mutually synchronised, we demonstrate that the microwave field created by the antenna can be used to reveal the mutual coupling, and quantitatively measure the coupling parameters by fitting a model developped for this specific purpose. In a situation where they are mutually synchronised, we demonstrate the existence of an intrinsic frequency for the phase oscillations, which can be resonantly excited by the microwave field and eventually lead to the destruction of synchronisation. Our simulations in chapter eight from the numerical integration of the Thiele equation back our explanation, and provide more insight on the destruction of synchronisation, which is explained as a chaotic behaviour spreading the auto oscillation frequency over the spectrum.

# Part I

# Background

# Chapter 1

# Basic concepts in spintronics

In this first chapter we introduce the fundamental concepts of spintronics. We start with description of the underlying physics, the giant and tunnel magnetoresistance effects, and the converse effect that is the spin transfer torque. We then discuss the dynamical equation of the magnetisation incorporating this effect.

## 1.1 Transport in magnetic materials

Two main classes of elements in the periodic table with ferromagnetic properties are the transition metals Fe, Co, Ni and the rare earths. Ferromagnetic materials have spin dependent density of states arising from the strong exchange interaction, which favours parallel alignment between neighbouring electrons. For metals the asymmetry happens at the Fermi level. For the transition metals (rare earths) the localised 3d (respectively 4f) electrons are responsible for the magnetic properties, while the conduction electrons are the 4s (5d and 6s) electrons which have highest mobility. Transition metals have the advantage of a high mobility while the 5d and 6s electrons in rare earths are rather localised. Spins have one preferential direction which induces energy splitting of the 3d conduction shell, so the 3d shell can be separated into two subshells associated with each spin direction. The 4s shell is filled and 3d shell is partially filled, so the 4s electron do not contribute to the ferromagnetic properties, whereas the 3d electrons allow for spin imbalance (see figure 1.1). The conduction is dominated by the unsplit 4s band, 4s electrons having a much higher mobility.

Resistivity in conducting materials is associated to scattering events. Impurities at the Fermi level increase resistivity. Localised 3d electrons act as diffusive centres for the sp electron drift current. Strong spin-dependent scattering probability results in different mean-free paths or relaxation times. The associated momentum relaxation time or scattering rate according to Fermi golden rule is proportional to the Density of States at the Fermi level and thus the resistivity is spin dependent.

Conduction in ferromagnetic materials is easily pictured by Mott's two-current model. In the low temperature limit ($T \ll T_C$, the temperature is small compared to the Curie temperature), spin-flip events are neglected and spins are expected to be conserved after scattering events. In this model the current flows through two largely independent conducting channels, corresponding to the spin "up" and spin "down" electrons, with

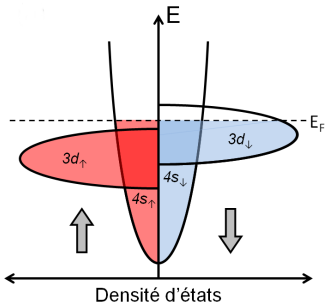


Fig. 1.1 *Density of states at the Fermi level of a ferromagnetic transition metal. The d bands are shifted depending of the spin polarity. Extracted from [2].*

respective resistances $R\uparrow$ and $R\downarrow$. [1]

$$R = \frac{R_\uparrow R_\downarrow}{R_\uparrow + R_\downarrow} \tag{1.1}$$

The resistivity for each channel depends on the DOS at the Fermi energy.

## 1.2 Giant magnetoresistance (GMR)

The Giant Magnetoresistance effect was discovered conjointly by the teams of Albert Fert [3] and Peter Grünberg [4] on effects predicted by Mott, for which they were awarded the Nobel prize in 2007. The basic idea was to tune the resistivity of up and down electrons channels by placing several magnetic layers on the electrons' path (with alternating normal metal layers), and change their relative magnetisation directions. Indeed in the absence of a magnetic field, the individual magnetisations of consecutive layers are alternate as a result of the antiferromagnetic coupling between successive layers. In the presence of a large external magnetic field, the ferromagnetic layers' magnetisations align with the applied field.

Two configurations can be envisaged. When the current is flowing along the layers' direction (CIP), the electrons diffuse in both layers, and the relevant characteristic distance is the electron mean free path, which typically is a few tenths of nanometers at room temperature (10 to 20nm for copper). It should be noted however that these values can vary largely depending on the material quality. On average electrons will have a harder path travelling in the anti-parallel configuration, as they undergo spin-related scattering events every time they enter a new magnetic layer. In the latter configuration electrons flow perpendicularly to the magnetic layers' direction (CPP) (see figure 1.2). The normal metal spacer must be thinner than the spin diffusion length, that is, the mean free path between two diffusive events leading to spin flip (around 90nm for copper at room temperature). In both cases the resistivity $\rho$ can be defined in the parallel (P) and antiparallel (AP) cases from those of the channels for spin "up" ($\uparrow$) and spin "down" ($\downarrow$) electrons. The two-current model then becomes, in the low temperature limit (which implies that no spin-flip occurs):

$$\rho_P = \frac{\rho^\uparrow \rho^\downarrow}{\rho^\uparrow + \rho^\downarrow} \quad \rho_{AP} = \frac{\rho^\uparrow + \rho^\downarrow}{4} \tag{1.2}$$

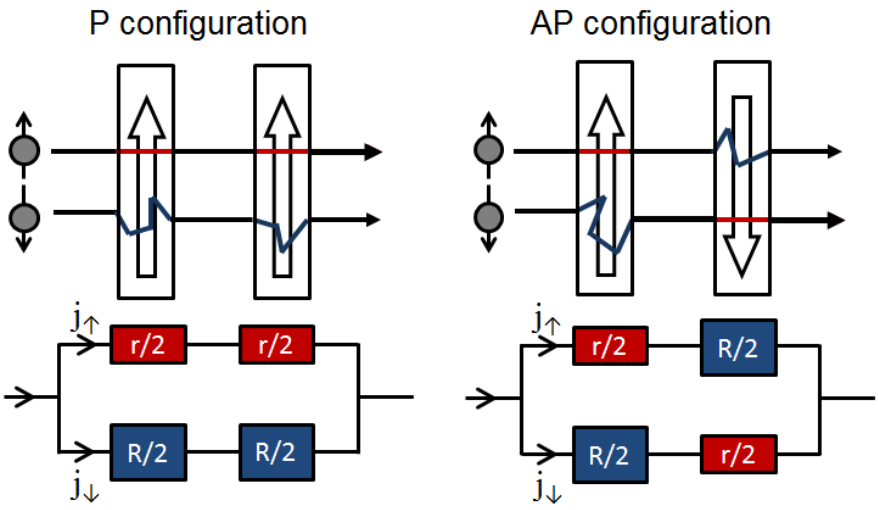


Fig. 1.2 *Two-current model applied to a spin-valve to explain the effect of GMR. Extracted from [5].*

Thus the magnetoresistive ratio

$$\mathrm{MR} = \frac{\rho_{AP} - \rho_P}{\rho_P} = \frac{(\rho^{\uparrow} - \rho^{\downarrow})^2}{4\rho^{\uparrow}\rho^{\downarrow}} \tag{1.3}$$

In the CPP configuration, the processes happen near the interface and can be seen as a competition between the spin accumulation phenomenon, which is due to the imbalance between the injected spin polarisations, and the spin relaxation, where the polarisation asymmetry is lost subsequently to diffusion processes. The Valet and Fert model [6] describes the spin-dependent transport based on an electrochemical potential related to the spin accumulation.

The simplest structure where this phenomenon can be observed is the spin-valve structure introduced by Bernard Diény *et al.* in [7], and is a typical configuration for GMR sensors today. The spin valve consists in a Non Magnetic (NM) metallic spacer sandwiched between two FerroMagnetic (FM) layers acting as the free and the fixed layer, so the free layer opens or closes the flow of electrons according to its orientation. This can be contacted either in the CIP or the CPP configuration.

The GMR is not limited to a binary value but can be expressed from the relative angle between the two magnetic layers. One way to look at it is to consider the first magnetisation layer as a polariser, by analogy with optics, and the second one as the analyser. Only the component of magnetisation vector of the spin-polarised current that is colinear with and parallel to the direction of the analyser is allowed through the analyser. So $\theta$ being the angle between the magnetisations of the two magnetic layers, the resistance of the structure can be written as

$$R = R_P \left(1 + \frac{\mathrm{MR}}{2}(1 - \cos\theta)\right) \tag{1.4}$$

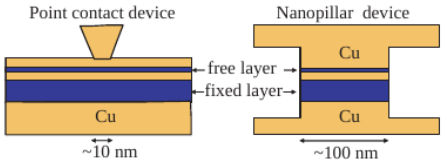


Fig. 1.3 *Two typical geometries where GMR and STT can be observed. From [12]*

## 1.3 Tunnel magnetoresistance (TMR)

GMR devices have limited magnetoresistive ratio of a few percent up to 10 percent. This has driven interest towards Tunnel MagnetoResistance. A magnetic tunnel junction stack is similar to a GMR stack but the spacer is an insulating layer through which electrons tunnel. Meservey and Tedrow demonstrated that spin was conserved during tunneling with a superconductor in 1970 [8]. Spin dependent tunneling between ferromagnets was realised by Jullière [9] at a temperature of 4K. A large TMR ratio was first measured in 1995 by Moodera [10] and Myazaki [11].

The tunneling current amplitude depends on the density of states of both layers at the interface, that is, the probability of finding an electron in electrode 1 at energy E and an unoccupied state in electrode 2 at energy $E + eV$. The transmission coefficient exponentially depends on the thickness of the spacer. In other words, the tunnel current can be tuned by the electrode density of states and the barrier parameters (potential and thickness).

In Jullière's model, the electron is assumed to conserve its spin during tunneling so the total conductance is the sum of spin-up and spin-down conductances. At 0 Kelvin, and considering only the electrons at the Fermi level

$$G_P = D_1^{\uparrow}(E_F)D_2^{\uparrow}(E_F) + D_1^{\downarrow}(E_F)D_2^{\downarrow}(E_F) \qquad G_{AP} = D_1^{\uparrow}(E_F)D_2^{\downarrow}(E_F) + D_1^{\downarrow}(E_F)D_2^{\uparrow}(E_F) \tag{1.5}$$

Defining the material polarisation at the Fermi level as

$$P = \frac{D^{\uparrow}(E_F) - D^{\downarrow}(E_F)}{D^{\uparrow}(E_F) + D^{\downarrow}(E_F)} \tag{1.6}$$

and reminding the definition of the GMR, the TMR can be calculated to be

$$\mathrm{TMR} = \frac{2P_1P_2}{1 - P_1P_2} \tag{1.7}$$

Similarly to the GMR in (1.4), the conductance of a TMR structure can be written as

$$G(\theta) = G_0\,(1 + P_1P_2\cos\theta) \tag{1.8}$$

Jullière's model turned out to be very satisfying in predicting TMR ratios. TMR have high requirements on the high crystallinity especially at the interface due to the spin filtering effect of the crystalline barrier.

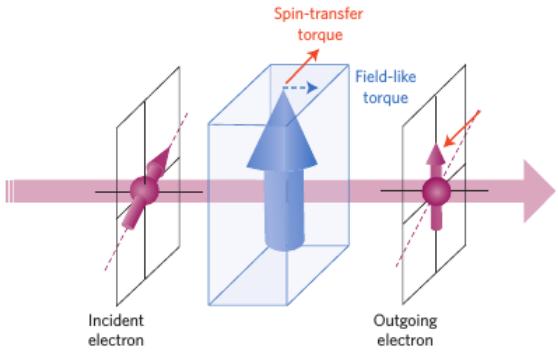


Fig. 1.4 *Schematical representation of the Spin Transfer Torque. Taken from [13]*

## 1.4 Spin Transfer Torque (STT)

### 1.4.1 Principle

Spin Transfer Torque is the reciprocal effect of the GMR/TMR, hence it can be observed typically in the same spin valve structure as the GMR/TMR reciprocal effect.

While going through a ferromagnetic layer, the spins of the conduction electrons rapidly align along the local spin direction. In reality this effect is mainly interfacial and the spin alignment happens in the accumulation zone, which is located within a few diffusion lengths around the non-magnetic/ferromagnetic interface. As the spins cross or are reflected by the interface they loose transverse spin angular momentum. Due to the principle of conservation of the angular momentum, the transverse component of the spin angular momentum has to be absorbed by the ferromagnetic layer. The current outgoing from the polarising layer carries spin momentum, which can be transferred to the second magnetic layer and eventually destabilise it (see figure 1.4). When the magnetisation is pushed away from its equilibrium direction, it starts precessing around this equilibrium. As damping is inherently present in every physical system, the amplitude of these precessions will decrease over time and the magnetisation will eventually go back to equilibrium. The STT will exert an anti damping torque if the current has the right polarity. If the current is strong enough, it may fully compensate the damping and induce self sustained precessions of the magnetisation or reversal of the magnetisation.

The effect of the STT will depend of the energy landscape which itself depends on the external applied field. This effect is at the origin of the Spin Torque Oscillator, a device which has been the subject of intense research since the first direct observation of oscillating voltage induced by STT in 2003 [14]. The STT induces the steady precessions of the magnetisation of the free layer, which is converted into resistivity oscillations thanks to the MR.

### 1.4.2 Equation of motion in the presence of STT

The dynamics of a ferromagnet in the microwave regime are well described by the Landau-Lifschitz equation [15]

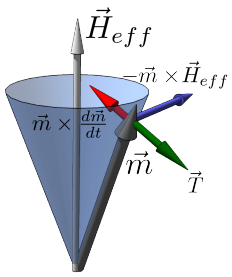


(a)

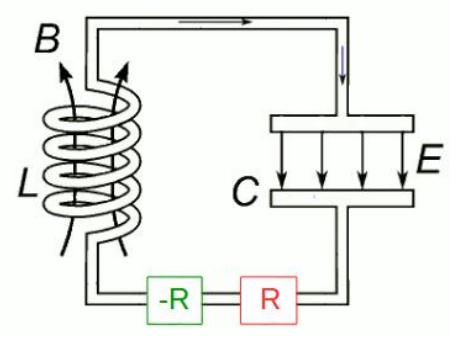


(b)

Fig. 1.5 *(a)Schematic representation of the effects of the various terms of the LLGS on the magnetisation of the free layer. (b)Equivalent RLC circuit. The STT plays the role of the negative resistance.*

$$\frac{d\mathbf{M}}{dt} = -\gamma\mathbf{M}\times\mathbf{H}_{\text{eff}} \tag{1.9}$$

In this equation $M$ is the magnetisation of the magnetic element, $\gamma = g\mu_B/\hbar$ is the gyromagnetic ratio, and $H_{eff}$ is the effective field. The effective field felt by the spins inside the magnetic material derives from the total magnetic free energy $\mathbf{H}_{eff} = -\frac{\delta\mathbf{E}}{\delta\mathbf{M}}$ and accounts for all the magnetic interactions acting on or inside the material, notably the exchange energy, the anisotropy energy, the magnetostatic energy and the Zeeman energy. From this equation the magnetisation will precess around the instantaneous effective field at the Larmor frequency after it has been tilted from its equilibrium position. The gyromagnetic ratio (typically $\gamma/2\pi \approx 30$GHz/T for ferromagnets) sets the timescale for oscillations.

As dissipation is inherent to any physical system, the magnetisation will eventually relax towards equilibrium. Gilbert completed this equation by introducing a viscous damping term [16][17] where $\alpha$ is a dimensionless parameter and $M_S$ is the saturation magnetisation:

$$\frac{d\mathbf{M}}{dt} = -\gamma\mathbf{M}\times\mathbf{H}_{\text{eff}} + \frac{\alpha}{M_s}\mathbf{M}\times\frac{d\mathbf{M}}{dt} \tag{1.10}$$

The Spin Transfer Torque (STT) was predicted by Slonczewski [18] and Berger [19]. Assuming that the magnitude of the magnetisation does not change, that the whole transverse part of the spin current is absorbed at the interface and that the incident spin direction is aligned along the first magnetisation layer, the amplitude of the transferred angular momentum can be calculated as

$$\begin{aligned}\overrightarrow{T} &= \tfrac{d\overrightarrow{m_2}}{dt} = -P_{spin}\tfrac{J}{e}\tfrac{g\mu_B}{2M_{s_2}t}(\overrightarrow{m_2}\times(\overrightarrow{m_2}\times\overrightarrow{m_1})) \\ &= \sigma J(\overrightarrow{m_2}\times(\overrightarrow{m_2}\times\overrightarrow{m_1}))\end{aligned} \tag{1.11}$$

with

$$\sigma = -P_{spin}\tfrac{1}{e}\tfrac{g\mu_B}{2M_{s_2}t}$$

$t$ is the thickness of the layer, $J$ is the current density, $P_{spin}$ is the spin polarisation, $\mu_B$ is the Bohr magneton, $g$ the Landé factor, $\overrightarrow{m_2}$ and $\overrightarrow{m_1}$ are the magnetisations of the free and pinned ferromagnetic layers respectively, $M_{S_2}$ is the saturation magnetisation of the free layer, and the change in magnetic momentum is directly deduced from the change in spin momentum $\Delta\overrightarrow{M} = -(g\mu_B/\hbar V)\Delta\overrightarrow{S}$. Adding this STT $\overrightarrow{T}$ to the LLG equation yields the so-called LLGS equation:

$$\frac{d\mathbf{M}}{dt} = -\gamma\mathbf{M}\times\mathbf{H}_{\text{eff}} + \frac{\alpha_G}{M_s}\mathbf{M}\times\frac{d\mathbf{M}}{dt} + \frac{a_J J}{M_s}\mathbf{M}\times(\mathbf{M}\times\mathbf{p}) \tag{1.12}$$

where $J$ is the current density, $a_J = \sigma M_s$ is a constant which describes the transfer rate of spin momentum from the current, and $\mathbf{p}$ is direction of the spin polarisation of the current arriving to the free layer, so the effective Slonczewski torque is colinear to the damping torque if $\overrightarrow{p} \parallel \overrightarrow{H_{\text{eff}}}$, and will act as positive or negative damping depending on the polarity of the current. The action of the various components are represented in figure 1.5(a). This last equation is often referred to as the Landau-Lifschitz-Gilbert-Slonczewski (LLGS) equation. This can be compared to an RLC circuit (see figure 1.5(b)), in which the voltage oscillates at a resonant frequency $\omega = 1/\sqrt{LC}$, but these oscillations are damped by the resistance $R$. This resistance can be compensated by adding an active component which will act as a "negative resistance". In a spin valve the STT plays the role of the negative resistance and compensates the intrinsic damping. STNOs are particularly interesting for their nonlinear properties. That is, for magnetisation precessions, the frequency of oscillations is a function of the oscillations amplitude.

In reality the Spin Transfer Torque should be described by two components, the Slonczewski Torque and the field-like Torque. The Slonczewski torque or damping-like torque is described in the previous equation and is colinear to the damping. The field-like torque is colinear to conservative term. This latter effect remains small compared to the former for CPP metallic junctions [20].

One can derive an analytical expression of the threshold current for self sustained auto oscillations of the magnetisation, at which the damping torque is exactly compensated

$$J_{thres} = -\frac{\alpha\gamma H_{eff}}{\sigma} \tag{1.13}$$

in a case where the magnetisation precessions are purely circular. Typically the order of magnitude for $J_{thres}$ is $10^{11}\text{A/m}^2$. The STT is an interfacial effect while the damping is a volume effect so the STT efficiency can be improved by reducing the layer thickness.

A crucial point for this thesis is that the precessions of the magnetisation are highly nonlinear [21], that is, the frequency of the precessions largely depend on their amplitude. The primary reason for the strong power-dependence of the frequency in spin torque oscillators is the contribution of the demagnetising field to the effective field, which in turn largely determines the resonant frequency of the auto-oscillations. As the oscillations amplitude increase, the precession angle around the effective field opens and the dipolar component of the effective field is varied [22]. These nonlinearity effects will be studied in more details in chapters 4 and 5.

## Summary

**In this chapter we have introduced fundamental processes governing the domain of spintronics, notably the concept of magnetoresistance. We have introduced the GMR and TMR effects, which are at the basis of spintronic devices today. We have also decribed the converse effect, the spin transfer torque, along with the LLGS equation which governs the dynamics of the magnetisation, and where the STT allows self-sustained precessions of the magnetisation.**

# Chapter 2

# Devices

Now we provide an overview of the fields of application of spintronic devices. We start with the GMR- and TMR- based sensors, with a particular attention to applications in magnetic recording. We then move on to applications involving in addition the spin transfer torque, with the spin torque nano oscillators and their applications in microwave devices, and with realisations of magnetic RAMs.

## 2.1 Magnetoresistive sensors

### 2.1.1 Overview of the main applications

Let us consider the spin valve, which is the basic building block today in spintronics. It consists in a pinned or fixed magnetic layer, which serves as a reference, a spacer and a free magnetic layer, whose orientation follows that of the *local magnetic field*. A Synthetic AntiFerromagnetic pinned layer increases the pinning field and reduces the hysteresis of the reference layer. The resistance of the spin valve directly depends on the relative orientation of the two layers. As opposed to coil sensors and SQUIDs, which are *flux* sensors, the sensitivity of the spin valve is not affected by size reduction as it is sensitive to the local field. Hall sensors are largely used, they are cheap and highly linear, but GMR sensors are now a thousand times more sensitive and do not depend on the magnitude of the field above a relatively low threshold [23].

The first industrial application of GMR sensors was read heads of hard disks. However applications of GMR sensors is much more widespread [24], especially in automobile industry where highly sensitive sensors would enable to replace the costly rare-earth magnets by cheaper ferrites and improve the automation efficiency.

As magnetoresistive sensors are intrinsically angle sensors, an immediate application was measuring the rotation of an object carrying a magnet thereby generating a rotating field. Yet another usage is measuring very weak field. Apart from magnetometers or electronic compasses, this is used to measure currents through the generated Oersted field. Currents can be measured down to the microampere. This has driven interest to monitor the changes in voltage of a discharging battery, were the voltage is converted into current through a well-calibrated resistive wire. The measurement circuit is then isolated from the measured current, and this current can be relatively high in automobile batteries, which can deliver voltages as high as 800V [23].

Magnetic Resonant Imaging (MRI) uses very high fields to obtain resonance at high enough frequency, what make such systems expensive and impractible for patients using a pacemaker. Namely magnetic coils sensitivity is quite poor at low frequencies. GMR sensors sensitivity can be improved down to the femtoTesla by hybridising with a superconductive loop [25]. Having efficient magnetic sensors at low frequencies would make low-field MRI possible [26].

Other biological applications are magnetocardiography [27], which maps the electrical activity of the heart using the generated magnetic field, and magnetoencephalography, which maps the electrical activity of the brain. It has been recently demonstrated that the neuronal activity could be measured using TMR sensors [28]. As a weak field sensor it may also be applied to measuring magnetic nanoparticules in blood vessels or for labelling assays [29][30].

### 2.1.2 Magnetic recording

The most striking application since the discovery of the giant magnetoresistance effect in 1988 as a very sensitive local field sensor has been for hard drive read heads since 1996, which has enabled a drastic increase in storage density.

Standard HDD read head incorporate a TMR sensor. The free layer switches according to the state of the magnetic bit and the information is indicated by the measurement of the resistance state of the TMR. The read speed is thus limited by the relaxation time of the TMR and tops below 1Gbit/s, and the bit size is limited by the SNR requirements. It was estimated [31] that the conventional Perpendicular Magnetic Recording scheme should top at 1 Terabit per square inch, allowing a 3 dB margin against thermal decay, adjacent track interference and other engineering issues.

Yet other technologies are emerging on the market. The roadmap presented in figure 2.1 serves a similar purpose as does Moore's law for the downscaling of transistors, and tracks the prospective dominant technologies for hard drives for the next decade. Heat Assisted Magnetic Recording is to be commercialised by Seagate next year with storage capacity of several terabits per inch squared [32]. In this technology the magnetic bit is heated by a LASER during the write process to ease the magnetic switching, while allowing a higher magnetocrystalline anisotropy to ensure data retention at room temperature. This should in principle increase the areal storage density by a factor of ten [33]. Shingle Magnetic Recording writes partially overlapping bits tracks, in the same way tile shingles on a roof overlap. This way the data storage density can be increased by at least 25% with the same bit size. Combined with 2D magnetic recording, it should be possible to reach areal densities of 10 terabit per inch squared with the same grain size [34]. Bit patterned media [35] would store bits on patterned magnetic island, as opposed to today's standard technologies where bits are stored on 20 to 30 magnetised grains.

## 2.2 Spin Torque Nano Oscillators (STNOs)

In Spin Torque Nano Oscillators (STNOs) a spin-polarised current with the proper direction brings angular momentum to a magnetic layer which exerts a torque opposed to the damping torque. If this anti damping torque is sufficiently strong to fully compensate the damping, this can lead to self-sustained oscillations of the magnetisation, which are then

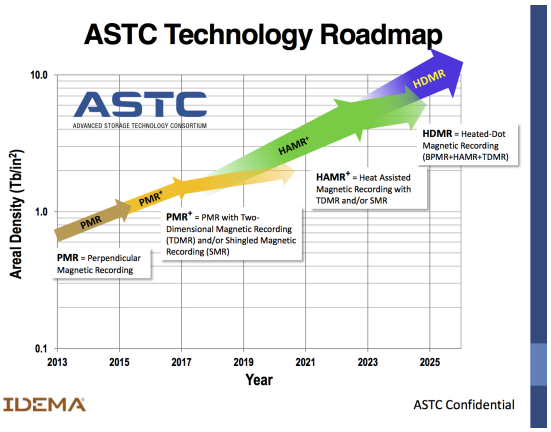


Fig. 2.1 *2016 technology roadmap according to the International Disk Drive Equipment and Materials Association. Extracted from [32]*

converted into voltage oscillations via the GMR effect. Such oscillators are particularly interesting for telecommunication devices, as their auto oscillation frequencies fall within the range of today's devices norms for mobile telecommunications.

### 2.2.1 STNOs in magnetic recording

It has been proposed to incorporate an STNO to perform both the reading and writing tasks. As for the reading process, the STNO frequency is very sensitive and very agile against external fields. The magnetic bits passing below the read head then modulates the STNO frequency and the frequency shift measured though standard techniques indicates the bit state [36]. The fast relaxation time enable a read speed of a few Gbits/s. For the writing process the rotating stray field of the STNO is a local source of oscillating magnetic field which would resonantly assist the magnetisation reversal of bits with prospects of increased density [37]. STNOs nontheless still do not meet the required figure-of-merit to reach the market. Solutions are to uses parametric locking with a reference signal at twice the free-running frequency, what works at least for proof-of-concept devices [36]. However applications are not limited to magnetic recording. Namely STNOs are sensitive to nanoscale magnetic fields in general because of their dimensions and could be designed to detect magnetic particles or as a fine local magnetic probe in general [38].

### 2.2.2 RF devices

The first applications that come to mind given the frequency range in which STNOs operate are microwave and information technologies. Yet because of their unusually high nonlinearity, STNOs endure poor noise figure which prevent them from reaching the market. Namely the amplitude and phase noise have been precisely measured [39, 40, 41] in the free running regime to be as high as -40 to -70dBc/Hz. This is still far from the targeted figure -120dBc/Hz of conventional Voltage Controlled Oscillators (VCO). Nevertheless they remain the object of a huge interest as they have other assets. Their dimensions are intrinsically submicrometric, both because the dimensions define the auto

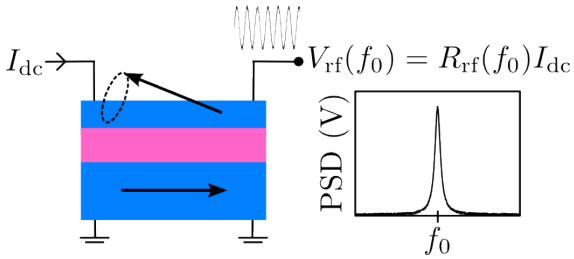


Fig. 2.2 *Basic principle of the generation of an RF voltage signal from a dc bias current in a STNO.*

oscillation frequencies and because the auto oscillation conditions require a high current density. On the opposite, typical electronic oscillators involve an RLC circuit with a diode varactor are much more space consuming. Their high nonlinearity is also responsible for a large bandwitdh of frequency modulation. As opposed to semiconductor components they are radiation hard, which is advantageous for satellite communications, and they remain compatible with CMOS technologies.

Another related issue is the small output power. For fully metallic systems the GMR ratio of a few percent limits the typical emission power a few pW [14], while the large current needed for self sustained oscillations make them virtually power inefficient. TMR have higher magnetoresistive ratio, with an order of magnitude of 100 percent. The challenge here is to maintain the tunnel barrier ultrathin to keep small resistance-area product, typically $RA = 1\Omega.\mu m^2$ so as to reach the required high current densities of $10^{11} A/m^2$. Commonly used materials for the barrier are MgO [42][43]. A last aspect to play with is to maintain large oscillation amplitude to benefit from the full magnetoresistive ratio, by oscillating between states as close as possible to the fully parallel and the fully antiparallel states [44]. In this last reference an extra intermediate layer was added to further increase the signal power.

In terms of performances the highest claims for maximum frequency based on spin torque oscillators are of 65 GHz [45]. Yet it should be possible using antiferromagnetic materials to reach the THz frequencies[46, 47].

**RF generators** The basic concept frequency generation is represented in figure 2.2.

STNOs outperform usual microwave oscillators that are Voltage Controlled Oscillators (VCOs), YIG Tuned Oscillators (YTOs) and Dielectric Resonator Oscillators (DROs) in terms of size and switching speed, and surpass YTOs in power consumption and VCOs and DROs in tunability range (see table 2 in [22]). Those nano size microwave generators oscillate at frequencies from a few hundred MHz [48] to several tenths of GHz [45]. However even when connected to dedicated wideband amplifier, they still lag behind in terms of power and spectral purity [39].

The high frequency tunability and agility could be exploited in large bandwidth Phase Locked Loops. A PLL divides the frequency, measures the phase error signal and generates a feedback current to correct the error. First experimental realisations of integration in a PLL [49, 50] have been performed but still do not meet the requirements. A technique to overcome the limited spectral purity was to incorporate a STNO synchronised to a quartz reference to stabilise the oscillations [51]. A very recent solution proposed to couple the

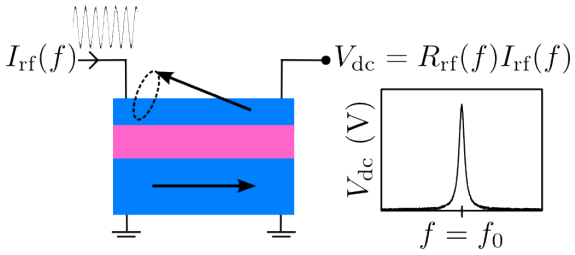


Fig. 2.3 *Basic principle of the detection of an RF signal by generating a dc voltage from a rectified RF bias current in a STNO.*

STNO to a High overtone Bulk Acoustic wave Resonator (HBAR) which generates a set of accoustic modes regularly spaced in frequency with a high quality factor. This is called a magneto accoustic oscillator and it is claimed to achieve a 200 times reduction of the linewidth without hampering the frequency agility, as the STNO successively locks to the accoustic modes of the Magneto Accoustic SH [52, 53].

**Signal processing** Now the integration of Spin Torque Oscillators in complete communication devices has been experimentally realised.

Information transmission schemes encode information by modulating the amplitude, frequency or phase of the signal. Indeed one of the most remarkable properties of STNOs is their highly nonlinear behaviour, what enables to modulate the signal. Experimental realisations of Frequency Shift Keying (FSK) schemes information transmission [54][39] display appropriate figures of merit. The upper limit of modulation frequency was measured [55] to be limited by the amplitude relaxation rate [56]. FSK with a data rate of 400Mb/s and a carrier frequency of 9.98GHz has been very recently demonstrated on an STNO fed by square current pulses [57]. It is expected that with Amplitude Shift Keying (ASK) an 1.5GHz encoding rate could be reached while ensuring a 12.5 dBm SNR [58]. A full transmission line has been tested with 2 antenna separated by 1m and encoding and decoding the information using STNOs.

Owing to the nanometric size and strong nonlinearities, several schemes can be envisaged such as using one generator and frequency mixer in one single device. A very standard signal processing scheme is the heterodyne frequency mixer. The fundamental idea is to create two new signals out of one incoming signal by mixing with that of a local oscillator, respectively the sum and the difference of the two frequencies, as to facilitate the post-processing. The former is then selected by low pass filtering. Using the STNO as local auto-oscillator and performing in-place mixing would make the scheme self-homodyne [42].

**Frequency detection** The standard frequency detection device rectifies an incoming signal using a Schottky diode and delivers a signal proportional to the input level (see figure 2.3. This strategy however is quite space consuming as it requires in addition a bypass capacitor and rf choke to return the dc current and fix the detection bandwidth. Another drawback of semiconductor devices is that they are sensitive to radiations and thermal fluctuations, what is problematic for satellite technologies.

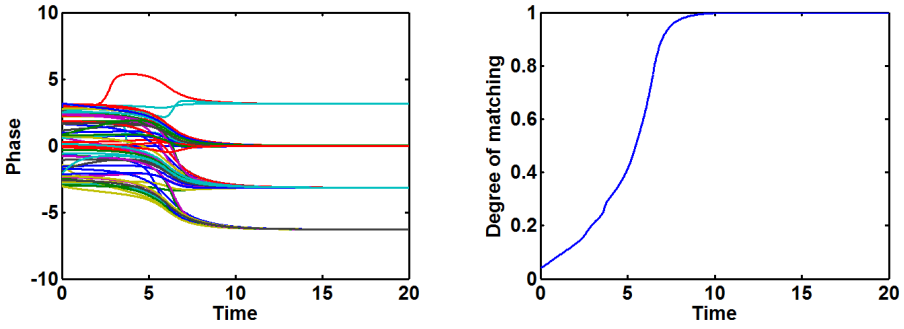


(a) (b)

Fig. 2.4 *Illustration of the convergence of an associative memory. As the phases of the individual elements (a) converge to a new distribution the degree of matching (b) converges towards a new score. Extracted from [65]*

It is possible to get a similar effect in STNO with the so called spin diode effect. An RF current is injected in the STNO, so the spin transfer torque oscillates at the same rate. The injected frequency is well chosen and matches one of the eigenmodes of the device, so the magnetisation dynamics amplified by ferromagnetic resonance [59]. The magnetisation oscillations are then converted into oscillations of the resistance at the same frequency as the magnetoresistive effects, so the mixing of the two generate a dc voltage across the device. This rectification process is the spin torque diode effect [60] to replace Schottky diodes as microwave detectors with [61]. This could be further enhanced by adding a dc bias current to the STT microwave detector to detection sensitivity 12mV/mW [62] at room temperature while diode based frequency detectors top at 3.8mV/mW. Of course the characteristics can be engineered with the proper geometry and magnetic properties, and can be tuned by adjusting the bias conditions [63]. Other schemes based on vortex oscillators envisage the resonantly induced switching [63] or resonant expulsion of the vortex core [64] as the detection mechanism. These resonant processes induce a sharp change in the Magnetic Tunnel Junction resistance and the detection is independant from the incoming amplitude. Latest results are claiming a 40mV/mW sensitivity. The full working device would discretise the full detection spectrum on several channels with several STNOs operating at different frequencies [64].

### 2.2.3 Associative memories

The applications of neural networks are to take inspiration from the brain to compute complex for recognition, classification and prediction tasks at low power consumption[66, 67]. Neural networks have been implemented softwarewise on traditional computers, but lacks physical implementation to fully benefit from their advantage, notably in terms of space optimisation and energy efficiency. Namely in traditional computing architectures processing and memory are performed by separated units, while in the brain both tasks are performed in place. Neurons are highly interconnected and the synapses are plastic, what allows the learning process. One of the main interest of neurons is their learning ability thanks to the plasticity if the synapses.

Associative memories are one particular application of bioinspired memories that are very interesting for their ability to recognise a noisy or incomplete pattern. One particular implementation is the Hopfield network algorithm. Such architectures require the implementation of a network of oscillators that can be synchronised and in which the coupling between individual oscillators can be dynamically tuned. They can be implemented in Hopfield networks, where the patterns to recognise are stored as attractors. These attractors in a network of oscillators are synchronisation states, and the input cause the network to converge to the closest attractor or synchronisation state as in figure 2.4. A degree of matching (DoM) according to some metric is used to evaluate the result. The states corresponding to the memorised patterns can be encoded in the circuit determining the frequencies of oscillators (Frequency Shift Keying) while the coupling constants are fixed, or in the phase difference between oscillators [65]. STNOs are particularly interesting building blocks for their nano size and nonlinear properties, and for their ability to synchronise easily to external signals, or mutually synchronise.

Architectures able to read the synchronisation state have already been proposed [68]. Other implementations are "reservoir computing" which expand the complexity in time instead of space, thus enabling to perform tasks on a single oscillator [69].

## 2.3 Magnetic Random Access Memory (MRAM)

One essential device of course is the Magnetic Random Access Memory (MRAM) [66, 70] schematically described in figure 2.5a. The basic principle is that information bits are stored in the relative orientation of two magnetic layers. The bit state is then read through the resistance state and the writing process is performed thanks to the Spin Transfer Torque. This memory is non-volatile contrarily to the CMOS RAMs, since the magnetisation of a magnetic layer can be retained. The design then results from a tradeoff between good data retention (high energy required from one state to the other) and high spin transfer efficiency to write with as little current as possible. For this latter reason perpendicular MTJ are preferred. STT-MRAM could be scaled down to 10nm from the magnetic and electrical point of view (etching damage cause variability which is a main issue in STT-MRAM processing up to date).

In the current architectures, different memory technologies obey a hierarchy according to the requirements from the working memory (fast, expensive and volatile) close to the processing units to the storage memory (slow, cheap and non-volatile). STT-MRAM should be able to have the density of DRAM, the speed of SRAM (both working memories) and the non-volatility of flash, as well as unlimited endurance and moderate to low power consumption [71]. The limitations that prevent STT-MRAM to replace current MRAMs are the complexity of the magnetic stacks, which require a significant technological investment, without ensuring a significant gain in storage density. Yet they could be introduced as DRAM, or in niche applications such as aeronautics where space is not an issue but radiation resistant devices are required.

MRAMs have been on the market for a few years now and 256Mb MRAM are currently shipped by Everspin [72, 73].

Still, STT-MRAM are not the only emerging non-volatile memory and has competitors. In Resistive RAM (Adesto) the number of conduction channels in a bit are changed

electrically and the information is stored in the cell resistance. Phase Change Memory (Micron, Samsung) is based on the change in resistance between crystalline and amorphous structure. In Nanotube-based RAM (Nantero) the applied electric field cause carbon nanotubes to electrostatically stick together and thereby change the individual cell conductivity.

Even among MRAMs, STT is not the only write technology. Field-induced switching, heat-assisted switching, domain wall motion, MRAM are other alternatives. STT has this advantage of being local, what favors downscalability, but also that the individual bit is written and read using the same physics, that are TMR and its complementary effect, that is, STT. A noteworthy and yet competitive scheme is the three-terminal device is demonstrated in [74], following the work in [75], which separates the read process using the classical TMR scheme, and the write process is performed by Spin Hall Effect (SHE). The SHE deviates electrons in a charge current according to their spin polarisation in normal metals with spin-orbit coupling, thereby creating a spin imbalance causing a spin current orthogonal to the initial charge current. This charge- to spin-current conversion is particularly efficient in heavy metals such as Pt with strong spin-orbit coupling. Main advantages of this latter scheme are that the high current density used for writing individual bits flows in the heavy metal only, and that the architecture of the memory is much easier (see figure 2.5b).

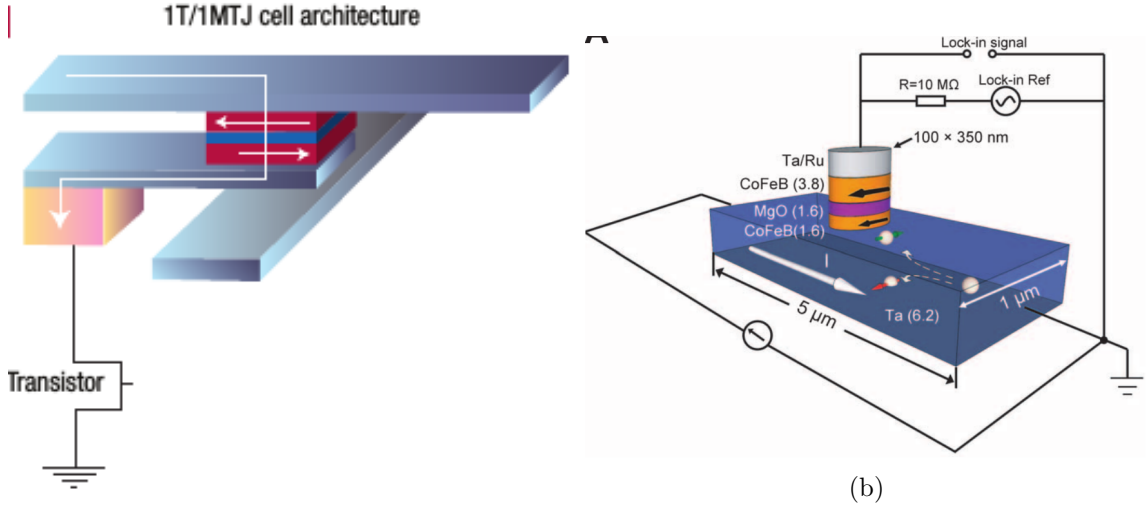


(a) (b)

Fig. 2.5 *(a) Individual MRAM cell. The binary information is stored in the relative orientations of the magnetisations of the two layers. For writing, current pulses are sent through the 'bit line' (top track) and the 'word line' (bottom track) simultaneously, and only the TMR at the crossing of the two lines is addressed. The bit state is read from the resistance of the addressed TMR. The transistor removes the unwanted current paths. Extracted from [76]. (b) Representation of the three-terminal device presented in [74]. The information is written via the SHE by sending a current in the bottom Pt slab, and read though a TMR measurement. Extracted from [74]*

## Summary

**In summary magnetoresistive sensors are well-established on the market, in a broad spectrum of applications, more particularly for hard disk drive read head which was the first motivation of their very fast development, but also in a variety of other applications. MRAMs are just emerging in industry but are already used in niche applications, and aim to replace SRAMs and DRAMs at some point. Spin torque oscillator based applications are more prospective since they still have limited performance, but their applicability have already been demonstrated in a number of prototype of microwave devices, and open the way to the realisation of bio inspired computation architectures.**

# Part II

# Passive devices

# Chapter 3

# Sensors

In this chapter we report on the development of a specific position sensor based on GMR structure which plays the role of an RF detector. This sensor is used in the framework of the development of two automotive applications, firstly a hydraulic pressure sensor, and secondly a velocity sensor for measuring the rotation velocity of a cog wheel. In a first place we discuss the issues that have to be considered in the design of a GMR sensor. We then describe the outline of and contextualise the developed device, and the subsequent steps for the validation of the feasability and characterisation with: experimental setup, simulations, and evaluation of the prototype.

## 3.1 GMR sensors background

Although the STNOs and the sensors presented in this thesis both rely on the same GMR effect, each will take advantage of a different geometry for optimised performances. Namely in spin torque oscillators it is necessary to contact the spin valve in the CPP configuration. GMR sensors can be designed in both CPP and CIP geometries, and in the latter case, can have dimensions from millimeter range down to micro range.

### 3.1.1 Noise

Of course noise is a key issue which must be treated in sensors. We will give a few essential elements but a more comprehensive review can be found in [77]. Noise is usually expressed as a Power Spectral Density (PSD) but may be as well by the square root of the PSD in $\mathrm{V}/\sqrt{\mathrm{Hz}}$ which can be directly compared to the signal.

Key characteristics for a sensor are detectivity and sensitivity. If the GMR sensor can be considered linear, then its output voltage writes as

$$V_{\mathrm{out}} = (R_0 + \frac{\delta R}{\delta H} H + O(H^2))I \tag{3.1}$$

and in this case the sensitivity may be defined as $\frac{\delta R}{\delta H}/R_0$ given in V/V/T. Then a convenient figure to compare different sensors is the detectivity, or field equivalent noise power spectral density, which is defined as the PSD divided by the sensitivity.

The most general noise to any system might be the frequency independent thermal noise or Johnson-Nyquist noise. The associated PSD is $S_V(\omega) = 4Rk_BT$ where $k_B$ is

Boltzmann's constant. The thermal noise cannot be reduced but is voltage independent, and since it is present at all frequencies its impact will be directly related to the working bandwidth. Shot noise is due to the quantized nature of electrons, and is detectable only if there is a barrier to cross, where this discrerte nature is revealed. So in our case, this shot noise will increase the noise figure in TMR but will not affect GMR. A $1/f$ magnetic noise may also exist due to domain fluctuations.

The low frequency noise is usually referred to as flicker noise or 1/f noise from the typical power law of this frequency decreasing noise. This noise is very general to all physical or even biological systems, and originates in GMR from resistance fluctuations, as opposed to the thermal noise which is related to voltage fluctuations. This has several implications. Firstly, the PSD scales as $I^2$ or $V^2$ (or even faster in cases where the resistance is modified by the current, for instance through heating). Secondly it is volume dependent. By considering the total resistance $R$ as a sum of $N$ small resistances $r$, then the fluctuations of $R$ are $\sqrt{N}$ larger than the individual fluctuations of $r$. So for a given $R$, the fluctuations are scaling with the square root of the volume. These two consequences are visible in Hooge's phenomenological law which describes the PSD of the 1/f noise as [78]:

$$S_V(f) = \frac{\gamma_H V^2}{N_c f} \tag{3.2}$$

where $\gamma_H$ is Hooge's parameter, $V$ is the voltage, $N_c$ is the number of carriers and $f$ is the frequency.

Random Telegraphic Noise arises from fluctuations between two levels of comparable energies over an energy barrier. In small devices it usually becomes visible when small defects start to dominate and depends on field, bias current and temperature.

Using a yoke can strongly reduce the magnetic noise characterised by domain wall formation, which can be visible as small jumps in the unsaturated part of the R(H) GMR response.

### 3.1.2 Shape

Contrarily to memory devices which rely on the magnetic hysteresis loop, a sensor needs to be linear to provide quantitative measurements (see figure 3.1a). The technique consists in insuring that the magnetisation angle between the free and the fixed layer is 90° at zero external field, by using an additional fixed field of a permanent magnet or by patterning the sensor's shape.

The sensitivity of GMR sensors is typically 2-4%/mT. TMR have a at least 20 times larger sensitivity, but at the cost of greater electric noise at low frequencies. As we move to small dimension ferromagnetic layers, there arise competitions between the short-range exchange interaction and the long-range dipolar interaction which tend to create magnetic domains in the ferromagnetic layer. This is problematic as the a non uniform domain leads to jumps in the magnetoresistance as the domains rotate non uniformly. This can be corrected by playing with the magnetic anisotropy, by designing the shape anisotropy of the sensor. The yoke shape as presented in figure 3.1b has this advantage of concentrating domain walls at the corners, while the ferromagnetic layer on the elongated part in between contains one single domain rotating homogeneously.

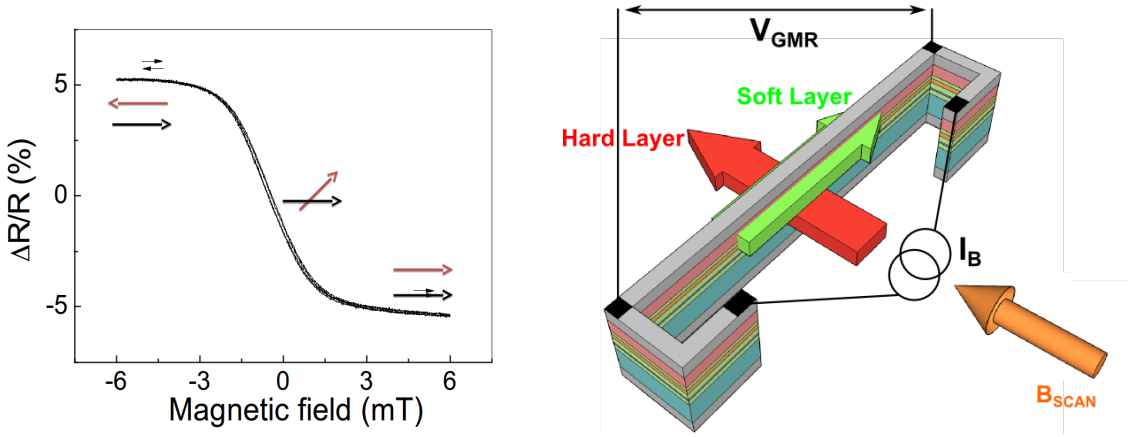


(a) *Typical linearised GMR curve.* (b) *3D rendering of a yoke. From [79]*

Fig. 3.1 *(a) Field dependence of the resistance of a linearised GMR, as the free layer rotates from parallel to antiparallel and back with regards to the pinned layer. (b) The yoke is rendered as to make several layers visible. The contact points for the bias current and the voltage measurement are different, so as to measure the voltage of a single domain.*

The meander shape is an extension of the Yoke shape in the sense that the domain walls are located at the edges and the magnetic domains inbetween are uniform thanks to the anisotropy, but then several of these structures are connected in series with contacts placed to short-circuit the non-uniform parts.

### 3.1.3 Electronics

One issue with GMR sensors is that the magnetic part of the signal, that is, the GMR signal, is only a small fraction of the signal. The major part lies in the constant part of the resistance. This may limit us for the following amplification stages as the amplified useless part of the signal may saturate the electronics.

One typical arrangement for GMR sensors is the Wheatstone bridge, depicted in figure 3.2, which allows to cleverly substract the non-magnetic part of the GMR signal and centre the useful signal around zero. For a current $I$ flowing from $V_+$ to $V_-$, the voltage for both shielded resistances are $RI/2$ and the voltages of both unshielded resistances (thereby sensitive to the magnetic field) are $(R-\Delta R)I/2$. The point at $V_+$ sees two currents with equal intensity departing and $V_-$ two currents with equal intensity arriving. However OUT+ and OUT- see one current arriving and one departing, or to put it differently, two current with opposite intensities. So if we measure the voltage between OUT+ and OUT-, the contribution to the voltage due to the nonmagnetic part of the resistance $RI/2$ cancels out with the contribution of the shielded GMR $RI/2$. This way the magnetic component only of the signal is measured.

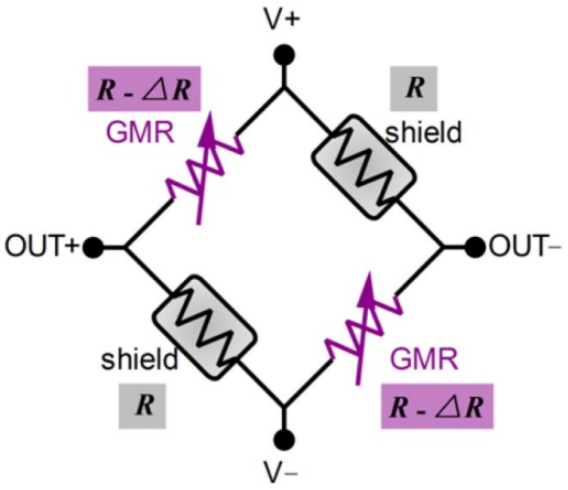


Fig. 3.2 *Bridge configuration for the GMR. The bridge is biased through $V_+/V_-$ and the output voltage is measured as $OUT_+ - OUT_-$. The two shielded GMR are used to remove the non-magnetic part of the GMR from the resistance signal. Extracted from [80]*

## 3.2 Objectives and applications

### 3.2.1 Principle

In automotive applications, a position sensor such as the one developped here could be used as a speed sensor, to measure the exact position of the engine and the wheels. This would enable to trigger gas injection at the right time, thereby reducing gas consumption. The requirements are typically an accuracy better than 0.1° on the position of the drive shaft. This is achieved by introducing a cog wheel fixed on the main axis of the engine. The cog wheel is dedicated to the velocity measurements. The sensor is placed outside the engine and measures the times at which the cog teeth pass by.

Our approach consists in using GMR sensors to measure the RF field generated by a magnetic coil and reflected by a metallic material. The sensor is in fact a proximity sensor and measures the distance to the metal surface. The advantage of using an RF field is that it will be reflected by any conducting material, what lifts up some constraints on the material. In addition, the sensitivity of GMR sensors allow to use small signals. The working range of GMR sensors is typically 1kHz ot 100MHz. Lastly, this solution avoids the use of costly rare-earth permanent magnets [23].

Since the developped sensor is a position sensor, it can as well be applied to pressure sensing. In this application the GMR sensor just measures the displacement of a membrane exposed to a pressure. The targeted application lies in the automotive field, and consists in measuring oil pressures. The challenge is to be able to measure pressures varying from 0 to 250bar with a 0.5bar accuracy on the entire range of measurement.

Pressure sensors range in a wide spectrum of technologies, dominated by the strain gauge, which is based on measurement of the deformation of a membrane using piezoelectric elements are available. But their long term reliability mainly due to assembly is presently a major issue.

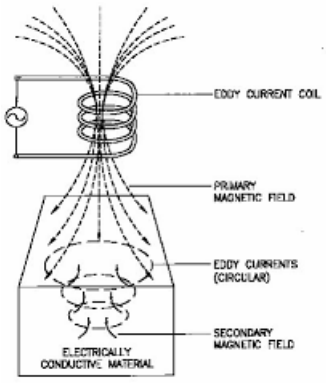


Fig. 3.3 *Basic principle of eddy currents. The magnetic field generated by the coil induces currents (therefore the name eddy) in the conducting medium, which in turn create a magnetic field opposed to that of the coil.*

### 3.2.2 Non Destructive Testing

Non-Destructive Testing (NDT) or Non-Destructive Examination (NDE) is a technique used to detect and measure the presence of defects in conductive materials [81]. This is of critical importance to inspect the reliability of devices, but also in aeronautics applications to detect fatigue defects. The conductive piece is exposed to an AC magnetic field which creates eddy currents (see figure 3.3). These eddy currents create in turn a magnetic field opposed to the first one, which can be measured as the reflected field. The presence of cracks and defects in the inspected sample disturbs the path of the eddy currents, and this can be measured by changes in the polarisation of the reflected field.

The principle of the device developped here is similar. The sensor is stuck to the coil and measures the total in-plane field created by both the coil and its image by the metallic slab.

The penetration depth of the magnetic field depends notably on the material conductivity and the signal frequency. The field amplitude inside the material decreases exponentially with a characteristic length that is the skin depth, which stems directly from Maxwell's equations and is defined as

$$\delta = \frac{1}{\sqrt{\sigma \mu \pi f}} \tag{3.3}$$

where $\sigma$ is the material conductivity, $\mu$ is the magnetic permeability of the material, and $f$ is the frequency. At 1MHz the skin depth is 82µm for aluminum and 7.8µm for steel.

### 3.2.3 Membrane Deformation

The basic principle of this pressure sensor is to measure the displacement of an elastic membrane subjected to an homogeneous pressure. The following formula tells us what is the displacement $w$ of a point initially located at coordinates $(r,\theta)$ of the disk.

$$w = \frac{3}{16}\frac{p}{Eh^3}(1-\nu^2)(a^2-r^2)^2 \tag{3.4}$$

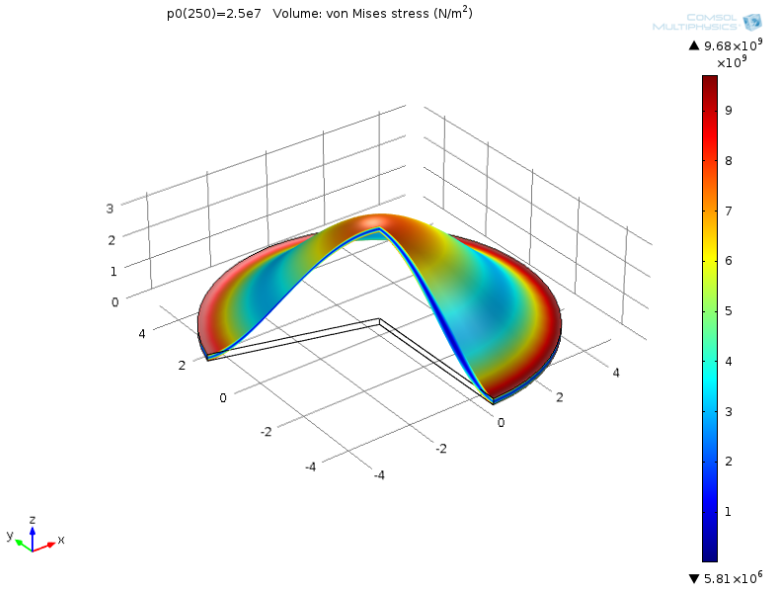


Fig. 3.4 *Deformation of a thin CuBe disk subjected to a 250 bar pressure. The maximum deformation is 2.5 mm. The colors show the stress modulus for each individual point, and is maximum at points where the material distortion is maximised.*

with $E$ Young's modulus, $p$ the pressure, $h$ the slab thickness, $a$ the disk radius, and $\nu$ the Poisson ratio. From this equation we know that the vertical displacement of each point of the membrane is linear with respect to the pressure, with a different amplitude of course according to the point's distance from the centre of the disk. The deformation profile calculated by COMSOL is presented in figure 3.4.

The choice of the material for the membrane is critical. Namely we want the membrane to deform sufficiently so the sensor has enough precision on the entire range of measurements. From the stress-strain deformation curves we learn that as the constraint increases, the material enters several domains before breaking, and these domains are delimited by several points. The first one is the proportional limit, up to which the stress and strain remain proportional to each other. Then is the elastic limit, which defines the maximum load below which the material will return to its original position when unloaded. Then the material enters the plastic regime, where the material undergoes micrometric rearrangements until it eventually breaks, so we want to keep below the elastic point. Namely one key issue is the plasticity of the membrane, which will allow the repeatability of the measurement and the lifetime of the sensor. An other process that enters in play as the material endures repeated loading/unloading cycles is the material fatigue, from the birth and propagation of microcracks in the material which will alter its properties and durability [82], as can be seen in figure 3.5.

### 3.2.4 Sensor design

To avoid confusion, let us specify that in this section, as the coils are flat and contain several turns in the same plane, we will often describe the coils as made of one single

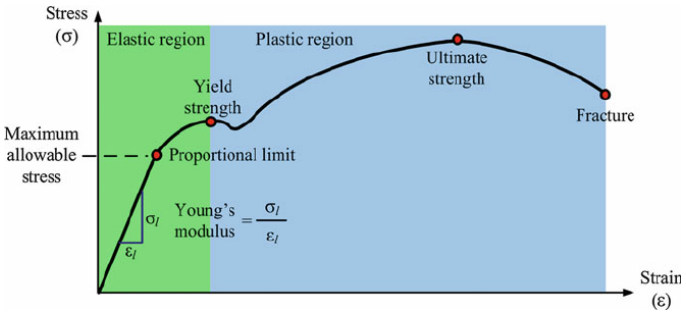


Fig. 3.5 *Stress – strain curve of a ductile material. Extracted from [83].*

ribbon, which in fact contains several turns tracks or wires aligned in the same plane.

Several configurations have been envisaged for the design of this sensor. One fundamental point is that the GMR sensor is a planar sensor and can only measure an in-plane field as a magnetic compass would do. The total signal is created by the coil and its image by the conductive plane, so we want to place the sensor at a point where most or all of the field is in-plane, that is, on the side of the coil. Because of the small size of the individual GMR, the measured field is mostly due to the local environment, so the field at the location of the sensor can be approximated to the one created by the ribbon beneath it (see figure 3.6(b)), which can be considered in-plane, plus its image by the reflective plane.

Two main configurations have been envisaged: single-coil (figure 3.6(b)) and double-coil (figure 3.6(d)). On both figures is marked a round point at the location of the sensor, and which defines the point where the z-axis crosses the coil plane. The single coil geometry has the advantage of its simplicity, for exploratory purposes at the begining of this study. Considering that the in-plane field sensed by the GMR sensor is mainly due to the one generated by the ribbon underneath, then the geometry of the double coil should have the advantage of creating a larger field for the same area occupation. This should not saturate much more the GMR sensor, as it is very local and from its small dimensions, it is sensitive essentially to the field created by the wire right underneath and not the whole ribbon. Of course the two coils should be fed with currents of opposite polarities, so the in-plane components at the GMR location do not cancel each other (see figure 3.6(e)).

Since the GMR sensor is very local, one way to get rid of the strong direct signal of the coil on the sensor is to introduce one additional track with a current of the coil with the same intensity but opposite polarity, so the field created is rotating in the opposite direction, and the local field may be cancelled out at one specific point. However since the field created by this counter-turn is strong only locally, but will be small at longer range compared to the one created by the rest of the coil, this should not affect the measured reflected signal.

A last problem that should be treated is the positioning and direction of the coil. Namely when measuring the position of the closest point to the coil, we assume that the coil is oriented parallel to the measured membrane, which might be imprecise as the coil alignment might not be perfectly aligned, or affect by thermal fluctuations or any other perturbation. The idea is then to consider that in a square coil, the centres of each side

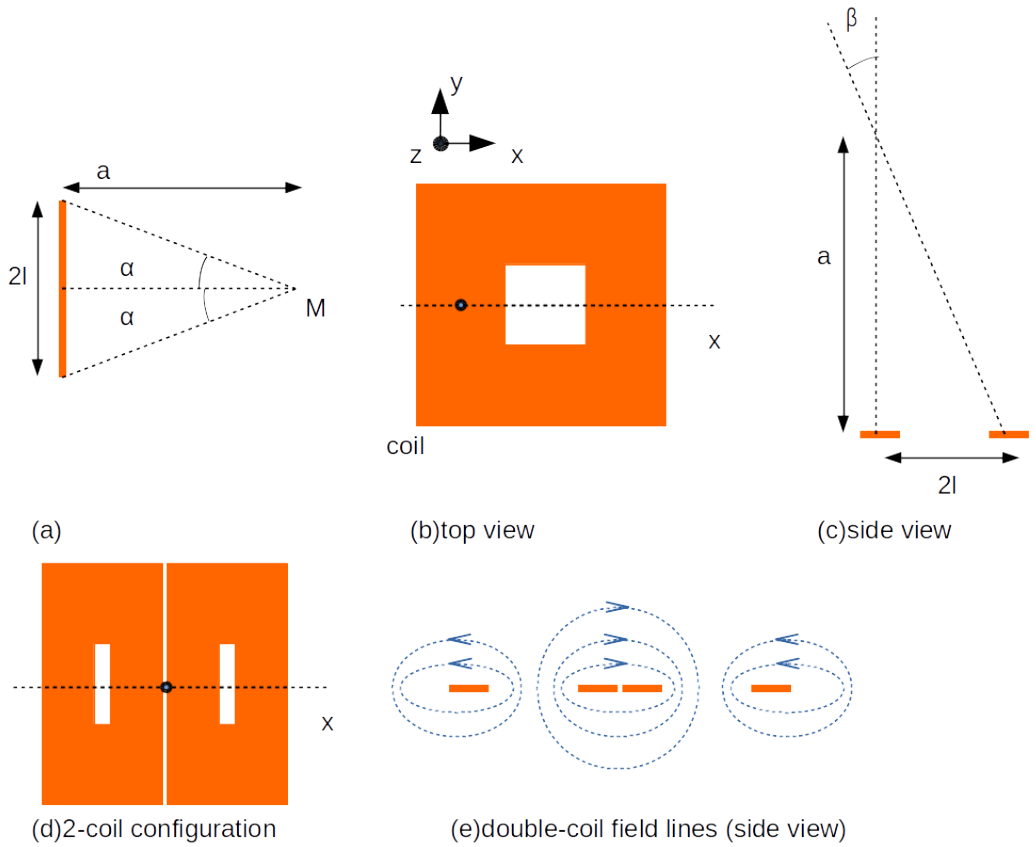


Fig. 3.6 *(a) Notations for the calculations of the field created by a wire of length 2l at a point M comprised in its middle plan. (b) Top view of the coil with the plane considered for the calculations indicated in a dashed line. The dot indicate the sensor location on the coil and the z-axis is crossing the coil plane at this point. (c) Side view of the problem for one coil. (d) Top view of the two-coil configuration. The dot indicate the sensor location between the coils and the z-axis is crossing the coil plane at this point. (e) Side view of the cut of (d) in the plane represented by the dashed line, with field lines within this plane.*

of the square are equivalent, but are well-separated. So by placing a GMR sensor on each side of the square coil, we have access to the relative orientation of the coil with respect to the membrane, and to compute the correct signal from the signal originating from each side of the coil apply the corrections needed.

## 3.3 Calculations

In a first approximation it may be considered that the field reflected by the metallic slab is dominated by the closest point to the coil/sensor ensemble. The main physical problem is being able to properly describe the in-plane magnetic field evolution at the location of the sensor/coil as the gap between the coil and the metallic slab widens.

### 3.3.1 First principle calculations

The evolution of the amplitude of the in-plane component field with respect to the distance from the coil can be derived and approximated in the long-distance limit.

Starting from the Biot and Savart law

$$d\overrightarrow{B} = \frac{\mu_0 I}{4\pi r^2}\overrightarrow{dl} \times \overrightarrow{u} \tag{3.5}$$

where $\mu_0$ is the magnetic permeability of vacuum, $I$ the current flowing through the wire, $\overrightarrow{dl}$ the length of the current infinitesimal element and $r$ the distance from the magnetic element to the point where the field is calculated

The field created in the plane crossing the middle but perpendicular to a finite-length wire of length $2l$ at a distance $a$ of the wire as indicated in figure 3.6(a) can be calculated by integrating the Biot and Savart law over the length of the wire.

$$B_r = \frac{\mu_0 I}{4\pi r}.2\sin\alpha = \frac{\mu_0 I}{2\pi r}\frac{2l}{\sqrt{a^2+4l^2}} \tag{3.6}$$

Now if we consider a square coil with a current $I$ flowing through the $N$ turns, and calculate the in-plane component of the magnetic field at a point located above the centre of one side of the coil marked as a dot on figure 3.6(b). Then from the symmetries we know that the field will be contained in the plane represented by the dashed lines, and that the contribution of the two wire parts parallel to this plane (with currents flowing in antiparallel directions) will cancel out each other. So we consider only the wires crossing this specific antisymmetry plane. The field created by the wire crossing the z-axis is parallel to the x-axis, according to the symmetries.

So the x-component of the field created on a point M at a distance $a$ by wire 1 writes

$$B_{1,x} = \frac{\mu_0 NI}{2\pi a}\frac{l}{\sqrt{a^2+4l^2}} = \frac{\mu_0 NI}{2\pi a^2}\frac{l}{\sqrt{1+4l^2/a^2}} \tag{3.7}$$

which can be approximated for $a \gg l$ by

$$B_{1,x} = \frac{\mu_0 NIl}{2\pi a^2}\left(1 - \frac{2l^2}{a^2} + O\left(\frac{l^4}{a^3}\right)\right) \tag{3.8}$$

This point M is located at a distance $\sqrt{a^2+(2l)^2}$ from the centre of the opposite wire (see figure 3.6(c)). So a similar calculus gives out

$$B_2 = -\frac{\mu_0 NI}{2\pi\sqrt{a^2+4l^2}}\frac{l}{\sqrt{(a^2+4l^2)+4l^2}} = -\frac{\mu_0 NI}{2\pi a^2\sqrt{1+4l^2/a^2}}\frac{l}{\sqrt{1+8l^2/a^2}} \tag{3.9}$$

where the minus sign comes from the fact that the current flows in the opposite direction in this branch. In order to get the x-component of $B_2$ we need to multiply the previous result by $\cos\beta = a/\sqrt{a^2+4l^2} = 1/\sqrt{1+4l^2/a^2}$, so the previous result becomes

$$B_{2,x} = -\frac{\mu_0 NI}{2\pi a^2(1+4l^2/a^2)}\frac{l}{\sqrt{1+8l^2/a^2}} \tag{3.10}$$

which can be approximated for $a \gg l$ by

$$B_{2,x} = -\frac{\mu_0 NIl}{2\pi a^2}\left(1 - \frac{4l^2}{a^2} + O\left(\frac{l^2}{a^2}\right)\right)\left(1 - \frac{4l^2}{a^2} + O\left(\frac{l^3}{a^3}\right)\right) \tag{3.11}$$

$$= -\frac{\mu_0 NIl}{2\pi a^2}\left(1 - \frac{8l^2}{a^2} + O\left(\frac{l^2}{a^2}\right)\right) \tag{3.12}$$

So, summing the two contributions

$$B_x = B_{1,x} + B_{2,x} = \frac{\mu_0 NIl}{2\pi a^2}\left(\frac{12l^2}{a^2} + O\left(\frac{l^2}{a^2}\right)\right) \tag{3.13}$$

$$= \frac{6\mu_0 NIl^3}{\pi a^4} + O\left(\frac{l^5}{a^5}\right) \tag{3.14}$$

So the x-component of the field scales as $1/a^4$ along this axis.

For the double-coil configuration the result is similar since the symmetry of the problem is similar, as can be observed from figure 3.6(e): the field $B_1$ is reinforced by the presence of the tracks of the second coil closest to the center, and the field $B_2$ is reinforced by the field created by the wires of the second coil farthest from the center.

### 3.3.2 COMSOL

COMSOL Multiphysics ® is a finite elements calculation software, conceived to simulate physics problems. One primary question in this kind of problem is to validate the reliability of the simulation tools for the specific problem we are dealing with, by comparison with experiments. A comparison of several simulation tools is given in figure D.1 (in appendix D).

In COMSOL Multiphysics® simulations the problem is calculated within a bounded volume, and the properties of the surfaces have to be well-defined. Using perfect magnetic conductors or insulators allows to take advantage of the symmetries of the system to perform the calculations on a smaller volume. The external borders of the problem can be pushed away by using "infinite domains" designed for that purpose, in which the dimensions are $10^3$ larger than the dimensions entered, so the problem limits may be considered to be at infinite distances. The coils are then defined using 2D flat cables and the mesh is designed in an adaptative manner. The mesh size is refined close to the coil, edges and smaller features.

In the first calculations the coils were fed with a 4mA current for 25 turns of wire, what makes a 100mA.turn for the whole ribbon. The outer dimensions of the coil where 2.2mm and the ribbon width was 300 microns wide. For the double coil configuration we kept the same total outer surface for the coils and the same ribbon width. The parameters in figure D.1 are slightly different: the single coil is fed with a 10mA current and has 30 wires having a total width of 600 microns.

From figure 3.7 one can observe that the field dependence has an $1/r^4$ power law at long range complies with the ab initio calculations. As for the comparison between the two-coil configuration and the single-coil configuration, there is a qualitative difference at small distance of the coil. This is not problematic since the monotonicity of the curve is not

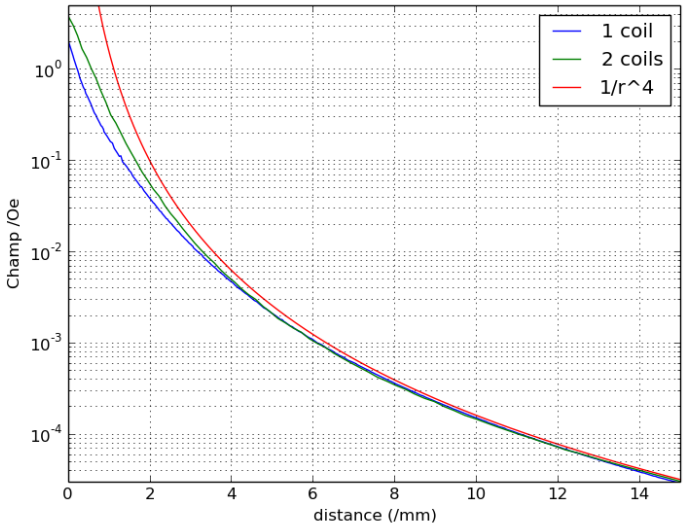


Fig. 3.7 *COMSOL calculations of the field evolution along the z-axis (see figure 3.6 for the 1-coil and 2-coil configurations). The $1/r^4$ curve is plotted just for comparison.*

affected, that is, the field measurement is not ambiguous for the distance measurement. Indeed this would even be an argument in favour of the double-coil congfiguration as the short-range measurements, however the difference between the two configurations fades very fast. The reason for the larger signal at short range can be simply explained by the fact that since the two coils are side-by-side, the ribbon which creates the dominating magnetic signal close to (that is, when the other parts of the coil can be considered very far). Indeed, the two configurations become equivalent after a range roughly equal to the outer dimensions of the coil.

## 3.4 Experimental setup

The experimental setup is described in figure 3.8. The configuration represented is the one used for the pressure evaluation, where the sensor faces the elastic membrane, but the principle remains the same for the other types of measurements. For the first proof-of-concept evaluations the hydraulic system was replaced by a 3d-positionner capable of positionning a device with a micrometric precision. The GMR sensor was screwed to a fixed structure, and the metal slab was displaced on top of a supporting column. It was important to keep all metallic parts several centimeters away from the sensor, to avoid couplings of the metallic parts with the coil. The coil and sensor are deposited together during the nanofabrication of the device, so they have the same substrate.

The coil and sensor are fed with an RF signal from the same synthetiser at MHz frequencies with a slight shift of 1kHz. The signal is created as a voltage signal, but thanks to the high resistances of the diverse elements (typically 1.5kΩ fot the GMR bridges and 800Ω for the coils, the GMR effect plays little role due to the small magnetoresistance

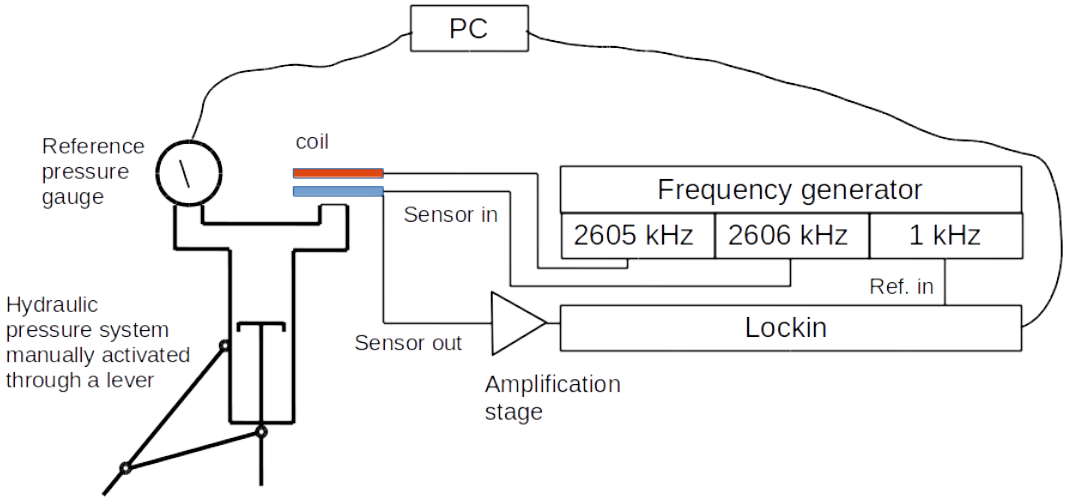


Fig. 3.8 *Experimental setup for the pressure measurements. The pressure gauge is used to calibrate the sensor. The measured signal is demodulated in situ by the GMR and measured with a lock-in. The computer is used to store the two measurements simultaneously.*

ratio) the conversion factor from voltage to current can be considered to be fixed. The signal is demodulated in situ by the GMR. Namely the magnetic field causes the GMR to oscillate at a frequency $\omega_1$, while the GMR is fed by a current oscillating at a frequency $\omega_2$. The measured voltage signal $V_m = R(\omega_1)I(\omega_2)$ thus mixes the two frequencies and two frequencies are present in the output signal, respectively at $|\omega_1 - \omega_2| = 1$kHz and at $\omega_1 + \omega_2$. The low-frequency signal is measured by the lockin after an amplification stage. The synthetiser generates a reference signal for the lockin at 1kHz, so the two devices use the same clock.

The measurements could have been performed with a dc output in principle, by setting the GMR bias current and the coil current at the same frequency. But it was decided to generate the output signal at 1kHz to avoid the $1/f$ noise.

### Pressure sensor

The membrane was part of a lid screwed on top of a tube under pressure. For metallic membranes, it was simply usinated by drilling a hole in the inner part of the lid, as to discharge the material up to the desired thickness. In the case of a crystalline membrane, the metallic lid was perforated with a small margin to allow sticking the crystal. Then the linearity of the membrane displacement with respect to pressure was evaluated using a LASER distance measurement system. To measure the membrane deformation we used a LASER proximity sensor from Micro Epsilon with a C-box connector as a reference. The pressure inside the cavity was measured by a DPI-104 Druck digital gauge test from General Electrics as a reference.

As mentionned above, one key issue of this device is the plasticity of the membrane. As part of our measurements we measured the evolution of the membrane deformation

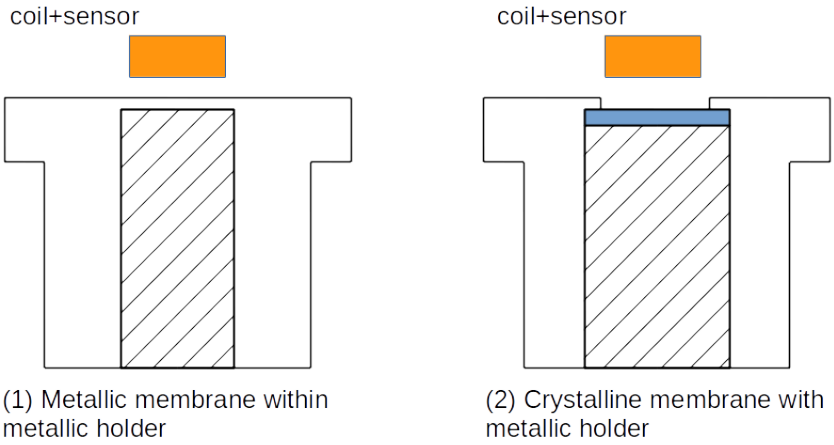


Fig. 3.9 *In the pressure sensor arrangement, the sensor is fixed to a cap and measures the deformations of either a metallic membrane, which is then part of the cap, or a crystalline membrane, which is then stuck to the metallic cap. In this latter case the membrane is slightly larger than the window opened in the metallic cap.*

after a 48h exposition to a permanent pressure of 200bar.

A first solution was to use crystalline membranes such as silicon or sapphire, coated with a thin metallic film, as indicated in figure 3.9. The difficulty was to immobilise the crystalline disk on the window opened in the metallic lid, without exerting a too strong constraint on the crystal to avoid breaking the crystal. We first placed the crystal in front of the window, and then sticking it. However it was not possible to find a hard enough glue, and the slow relaxation of the glue after unloading was problematic as it caused slow relaxation of the membrane to its initial position. Additionaly it was difficult to control the deposition of the glue to ensure equal repartition of the effort over the entire membrane.

With metallic membranes we had the advantage that the entire lid could be made of the same material as the membrane, but then arose the issue of the relaxation. After several loading/unloading cycles over time the membrane would deform and not return to its initial position. This eliminated the brass and CuBe from the possible materials. Ti alloys or steel alloys were finally found to have the appropriate elasticity for our purposes.

As well one measurement consisted in heating up the membrane by putting the cap in contact with a solder, to check the endurance of the membrane to a long time exposition to high pressure and therefore high stress, with high temperature conditions.

In a first row of measurements the sensor was wire-bonded and isolated from its environment with a glue bubble on top. This technique is limited as the thinner cover layer that could be achieved at the time was in the order of magnitude of 500 microns. Later the sensors will be integrated circuits produced by Allegro microsystems ® already capped with a 200 microns capping, so the sensor could be approached much closer. This is essential as the sensitivity of the sensor decreases very fast as the distance increases.

## 3.5 Measurements

From the measurements in figure 3.10 the evolution of the measured signal against coil-reflector separation, where the reflecting metallic slab is positionned using a 3d-positionner. This was measured with a copper slab positionned with micrometric precision. The same measurement is performed for several frequencies. The phase is plotted between $-180°$ and $180°$ and a modulo operation is applied, this is why the phase increasing over $180°$ is seen as a jump. There is a continuous phase evolution in the reflected signal on each curve, although the wavelength of the frequencies used here for signals ranging from a few kHz to a few MHz. The signal is decomposed between amplitude and phase, this is why we can see the amplitude going to zero and increasing again in absolute value, while the phase increases beyond $180°$. The total signal evolution is in fact evolving monotonously. The varying intensity of the signal with respect to the frequency should be put into relation with the frequency-dependent impedance of the coils. The signal at long coil-reflector separation is due to a coupling with an external element. The area of interest in figure 3.10 is located within the 5 first millimeters, which gives us in the best case a 2.5mV dynamics, thus a resolution of 50nV/µm.

Now let us consider the measurement in figure 3.11, which is an actual pressure measurement performed with our GMR sensor. In the following measurement the coil was fed with a 20Vpp signal. Taking a 800Ω resistance, this gives a 2.5mApp current to create the magnetic field. The GMR sensor was fed with a 5Vpp field, which is converted by the 1.5kΩ into a 3.5mApp bias current.

The measurements in plot 3.11 were performed during a pressure unloading. The system is initially loaded with a 200bar pressure. At the starting time of the experiment, the valve is opened and both the demodulated signal from the GMR sensor and the pressure measured by the pressure gauge are taken simultaneously at regular times. Comfortingly, the dependence between the two quantities is linear. This validates the principle of functionning of the sensor. More points are taken at low pressure since the unloading is slower when the pressure difference with the outer space is smaller, and the points are taken at regular time intervals. As for the sensitivity, the signal ranges from 3.0V to 4.8V to cover the range of 0 to 200bar, what corresponds to a sensitivity of 9mV/bar. From this data we measure a 20.7mV standard deviation of the signal, which is not acceptable if we want a resolution better than 0.5bar. However in this measurement the signal is originating from a single sensor. The noise component due to vibrations can be eliminated by using a second sensor located on the opposite side of the coil, so the two sensors are in principle vibrating together, and perform a gradiometer measurement. It should also be noted that the reference for the pressure measurements is itself subjected to noise, which adds up to the sensor's noise. In addition this is the raw signal without any form of processing, so it is still possible to improve the signal-to-noise ratio by applying proper post-processings. Other sources of noise are the electronic devices, which can be reduced by employing dedicated signal generators and amplifiers with the packaging.


Fig. 3.10 *Dependence on signal frequency of sensor measurements for a 1mm reflective copper surface. Note that the signal is decomposed between phase and amplitude, so the zero-crossing is not obvious at first sight.*

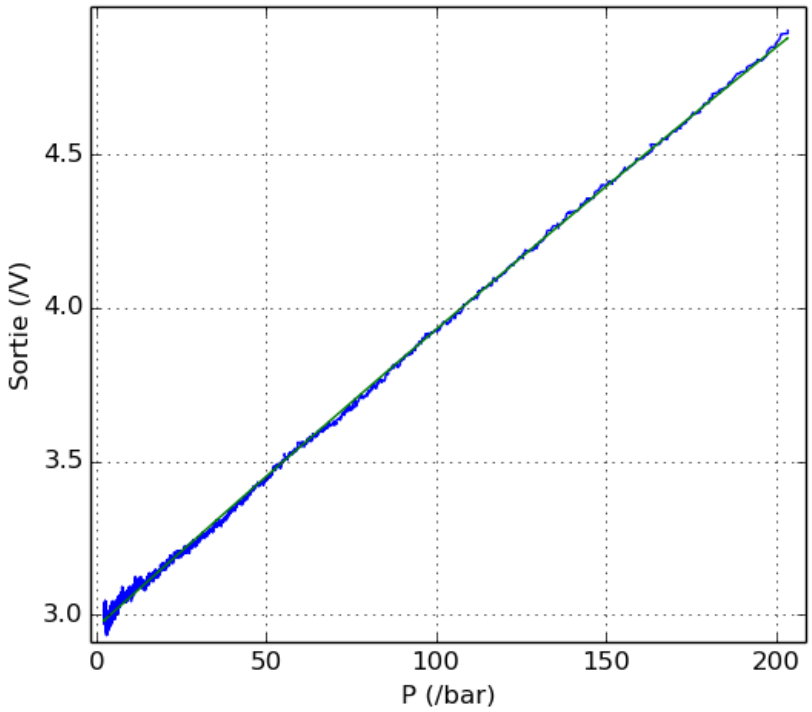


Fig. 3.11 *Measurement of the signal dependence versus pressure. The green line is a linear fit.*

## Summary

**In this chapter we have presented the different stages of the development of a position sensor measuring with a GMR the field created by a coil and reflected by a metallic surface, in the framework of its application as a pressure sensor and a velocity sensor. We have explained the design of the sensor, along with the mechanical and electrical considerations that are involved in the finite product. Using COMSOL simulations and analytical calculations we have provided a model for the filed distribution in space. Then we have validated the feasability with our experimental setup.**

**This sensor presents several advantages on other technologies. Namely it is able to measure a large range of pressures with a good sensitivity. It is rather insensitive to and temperature variations. For the velocity sensor it remains cheap and the design is adapted for the targeted application in automotive environment. The study did not lead to the full realisation of a final product but provided a prototype which validated the principle of functionning of the device with sufficient performances. From an experimental point of view we have realised a cheap easily integrable multi purpose sensor.**

# Part III

# Spin Torque Nano Oscillators

# Chapter 4

# Nonlinear oscillator theory

This chapter is preliminary to the introduction of spin torque oscillators, and describes the formalism of non linear oscillators and the implications of those nonlinearities. One main feature of nonlinear auto-oscillators is their large synchronisation bandwidth. STNO are highly nonlinear, what requires a specific theoretical treatment which was provided by [21] to quantitatively describe the synchronisation phenomena in strongly nonlinear auto-oscillators. First we introduce the concepts of nonlinear auto-oscillators and the equations. Then we discuss the impact of external pertubations of several natures, to introduce phase-locking to an external signal, mutual synchronisation to an other oscillator, and noise. Last we introduce elementary concepts of stability analysis, which will be useful to understand chapter 8.

Synchronisation refers to the phenomenon by which two auto-oscillators adapt their individual frequencies to oscillate in unison. Reference [84] outlines that synchronisation implies certain conditions on the synchronised systems, that are:

- The oscillators must be autonomous, that is, the isolated oscillators should be able to generate self sustained oscillations.
- The synchronised oscillators should be stable.
- The oscillations should be independent on the initial conditions, that is, purely determined by the system's parameters.

This distinction between resonance and synchronisation is important for the following as although the main focus here is synchronisation phenomena with autonomous oscillators, resonance will be used in experiments as a characterisation tool in the non autonomous regime. The material in this chapter is largley inspired from [21] and [84].

## 4.1 Nonlinear auto-oscillator model

### 4.1.1 Self-sustained auto-oscillations

Now let us consider a single mode oscillator with a complex amplitude $c(t)$. The "limit cycle" of oscillations corresponds to a closed trajectory of the non naught solution $c$ for the amplitude in the complex plane. Self-sustained oscillations can be defined as non decaying

stable oscillations in an autonomous dissipative system. Dissipation is intrinsic to every physical system, so the oscillator requires an internal energy source to compensate the dissipated energy for sustained oscillations. Strictly speaking a stable system cannot be conservative, else every perturbation would drive the oscillator to a new limit cycle and every oscillation amplitude would be equivalent. The role of the dissipative processes is to drive the oscillator back to its limit cycle. It would then be more appropriate to refer to quasilinear oscillators. In fact the crucial distinction between linear and nonlinear oscillators in the present context is that for a linear oscillator the phase dynamics are decorrelated from the amplitude, and the description of the dynamics can be restricted to the phase equations.

### 4.1.2 Equation

The generalised non linear auto-oscillator model as described in [21] is based on the assumption that only one oscillatory mode is excited – described by one amplitude $c$. This first assumption usually makes sense as all modes compete for the same limited energy source to compensate their losses. Then the mode of largest amplitude leaves less energy for all other modes and is therefore the only one to gather enough energy to auto-oscillate.

The general equation for nonlinear auto-oscillators is

$$\frac{dc}{dt} + i\omega(|c|^2)c + \Gamma_+(|c|^2)c - \Gamma_-(|c|^2)c = f(t) \tag{4.1}$$

where $\omega$ is he resonant pulsation of the oscillator, $\Gamma_+$ is the positive damping rate, $\Gamma_-$ is the negative damping rate. $\Gamma_+$ describes the energy dissipated by the system and $\Gamma_-$ describes the energy brought by the system to compensate those losses. This latter term plays the same role as a negative resistance in an RLC circuit. The four terms in the left-hand part can be put in parallel with the LLGS equation (1.12), where the gyroscopic term is the resonant term, the third term is the damping and the STT term plays the role of the negative damping. $f(t)$ describes the impact of the external environment [85]. In the case of an isolated system $f(t) = 0$ and the previous equation can be rewritten as

$$\begin{cases} \frac{dp}{dt} = & -2\left[\Gamma_+(p) - \Gamma_-(p)\right]p \\ \frac{d\phi}{dt} = & -\omega(p) \end{cases} \tag{4.2}$$

with $p = |c|^2$ and $\phi = arg(c)$. From the above it is clear that both equations are coupled even in the absence of external action. According to the equations system (4.2) $p = 0$ is a trivial solution to the stationary power. The other solution $p_0$ is so that $\Gamma_+(p_0) - \Gamma_-(p_0) = 0$. In most physical systems $\Gamma_+$ increases with $p$ while $\Gamma_-$ decreases with $p$, so there is a unique stationary solution to the power. This also means that if $p > p_0$, the energy losses of the system are no longer compensated by the energy source and the oscillations power tends to decrease. Alternatively if $p < p_0$ the system overcompensates the dissipative phenomena and the oscillations power tends to increase, so the solution is unique and stable. This also outlines the necessity of the nonlinearity of the damping term for stable auto-oscillations.

For small variations $\delta p$ of the power around equilibrium $p_0$, equations (4.2) involve an effective damping $\Gamma_p$ defined as

$$\frac{d\delta p}{dt} = -2\left[\frac{d\Gamma_+}{dp} - \frac{d\Gamma_-}{dp}\right] p_0\delta p = -2[G_+ - G_-]p_0\delta p \tag{4.3}$$

$$= -2\Gamma_p\delta p \tag{4.4}$$

which describes how fast the oscillator amplitude relaxes towards the limit cycle.

Additionnaly the nonlinear frequency shift is described by

$$N = \frac{d\omega}{dp} \tag{4.5}$$

So for small perturbations around equilibrium the system can be approached by

$$\begin{cases} \frac{d\delta p}{dt} = & -2\Gamma_p\delta p \\ \frac{d\phi}{dt} = & \omega_0 + N\delta p \end{cases} \tag{4.6}$$

One can introduce the dimensionless ratio between the nonlinear frequency shift and the amplitude relaxation rate for small variations around the limit cycle

$$\nu = \frac{Np_0}{\Gamma_p} = \frac{N}{G_+ - G_-} \tag{4.7}$$

which describes the coupling between phase and amplitude.

Deriving the exact analytical expression for each term usually is a complicated task. However for small perturbations from a stable trajectory, these can be derived in Taylor expansions.

In a first order approximation

$$\omega(p) = \omega_0 + Np = \omega_0(1 + \zeta p) \tag{4.8}$$

$$\Gamma_+(p) = \Gamma_0(1 + Qp) \tag{4.9}$$

$$\Gamma_-(p) = \Gamma_s(1 - Q_s p) \tag{4.10}$$

where $\zeta = N/\omega_0$ is the relative frequency variation rate against power, and $Q$ and $Q_s$ are the relative variation rates against power of the positive and negative damping respectively.

### 4.1.3 Non-isochronicity

In a case when the oscillator motion in the phase space is restricted to the limit cycle, this motion can be described with a phase $\phi$ which increases by $2\pi$ every cycle. So one can define the natural pulsation

$$\frac{d\phi}{dt} = \omega_0 \tag{4.11}$$

and the period $T_0 = 2\pi/\omega_0$ by which the phase performs a complete cycle.

Now if we observe the system stroboscopically at an exact time period $T_0$, all points on the limit cycle appear to be fixed points. Because the limit cycle is stable, all points in

the vicinity are directly attracted to it. All the points of the plane attracted to the same point of the limit cycle under the transformation $x(t) \to x(t+T_0)$ form an hypersurface crossing the limit cycle at this specific point. So those isochrones appear invariant when the system is observed stroboscopically with a time interval $T_0$.

The frequency is defined as the angular rotation velocity. If the frequency is amplitude-independent (isochronous oscillations) the phase will be invariant under the transformation $x(t) \to x(t+T_0)$. Thus if we look at the oscillator stroboscopically at $T_0$ intervals the oscillator will always have the same phase, and the isochrones will be orthogonal to the limit cycle. Alternatively if the frequency is power-dependent the phase will undergo an extra $\int_t^{t+T_0} \omega(p(s)) - \omega(p_0))ds$ shift due to the nonlinearity. This will deform the isochrones into logarithmic spirals at the first order (non-isochronous oscillations).

The concept of isochrones may be used to illustrate the effect of the nonlinearities characterised by $\nu$. Namely if we write $\delta p = p - p_0$ with $p_0$ the oscillations power on the limit cycle, then for a short time $\Delta t$ the phase increment due to nonlinearity will be $\Delta\phi = N\delta p\Delta t$. During the same amount of time the power will change by $\Delta(\delta p) = -2\Gamma_p\delta p\Delta t$ by linearising equation (4.6). The phase change rate over the power change rate is $\Delta\phi/\Delta(\delta p) = -N/(2\Gamma_p) = -\nu/(2p_0)$. Hence, $\nu$ actually describes the conversion of relative amplitude $\delta a/a_0$ relaxation into phase relaxation $\Delta\phi = -\nu\Delta(\delta p)/(2p_0) \approx -\nu\Delta(\delta a)/a_0$.

So $\nu$ determines the angle at which the nonlinear isochrone crosses the linear isochrone on the unit limit cycle, as depicted in figure 4.1(d).

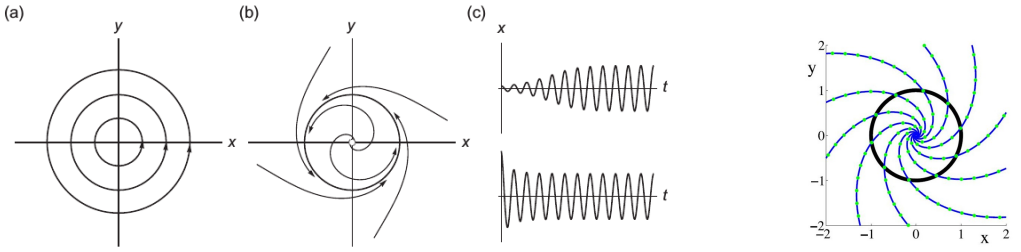


(a) *Linear oscillator. All amplitudes are equivalent. (b) Nonlinear auto-oscillator. The trajectories are attracted by the limit cycle. (c) Transient from inside or outside the limit cycle. From [86]*

(d) *Representation of isochrones (blue and green curves) for the nonlinear Stuart-Landau oscillator model. The limit cycle is the black curve. From [87]*

Fig. 4.1 *Description of a nonlinear auto-oscillator*

In the theory developped by Slavin and Tiberkevich [21], the derivations are adapted to STOs where the magnetic layers have a uniform out-of-plane magnetisation, and $\nu \gg 1$. In this case $\arctan\nu \approx \pi/2$ and the isochrones are almost tangent to the limit cycle, so even small power variations will result in significant phase change. In the opposite if $\nu \ll 1$ then $\arctan\nu \approx 0$, isochrones are almost orthogonal to the limit cycle and changes in amplitude do not affect much the phase dynamics.

## 4.2 External perturbations

In this section the autonomous system is no longer isolated from its environment and $f(t) \neq 0$. This allows us to derive expressions of the phase-locking bandwidth to an external source, mutual synchronisation, and to study the influence of noise using the same formalism.

### 4.2.1 Phase locking

In this subsection we describe the dynamics of an auto-oscillator under the action of a deterministic harmonic signal. Taking back to the distinction between synchronisation and resonance, a passive oscillator or an overdamped auto-oscillator will display a resonance with a strong response when the external frequency approaches the natural oscillations frequency of the system. An active auto-oscillator will start to generate at the exact frequency of the external "driving" signal when the difference between the external frequency and the free-running frequency of the auto-oscillator is small enough. This phenomenon is referred to as phase locking or injection locking.

The equation is then

$$\frac{dc}{dt} + i\omega(|c|^2)c + \Gamma_+(|c|^2)c - \Gamma_-(|c|^2)c = f_e e^{-i\omega_e t} \tag{4.12}$$

for an external drive with amplitude $f_e$ and pulsation $\omega_e$.

Under the assumption of a weak external signal, the power variations $\delta p$ can be considered small, and the complex equation can be rewritten conveniently

$$\frac{d\delta p}{dt} + 2\Gamma_p \delta p = 2F_e\sqrt{p_0}\cos(\omega_e t + \phi) \tag{4.13}$$

$$\frac{d\phi}{dt} + \omega_0 + N\delta p = -\frac{F_e}{\sqrt{p}}\sin(\omega_e t + \phi) \tag{4.14}$$

In the rotating frame of the external source, assuming slow variations of the amplitude and reinjecting (4.13) in (4.14), the phase equation can be rewritten as

$$\frac{d\theta}{dt} = \Delta\omega - \sqrt{1+\nu^2}\frac{F_e}{\sqrt{p_0}}\sin(\theta + \arctan\nu) \tag{4.15}$$

with

$$\theta = \omega_e t + \phi \tag{4.16}$$

$$\Delta\omega = \omega_e - \omega_{0,osc} \tag{4.17}$$

and is known as Adler equation [88]. One main advantage of this approach is that it conveniently reduces the problem to one equation but remains a good approximation for the weak external force.

The phase-locked oscillator rotates at the exact same frequency as the external source, or in other words the phase of the oscillator is constant in the rotating frame of the external source. This situation corresponds to stationary solutions of Adler's equation and is possible only for

$$\Delta\omega < \sqrt{1+\nu^2}\frac{F_e}{\sqrt{p_0}} \tag{4.18}$$

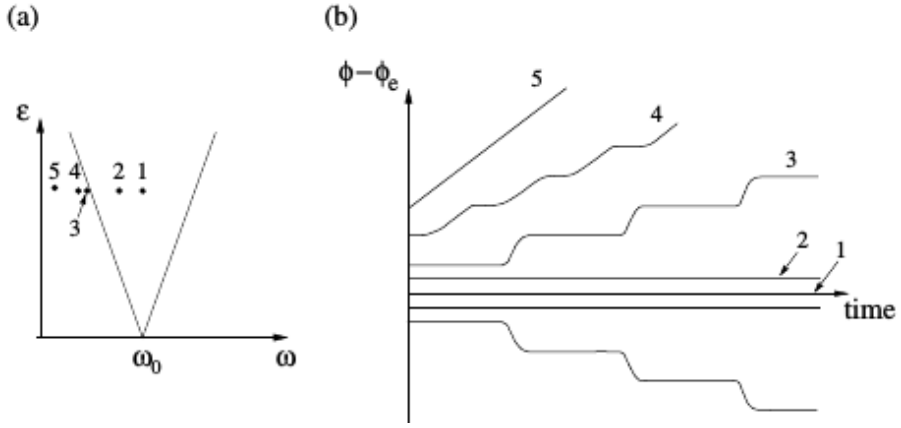


Fig. 4.2 *(a) Stability diagram of the phase of a nonlinear oscillator under the action of an external source, in the strength/frequency of the source plane. Points 1 and 2 are within the Arnold tongue, where the oscillator will eventually synchronise to the external source. Points 4 and 5 are located in an area where the detuning with the source frequency is too large, or alternatively the forcing is too weak for the oscillator to phase-lock. (b) The corresponding time traces of the phase of the oscillator in the rotating frame of the external source. Extracted from [84].*

what defines the locking bandwidth.

It is clear that for quasi-linear oscillators with $|\nu| \ll 1$, the nonlinearity does not bring significant change to Adler's linear theory. However for Spin Torque Oscillators $|\nu|$ can be very large and the phase locking is increased by nonlinearity. This is typical of STOs and was the initial motivation for Slavin and Tiberkevich to adapt the synchronisation theory to nonlinear oscillators in [21]. For the STOs used in this thesis, $\nu$ is typically of the order of magnitude of 1 to 5.

The phase and power evolution within the locking range can then be expressed at equilibrium in the first order as [5]

$$\begin{cases} \delta p_0 &= p_0 \frac{\nu + \sqrt{(1+\nu^2)F_e^2 - \Delta\omega^2}}{(1+\nu^2)F_e^2} \\ \theta_0 &= \arctan \nu - \arcsin\left(\frac{\Delta\omega}{\sqrt{1+\nu^2}\frac{F_e}{\sqrt{p_0}}}\right) \end{cases} \tag{4.19}$$

$\theta_0$ increases from $-\pi/2$ to $+\pi/2$ from edge to edge of the phase-locking bandwidth.

Lastly one should note that the approach to synchronisation is not abrupt. When the free-running frequency and the external frequency are very close but not close enough to synchronise, the phase difference between the source and the oscillator will be constant with periodic $2\pi$ phase shifts (see figure 4.2). As the two frequencies get closer to each other these $2\pi$ shifts become more and more occasional until they totally disappear. This can be modelled in the framework of the Adler equation and will be observed as a frequency pulling of the auto-oscillator.

### 4.2.2 Mutual synchronisation

In the case of two mutually interacting auto-oscillators, the problem increases in complexity as this interaction is now reciprocal. The mutual interaction between two oscillators $k$ and $l$ is described in the complex equation for each oscillator by a complex mutual coupling term.

$$\frac{dc_k}{dt} + i\omega_k(|c_k|^2)c_k + \Gamma_{+,k}(|c_k|^2)c_k - \Gamma_{-,k}(|c_k|^2)c_k = \Omega_{k,l}e^{i\beta_{k,l}}c_l \tag{4.20}$$

where $\Omega_{k,l}$ and $\beta_{k,l}$ are the real coupling frequencies and phase of the interaction between oscillators $k$ and $l$.

It can be shown that similarly to the case of injection locking these equations can be reduced to

$$\frac{d\phi_k}{dt} + \omega_{0,k} = \Omega_{k,l}\sqrt{\frac{p_{0,l}}{p_{0,k}}}\left(\cos(\phi_l - \phi_k) + \nu_k \sin(\phi_l - \phi_k)\right) \tag{4.21}$$

This model is known as the Kuramoto model and may of course be generalised to the case of $N$ mutually coupled oscillators, with $N \to \infty$ [89, 90].

Similarly to the previous case, the stationary solutions for the phase difference determine the mutual synchronisation bandwidth for two oscillators which differ only by their free-running frequencies. The coupling parameters and the nonlinearities are set identical (*id est* $\Omega_{k,l} = \Omega_{l,k} = \Omega$, $\nu_k = \nu_l = \nu$, $\beta_{k,l} = \beta_{l,k} = \beta$):

$$\Delta = 2\sqrt{1+\nu^2}|\Omega|\cos(\beta - \arctan\nu) \tag{4.22}$$

where $\beta$ is the phase of the coupling. For a conservative coupling such as dipolar coupling, which will be studied more in details in section 5.4 and studied experimentally in sections 7.3 to 7.5 $\beta = \pi/2$. For this specific situation two linear oscillators (i.e. $\nu = 0$) which differ only by their free-running frequency cannot synchronise. So the effect of $\nu$ is even more drastic in this case, as nonlinearities allow identical oscillator to synchronise via conservative coupling.

It should be noted that solving analytically the general case of two mutually coupled nonlinear oscillators is far from trivial, therefore it may be interesting to numerically simulate the system, as will be done in chapter 8.

### 4.2.3 Noise

Noise is usually not a big issue for macroscopic oscillators, but can become of critical importance for nano size oscillators, where the energy of the noise is comparable to that of the oscillations. From the previous subsections it has been determined that nonlinear oscillators have a wider synchronisation bandwidth than their linear counterparts. Then one can intuitively presume that a nonlinear oscillator will be more sensitive to white thermal noise, where all frequencies are present, than a linear oscillator.

The auto-oscillator now obeys a Langevin stochastic equation

$$\frac{dc}{dt} + i\omega(|c|^2)c + \Gamma_+(|c|^2)c - \Gamma_-(|c|^2)c = f_b(t) \tag{4.23}$$

where $f_b(t)$ is defined by a stochastic process. Let us first consider the most general case of a white gaussian zero-centered thermal noise. The model can be completed by adding

other sources and types of noises for specific situations. This stochastic process has second order moments

$$\langle f_b(t) f_b(t') \rangle = 0 \qquad \langle f_b(t) f_b^*(t') \rangle = 2D_b \delta(t - t') \tag{4.24}$$

$D_b$ is a diffusion factor which quantifies the fluctuations amplitude.

A full derivation can be found in [21], which will not be presented here but leads to the determination of the linewidth. The diffusion constant can be identified as the positive damping times the ratio between the thermal energy and the system's energy. In particular in the overcritical regime, that is, where a stable solution $p_0 \neq 0$ exists, the diffusion constant can be approximated as

$$D_b(p_0) = \Gamma_+(p_0) \frac{k_B T}{\mathcal{E}(p_0)} p_0 \tag{4.25}$$

$$= 2\pi \Delta f_0 p_0 \tag{4.26}$$

and $2\pi\Delta f_0 = \Gamma_+(p)\frac{k_B T}{\mathcal{E}}$ is the "linear" linewidth.

A motivation for deriving the phase noise is to determine the linewidth of the signal, defined as the Full Width at Half Maximum (FWHM). A more complete derivation can be found in [91]. One can distinguish two limit cases with respect to the power damping rate $f_p = \Gamma_p / 2\pi$:

- FWHM$\ll f_p$ and the oscillation spectrum has a lorentzian distribution with FWHM

$$\text{FWHM} = \Delta f_0 (1 + \nu^2) \tag{4.27}$$

  with $\Delta f_0$ the linear linewidth defined from 4.25.

- FWHM$\ll f_p$ the spectrum has a gaussian distribution with

$$\text{FWHM} = \nu \sqrt{\Delta f_0 f_p} \tag{4.28}$$

The appropriate case for our study is the former.

It is worth noting that as counter intuitive as it might be, a small damping constant does not necessarily result in a smaller linewidth. Truly the linewidth for the linear case is directly proportional to the damping. However in the nonlinear case a smaller damping increases the phase-amplitude coupling, so more amplitude noise is transferred to phase noise. Namely if we consider again equation 4.27, we can identify two contributions to the linewidth. $\Delta f_0$ is the linear component of the linewidth and is proportional to $\alpha$ via the expression for the positive damping $\Gamma_+(p_0) = \alpha\omega(p_0)$. The nonlinear contribution is characterised by the nonlinear parameter $\nu^2 \propto 1/\alpha^2$ since $\Gamma_p \propto \alpha$ and $\nu = N/\Gamma_p$. To put it differently, if the power damping is smaller, then the noise perturbation will persist a longer time. So there is an optimum for damping depending on the other parameters of the system.

## 4.3 Basic concepts of stability analysis

From the constitutive equations of the system it is possible to describe its equilibrium states and determine their stability. Here we provide a few introductory concepts to the stability study of equilibria, which can be found in any stability notebook [92].
Let us consider the (nonlinear) n-dimensional system of ordinary differential equations (ODEs)

$$\dot{X} = f(X), X \in \mathbb{R}^n \tag{4.29}$$

where

$$X = \begin{pmatrix} x_1 \\ \vdots \\ x_n \end{pmatrix}, f(X) = \begin{pmatrix} f_1(x_1, \cdots, x_n) \\ \vdots \\ f_n(x_1, \cdots, x_n) \end{pmatrix} \tag{4.30}$$

A solution $X(t) \in \mathbb{R}^m$ of this ODEs system is an equilibrium if $f(X(t)) = 0, \forall t$. The equilibrium (or fixed point) $X^e$ to the previous equation is stable (in the sense of Lyapunov), if

$$\forall \epsilon > 0, \exists \delta > 0, ||X(0) - X^e|| < \delta \Rightarrow ||X(t) - X^e|| < \epsilon, \forall t > 0 \tag{4.31}$$

The intuitive idea of stability is that for "small" perturbations from the equilibrium state should not lead to too large deviations.

In addition if

$$\lim_{t \to +\infty} ||X(t) - X^e|| = 0 \tag{4.32}$$

the solution is asymptotically stable. This condition is stronger as it ensures return to equilibrium. Else the system is neutrally stable.

If $X^e$ is a stable periodic solution of the system, that is, a closed trajectory, the system is said to be orbitally stable. A limit cycle is a special case of asymptotic orbital stability.

A linear system can be reduced to a matrix equation

$$y' = Ay \tag{4.33}$$

For a system of nonlinear ODEs, the system can be linearised around the equilibrium to study its stability as stablility is per definition a local property. In this latter case the asymptotic dynamics depend on the eignevalues $\lambda$ of the Jacobian matrix $A = f'(X^e)$ at the equilibrium. The stability is then determined from the eigenvalues and eigenvectors of the resulting matrix.

- If all eigenvalues have strictly negative real parts, the equilibrium is asymptotically stable (in the sense of Lyapunov)
- If pairs of purely imaginary complex-conjugate eigenvalues with distinct imaginary parts, the corresponding solutions are purely oscillary
- If at least one solution has a strictly positive real part, then the equilibrium is not stable

A few concepts are defined below since they will be mentionned in chapter 8.

- A manifold regroups all the points that are topologically equivalent, that is, lead to the same equilibrium.
- A bifurcation is a qualitative change in the stability or number of equilibria of a system of ordinary differential equations as one parameter is shifted. Bifurcation types are given different names.
- For periodic stable states, other analysis tools exist. The Poincaré map for instance plots the successive states of a system at set time intervals.
- Chaos is quite complex to define. One characteristic is a high sensitivity to initial conditions. A small change in initial condition can lead to significant changes in the system evolution, so the evolution of the system is almost unpredictable although it is fully deterministic.

## Summary

**In this chapter we have introduced the model of a single mode nonlinear auto-oscillator developped in [21] along with graphic representations to qualitatively explain the physical implications of nonlinearities. Similarly we have illustrated the phenomena of phase-loking and mutual synchronisation. We have introduce a parameter $\nu$ to characterise the nonlinearity, and to explain the increased synchronisation bandwidth. From noise considerations we have analytically described the linewidth. Lastly we have explained basic ideas of stability analysis, and introduced a few relevant concepts.**

# Chapter 5

# Vortex Oscillators

In this chapter, we first review the state-of-the-art for the realisation of STNOs and their performances, and we consider more particularly the cases of phase-locking and mutual synchronisation. We describe the vortex and the effects of external bias parameters, and move on to the gyrotropic mode of magnetic vortices, which will be the focus of our experiments. We put a particular stress on the discussion of the dipolar interaction between two neighbouring vortices. Laslty we demonstrate the equivalence between the formalism of nonlinear oscillators described in the previous chapter and the Thiele equation, which describes the gyrotropic mode.

## 5.1 State-of-the-art

### 5.1.1 Mechanisms to exert a spin torque

The prediction by Berger and Slonczewski of current-driven excitation of auto-oscillations in a magnetic layer was first realised experimentally in a nano contact Co/Cu multilayer by Tsoi *et al.* [93]. However in this paper excitatin of spin waves was only indirectly measured through the field-dependence of the threshold current for changes in dc resistance. First direct electrical observation of full compensation of the damping by spin transfer, leading to self-sustained precessions of the magnetisation was performed in [14], making it the first experimental demonstration of a spin torque oscillator.

Several mechanisms exist to bring in angular momentum to excite the dynamics of spin torque nano oscillator.

Spin Torque Oscillators based on the CPP configuration are declined in two main geometries, that are the nanocontact and the nanopillar. In the nanocontact geometry an electrical contact is opened through an insulating layer on top of a multilayer stack. This is the equivalent of the earlier point contact where a thin metallic wire was mechanically contacted on top of the multilayer. This geometry is less sensitive to thermal noise than the nanopillar as a larger volume is excited. This geometry also allows propagating modes and localised bullet modes [22]. In a nanopillar the FM/NM/FM layers are lithographied as a cylinder, and the generated mode is very sensitive to the diameter and thickness of the free layer. A homogeneous precession of the magnetisation can be driven by STT, but the confinement can also result in stabilising a vortex in the nanopillar, which will be developped further in this chapter.

Spin Hall Oscillators use different geometries. The spin is not brought here by a spin-polarised charge current but instead by a pure spin current. The Spin Hall Effect (SHE) originates from the coupling of orbital and angular momenta, which introduces a spin-orbit term in the Hamiltonian of the electron which depends on the scalar product of the two momenta [94]. For electrons undergoing scattering events, the trajectories that minimise the spin-orbit contribution cause the electrons with opposite spin to be scattered in opposite directions. The generated spin imbalance causes a pure spin current to flow perpendicularly to the electrical current. The spin Hall angle measures the charge- to spin-current conversion rate $\theta_{SH} = J_S/J_e$, where $J_e$ is the current charge density and $[\hbar/2e]J_S$ is the spin-current density. In high spin Hall angle metals, accounting notably transition metals or "heavy metals" such as Pt, a pure spin current can be efficiently generated from an electrical current by selectively deviating the electrons according to their spins. A typical setup consists in generating the pure spin current by flowing a current through a Pt layer, and observe its effect on a magnetic layer deposited on top. The efficiency of this process is enhanced by the fact that when an electron transmits its spin momentum by scattering at the interface, it is reflected in the Pt and can be deviated to contribute again to the generation of the spin current. So the same electron can be used several times to generate the spin curret in the magnetic layer.

The first experimental demonstration of an auto-oscillator driven by a pure spin current was performed in a platinum (bottom)/permalloy (top) nanodisk with two top electrodes separated by a nanogap [95]. The electrical current passing through the Pt layer generates a pure spin current via the Spin Hall Effect flowing orthogonally through the Pt/Py interface. Additionnaly a single mode is oscillating as higher frequency modes killed by enhanced high frequency radiative losses. This result was rapidly followed by [96] reporting a spin Hall nano oscillator using a nanoconstriction to reach high current densities. In this configuration both the ferromagnetic layer and the Pt layer are patterned. This configuration can be realised in an array of parallel oscillators fed by the same electrical current and coupled by propagating spin waves [97]. However these devices generate an electrical signal based on the Anisotropic MagnetoResistance (AMR) effect weaker than STNOs which rely on the stronger GMR or TMR effect. The TMR effect can be used in a three-terminal device [74], where the free layer is deposited on top of an extended Pt or Ta slab.

A similar result of auto-oscillations driven by a pure spin current has been realised in a Pt/YIG bilayer [98], in a study which I was involved. This last result is remarkable as demonstrating the generation of auto-oscillations in a magnetic insulator driven by SHE. Namely Yttrium Iron Garnet (YIG) is a remarkable material for it has the lowest known intrinsic damping $\alpha$, and is an electrical insulator.

STOs have a relatively broad linewidth, mainly because they are highly nonlinear, that is, have strong phase-amplitude coupling, the phase noise is increased with respect to that of a quasi linear oscillator by amplitude noise converted into phase noise [41]. Additionally they are very sensitive to thermal noise because of the small oscillating volume. An other source of noise is inter mode coupling and mode hopping when several modes are excited or energy can relax into other modes close in energy [99]. The best experimental result reported in vortex STNOs is 74 kHz [100] in a 300 nm Magnetic Tunnel Junction (MTJ) vortex with 10 nm thick FeB free layer, and 40kHz in a fully metallic (that is, the signal is due the the GMR effect) vortex STNO [101], while typical linewidth rather lay in the

MHz range, and even tens of MHz for homogeneous precession.

In terms of performances, the highest frequency reported experimentally tops at 46 GHz and is extrapolated to potentially reach 65 GHz [45]. The auto-oscillation frequency is essentially determined by the effective field, which can be increased through the external applied field, the exchange field by reducing the dot diameter, the anisotropy field by well-chosen materials with an ultimate limit beyond 200 GHz [102, 103]. Output powers now score in the microWatt range with a reported 3.6 μW for vortex oscillators [100] and 2 μW for uniform mode oscillation in a nanocontact with perpendicular anisotropy free layer [104].

### 5.1.2 Spin Torque Vortex Oscillators (STVOs)

Vortex oscillators, first demonstrated in [105] are a particular situation where the magnetisation distribution of the magnetic layers is strongly non-uniform and forms a vortex, that is, a curling of the magnetisation in the plane of the disk around an out-of plane singularity. These have many assets, among which an essentially naught operating bias field and a comparatively narrow linewidth. Namely it has a comparatively small nonlinear parameter $\nu$ (typically $\lesssim 5$ [106]), which is at the origin of the large linewidth of nonlinear oscillators, and a low frequency. The lowest energy mode is the gyrotropic mode, in which the vortex core gyrates around its equilibrium position. This mode is very far from higher energy modes, which is favorable for phase noise as this prevents intermode coupling and mode hopping. A first motivation for the investigation of spin torque vortex oscillators in particular was a narrowing of the linewidth. Namely as the lowest energy (gyrotropic) mode is well separated from the higher energy modes, it is expected that this non degeneracy of modes improves the coherence of the signal, or equivalently reduce the linewidth [107]. A common quality factor used in the domain of STOs is defined as the ratio of the linewidth over the carrier frequency $Q = \Delta f / f_c$. The record quality factor to the author's knowledge tops at Q=19000 [108] with a 40 kHz linewidth.

The area responsible for the GMR signal and the STT essentially lays in the region enclosed by the orbit of gyration. In a nanocontact the vortex can perform gyrations largely outside the contact area [109].

An other asset of vortex oscillators is that they can operate in the absence of external magnetic field [110]. Additionally they owe their frequency agility mainly to the Oersted field of the applied current instead of relying only on their nonlinearity. So the standard strategy of improving output power and linewidth by synchronising several such oscillators can be done witout losing the frequency agility [101].

### 5.1.3 Synchronisation to external source

The most remarkable property of spin torque oscillators is their high phase-amplitude coupling, or nonlinearity, which is uncommonly large in the physics of oscillators. In particular this drastically enhances the synchronisation bandwidth. The first experimental realisation of synchronisation to an external signal was the synchronisation to an RF current, also referred to as injection locking [111][112][113]. Later it was demonstrated that such a device could be synchronised to the RF magnetic field from an external source [114] [115]. This latter reference additionnaly measured a drastic improvement of the linewidth

of the parametrically phase locked STO below 1kHz [115]. Phase-locking also leads to a decrease of phase noise to -90dBc at 1MHz [51] while for free-running STO typical phase noise figures rather -40 to -70dBc at 1MHz distance from the carrier frequency [41]. The increased stability of a signal phase-locked to a weak but stable reference is a well-known procedure [**?** ].

### 5.1.4 Mutual synchronisation

From section 4.2.2 it emerges that the mutual synchronisation of several STO would help increase the emitted power and improve their linewidth to meet the requirements for applicative devices. Namely synchronising $N$ STOs would multiply the total output power by $N^2$ and decrease their linewidth by $1/N$ (or alternatively, increase the oscillations coherence by $N$) [**?** ].

Over the past 12 years several schemes have proved efficient for mutually synchronising STOs. The main results are summarised in figure 5.1. Nanocontacts have this geometry where the STO belong to the same extended magnetic thin layer (see figure 5.1(a)). When an STO oscillates, it excites spin waves which decay over a few hundreds of nanometers. Two studies have shown in 2005 that coupling through spin waves was strong enough to synchronise two adjacent nanocontacts. [116] performed the study for one single separating distance but two individual current sources for the two nanocontacts, while in [117] two nanocontacts were fed in parallel devices and several separating distances were tested. One characteristic of coupling via spin waves (which is of diffusive nature, as opposed to electrical or dipolar coupling which are conservative) is the oscillation of the coupling strength against the separating distance due to interferences between spin waves, what was calculated in figure 13 of [21].

In the specific case of vortices, [118] increased the number of synchronised nanocontacts to 4 based on exchange coupling. There the nanocontacts were fabricated by indenting a resist with an AFM tip. The vortex configurations in the 2D layer were stabilised under the contacts by the Oersted field of the feed current and the interaction between vortices was mediated by antivortices. The data display 4 individual peaks merging into one as the current is increased (see figure 5.1(b)).

A second way to synchronisation is electrical coupling [**?** ], where the STNOs interact through the self-modulating current transported on potentially much long distances via the electric wires. In the recent experimental realisation [120] (see figure 5.1(c)) with STNOs connected either in parallel or in series, it is noted the possibility to tune the coupling between the two MTJ-based STNOs by playing on the phase of the coupling either with the electrical delay between the two, or with the ratio of the Slonczewski and field-like torques to address directly the intrinsic phase of the coupling.

A last coupling mechanism is the dipolar interaction, via the magnetic stray field of each STNO. Namely as the origin of the signal are self-sustained precessions of the magnetisation (which are then converted into a voltage signal thanks to a magnetoresistive effect), each STNO generates a magnetic field rotating at its own individual frequency, which can affect the dynamics of its neighbour [119] (see figure 5.1(d)). This will be developped later.

The world record to date in number of mutually synchronised oscillators is set to 9 nanoconstrictions fed by a common current injected by Spin Orbit Torque [97]. Moreover

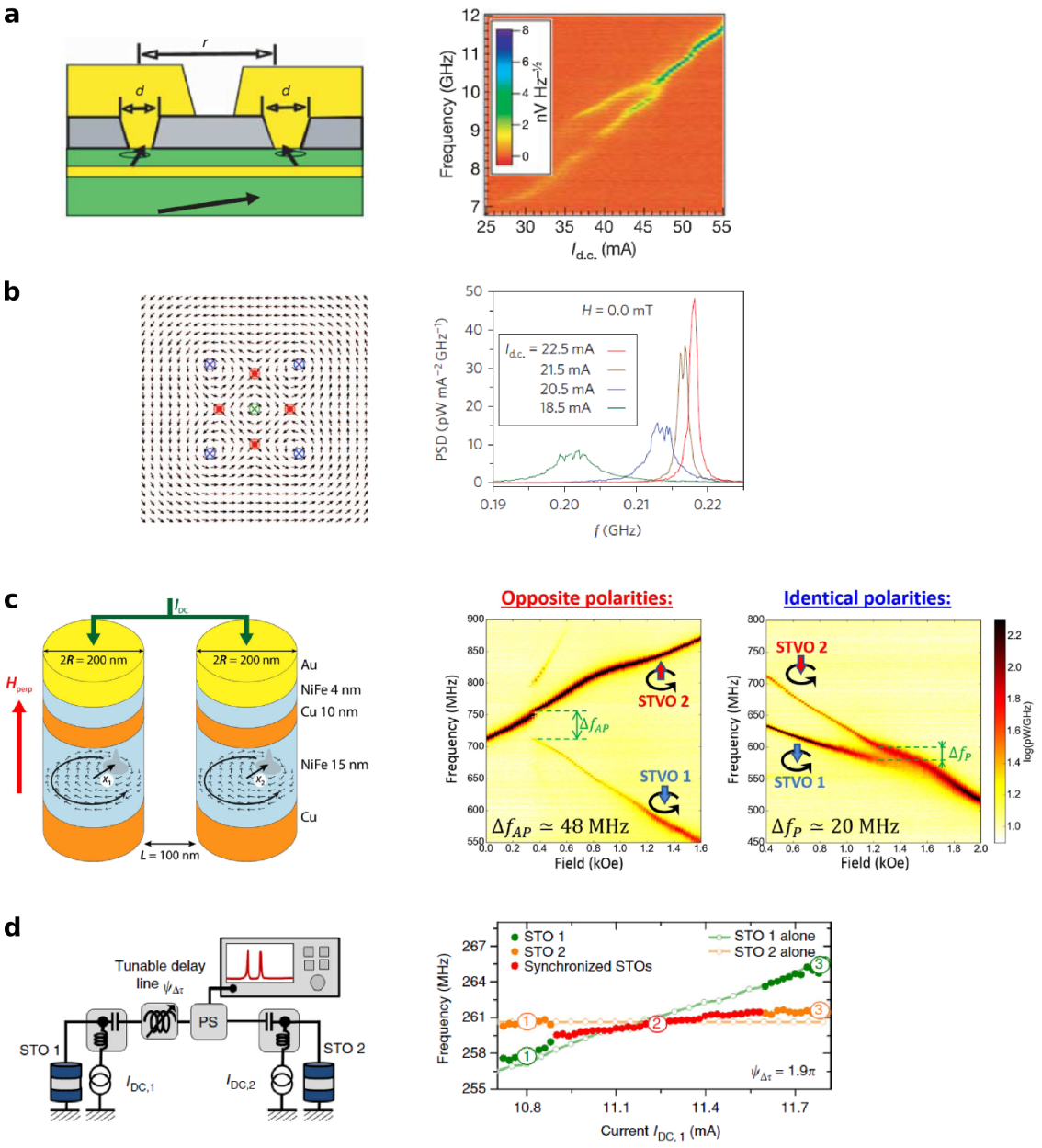


Fig. 5.1 *(a) Two nanocontacts sharing a common magnetic medium and mutual synchronisation of two similar nanocontacts via spin wave coupling. Extracted from [116] and [117] respectively. (b) Mutual synchronisation of 4 nanocontacts with vortex magnetisation sharing a common medium via exchange coupling (mediatied by antivortices). As the current is swept the four auto-oscillation signals merge into one. Extracted from [118]. (c) Mutual synchronisation of two nanopillars with a magnetic vortex distribution via dipolar coupling in the antiparallel and the parallel states. Extracted from [119]. (d) Mutual synchronisation mediated by the electrical coupling. Extracted from [120]*

micromagnetic simulations demonstrate that it should be possible in principle to synchronise an arbitrary number of vortex oscillators through magneto dipolar coupling [122], and suggests that connecting the vortices increases the coupling constant by decreasing the magnetic charges.

### 5.1.5 Fractional synchronisation

Synchronisation is not limited to close frequencies of the two oscillators or the oscillator and the source, but can also happen when one of the frequencies is close to a fraction or a multiple of the other. This is experimentally demonstrated for the phase locking of an STO to an external signal [114, 113]. Depending on the ratio between the two frequencies involved, the locking range is larger or smaller. When the frequency of the STO is linearly increased this is observed as irregular steps as the frequency of the (fractionally) phase-locked STO is constant. This is sometimes referred to as *the Devil's staircase*. This can be described by extrapolating the Kuramoto model to higher orders.

## 5.2 Static vortex state

### 5.2.1 Magnetisation distribution

A magnetic vortex is a magnetisation distribution which is stable for certain geometries. In our case we are studying magnetic strucures of confined geometries, where the magnetic distribution results from a competition between the magnetostatic energy, the exchange energy, and the anisotropy energy. More specifically in this study we will deal with dots with radius $R$ and thickness $L$. The vortex is stable for certain aspect ratios $\beta = L/R$, where $R$ has to be large enough before the exchange length and the thickness $L$ has to be large enough so that the magnetisation is not constrained in-plane. The vortex is usually decomposed in two distinct parts according to a plane containing the dot radii, that are the vortex core ($|r| < b$) and the vortex body ($|r| > b$). Namely the circulation in the vortex body minimises the magnetostatic energy by ensuring a closed flux, while the out-of-plane anomaly in the vortex core minimises the exchange energy. The spins in the vortex body are curling in-plane around an out-of-plane sigularity that is the vortex core. The vortex is characterised using three topological parameters. The *vorticity* or alternatively the *magnetic charge* equals 1 (-1 is referred to as an anti vortex). The *chirality* C=+/-1 whether the vortex curls clockwise or counterclockwise. The *polarity* P=+/-1 whether the vortex is pointing up or down. The polarity is usually defined against the external applied field.

The centered vortex is then described in the cylindrical coordinate basis ($\rho$,$\chi$,$z$) by the several components of the magnetisation

$$\begin{cases} m_\rho &= 0 \\ m_\chi &= C\left(1 - \cos^2(\Theta(\rho))\right) \\ m_z &= cos(\Theta(\rho)) = P\exp\left(-\ln 2(\frac{2\rho}{b})^2\right) \end{cases} \tag{5.1}$$

according to the model by Feldtkeller *et al.* [123] where $b$ is the vortex core radius and $\Theta(\rho)$ the angle between the local magnetisation $\vec{m}$ and the unit vector $\vec{z}$. There are other

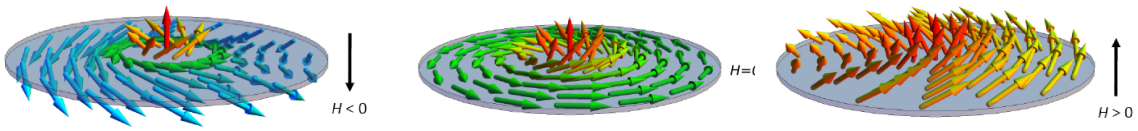


(a) *Negative cone state* (b) *Zero cone state* (c) *Positive cone state*

Fig. 5.2 *Dependence of the vortex magnetic distribution on the perpendicular bias field.*

models describing the vortex state magnetic distribution, especially the distribution inside the core, but the essential features are present, that are: the magnetisation is circulating in-plane around the vortex core, and is tilting abruptly out-of-plane inside the vortex core.

Usov first described the distribution of a centered vortex in a dot using a variational method [124]. The core minimises the exchange energy, while the vortex shape minimises the total free energy. The magnetic volume of the core remains very small compared to that of the body (typically $b \approx 2l_{ex}$) so the dynamics will be dominated by the body.

**Vortex shifted from its centre** Two models are commonly used to describe the vortex magnetisation distribution. The Single Vortex Ansatz (SVA) also known as the Travelling Wave Ansatz considers a rigid vortex, and the magnetisation distribution of the shifted vortex is just a translation. This model is used for the development of the Thiele framework.

One main issue of the SVA is that magnetic charges arise at the surfaces of the dot, so a displacement of the core results in an increase of the magnetic energy. To avoid magnetic charges at the edge surfaces, the Two Vortex Ansatz (TVA) or Image Vortex Ansatz considers one vortex whose core is at a position $\overrightarrow{X} = (\rho,\theta)$ and a virtual image vortex outside the disk at a position $\overrightarrow{X}_I = (R^2/\rho,\theta)$ [125, 126].

Importantly enough as the vortex core is shifted from its centre, more in-plane spins are pointing in one direction than the other, thus resulting in a net magnetisation. This is critical in the following as this net magnetisation determines the efficiency of the spin torque through which the gyrotropic motion is excited. Secondly this net magnetisation is also responsible for a magnetic field through which the vortex will interact with its environment, with a phase that is directly related to that of the vortex core. This has been analytically determined in [127] for gyration radii $\rho < 0.6R$, the net magnetisation amplitude depends linearly on the core position shift

$$\overrightarrow{M_{//}} = \frac{2}{3}\frac{CM_s}{R}\overrightarrow{X} \times \overrightarrow{e_z} \tag{5.2}$$

### 5.2.2 Stability

The vortex is stabilised by a confined geometry. The vortex stability essentially results from a proper ratio between the exchange length, the thickness and the radius of the dot (see figure 5.3). There is a competition between the short-range exchange interaction,

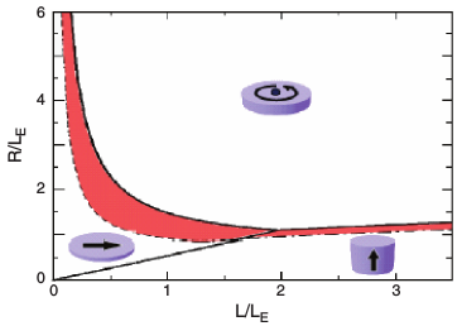


Fig. 5.3 *Diagram of stability of the vortex state when varying the dot radius R and thickness L ($L_E$ is the material exchange length). The red area is a region of bi-stability. Taken from [128]*

which tends to align neghbouring spins, and the long-range dipolar interaction, which favours antiparallel alignment. The relevant characteristic length is the exchange length. So on a thin

However vortices are not limited to circular dots but also exist in square geometries, or can be stabilised by the bias conditions.

### 5.2.3 Effect of a dc magnetic field

#### Effect of an out-of-plane magnetic field

When the vortex is placed in an OOP magnetic field, the magnetisation's in-plane distribution does not change qualitatively but the z-component is affected. Two cases should be considered. If the external field is parallel to the vortex polarity, the vortex goes in the so-called cone state (see figure 5.2) where the spins are tilted and the OOP component increases as $m_z = H_\perp/H_s$, where $H_s$ is the saturation field. When the saturation field is reached, the vortex state becomes the fully saturated out-of-plane state. Dussaux *et al.* [129] showed that the magnetisation profile keeps its sombrero shape, the curling state is conserved, in agreement with the measurements by Loubens *et al.* [130] partly reproduced in figure 5.4. The core size according to Ivanov [131] increases linearly with the OOP field. This however affects the dynamics as will be seen for the gyrotropic mode in the following chapter. When the field is anti parallel to the vortex polarity, the core polarity switches before saturation is reached [132].

#### Effect of an in-plane magnetic field

An IP magnetic field will exert a Zeeman torque which will linearly push the vortex core out of the center of the disk.

$$\overrightarrow{X} = \frac{5}{2\pi}\frac{\beta RC}{M_s}\overrightarrow{e_z} \times \overrightarrow{H}_{IP} \tag{5.3}$$

At some point the vortex core becomes unstable as it reaches the border of the dot. The dot reaches a uniform in-plane magnetisation for a certain anihilation field $H_{an}$. The

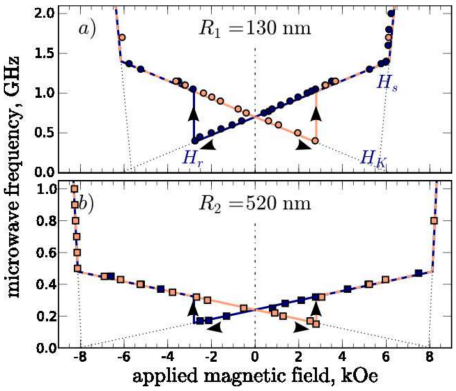


Fig. 5.4 *Micromagnetic simulation of dot a) magnetisation and b) frequency dependency against an out-of-plane dc magnetic field. The vortex core reversal is hysteretic. In the gyrotropic regime the oscillations frequency varies linearly with the applied field and the slope sign is that of the vortex polarity. Once the magnetisation is saturated the resonant frequency is that of the Kittel mode. Taken from [130]*

vortex is nucleated again as the field is decreased. This process is hysteretic and the nucleation field is smaller than the anihilation field. The vortex first enters the dot in a C-state, which can be pictured as an incomplete vortex where the core would still be outside the dot. The cycle is described in figure 5.5

### 5.2.4 Effect of a dc current

In spin torque vortex oscillators, the vortex is fed with a dc current to excite its dynamics. This is the typical textbook exercise of the field created by an electrical current flowing through a conducting wire. As the current is usually quite large the Oersted field has to

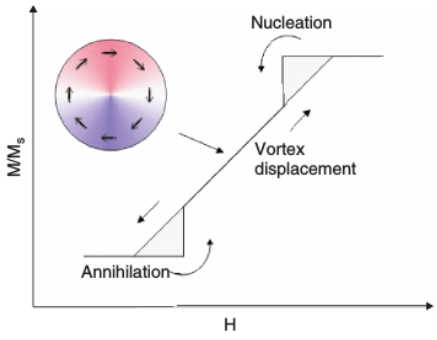


Fig. 5.5 *Magnetic vortex magnetisation versus in-plane dc field. When the field is sufficiently high the vortex is expelled from the dot and the magnetisation is uniform. The vortex anihilation/nucleation process is hysteretic. Taken from [128]*

be considered in calculation. The field inside the wire can be calculated as

$$\overrightarrow{H_{Oe}} = \frac{C_{Oe}}{2\pi R^2}|I|\rho\overrightarrow{e_\chi} \tag{5.4}$$

and the Zeeman torque stabilises vortex chiralities parallel the Oersted field chirality and destabilises the opposite chirality. A strong enough current can even impose its chirality to the vortex. The stable chirality configuration against the current is presented in figure 5.6.

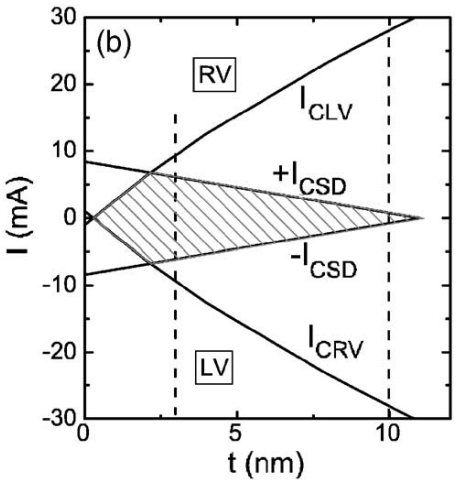


Fig. 5.6 *Stability diagram of the chirality depending on the dot thickness and the bias current. RV refers to a right-handed (clockwise) chirality of the vortex state, and LV left-handed (counterclockwise) vortex, while SD refers to a uniformly magnetised Single Domain state. The LV state is stable at $I < I_{CLV}$, the RV state is stable at $I > I_{CRV}$, and the SD state is stable at $|I| < I_{CSD}$. All three states are stable in the hatched region. Dashed vertical lines are not relevant here. Extracted from [133]*

## 5.3 Gyrotropic mode

### 5.3.1 Description

The vortex core inside a dot may be seen as a quasi particle trapped inside a potential well. When the vortex is shifted from its equilibrium position, it will undergo a restoring force. The gyroforce acts against this restoring force, allowing the vortex core to gyrate along iso energy trajectories in a conservative system. In a real system the damping goes against the velocity of the vortex and the core eventually goes back to the centre of the dot. This is referred to as the gyrotropic mode and is the lowest energy mode of the vortex.

The shape of the potential well actually depends on several ingredients, such as the dipolar magnetic field, the Zeeman energy, the Oersted field, as mentionned beforehand.

### 5.3.2 Thiele equation

Let us recall the LLGS equation

$$\frac{d\overrightarrow{M}}{dt} = -\gamma\overrightarrow{M} \times \overrightarrow{H}_{\text{eff}} + \frac{\alpha}{M_s}\overrightarrow{M} \times \frac{d\overrightarrow{M}}{dt} + \frac{a_J J}{M_s}\overrightarrow{M} \times (\overrightarrow{M} \times \overrightarrow{p}) \tag{5.5}$$

The LLGS equation convoluted to the magnetisation distribution under certain assumptions can be derived into the Thiele equation [134] which is more convenient to describe the motion of magnetic domains using collective degrees of freedom. The main assumption is that the magnetisation distribution is not distorted and evolves only by translation. Thus the dynamics can be described by a single point in a similar way the solid restricted to its centre of inertia.
The calculation details can be found in several references [134]. The principle of the calculation is to integrate the various contributions to the variations of the magnetisation energy $\mathcal{E}$. The effective energy $\mathcal{E}$ is defined locally by

$$\overrightarrow{H}_{eff} = -\frac{\delta\mathcal{E}}{\delta\overrightarrow{M}} \tag{5.6}$$

$$= -\frac{1}{M_s}\left[\frac{\delta\mathcal{E}}{\delta\theta}\overrightarrow{u_\theta} + \frac{1}{\sin\theta}\frac{\delta\mathcal{E}}{\delta\phi}\overrightarrow{u_\phi}\right] \tag{5.7}$$

Integrating the energy over the magnetisation distribution according to equation (5.5) and considering the gyrotropic mode in the simple vortex ansatz, the magnetisation is written as $\overrightarrow{M}(\overrightarrow{r}) = \overrightarrow{M}(\vec{r} - \overrightarrow{X}(t),\dot{\overrightarrow{X}})$ where $\overrightarrow{X}(t)$ is the (reduced) vortex core position (that is, when $X = 1$ the vortex core in on the edge of the disk).

$$\overrightarrow{G} \times \dot{\overrightarrow{X}} - D(\overrightarrow{X})\dot{\overrightarrow{X}} + \overrightarrow{F_{STT}}(\overrightarrow{X}) - \frac{\partial E}{\partial\overrightarrow{X}} = \overrightarrow{0} \tag{5.8}$$

where four terms appear. The action of the corresponding forces is represented schematically on figure 5.7 The upper dot stands for time derivative.

The energy term $E = E_{ms,V} + E_{ms,S} + E_{ex} + E_{Oe} + E_Z$ is the total micromagnetic energy and describes the confinement of the vortex core inside a potential well. It includes the volume and surface magneto static energy, the exchange energy, the Zeeman energy due to the external applied field and the Oersted field energy induced by the dc current.

### 5.3.3 Effects of the forces on the dynamics

#### The gyroforce

The gyroforce is conservative and is responsible for the vortex gyrations around the dot centre, in the same way a spin precesses around its equilibrium position. In the simplest model of a rigid vortex proposed by Usov *et al.* [124], the gyrovector can be expressed as a constant

$$\overrightarrow{G} = -2\pi\frac{PLM_s}{\gamma}\overrightarrow{e_z} = -PG\overrightarrow{e_z} \tag{5.9}$$

where $\gamma$ is the gyromagnetic ratio, $P$ is the vortex core polarity, L the thickness and $M_s$ is the saturation magnetisation. $2\pi$ is the solid angle that the spin distribution makes on the unit sphere. In the cone state, $\overrightarrow{G}$ varies because the in-plane spins are tilted. This is the reason why the gyrotropic frequency varies.

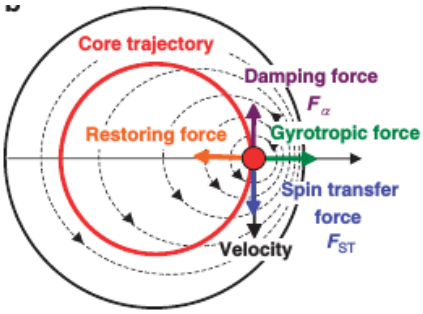


Fig. 5.7 *Representation of the effects of the forces in the Thiele equation on the vortex core. Taken from [48]*

**The confinement**

The confinement force derives form the gradient of the potential energy $E(\overrightarrow{X}) = E(\overrightarrow{0}) + \frac{1}{2}kX^2 + O(X^4)$ first order Taylor expansion. When the vortex core is shifted from the dot centre, the in-plane spin imbalance results in a net magnetisation, thereby increasing the magnetostatic energy. The confinement thus exerts a restoring force on the vortex core which can be modelled with a stiffness $k_{ms}$ which can be calculated from the dot sucsceptibility. The nonlinear contributions to $k_{ms}$ can be found in [135][136][137], and under certain hypothesis can be written as [135]

$$k_{ms} = \frac{20}{9}\frac{M_s^2 L^2}{R}\frac{1}{1-(X/2)^2} \tag{5.10}$$

The STO is fed by a large dc current which creates an Oersted magnetic field and contributes to the total Zeeman energy as a function of the vortex core position [138]. The contribution of the Oersted field to the confinement can be expressed as [139]

$$k_{Oe} = \frac{0.85CM_sLR}{5}(1-0.5X^2) \tag{5.11}$$

The vortex gyrotropic frequency is deduced from the confinement [129]

$$\omega_0 = \frac{k}{G} = \frac{k_{ms} + Jk_{Oe}}{G} \tag{5.12}$$

where $J$ is the current density.
From this equation one can deduce the auto-oscillation frequency at zero bias [140]

$$\omega_G = \frac{20}{9}\gamma M_S \frac{L}{R} \tag{5.13}$$

The effect of an external out-of-plane magnetic field $H_\perp$ has been directly measured using the MrfM technique [130]. The effect pf $H_\perp$ on the gyrovector and stiffness arising

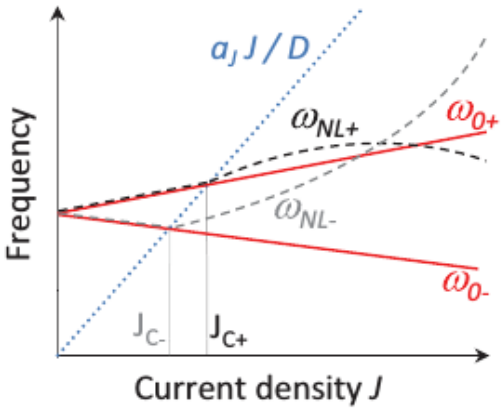


Fig. 5.8 *Current density dependency of the gyrotropic frequency.* $\omega_0$ *and* $\omega_{NL}$ *denote the linear and nonlinear components of the resonant frequency respectively. The +/- signs denote the vortex chirality with respect to the current direction.* $J_C$ *denotes the critical current for auto-oscillations. Taken from [129]*

from the magnetostatic and Oersted confinements is given by

$$G(H) = G(0)(1 - P\cos(\Theta_0)) \tag{5.14}$$
$$k_{ms} = k_{ms}(0)\sin^2\Theta_0 \tag{5.15}$$
$$k_{Oe} = k_{Oe}(0)\sin\Theta_0 \tag{5.16}$$
$$cos\Theta_0 = \frac{H_\perp}{H_S} \tag{5.17}$$

where the angle $\Theta_0$ is defined to describe the in-plane spins tilting. In particular the gyrovector increases (decreases) linearly with the out-of-plane field, until saturation where the gyrotropic mode does no longer exist.

The gyrotropic frequency is subsequently affected according to $\omega_0 = \omega_{ms} + J\omega_{Oe}$

$$\begin{cases} \omega_{ms}(H_\perp) = & \omega_{ms}(0)\left(1 + P\frac{H_\perp}{H_s}\right) \\ \omega_{Oe}(H_\perp) = & \omega_{Oe}(0)\sqrt{\frac{1+P(H_\perp/H_s)}{1-P(H_\perp/H_s)}} \end{cases} \tag{5.18}$$

### The dissipative forces

The first dissipative term describes the damping force which acts against the vortex velocity and is responsible for its return to the center of the dot. In the frame of Usov's model, the damping tensor is found to be diagonal and the damping force may be expressed as $D = -\frac{\alpha\pi M_s L}{\gamma}(5/4 + \ln(R/b))$ [140], where $R$ is the nano disc radius and $b$ the vortex core radius.

However this expression is no longer valid for larger amplitudes of the core displacement. A second order derivation can be found in [129], based on energy dissipation calculation of the vortex dynamics in the frame of the TVA, as opposed to the Thiele formalism which

makes use of the SVA.

$$D(X) = 2\pi\alpha L\frac{M_s}{\gamma}\left(\ln\left(\frac{R}{2b}\right) - \frac{1}{4} + \frac{1}{6}X^2\right) = \alpha G\eta(X) \tag{5.19}$$

where $R$ is the dot radius and $b$ is the core radius.

The Spin Transfer Torque acts as a negative damping. Its analytical expression depends on the polariser. [2] developped analytical expressions of the spin transfer torque for a uniform polariser, a circular polariser based on the nonuniform polariser introduced in [141] and even an expression for a centered vortex based on [142]. The case of a gyrating vortex however is a more complex problem. In the most simple case of a uniform polariser as used, the torque is purely linear and does not depend on the vortex position. Namely by considering simple shifts of the vortex core from the dot centre, one easily see by superposing the two uniform planar and the vortex magnetic configurations that the STT efficiency is not affected by the amplitude of the shifts. More complex polariser distributions are studied in this same reference, namely the static circular and vortex configuration.

In the simplest case of a uniformly perpendicularly polarised current the torque has the form

$$\overrightarrow{F_{\mathrm{STT}}}(\overrightarrow{X}) = P\lambda(X,J)\left[\overrightarrow{e_z}\times\overrightarrow{X}\right] \tag{5.20}$$

with $P$ the polarity, $\lambda$ the torque efficiency, and $J$ the current density.

### 5.3.4 Dynamical reversal mechanisms of the polarity

When the vortex gyrotropic motion is excited, the vortex gyrates at a linear speed increasing with its orbit radius until a critical speed is reached, at which the vortex polarity is dynamically switched. The mechanism for this dynamical reversal is explained by [143] as an effective field originating from the spatio-temporal dynamics of the moving vortex and concentrated near the vortex core, deforming the core profile until polarity reversal. The critical speed is estimated as $v_c \approx \gamma M_s b \approx \gamma(2A)^{1/2}$ where $b$ is the core radius and $A$ is the exchange stiffness.

Originally, it was demonstrated that the vortex core polarity could be resonantly reversed by absorbing an external RF magnetic field [144]. This has been studied more precisely in Pigeau's PhD thesis in a vortex magnetic dot with repeated short pulses of microwave magnetic field [145]. The same mechanism as for STT-induced reversal still holds as it depends on the vortex velocity only and not the exciting force. This reversal is also observed in STT driven vortex dynamics [146].

## 5.4 Double vortex dynamics

In this part, we discuss the influence of the dipolar coupling on the dynamics of a pair of vortex oscillators. We first describe in general terms the dipolarly coupled equations of two magnetic oscillators to remind the two main effects of the the dipolar coupling, which are to hybridise the eigen-modes of the system and to renormalize the eigen-frequencies. Then, we discuss more specifically the case of dipolar coupling in two adjacent vortex oscillators, where gyrotropic dynamics is excited. Finally, we remind the main results of

the analytical model of mutual synchronisation between adjacent STVOs through dipolar coupling based on the Thiele formalism.

### 5.4.1 Collective dynamics in a pair of dipolarly coupled magnets

Let us consider two magnetic oscillators, labeled by $i = 1,2$, having isolated frequencies $\omega_i$, and let us denote by $c_i$ the amplitude of the associated eigen-mode in each of them. When these two oscillators are sufficiently close to each other, they will experience the dipolar field generated by the dynamics in the neighbouring oscillator. By calling $h_{i\to j}$ the dynamic dipolar component from oscillator $i$ felt by oscillator $j$, the coupled equations of the system read (damping terms are neglected):

$$\frac{dc_1}{dt} = -i\omega_1 c_1 + i\gamma h_{2\to 1} c_2 \tag{5.21a}$$

$$\frac{dc_2}{dt} = -i\omega_2 c_2 + i\gamma h_{1\to 2} c_1 \tag{5.21b}$$

The solutions of this system, are, for the eigen-frequencies:

$$\omega_{A,B} = \frac{\omega_1 + \omega_2}{2} \pm \sqrt{\left(\frac{\omega_1 - \omega_2}{2}\right)^2 + \left(\frac{\Omega}{2}\right)^2}, \tag{5.22}$$

where $\Omega^2 = 4\gamma^2 h_{1\to 2} h_{2\to 1}$, and for the eigen-modes:

$$C_A = c_1 + \frac{\omega_1 - \omega_A}{\gamma h_{2\to 1}} c_2 \tag{5.23a}$$

$$C_B = \frac{\omega_2 - \omega_B}{\gamma h_{1\to 2}} c_1 + c_2\,. \tag{5.23b}$$

This shows that the two main effects of dipolar coupling on the dynamics are to split the frequencies by an amount $\Omega$, which quantifies the strength of the dipolar interaction, and to hybridise the dynamics, which becomes collective, as each oscillator is involved in each eigen-mode. This is illustrated in figure 5.9, which shows the typical frequency anti-crossing as the isolated frequencies of the oscillators get closer to each other (figure 5.9(a)) and the collective character of the dynamics at this anti-crossing, where in laterally separated nanomagnets, the lower energy mode is the accoustic mode, with the magnetisations in each oscillator oscillating in phase, and the higher energy mode is the optical mode, with them oscillating in anti-phase (figure 5.9(b)).

### 5.4.2 Dipolar interaction between two vortex oscillators

The remanent field of a vortex at rest is quasi naught, but once the gyrotropic mode is excited the net magnetisation caused by the shift of the vortex core and given by equation (5.2) induces an interaction between two neighbouring vortices. The exact analytical treatment of this magneto-dipolar interaction is a difficult task as it involves multipole expansions [137].

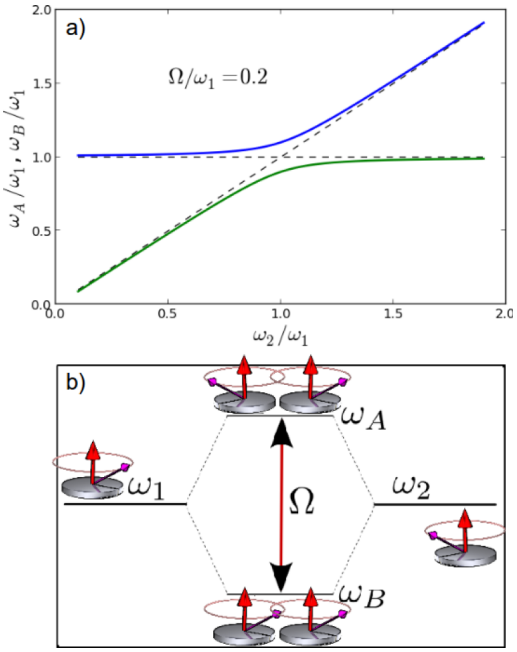


Fig. 5.9 *(a) Eigen-frequencies vs. mismatch between isolated frequencies. (b) Energy level diagram when $\omega_1 = \omega_2$. The magneto-dipolar interaction hybridises the system in binding and anti-binding coupled modes separated in frequency by the dynamical splitting $\Omega$.*

The simple picture, which will shall use to interpret our experimental results, is based on considering two macrodipoles $\vec{M}_1$ and $\vec{M}_2$ rotating in-plane and placed at the centers of the discs [147, 148]. In that case, the dipolar interaction between these dipoles is:

$$W_{int} = \frac{\vec{M}_1 \cdot \vec{M}_2 - 3(\vec{M}_1 \cdot \vec{e}_{12})(\vec{M}_2 \cdot \vec{e}_{12})}{d^3} \tag{5.24}$$

where $d$ is the distance between the centers of the disks and $\vec{e}_{12}$ is the unit vector joining them. From this expression, it can be seen that the dipolar interaction not only quickly decays with the separation ($\propto 1/d^3$) but also depends on the relative spatial arrangement of the two vortex oscillators, which in our experimental cases could be either superposed on top of each other or laterally separated.

In the case where the two vortices are superposed, the second term of equation (5.24) vanishes due to the cylindrical symmetry of the system (the in-plane macrodipoles $\vec{M}_i$ are perpendicular to $\vec{e}_{12}$). The coupling between the vortices can be very strong, moreover the interaction between the vortex cores is also relevant for small separations, and should be considered. A more complete description of the coupled vortex dynamics in this case can be found in reference [2]. In all possible cases for the vortex parameters, two hybridised frequencies with associated damping emerge, which are analogous to the two hybridised states of a diatomic molecule [149], as in the general case treated in the previous subsection, and depicted in figure 5.9.

The situation is more complex where the two vortices are placed side-by-side, since the axial symmetry is broken. All the directions are not affected equivalently in the

vortices plane and the core trajectories become elliptical. The above macrodipole model has been compared with micromagnetic simulations, and provides a hand-model for an easy comprehension of the interaction: namely the average interaction energy will be minimal for two dipoles rotating in phase [148]. For side-by-side vortex oscillators, which will correspond to our experimental case when we will study the mutual synchronisation between two adjacent STVOs (sections 7.3 to 7.5), the dipolar interaction can be rewritten in the following form [148, 119] :

$$W_{int} = C_1 C_2 (\mu^{\mathrm{AP}} X_1 X_2 \cos(\phi_1 + \phi_2) - \mu^{\mathrm{P}} X_1 X_2 \cos(\phi_1 - \phi_2)) \tag{5.25}$$

where the vortex cores in each disk are tracked by their polar coordinates $\vec{X}_i(X_i,\phi_i)$, $C_i$ denotes the chirality of vortex $i$, and $\mu^{\mathrm{P/AP}}$ are coefficients which can be found combining equation (5.2) and equation (5.24):

$$\mu^{\mathrm{AP}} = 3\frac{\pi^2\xi^2R^2L^2M_s^2}{2d^3} \tag{5.26a}$$

$$\mu^{\mathrm{P}} = \frac{\pi^2\xi^2R^2L^2M_s^2}{2d^3}\,. \tag{5.26b}$$

where $\xi = 2/3$, and $R$ and $L$ the radii and thicknesses of the disks, respectively, assumed to be identical.

In equation (5.25), the phase evolution of the vortex cores is given by $\dot{\phi}_i = P_i\omega_i$, where $P_i$ is the vortex polarity of oscillator $i$ and $\omega_i$ its absolute gyrotropic frequency. As a consequence, the term related to $\mu^{\mathrm{AP}}$ oscillates at $(P_1\omega_1 + P_2\omega_2)$, and the one related to $\mu^{\mathrm{P}}$ oscillates at $(P_1\omega_1 - P_2\omega_2)$. Therefore, two cases can be distinguished, depending whether the vortex polarities in the two disks are parallel (P) or antiparallel (AP). In the former case, the $\mu^{\mathrm{AP}}$ term is a fast time varying term, which quickly averages to zero, and the $\mu^{\mathrm{P}}$ term dominates at the anti-crossing, when $\omega_1 \simeq \omega_2$. In the latter case, the situation is opposite.

From the form of equation (5.25), the dipolar interaction is responsible for a new force in the Thiele equation of oscillator $i$, $\vec{F}_{int}^{j\to i} = -\frac{\partial W_{int}}{\partial \vec{X}_i}$. With the previous considerations on the distinction between P and AP polarities alignment in the neighbouring disks, the following effective strengths of the dipolar interaction can be found:

$$\Omega_P^{eff} = \frac{\mu^{\mathrm{P}}}{G} \tag{5.27a}$$

$$\Omega_{AP}^{eff} = \frac{\mu^{\mathrm{AP}}}{G}\,, \tag{5.27b}$$

where $G$ is the gyrovector (see equation (5.9)), assumed to be identical for both oscillators. This result shall be rederived in details in section 7.4. These two effective strengths differ by a factor 3, which results from the in-plane anisotropy of the magneto-dipolar interaction noted above, that can be seen directly in equation (5.24) as well. This can also be seen in figure 5.10(a) where the time evolution of the dipolar interaction between the two vortices is plotted. If one would take into consideration the exact magnetisation distribution in the moving vortices, this ratio would be slighlty different than 3, which is shown in the inset of figure 5.10(b) which is the result of micromagnetic simulations [148, 119].

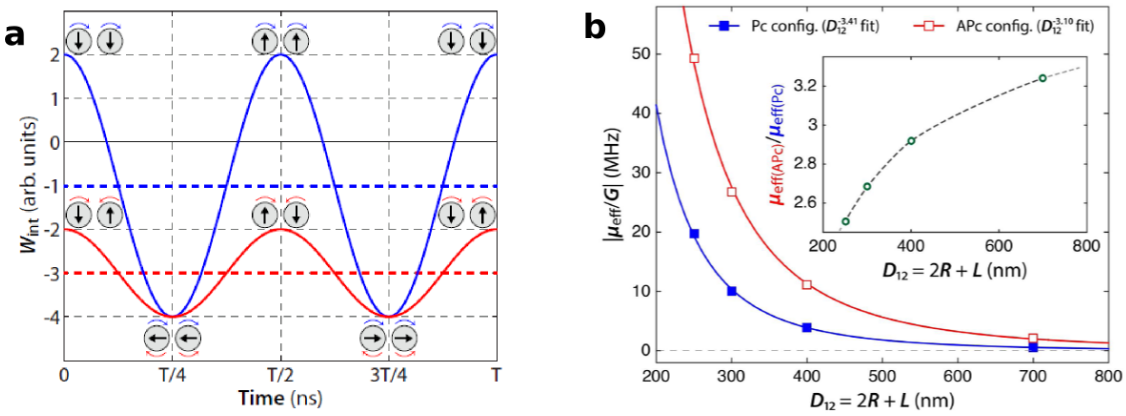


Fig. 5.10 *(a) Dipolar energy ($W_{int}$) evolution of two vortices modeled as macrodipoles oscillating at the same frequency. The blue curve describes the parallel polarity (P) state, and the red curve the antiparallel polarity (AP) state. The corresponding average values of the coupling energy are plotted as dashed lines. Extracted from [148]. (b) Average interaction energy versus interpillar distance extracted from micromagnetic simulations for the case of two identical synchronised oscillators with radii $R = 100$ nm, when vortices have identical polarities (blue line and filled squares) and opposite polarities (red line and open squares). Extracted from [119].*

### 5.4.3 Mutual synchronisation in a pair of dipolarly coupled STVOs

Using the previous expressions of the magneto-dipolar interaction between adjacent vortex oscillators, derived in the macrodipole-macrodipole approximation, and the results recalled in section 4.2.2 on the mutual synchronisation bandwidth between two nearly identical coupled auto-oscillators (i.e., differing only by their frequency), one can deduce that the latter is larger by a factor about 3 when the vortex polarities in adjacent oscillators are antiparallel (AP) than when they are parallel (P), which is the main experimental result reported in ref. [119]. A complete derivation of the synchronisation bandwidths in the two cases, based on the Thiele formalism, can be found in the supplemental material of the same reference, also recalled in 7.5.3:

$$\Delta\omega_P = 2\Omega_P^{eff}(\alpha\eta + \nu) \tag{5.28a}$$

$$\Delta\omega_{AP} = 2\Omega_{AP}^{eff}(\alpha\eta + \nu)\,. \tag{5.28b}$$

This shows that two mechanisms contribute to the mutual synchronisation between the vortex auto-oscillators. The first one corresponds to the direct action of the dipolar force on the oscillator phase (term proportional to the damping $\alpha\eta$, where $\eta$ is defined in equation (5.19)). The second one corresponds to the action of the dipolar force leading to the modification of the vortex core orbits, hence of their gyration frequency (term proportional to the dimensionless nonlinear parameter $\nu$, which can be linked to the different nonlinearities in the Thiele equation [129], see also section 8.1.2). Even in vortex-based oscillators, where the latter is not as strong as in other types of STNOs (typically, $1 \leq \nu \leq 5$), it is clearly the dominant mechanism as the damping term is of the order

0.01.

## 5.5 Non linear oscillator formalism applied to the vortex oscillator

The Thiele equivalence with the Slavin and Tiberkevich model has already been very well introduced in [150], and is summarised below.

Strictly speaking all terms are nonlinear. Some specific studies require taking into account the vortex core deformation will add a third derivative or other nonlinear terms [151, 152]. As the vortex core position is constrained to in-plane displacement, its dynamics may be described in polar coordinates $\overrightarrow{X(t)} = X(t)\overrightarrow{e_\rho}$, so that its time derivative $\dot{\overrightarrow{X(t)}} = \dot{X}\overrightarrow{e_\rho} + \dot{\phi}X\overrightarrow{e_\phi}$. Alternatively $\mathbf{X}(t) = X(t)e^{i\phi(t)}$ is the coordinate of the vortex core in the complex plane and its time derivative $\dot{\mathbf{X}} = (i\dot{\phi}X + \dot{X})e^{i\phi(t)}$.

Let us introduce a confinement force $\overrightarrow{F_{conf}} = (\partial E/\partial X)\overrightarrow{X}$. This is justified as in the following the confinement potential will be expressed as a polynome of $X^2$. The Spin Transfer Force, if we consider only the Slonczewski-like torque, will be directed perpendicularly to the vortex core position $\overrightarrow{F_{STT}} = \overrightarrow{f_{STT}} \times \overrightarrow{X}$. In this case the Thiele equation can be decomposed along the two vectors

$$\begin{cases} G\dot{\phi}X = & -D(X^2)\dot{X} + F_{conf}(X^2)X \\ G\dot{X} = & -D(X^2)\dot{\phi}X + f_{STT}X \end{cases} \tag{5.29}$$

By reinjecting each equation of the system into each other, rearranging the terms and simplifying the first one by $X$ the previous system can be transformed into

$$\begin{cases} \left(1 + \frac{D(X^2)^2}{G^2}\right)\dot{\phi} = & -\frac{D(X^2)f_{STT}(X^2)}{G^2} + \frac{F_{conf}(X^2)}{G} \\ \left(1 + \frac{D(X^2)^2}{G^2}\right)\dot{X} = & -\frac{D(X^2)F_{conf}(X^2)}{G^2}X + \frac{f_{STT}(X^2)}{G}X \end{cases} \tag{5.30}$$

Additionnaly considering $dp/dt = d(X^2)/dt = 2XdX/dt$ and the fact that typically $D^2/G^2 \ll 1$ this results in

$$\begin{cases} \dot{\phi} = & -\frac{D(p)f_{STT}(p)}{G^2} + \frac{F_{conf}(p)}{G} \\ \dot{p} = & -2\left(\frac{D(p)F_{conf}(p)}{G^2} - \frac{f_{STT}(p)}{G}\right)p \end{cases} \tag{5.31}$$

So the terms can be identified to those of the general nonlinear auto-oscillator equation.

$$\omega(p) = -\frac{D(p)f_{STT}(p)}{G^2} + \frac{F_{conf}(p)}{G} \tag{5.32}$$

$$\Gamma_+(p) = \frac{D(p)F_{conf}(p)}{G^2} \tag{5.33}$$

$$\Gamma_-(p) = \frac{f_{STT}(p)}{G} \tag{5.34}$$

Given that the positive and negative damping are the same order of magnitude, one can easily deduce that the phase equation is largely dominated by the confinement term. Namely $(D/G)f_{STT} \sim (D/G)^2 F_{conf} \ll F_{conf}$.

One interest of the model developped by Slavin and Tyberkevych is that it allows to apply previous results calculated with a simple phase model taking into account the nonlinearities, which resembles the Kuramoto model. We will take advantage of this equivalence for our numerical calculations in sections 7.3 to 7.5.

## Summary

**From the review of spin-torque oscillators, it appears that although they still display limited performances in terms of output power and spectral coherence, the interest they have driven for almost twenty years for their nonlinear properties, large synchronisation bandwidth, high tunability, has led to significant improvements. Now mutual synchronisation has been demonstrated up to nine STNOs. Vortex oscillators are particularly interesting for their relatively narrow linewidth, and their gyrotropic dynamics can be described from the position of the vortex core. We have introduced the vortex distibution, which has been well-studied for more than a decade, and put into equation the effects of the bias conditions which are now well-understood. Important as well is the Thiele equation which describes the dynamics of the vortex core in the gyrotropic mode, where the vortex core gyrates around its equilibrium position. The Thiele equation includes all the nonlinear terms present in the nonlinear auto-oscillator model, and has been demonstrated to be equivalent to the nonlinear auto-oscillator equation. Lastly, quite simple analytical equations have been developed in the macrodipole approximation, to describe the mutual dipolar coupling of neighbouring vortices, either on top of each other in double vortex STNOs, or next to each other, in terms of mode hybridisation and mutual synchronisation.**

# Chapter 6

# Experimental setup

The main object of this thesis, as far as STNOs are concerned, is studying the manipulation of a pair of mutually coupled STNOs using an external signal. Our system therefore consists of two nanopillars, lithographied very close to each other, so they interact with each other via their generated stray fields. The gold stripline deposited on top allows to generate a microwave magnetic field, to act on the STNO pair. We first describe the setup in details, then the measurement methods.

## 6.1 Samples

The working principle of an individual device is presented in figure 6.1. The pair of STNOs (or the individual STNO) are connected in parallel by a gold wire which feeds the dc bias current. The STNOs used are metallic Py(15nm)/Cu(10nm)/Py(4nm) (see figure 6.2a) circular nanopillars. Because of the close distance, they are mutually coupled through the dipolar magnetic field generated by each other, as opposed to nanocontacts which would interact through spin waves in a shared magnetic medium. The originality of this work is the 150nm thick gold microstrip antenna lithographied on top, which is isolated from the STNOs with a 200nm thick SU8 resist, and will be used to generate an in-plane microwave magnetic field. The antenna is in fact 5 microns wide, so it largely overlaps the STNO pair (the largest one being two 400nm diameter nanopillars with 200nm separation). Additionnaly the RF field felt by the STO pair is uniform and oriented in the plane of the STOs.

The layout presented in figure 6.2b (labelled as 1A) is the actual of the principle presented in 6.1. The large tracks on the left-hand side are the electrodes connecting the STNOs, with the single central electrode with an empty square window on top of the STNOs and the other two departing from the bottom. This arrangement should optimise the current repartition, so it flows equally through both STNOs. The right-hand part is the antenna. The squares at the center are insulating layers isolating respectively the antenna from the electrodes and the electrodes from each other. The circuit was designed to minimise the coupling between the antenna and the electrodes.
The electrodes and the antenna are then contacted by picoprobes connected to the rest of the circuit described in figure 6.3. The devices were deposited as a batch of $8 \times 8$ samples. Each column labelled A-H corresponds to a different device geometry. The STNOs are

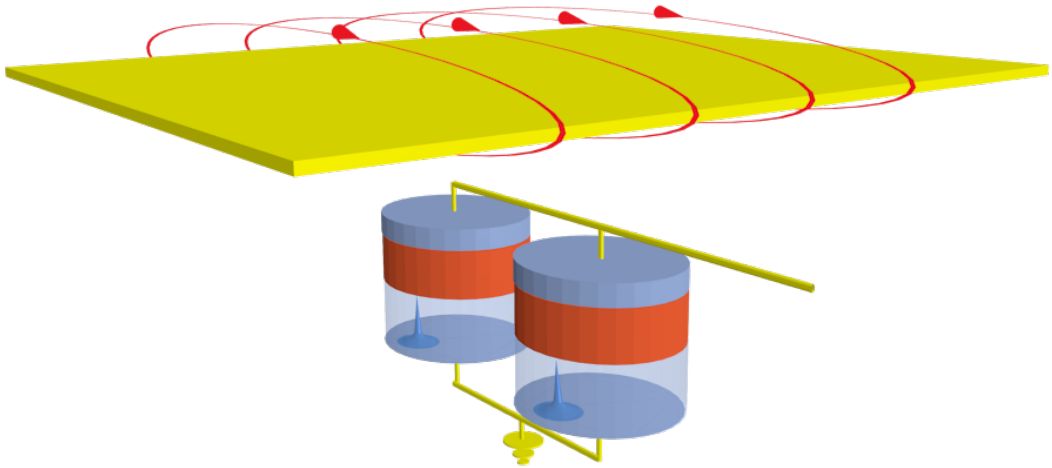

Fig. 6.1 *Schematic of an individual sample. The field lines of the microwave field generated by the antenna are represented in red. The vortex cores are represented in the thick layers. The current feeds the two pillars in parallel.*

Table 6.1: Expected values of the coupling amplitude for the various geometries of the STVO pairs estimated from a macrodipole interaction model.

| diameter (nm) | 200 | | | 400 | | |
|---|---|---|---|---|---|---|
| separation (nm) | 50 | 100 | 200 | 50 | 100 | 200 |
| $\Omega_P^{eff}/(2\pi)$ (MHz) | 7.6 | 4.4 | 1.9 | 5.2 | 3.8 | 2.2 |
| $\Omega_{AP}^{eff}/(2\pi)$ (MHz) | 22.8 | 13.2 | 5.7 | 15.6 | 11.4 | 6.6 |

cylindrical nanopillars with either 200nm or 400nm diameter, and devices containing pairs of STNOs have varied interpillar separations. Figure 6.2a reproduces the full batch, and on top the various geometries produced. The expected coupling values between the thick layers in the vortex state estimated using equation (5.27) are listed in table 6.1.

## 6.2 Transport measurements

### 6.2.1 Spectrum analyser measurements

The aim of this measurement is to electrically detect the auto-oscillation signal from the samples. Most of the measurements in this thesis are performed at frequencies of a few hundreds of MHz to a few GHz, as this is the targeted range for potential applications of STNOs.

The auto-oscillation voltage signal measured from an STNO originates from oscilla-

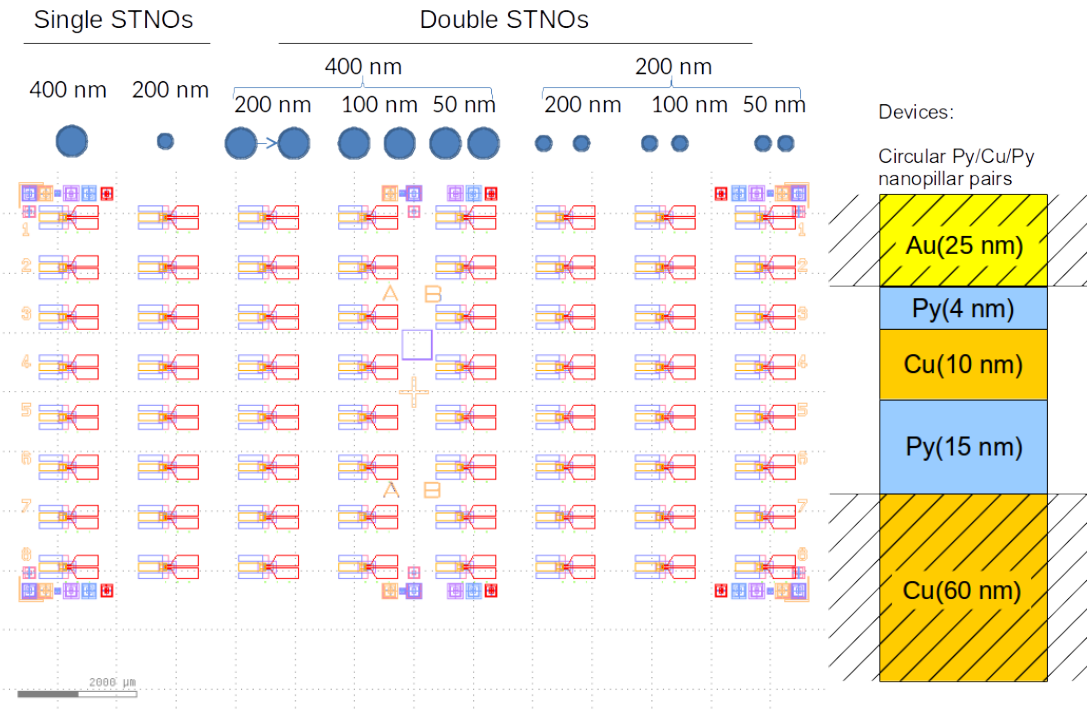


(a) *General layout of the batch of samples. Samples of a same configuration are grouped by column and labelled 1 to 8.*

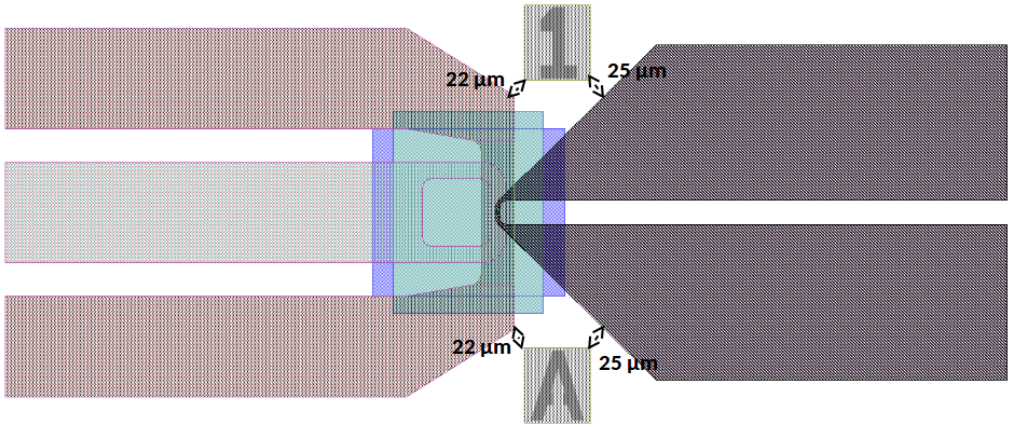


(b) *Individual device configuration.*

Fig. 6.2 *Lithography layout including most layers.*

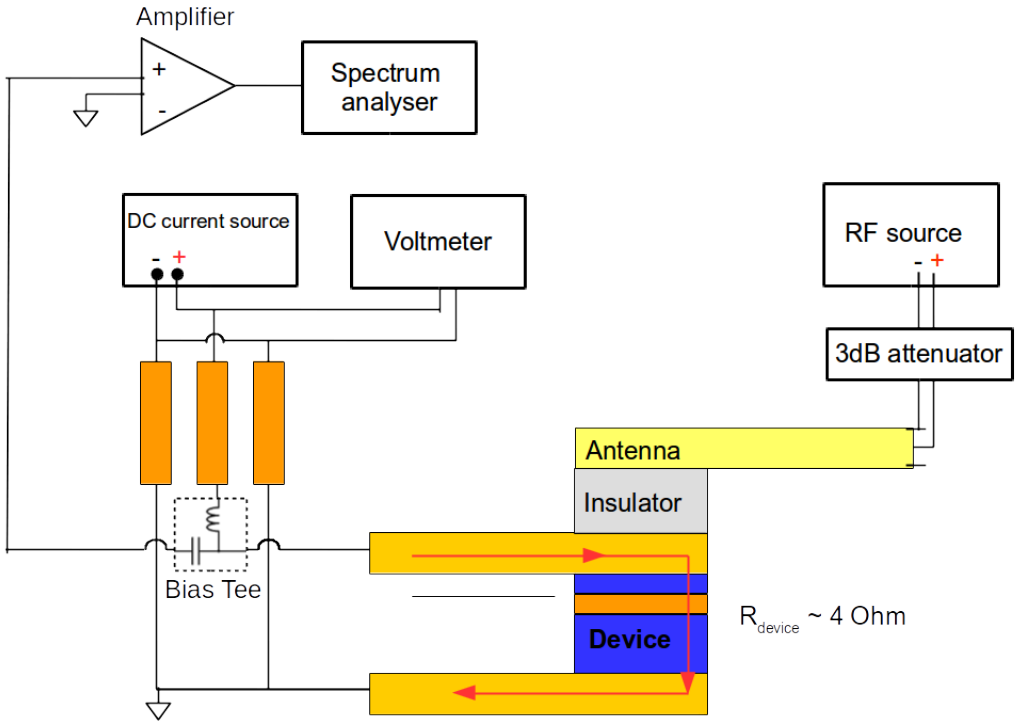


Fig. 6.3 *Schematic of the electrical connections in the experimental setup for the spectrum analyser measurements.*

tions in the GMR $V(\omega) = R(\omega)I_{dc}$, where $I_{dc}$ is the bias current creating the STT which causes the steady precessions of magnetisation of the thin layer. These self-sustained oscillations of the magnetisation are converted into oscillations of the resistance, which are then converted into oscillations of the voltage through the dc current.

The STNOs are connected in parallel to a dc current source which will provide the bias current. The measurement circuit additionnaly includes a voltmeter to analyse the dc voltage, and a spectrum analyser preceded by a low-noise amplifier to analyse the ac component of the voltage. The ac and dc circuit are isolated from one another by a bias tee. The antenna is connected to an RF source through a 3dB attenuator, to reduce reflections. Namely there might be impedance mismatches related to the contacts of the picoprobes.

An aluminum pole places the sample holder at the centre of an electromagnet, which is able to generate a dc magnetic field up to 11kG. The electromagnet can be rotated around the pole axis. In the folowing when an in-plane magnetic dc field is mentionned, it is directed parallel to the alignment of the two STNOs.

It can been calculated that the microwave field generated by the antenna felt by the magnetic layers is around 0.8mT (8 Gauss) for a 0dBm input power from the synthetiser, considering that for the short-circuit antenna

$$\mu_0 h_{rf} = \frac{\mu_0}{w}\sqrt{\frac{P_{in}}{2Z_0}} \tag{6.1}$$

where $w = 5\mu$m is the stripline width at the shortcut, $P_{in}$ is the power of the signal arriving to the shortcut with an estimated 2 to 3dB loss between the synthetiser and the shortcut, and $Z_0 = 50\Omega$ is the adapted impedance of the antenna.

In the setup described in figure 6.3, the spectrum analyser from Agilent is able to measure frequencies from 9kHz to 26GHz for frequency domain analysis. The spectrum analyser is preceded by a low-noise amplifier. In our measurements we used the Narda-Miteq AMF-3F-00100400-10-10P with 35dB gain and the AMF-2F-00100100-07-10P with 33dB gain.

### 6.2.2 Electrically detected ferromagnetic resonance

In this technique both a dc current and an RF field are applied, while the dc voltage is measured across the sample. The dc current indeed exerts a torque on the thin layer, but this is not necessarily sufficient to excite the auto-oscillation mode, so the existing modes are damped. This technique provides access to the dynamics of the system in the subcritical regime, as to locate the existing modes and understand the configuration of the STNOs. From the resonance peaks one is able to observe the modes even without auto-oscillation.

In the case when we are performing a voltage-FMR measurement, the RF-part of the measurement circuit can be replaced by a lock-in, which is then synchronised with the emissions of the RF source.

To reduce the effect of both the background and noise, the microwave signal generating the microwave magnetic field is switched on and off at a frequency of a few tenths of kHz, and the modulated signal is measured with a lock-in amplifier. There also is a baseline due to the reflections and the frequency-dependent coupling between the antenna and the measurement circuit. This former effect is hampered by the 3dB attenuator inserted after the RF source.

The RF field excites the dynamics of the magnetic device, what changes its dc resistance. The primary use of the dc current is to create a dc voltage signal from this resistance variation. This signal therefore is proportional in amplitude to bias current $V_{dc} = \Delta R_{\mathrm{FMR}} I_{dc}$. This effect is resonant at the frequencies of the eigenmodes, where the excitation is more efficient.

The measured signal is in reality complicated by the ac current leaked from the antenna imperfectly isolated from the STNOs, which is rectified by the alternating resistance according to the so-called spin diode effect [59, 60], and generates a dc voltage. This rectified voltage should in principle be zero for circular trajectories (one single circular nanopillar), but could be used in our case for pairs of STNOs where the symmetry is broken and the bias current of the STNOs affects the dynamics of each other. This part of the signal remains weak however. Namely the oscillations in resistance are weak since the oscillators are very symmetrical, however they still exist since we can observe an auto-oscillation signal for overcritical bias currents. Additionaly the leakage current remains small as the isolation between the two circuits, although it cannot be perfect, was well-studied [153].

A second mechanism for the generation of a dc voltage is the rectification of spin currents emitted by the precessing magnetisation [154], but this last mechanism is a few orders of magnitude below the main signal originating from the dc change in resistance, and can be easily neglected.

## Summary

**In this chapter we have presented the studied samples, which consist in single nanopillars and pairs of nanopillars with a small separation, with various geometries which will enable us to quantitatively study mutual synchonisation phenomena. The antenna on top will enable to study the effect of a third "ideal" auto-oscillator, and perform spectroscopic measurements. Auto-oscillation measurements provide directly the electrical output signal spectrum. Voltage-FMR is a spectroscopic technique which enables to probe mode frequencies even when the STNOs are not auto-oscillating.**

# Chapter 7

# Experimental results

This chapter gathers the measurements obtained from the experimental setup described in the previous chapter. First we characterise the static and dynamic properties of our samples in the passive and autonomous regimes. In particular we clearly demonstrate that mutual synchronisation can be achieved in pairs of STVOs thanks to the magneto-dipolar interaction. Then we make use of the antenna as an "ideal oscillator" to introduce original measurements. We probe the pair of mutually coupled STVOs in two states: first when they are out of synchonisation, second when they are mutually synchronised.

## 7.1 Static measurements

The first characterisation measurements that can be taken is simply measuring the resistance value for each sample. The 14 samples marked with capital "X" in table 7.1 were displaying either infinite (open circuit) or naught (short circuit) resistance, leaving 50

Table 7.1: Resistance (Ω) / GMR (mΩ) of measured devices. X: not connected (as received); x: not connected (wrong manipulation); empty: not measured. The samples highlighted in the gray boxes are those for which data are presented in this manuscript.

| diameter (nm) | 400 | 200 | 400 | | | 200 | | |
|---|---|---|---|---|---|---|---|---|
| separation (nm) | single | single | 200 | 100 | 50 | 200 | 100 | 50 |
| 1 | X | | 2.7 / 2.5 | | 4 / none | 8.1 / 9 | x | 4.2 / 3 |
| 2 | | | X | | 3.9(3.5) / 2.7 | 7.1/ 10 | x | 4.8(3.6)/ 6(3) |
| 3 | **3.4 / 4.5** | | 3.2 / 2.5 | | | 5.1 / 11 | X | 3.8 / 6 |
| 4 | | 4.1 /13 | 2.8 / 2.6 | | | 5/ 10 | X | 4.6 / none |
| 5 | X | X | 2.7 / 2.6 | X | | 7.3 / 9 | x | X |
| 6 | X | X | **4.0(2.9) / 2.7** | 4 / 2.8 | | 9.5/ 6 | x | |
| 7 | 3 / 4 | **4.8 / 18** | X | X | | 8(6) / 12 | X | **4.7 / 8** |
| 8 | 3.2 / 4.5 | 4.9 / 18 | 3.7(7.6) / 2.5 | X | | 5.6 / 10 | x | |
| | A | B | C | D | E | F | G | H |

measurable samples out of 64. Following mismanipulations, 45 samples out of 64 could finally be measured. Out of the measured samples the data of four ones were selected as representative of the rest of the batch. These are highlighted in table 7.1

It should be noted that the GMR ratio (black data in table 7.1) is roughly twice as large for single oscillators when compared to double (columns A vs C,D,E and B vs F,G,H) as the transverse area is twice as large for double nanopillars. In a similar way the GMR of 200nm diameter nanopillars is roughly four times as large as that of 400nm-diameter nanopillars as their transverse area is quadrupled. The resistance data (red data in table 7.1) is less relevant as it is dominated by the resistance of the rest of the electrical circuit.

Simulations indicate the presence of a magnetic vortex in each magnetic layer for sufficient dc-current (see figure A.1). In fact the stability of the vortex state magnetic distribution is dictated in principle by the geometry of the magnetic layer, which acts on the competition between the exchange interaction and the magneto-dipolar interaction (see figure 5.3), as well as the Oersted field created by the bias current (see figure 5.6). As outlined previously, polarity and chirality are two key parameters to characterise a magnetic vortex behaviour and can both take two values that are $\pm 1$. For a single nanopillar, with one vortex in each layer, this gives rise to 4 possible combinations. With two nanopillars, this gives rise to 8 possible combinations.

Figure 7.1 illustrates the characterisation method to check the existence of GMR in each sample. These data are the most representative of the batch, but the other measured samples give out similar results.

First let us consider a single-pillar sample (panels 7.1(a),(b),(e),(f)) at zero bias field.

Let us start with panel 7.1(a), which is a 400nm-diameter single nanopillar. The dc bias current is swept from high positive values to high negative values and back to positive. The parabolic component of the curve shape should be attributed to thermal effects. Namely if we consider a current of a few tenths mA flowing through a pillar with a $(400\text{nm}/2)^2\pi \approx 0.1\mu\text{m}^2$, then a quick calculation gives an estimate for the current density of $10\text{mA}/0.1\mu\text{m}^2 = 10^{11}\text{A}/\text{m}^2$, and this high current density will heat up the sample.

Panel 7.1(b) displays the same data as figure 7.1(a), but the branches with decreasing current absolute value $|I_{dc}|$ are substracted to the branches with increasing $|I_{dc}|$. This way the hysteretic features present in the top branches can be extracted.

As a large dc bias current $|I_{dc}|$ flows through the device, the current-induced Oersted field imposes its chirality to the vortices in all magnetic layers. The current absolute value $|I_{dc}|$ is then decreased until the current $I_{dc}$ eventually changes sign. This change in current polarity is accompanied by a change in the chirality of the Oersted field. As the current changes sign, a qualitative change can be observed as a jump in resistance. This jump can simply be explained by a change in the magnetoresistance related to a chirality change, since the current does not affect the vortex polarity at low current densities. It implies that the magnetisation distribution in both the thin and the thick layers are in the vortex state. One can guess that the thick layer or pinned layer has a larger magnetic volume and will be less affected by external perturbations than the thin layer. In particular the chiralities of each layer will be switched at two different current values, and for a certain current range they will be opposite chiralities, what increases the magnetoresistance.

In a double-pillar sample (panel 7.1(c),(d)), each of the four magnetic layers contain one vortex. The chiralities of the four vortices in the pair of STVO (two for each STVO, one in the thick Py(15 nm) disc and one from the thin Py(4 nm) disc), which define the

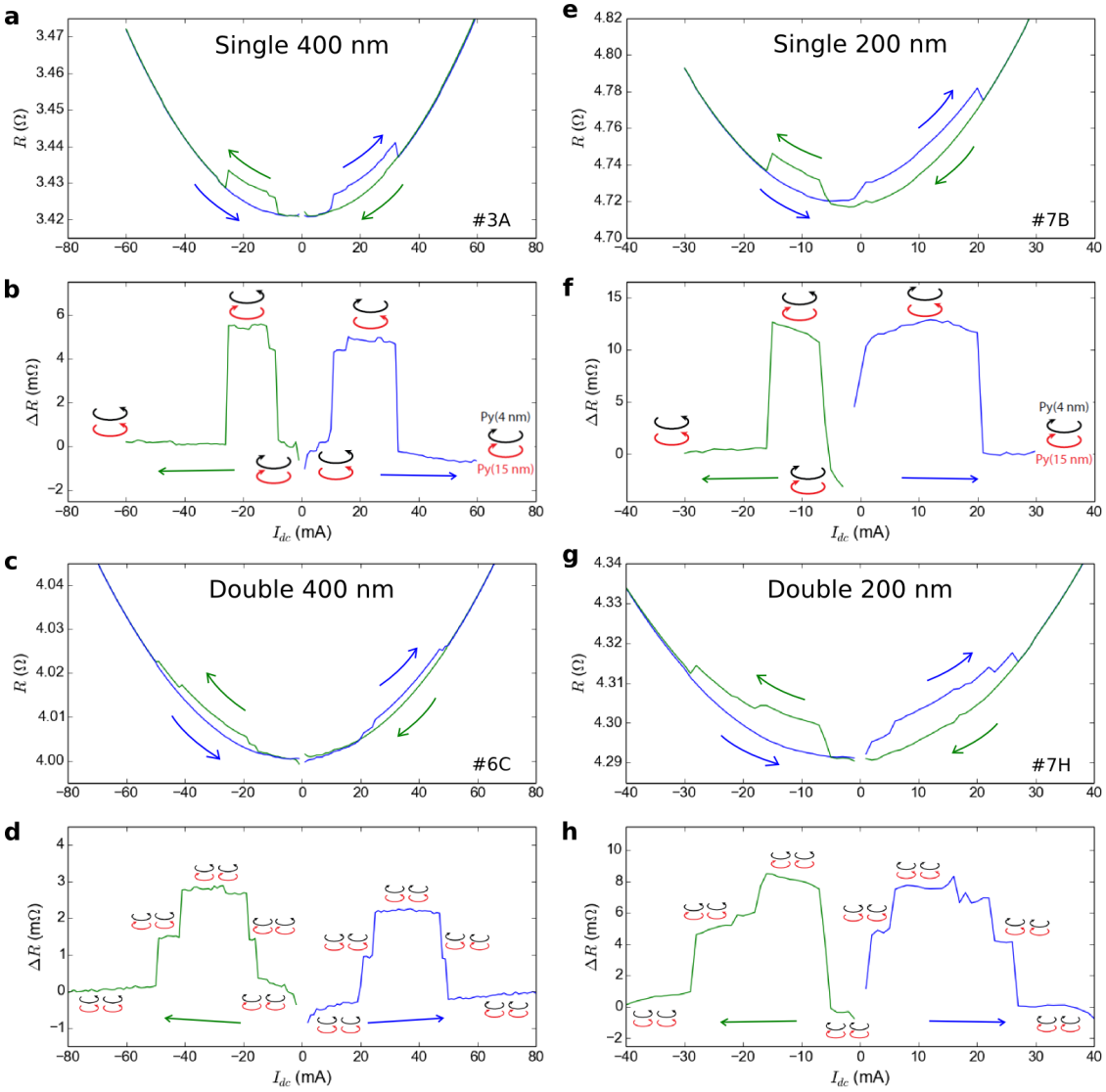


Fig. 7.1 *Evolution of the resistance of the sample as the current is swept from positive to negative values and vice versa. The parabolic component is related to thermal effects. Each jump corresponds to a reversal in chirality of one magnetic layer: a single device (panels (a),(b),(e),(f)) counts 2 magnetic layers and a double nanopillar (panels (c),(d),(g),(h)) counts 4 layers. In panels (b), (f), (d), (h) the branch with decreasing current is substracted to the branch with increasing current to make the resistance jumps more visible. The red and black circular arrows represent the chirality states in the thick and thin layer, respectively.*

curling direction of the magnetization around vortex core, can be accessed again by the magnetoresistance effect. Figure 7.1(c) shows the hysteresis loop of electrical resistance ($R$) of the sample as a function of current ($I_{dc}$) at zero biasing field. The resistance difference $\Delta R$ between the upper and lower branches is extracted in Figure 7.1(d). When the absolute value of $I_{dc}$, or $|I_{dc}|$, is above 60 mA, the chiralities of the two Py layers in each STVO are the same, both clockwise for $I_{dc} > 0$ and counter-clockwise for $I_{dc} < 0$. The magnetoresistance is minimized due to parallel magnetizations in each STVO. By reducing $|I_{dc}|$ and reversing its sign, two abrupt resistance increases are firstly observed when $|I_{dc}|$ is around 20 mA corresponding to the chirality switchings of the two Py(4 nm) layers. Keeping increasing $|I_{dc}|$, two additional jumps can also be observed when $|I_{dc}|$ is between 40 and 50 mA corresponding to the chirality switchings of the two Py(15 nm) layers. Since the two pilllars cannot be exactly identical, all 4 chirality reversals happen at different currents and 4 jumps are visible on each branch. The individual vortex polarities are represented for each "plateau" (that is, between two successive jumps) with a curling arrow. This way we ensure that two STVOs are "alive" in this device. Since the 4 jumps are of similar amplitude, one can imply that the current is roughly equally distributed through both nanopillars.

Owing to the similar chirality switching currents and amplitudes of resistance jump, the data show that the two 400nm nanopillar spin valves are close in geometry as designed. It also shows that at the working current of $I_{dc} = 95$ mA, which will be used in sections 7.3 and 7.4, the four chirality states are ensured to be the same. The bias current used for 200nm nanopillars also is high enough to impose parallel chiralities in each nanopillar (see figures 7.1(g) and (h) and figure 7.3).

From this section we know that for each STVOs a vortex is present in both the thin and the thick layers, and that the STVO actually displays a GMR effect. It should be noted however that the amplitude of the jumps is intrinsically smaller than the full magnetoresistance, which we also have measured by sweeping the bias field to prepare the states where the magnetic layers are fully parallel and fully antiparallel.

## 7.2 Single oscillator dynamic measurements

In this section we focus on samples #3A and #7B for single devices, but the other devices display similar results. The objective is essentially to ensure that we are able to measure the same effects as can be found in the litterature [**?** 2] for this type of STVO.

### 7.2.1 Voltage-FMR

As indicated in section 6.2.2, the resonant frequency of an STVO can be characterised by FMR, even when no auto-oscillating mode is excited. In figure 7.2 we introduce a dynamical solution to detect and control the polarity and chirality of the vortices. In panels (a) and (b), the vortex polarities are imposed by the strong perpendicular bias magnetic field, which is then swept towards the opposite sign. We know from equation (5.18) that the gyrotropic frequency of the vortices is linearly dependent with the bias field, and its slope sign is that of the vortex polarity. Here the mode observed is the mode dominated by the thick layer. This mode is selected both due to its large magnetic volume and due to the current polarity, which then flows from the thin to the thick

layer. In voltage-FMR the modes dominated by each magnetic layer should be visible, but the mode dominated by the thin layer gyrates at typically a three to four times lower frequency, due to the thinner layer thickness (see equation (5.13)) and is not visible in this range of frequencies. The polarity of the vortex in the thick layer thus determines the sign of the slope of $\omega_G(H_\perp)$, and the frequency range. The FMR measurements allow to track the main mode over a large domain and observe the large hysteresis as the polarity reversal happens at $\pm$1.5kOe.

This splitting between two modes according to the vortex polarity was revealed in [130]. In this reference, an MRFM measurement of a magnetic vortex in a nanodisc is described as a spectroscopic tool to reveal the vortex polarity. In fact because there are two possible core polarities, there exist two rotational modes of the vortex of the thick layer corresponding to each polarity, and these two modes have opposite field dependence. For small bias field there exists a window where the vortex is bistable and each of the two modes can be selected.

Similarly in panels (c) and (d) the current dependence of the mode frequency can be tracked using FMR. Once again the dynamics is dominated by the thick layer. Again the process of chirality reversal is largely hysteretic. There is a small area in between the dashed lines where the chiralities of the two vortices are opposite, and this area is characterised by an increase in the dc resistance of the sample, as indicated by the black $R(I)$ curve on top of the plots. Figures 7.2(c) and (d) should be put in perspective with figure 7.1 and equation 5.12. Namely the thin layer vortex chirality follows the Oersted field from the bias current quite well and switches polarity close to zero field, while the thick layer displays a larger hysteresis. With this measurement we reveal the effect of the Oersted field on the gyrotropic mode described in [129]. The current creates an Oersted field which linearly contributes to the confinement.

The hysteresis originates from the relative polarity reversal between the two vortices due to the bias field sign reversal in (a) and (b), and to the relative chirality reversal in (c) and (d). Oscillations in the baseline are attributed to the fact that the impedance cannot be adapted to every frequency.

This measurement can be performed on 200nm- and 400nm- diameter STVOs, and on double STVOs as well. From those measurements can be extrapolated the gyrotropic frequency in table 7.2. The fundamental frequency of the single 200nm devices as displayed in column #B of table 7.2 (extrapolated at zero current and zero field from voltage-FMR measurements) are typically close to twice that of the 400nm single devices in column #A, in agreement with the expression for the fundamental magnetostatic frequency $\omega_G = (20/9)(L/R)\gamma M_S$. The fundamental frequencies of pairs of STVOs is typically slightly smaller than that of single STVOs.

### 7.2.2 Auto-oscillations

The data presented in this section reproduce results performed in [108] and [101] on similar double-vortex STVOs with 200nm diameter, and complete them by adding results from similar measurements on 400nm-diameter STVOs.

The data plotted in figure 7.3(a) is typical from single STVOs. Let us emphasize, that we only have to consider the parallel chiralities case since the high current injected through the STVO stabilises one specific chirality in the two vortices.

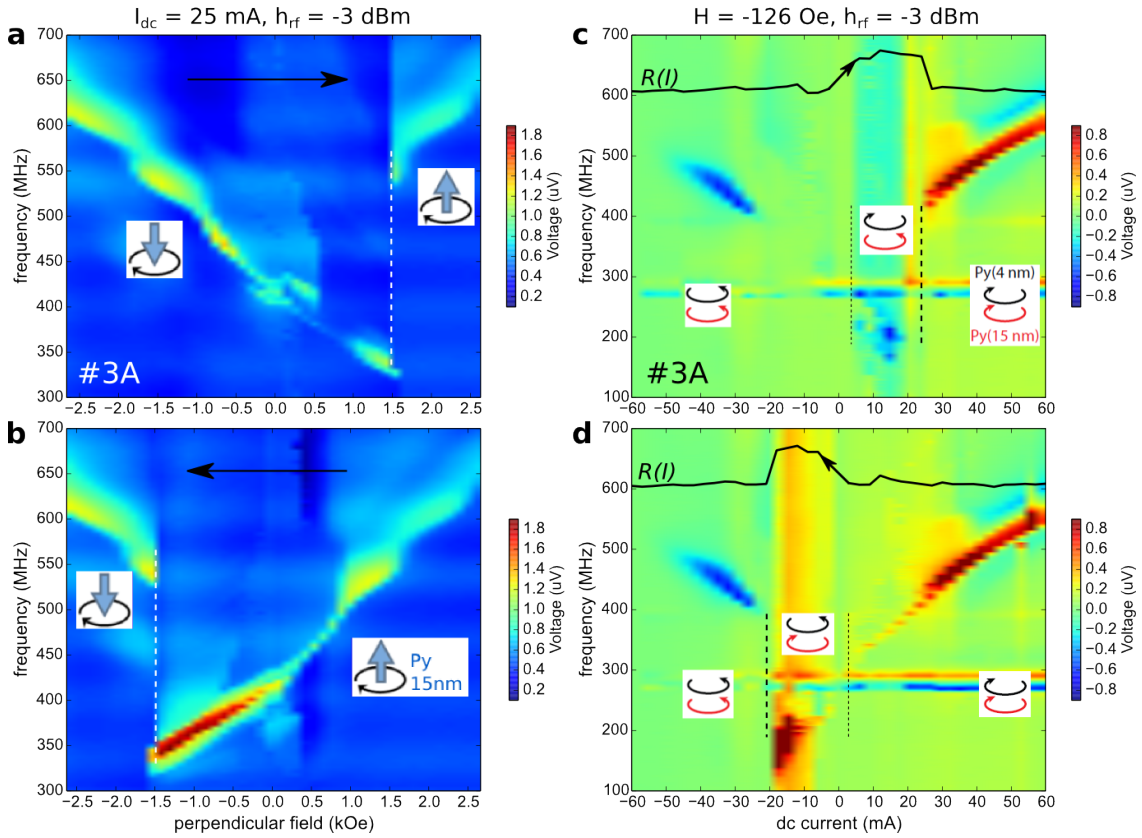


Fig. 7.2 *Voltage-FMR of a 400 nm diameter sample versus dc bias field sweep up (a) and down (b) and versus dc bias current sweep up (c) and down (d). The hysteresis between (a) and (b) is due to the hysteresis in the polarity reversal of the thick layer. The hysteresis between (c) and (d) stems from that of the chirality reversal due in the thick layer.*

From [108] we know that in such devices, an auto-oscillation signal is visible only under the condition of opposite polarities of the vortices in the thick and thin layer. At, say, high positive out-of-plane field, the polarities of the vortices in both layers align with the external magnetic field, so no signal is visible. As the external field changes sign, the polarity of the thin layer reverses. Since the magnetic volume of the thin layer is smaller than that of the thick layer, it reverses at a lesser field magnitude. A signal is now visible, and the sign of the slope of the auto-oscillation frequency dependence versus field is in principle that of the vortex polarity with respect to the external out-of-plane bias field. The two vortices in one single pillar are one above the other and separated by only 10nm, so they display a coupled behaviour. Because of the polarity of current creating the STT the thick layer still dominates the dynamics of the two layers, while the mode dominated by the thin layer Py(4nm) is damped. There is a clear signature of this as the auto-oscillation signal is visible for opposite polarities of the thick and thin layer, and the sign of the slope clearly indicate the thick layer is dominating (most hysteretic vortex polarity). An auto-oscillation signal is visible as the bias field $H_{\perp}$ is swept from -450G to 1.67kG and the bias current fixed at 25 mA, with a frequency decreasing from

Table 7.2: Extrapolated gyrotropic frequency in MHz at zero external field and zero current from FMR voltage measurements.

| diameter (nm) | 400 | 200 | 400 | | | 200 | | |
|---|---|---|---|---|---|---|---|---|
| separation (nm) | single | single | 200 | 100 | 50 | 200 | 100 | 50 |
| 1 | X | | | | | | x | |
| 2 | | | X | | | | x | |
| 3 | **300** | | 250 | | | 400 | X | 300-400 |
| 4 | | 600-650 | | | | 500 | X | |
| 5 | X | X | | X | | | x | X |
| 6 | X | X | **280** | | | | x | |
| 7 | 300-350 | **500-600** | X | X | | 350-400 | X | **500** |
| 8 | 300-350 | 500-600 | | X | | 400 | x | |
| | A | B | C | D | E | F | G | H |

817MHz to 560MHz with a slope of -119kHz/G. These values fall within the range of expected values for the gyrotropic frequency of the thick layer, augmented by the Oersted field and the coupling with the gyrotropic mode of the thin layer [156].

The field dependence of the auto-oscillation frequency versus field corroborates the frequency dependence of the thick layer mode that was observed in figure 7.2(a) and (b), but for auto-oscillations a signal is visible only when the polarities of the two layers are opposite. However in addition to that, it is possible to observe the influence of the damped mode dominated by the thin layer Py(4nm) through the oscillations in the linewidth in figure 7.3(b), according to the analysis in [101]. In this study, the STVO was estimated to be quasi-isochronous. The STVOs remains highly tunable with respect to the current under this hypothesis, since for vortex-based oscillators, current tunability of the gyrotropic mode is largely due to the contribution of the Oersted field to the confinement potential. In fact for a certain value of the bias current the nonlinearities due respectively to the magnetostatics and the Oersted field can compensate each other [129], and the linewidth becomes comparatively narrow for this point. More generally vortex-based STVOs display a relatively narrow linewidth, because of their smaller nonlinearity, when compared to their other STVO counterparts, while keeping a good current tunability and frequency agility.

So according to [101] the linewidth broadening should be attributed to the coupling between the overdamped gyrotropic mode dominated by the thin layer and its harmonics and the excited mode dominated by the thick layer. When the frequencies of the excited mode and the overdamped mode are commensurate, or in other words the harmonics of the two modes cross each other, the frequency dispersion softens [157] as these conditions provide an additional relaxation channel. The coherence time of the auto-oscillations is thereby decreased, and the linewidth increases. This explains why the local character of

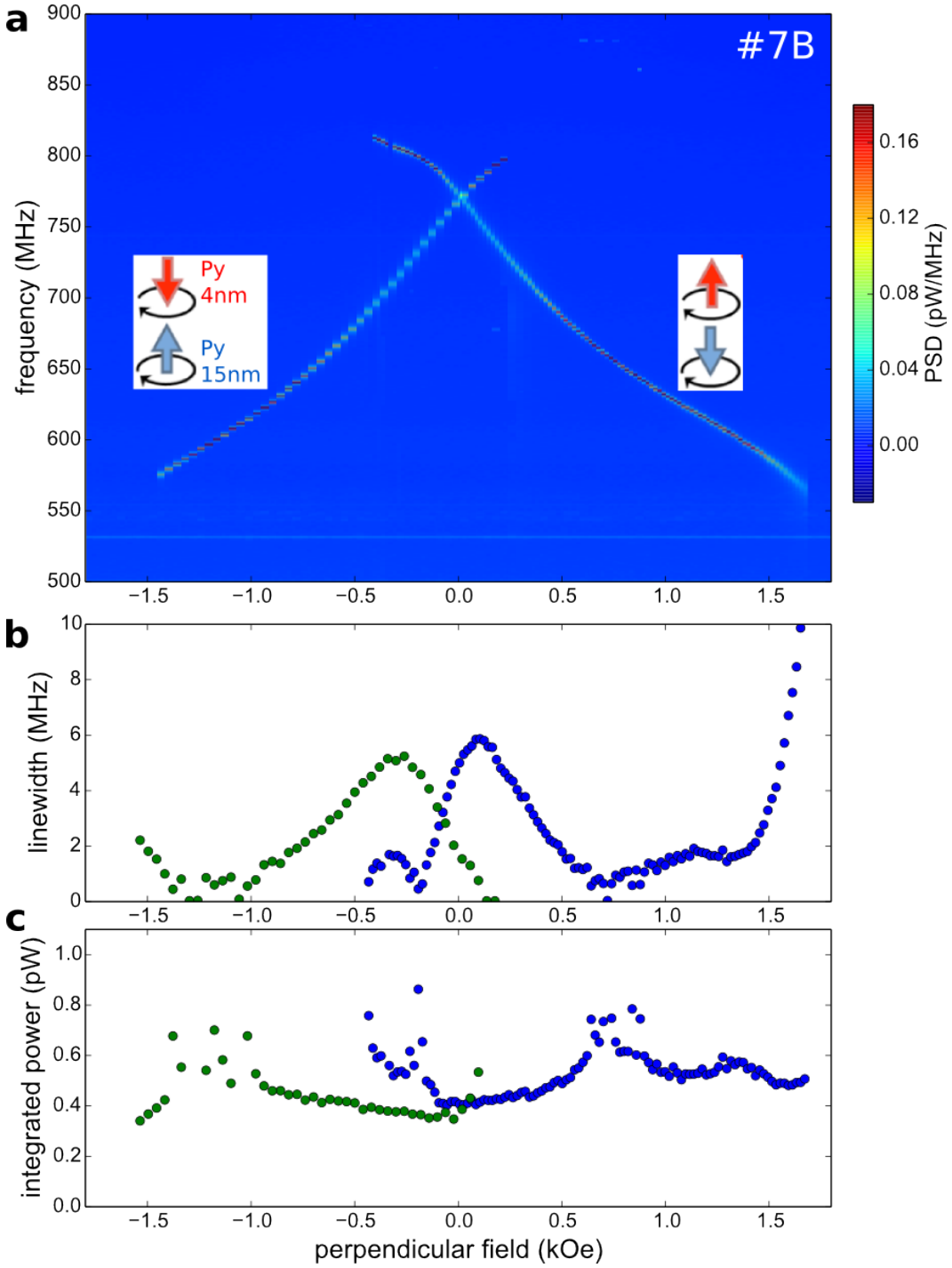


Fig. 7.3 *(a) Frequency dependence against the out-of-plane applied dc magnetic field for a single 200nm-diameter STVO. The data for an increasing and for a decreasing field are superposed. (b) Linewidth fitted from the data presented in (a). (c) Integrated power estimated as the peak amplitude times linewidth product from the fits. The 1MHz resolution bandwidth of the spectrum analyser limits the validity of fits where the linewidth is minimum.*

frequency broadening and the oscillations in the linewidth.

In order to complete this analysis let us consider figure 7.3(c). The supercriticality is roughly constant in these measurements and the emitted power can be quickly estimated from a simple linewidth times peak amplitude product. We estimate a 0.4pW integrated power within the entire domain of existence of the signal. This is similar to the analysis of [101] and the fact that the energy is not lost but transferred between the two modes.

In figure 7.4 the spectra are plotted versus dc current for several bias fields. Note that in this figure the nanopillar diameter is 400nm instead of 200nm. The measurement at -385Oe was taken for a polarity opposite to that at 249Oe, this is why it has a lower frequency. From those measurements one can check again the linear dependence of the frequency on the current $\omega(J) = \omega_{ms} + J\omega_{Oe}$, as stated in equation 5.12, and in accordance with figure 7.2(c) and (d). Equally one can locate the threshold for auto-oscillations around 35mA, although the field dependence of the threshold is non trivial. Namely as observed earlier with the oscillating linewidth versus field, the damping will change with field and thus the STT necessary to compensate this damping will not be constant. The linewidth (panel (b)) first decreases as the current $I$ increases above $I_{th}$, reaches an optimum, and then increases again. The integrated power (panel (c)) increases above $I_{th}$ until it saturates, and even slightly decreases.

The current tunability is measured around 3.5MHz/mA for 400nm-diameter STVOs and 7.5MHz/mA for 200nm-diameter STVOs. The Oersted component of the frequency writes as $J\omega_{Oe} = J.0.85M_S LR/5$ where $J = I/R^2$ is the current density, so as the STVO diameter is doubled we expect the current tunability to be divided by two.

Furthermore the measured threshold for auto-oscillations in 200nm-diameter STVOs is around 8 to 10mA, which is roughly four times smaller than the 35mA mentionned for the 400nm-diameter STVO in the paragraph above. This is coherent with the fact that the cross-section area is four times smaller, so a smaller current is needed to reach the same current density and provide the threshold STT.

Lastly, the linewidth in 400nm-diameter STVO is typically larger than that of 200nm-diameter STVOs. This result is systematic and we cannot provide a definite justification for this behaviour. One first lead to explore would be the coupling with the thin layer [101, 106].

### 7.2.3 Synchronisation to an RF field

The RF field is the excitation which has the proper symmetry to couple to the gyrotropic mode [**?** ]. In the double vortex STVO, the RF current flowing through the sample cannot as it has a circular geometry. The synchronisation of an STVO to an RF field was already studied thoroughly in [**?** ] for a 200nm-diameter vortex STVO. Here we confirm that the phase-locking of an STVO to an RF field with a 400nm-diameter STVO.

Figure 7.5 complies with the measurements of [114] displaying phase-locking not only at the frequency $f_0$ of the external source, but also at its multiples $2f_0$, $3f_e$... The signal of the external source is directly visible on the spectrum analyser as the antenna cannot be perfectly isolated from the circuit feeding the STVOs. The spectrum under this signal therefore cannot be directly observed. However the same experiment can be performed by doubling the external frequency, so the direct signal of the antenna does not perturbate the measurement. We emphasize that similar phase-locking events of the auto-oscillator

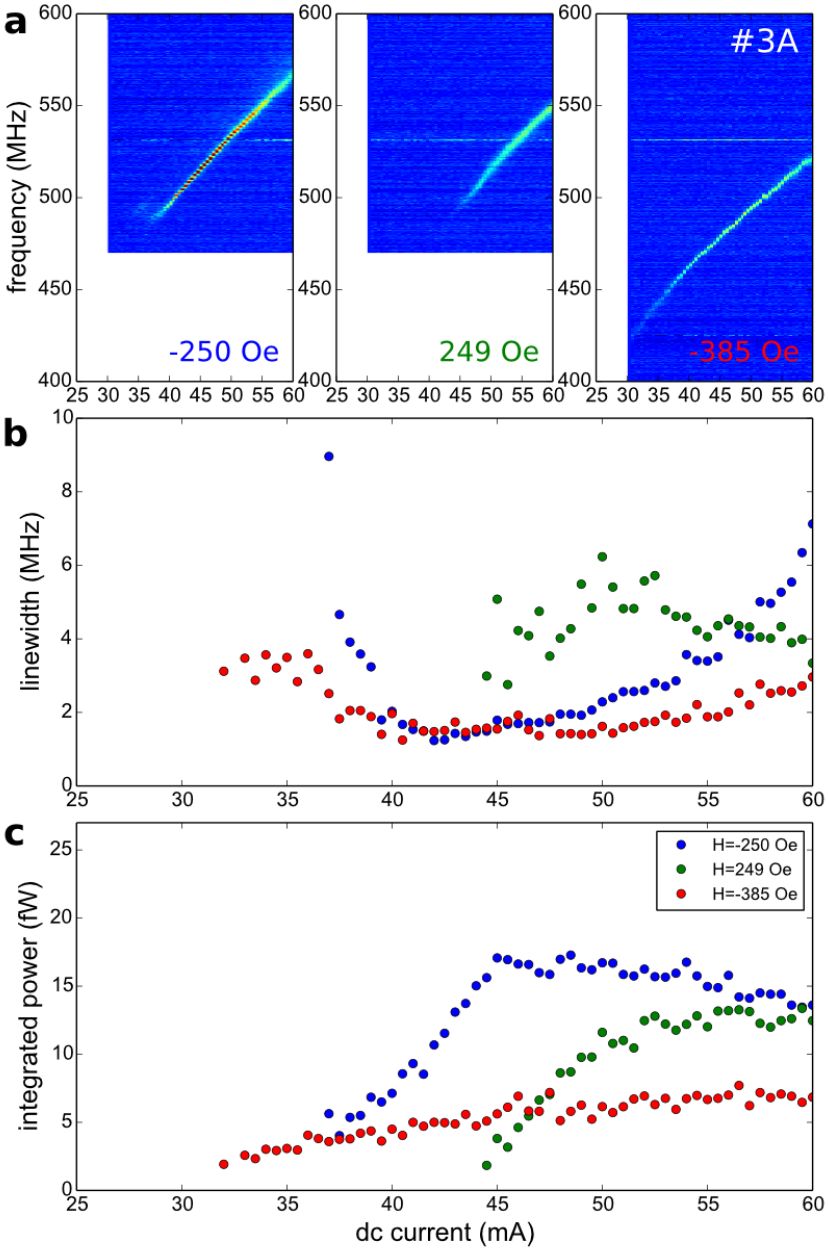


Fig. 7.4 *(a) Variations in the auto-oscillation frequency against dc bias current for several bias fields for a 400nm-diameter nanopillar. Fitting curve for the linewidth (b) and integrated power (c).*

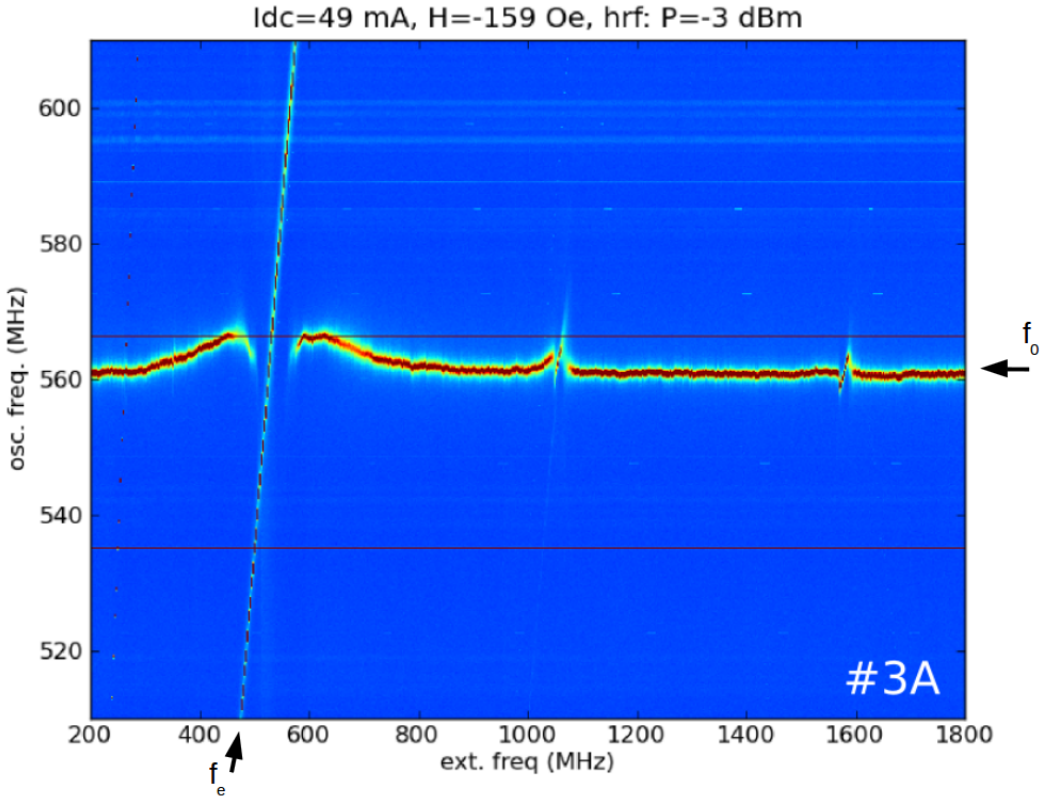


Fig. 7.5 *Synchronisation of one single 400nm-diameter STVO to an external RF magnetic field. The signal due to the external source is clearly visible on the plots. As the frequency $f_e$ of the external microwave field crosses the auto-oscillation signal $f_0$, the STVO phase-locks to the external signal. Phase-locking is also observed at $f_e = 2f_0$, $f_e = 3f_0$...*

happen at fractional values of the external frequency $f_0/2$, $2f_0/3$... similarly to the ones reported in [51].

The locking range at $f$ is approximately 50MHz, that is, 10 percent of the auto-oscillation frequency, while according to the calculations in previous chapter, a power of the RF signal of -3dBm sent to the antenna would create a $0.8/\sqrt{2}$mT field on the STVO. The coupling to the field is efficient, and may even be perfect as was demonstrated for a 200nm-diameter STVO in [115], where the linewidth of the phase-locked signal was finer than the finest resolution of the measuring devices.

## 7.3 Double oscillators dynamic measurements

Because of the small lateral separation in STVO pairs, the two oscillators are dynamically coupled through their dipolar field [147, 119]. We note that owing to their much smaller volumes and limited dynamics, the contribution of the thin layer vortices to the oscillator-oscillator coupling is weak. Moreover, their vortex core polarity is not purposely controlled

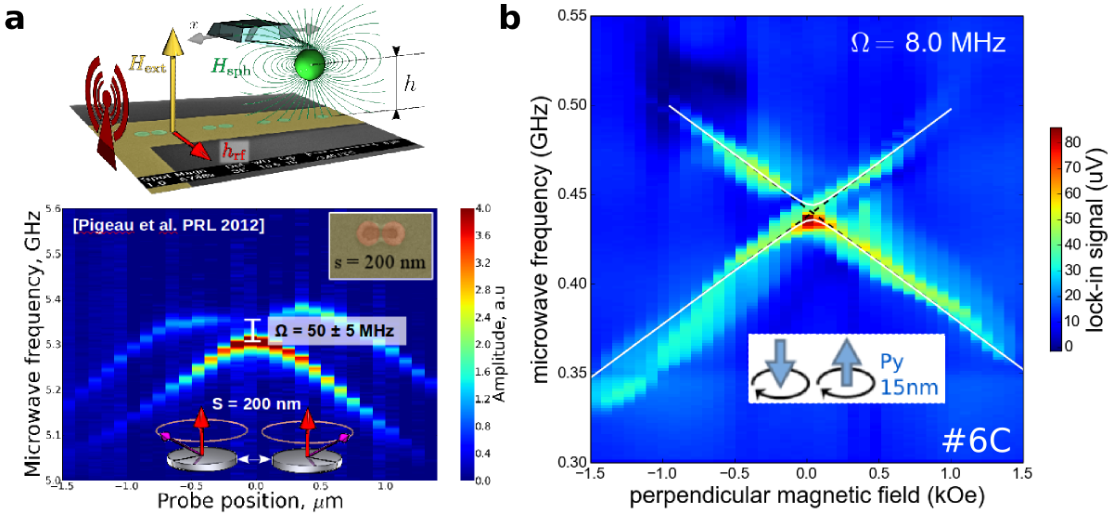


Fig. 7.6 *(a) Anticrossing obtained for a pair of dipolarly coupled nanodiscs observed using MRFM measurements. The right-hand-side plot (b) reproduces the same type of experiment on a pair of STVOs by transport measurements (400nm-diameter nanopillars separated by 200nm, sample 6C). On top is plotted the theoretical curve, using the hybridisation formula (equation (5.22)) and approximating the frequency field-dependence to be linear.*

in this study. In the following, we will thus refer exclusively to the vortices in the thick Py layers of each oscillator, labeled 1 and 2.

We focus on samples #6C and #7H, for which the results are the most abundant, and the most remarkable. The highlights of the last results presented in this chapter are

- The control of the relative polarities in a pair of STVOs
- A clear signature of the mutual coupling and of the synchronisation between two oscilators
- Remarkable effects in the dynamics of two mutually synchronised STVOs

### 7.3.1 Voltage-FMR

In order to put into evidence the dipolar coupling using FMR, we would like to observe an anticrossing, as presented in section 5.4. For this we need to make the two resonant frequencies to cross. This is possible with MRFM measurements on uniformly magnetised nanodiscs, where the stray field of the tip displaces the resonant frequencies of the two discs dysymmetrically as it passes over the pair, allowing the resonance to cross when it is in between the two. With voltage-FMR, this is possible on vortex oscillators if we manage to make the polarities of each STVO antiparallel.

Here we reproduce a similar measurement to the voltage-FMR measurement we undertook on a single STVO in figure 7.2, but this time with two STVOs. Thus we expect to observe two modes, and a signature of the interaction between the two STVOs.

In figure 7.6 we try to reproduce the observation from [157] described in panel (a). Figure 7.6(a) is an MRFM measurement of two neighbouring magnetic disks in the saturated state. As the MRFM probe is swept over the pair, the stray field produced by the magnetic tip is used to tune and detune the relative resonant frequencies between the two nanodisks. Namely because one disk has to be further than the other to the probe, they feel different total bias fields. Two modes can be observed. When the probe is at the centre between the two discs, the modes do not cross but instead anti-cross. This anticrossing at the center of the plot reveals the hybridisation of the modes, and allow to make a distinction between accoustic and optical modes. The measured frequency splitting between the binding and the anti-binding mode is related to the dynamical mutual dipolar coupling between the two dots.

The same experiment cannot be performed in the vortex state, because the stray field of the probe nonuniformally displaces the vortex cores, and the gyrotropic frequency is changed significantly [137].

In our experiment (panel (b)), the two STVOs are prepared with opposite polarities, and their frequencies are linearly varied with the common bias field. Namely if we consider again the plots (a) and (b) in figure 7.2, which describe respectively the modes corresponding to the two vortex polarities, then the plot in figure 7.6(b) is a combination of the two. Yet it is not precisely a superposition, since an anticrossing is observed instead of a crossing at zero field, which should be compared to that observed in panel (a). The white line plotted over the spectra is simply calculated from the hybridisation formula presented earlier in equation 5.22, and fits the data very well for a value of the coupling $\Omega = 8$MHz, in good agreement with the expected value in table 6.1 and in agreement with later measurements (see section 7.4.3).

### 7.3.2 Mutual synchronisation through dipolar coupling

#### Description of the phenomenon

In a typical mutual synchronisation measurement, one observe two auto-oscillation signals getting closer and closer frequencywise as one parameter is continuously swept, until they are close enough so they effectively synchronise. The two signals then merge to one single auto-oscillation signal (see figure 5.1). In [119] it was demonstrated that two STVOs could efficiently synchronise through the magneto-dipolar interaction in a pair of 200nm-diameter vortex STVOs separated by 100nm. Additionally here it is demonstrated the key role of the relative polarities of the two STVOs in the determination locking bandwidth, which can be of a few tenths of MHz. In the antiparallel configuration, the synchronisation bandwidth is typically three times larger than in the parallel configuration (*confere* section 5.4).

This can be explained by averaging the interaction energy in a simple dipole-dipole interaction model. As the gyrotropic mode is excited the vortex core is shifted from its center, and from the subsequent spin imbalance results a net in-plane magnetisation, which is modelled as a magnetic dipole, rotating at the same speed as the vortex core. The vortex polarity determines the sign of the gyrovector in the Thiele equation, and thus the sense of gyration. Then one can see by this simple hand-model that the average interaction energy is three times larger on average for the case of parallel polarities than for the case of antiparallel polarities (see figure 5.10).

From a more general point of view, theoretical explorations of the phenomenon of mutual synchronisation have been ongoing for decades in particular within the framework of the Kuramoto model [89], where phase coupling is simplified as a sinusoidal function of phase difference:

$$\frac{d\varphi_i}{dt} = \omega_i + \sum_j \Omega_{ji} \sin(\varphi_j - \varphi_i + \beta_i) \tag{7.1}$$

where $\varphi_i$ is the phase of $i$th oscillator, $\omega_i$ is its free-running frequency, $\Omega_{ji}$ is the coupling strength between $j$th and $i$th oscillators and $\beta_i$ is an intrinsic phase shift related to the nature of the coupling and to the nonlinearity of the oscillator [21].

**Evidence of synchronisation on our system**

Now let us examine the evidence that two STVOs synchronise in our systems for a pair of 400nm-diameter STVO in the anti-parallel state (sample #6C, figure 7.7) and for a pair of 200nm-diameter in the parallel state (sample #7H, figure 7.8).

For sample #6C we first examine the microwave signals associated with auto-oscillations in each oscillator. Figs. 7.7(a-d) show the color maps of the power spectral density as a function of perpendicular field $H$. In each graph, two branches corresponding to the gyrotropic modes of the thick layer vortex in each oscillator are observed. The four combined vortex polarity states for oscillators 1 and 2 can be obtained after applying well-chosen perpendicular switching fields [108]. The polarity state of oscillator $i$ is defined as $< i \uparrow >$ ($< i \downarrow >$) for vortex core magnetization parallel (antiparallel) to the positive biasing field direction, which corresponds to a positive (negative) frequency-field slope [130, 129].

Next we demonstrate the existence of dipolar coupling by the observation of mutual synchronisation. Figs. 7.7(e,f) compare the zoomed-in power spectra of $< 1 \uparrow 2 \uparrow >$ and $< 1 \downarrow 2 \uparrow >$ states for $0 \leq H \leq 500$ Oe, as labeled by the red boxes in Figs. 7.7(a) and (d), respectively. By switching the polarity of vortex oscillator 1, a clear gap of the auto-oscillation branch for oscillator 2 is found between $H = 175$ and 260 Oe in $< 1 \downarrow 2 \uparrow >$ state, while for $< 1 \uparrow 2 \uparrow >$ state the branch is continuous. This gap, accompanied by a bright lower-frequency branch, is associated to the synchronisation of the two oscillators. From the right edge of the synchronisation bandwidth we deduce that the maximal frequency mismatch for mutual synchronisation is 28 MHz. The frequency mismatch corresponding to the unlocking of the two oscillators at the left edge is smaller. We attribute this to the fact that the amplitude and linewidth of oscillators can vary with the perpendicular field [101], which will change the effective dipolar coupling. The results above show that the dipolar interaction is strong enough to synchronise the two oscillators. Still, a quantitative evaluation of its strength $\Omega_{ji}$ and phase shift $\beta_i$ is lacking at this point of the analysis.We will reproduce these results qualitatively with numerical simulations in section 8.2.1.

For sample #7H we proceed slightly differently. Again let us consider the 4 possible polarity combinations ($< 1 \uparrow 2 \uparrow >$, $< 1 \downarrow 2 \uparrow >$, $< 1 \uparrow 2 \downarrow >$, $< 1 \downarrow 2 \downarrow >$). From figure 7.7 it appears that for well-chosen fields and opposite vortex polarities, the gyrotropic frequencies of the two oscillators are well-separated, whereas for parallel polarities their frequencies are very close. Starting from this constatation, we consider one specific frequency window and consider three out of the four possible polarity combinations, as for sample #7H we just want to demonstrate mutual synchronisation for this very point.

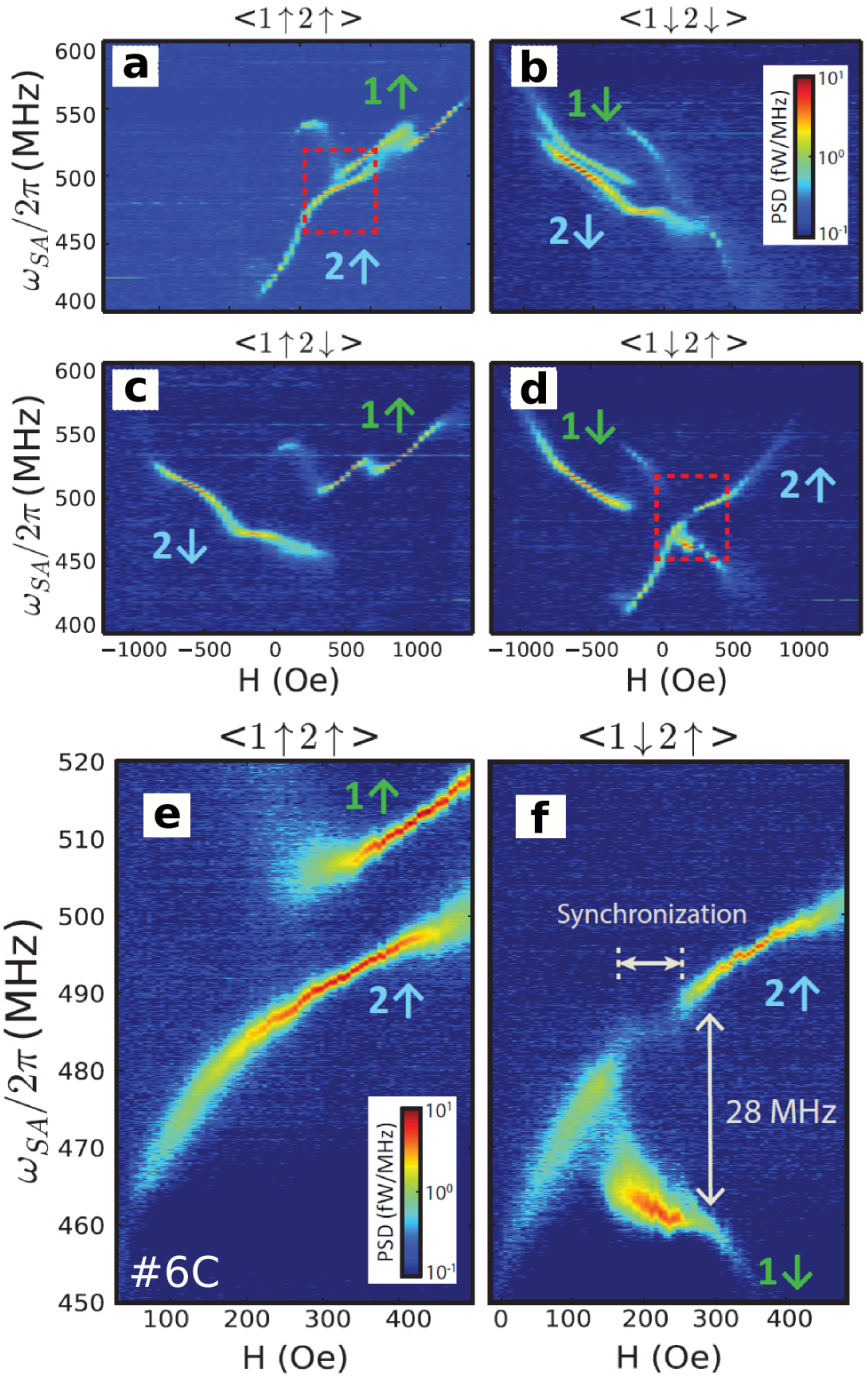


Fig. 7.7 *Sample #6C. Power spectral density maps of auto-oscillation modes in log scale. Four different polarity states of the two thick Py vortex layers are shown: (a)* $< 1 \uparrow 2 \uparrow >$*, (b)* $< 1 \downarrow 2 \downarrow >$*, (c)* $< 1 \uparrow 2 \downarrow >$ *and (d)* $< 1 \downarrow 2 \uparrow >$*. (e,f) Zoomed-in power spectral density data of* $< 1 \uparrow 2 \uparrow >$ *and* $< 1 \downarrow 2 \uparrow >$ *for the red box regions of (b) and (e), respectively. Mutual synchronisation is observed between 175 and 260 Oe in* $< 1 \downarrow 2 \uparrow >$ *state.*

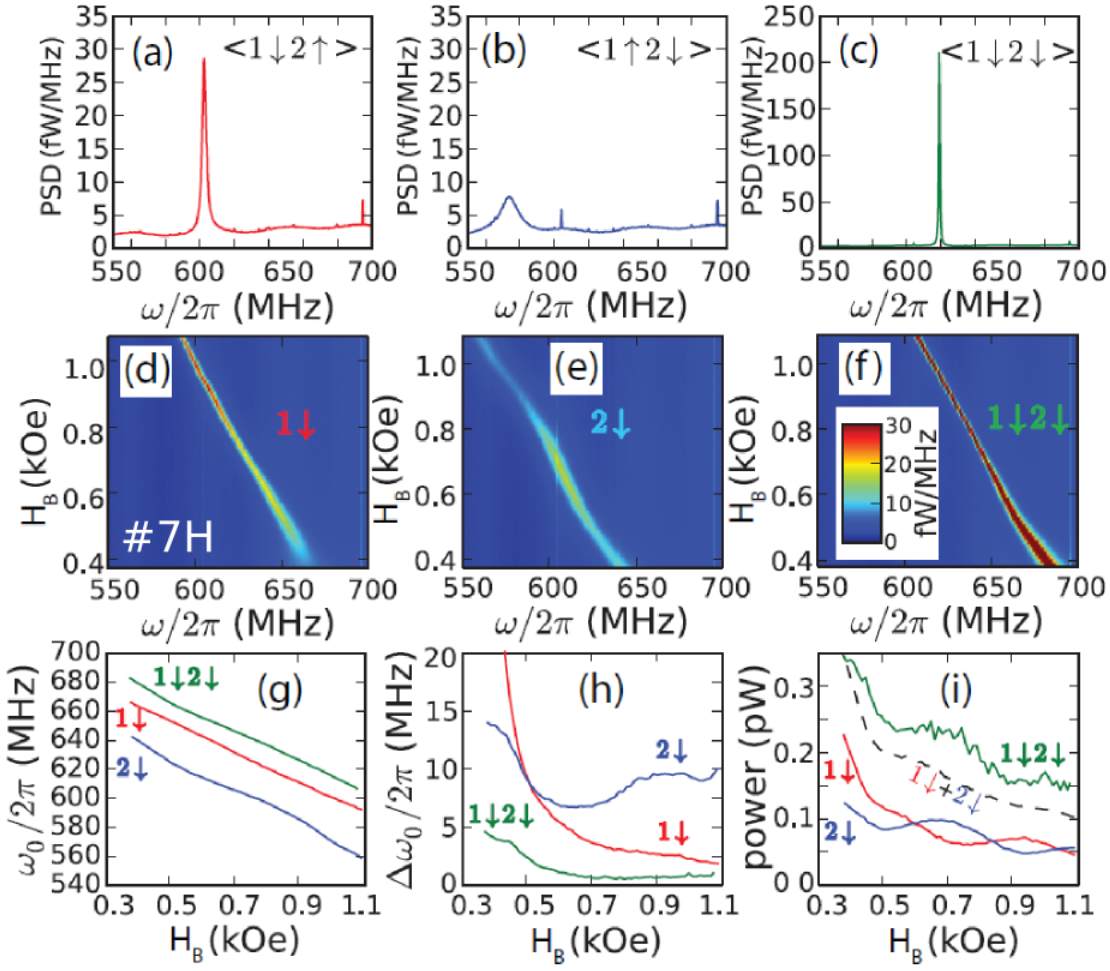


Fig. 7.8 *Sample #7H. (a-c) are extracted from panels (d-f) for a bias field of 1kOe. Not that the y-scale in (c) is different from (a-b). Plots (g-h) summarise the fits of the peaks in (d-f) with the frequency (g), linewidth (h), and integrated power (i) data.*

So in figure 7.8 three states are prepared by adjusting the individual polarities of each oscillator, two with opposite polarities to virtually isolate the oscillators, and one with parallel polarities.

The first row of figure 7.8 presents the spectrum analyser screen for the three prepared states at a specific bias field. The second row plots the field dependence of the spectrum for the three prepared states. The third row provides a combined analysis of the previous row. In this perspective in the configurations corresponding to the first two columns of figure 7.8, oscillators 1 and 2 may be considered to be far from each other, and close to each other in plots (c) and (f). It is clear that plots (c) and (f) are not the summation of plots (a) and (b) or plots (d) and (e) respectively, but instead the auto-oscillation peaks of the two isolated oscillators merge into one single, more intense and narrower peak. This is taken as a clear signature of mutual synchronisation. In addition the analysis in

the third row of the field-dependence of the frequency (g), linewidth (h) and peak power (i) are consistant with this deduction in this that despite the strong field-dependence of these three characteristics, these criteria are always verified. Plot (g) gives a typical 20MHz separation for the peaks of the isolated oscillators, so the coupling has to be stronger to ensure mutual synchronisation. A sharp-eyed reader will not fail to remark that the frequency of the synchronised signal is not located between the two individual frequencies but instead at a higher frequency. This should be accounted for the fact that the two oscillators are not strictly speaking isolated, so the corresponding modes are slightly hybridised, and the observed frequency is not necessarily the natural frequency of the isolated STVO. In addition it should be reminded the unusally high nonlinearites of this type of oscillators, which might play a role as well. The linewidth of the isolated oscillators is of several MHz up to 10MHz, whereas the synchronised oscillator linewidth falls below the MHz level for a large range of fields. Last, although the integrated power of the synchronised signal is not four times as large as that of one single STVO, as would be expected in the case of two synchronised in-phase oscillators, it is always larger than the sum of the two individual signals. One may assume that this is due to the non-naught phase $\beta_i$ of the coupling in the Kuramoto equation [120]. Additionally the two individual oscillators have similar integrated power, so one could expect that they are similar enough and that the synchronised mode is not dominated by one of the STVOs rather than the other.

The mutual synchronisation can be also evidenced by the interaction of the STVOs dynamics with a microwave field. In sample #7H, we set the biasing field to $H_B = 970$ Oe where $\langle 1 \downarrow \rangle$, $\langle 2 \downarrow \rangle$ and $\langle 1 \downarrow 2 \downarrow \rangle$ spectra give clear auto-oscillation outputs in figure 7.9(a-c). A weak microwave power $P_e = -16$ dBm is applied, which corresponds to a linear amplitude of about $h_{rf} = 1$ Oe. By sweeping its frequency, phase-locking to the microwave field is observed for $\langle 1 \downarrow \rangle$ (figure 7.9(d)) and $\langle 2 \downarrow \rangle$ (figure 7.9(e)) peaks with locking bandwidth $\Delta_e/2\pi$ of 10 MHz and 5 MHz, respectively. In contrast, the $\langle 1 \downarrow 2 \downarrow \rangle$ peak is barely influenced by the microwave field and the phase-locking bandwidth is negligible. In fact the resilience to noise and external microwave field share the same physical origin. By increasing the total power due to synchronisation, the two-STVO system is more resistant to environmental noise in the former case and to the microwave field in the latter case. The observations in figures 7.8 and 7.9 prove that dipolar-field-induced synchronisation can improve the stability of STVO output.

Having demonstrated this, we now keep the external source in the system to act as a third "ideal" oscillator. This we will do in two distinct situations:

- The two STVOs have very different auto-oscillation frequencies so they cannot synchronise but remain mutually coupled.

- The two STVOs are mutually synchronised.

## 7.4 Mutually coupled with an external source

In this sections all the results are presented from measurements on sample #6C, in which it was shown in figure 7.7 that we can achieve control of relative vortex polarities in the pair of STVOs.

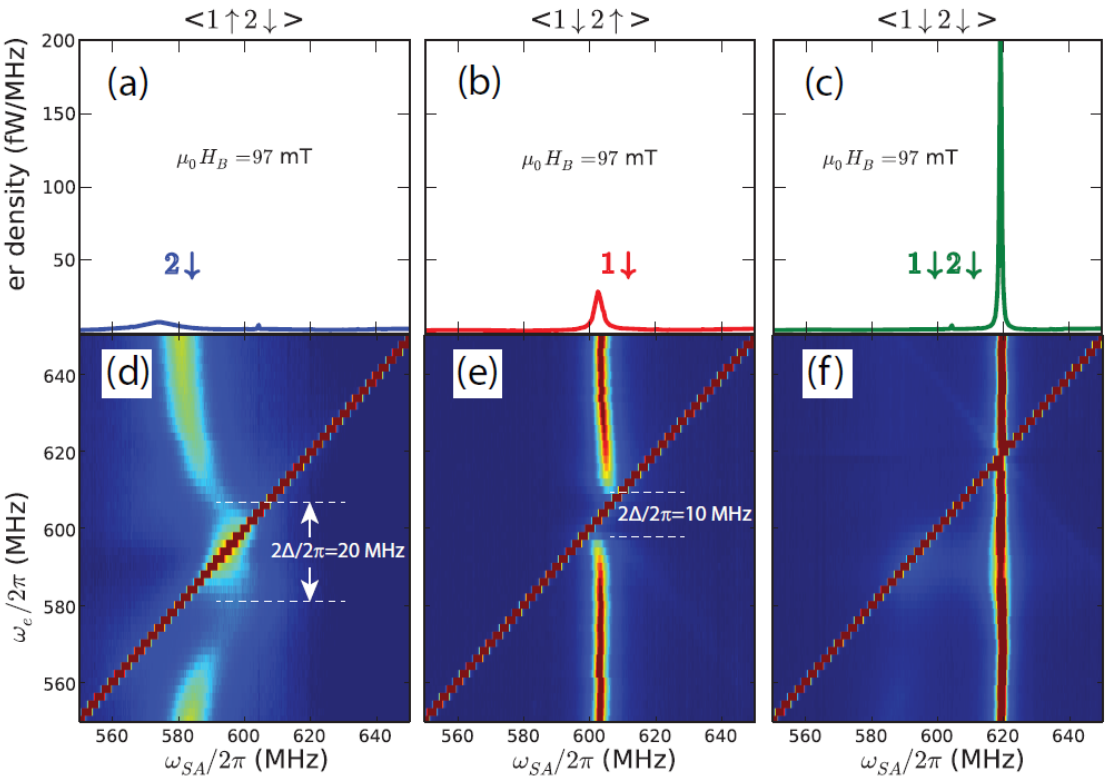


Fig. 7.9 *Sample #7H. Power density spectra at 970 Oe (see figure 7.8(a, b, c)) for the (a) $\langle 1 \uparrow 2 \downarrow\rangle$ state (STVO 2 only visible), (b) $\langle 1 \downarrow 2 \uparrow\rangle$ state (STVO 1 only visible), (c) $\langle 1 \downarrow 2 \downarrow\rangle$ state (STVO 1 and 2 mutually synchronised). (d, e, f) Phase-locking to an external RF magnetic field of the signals in (a,b,c) respectively with a source power of -16 dBm.*

### 7.4.1 Main experimental result

In this work we employ a third reference "oscillator", namely, an external microwave field with tunable frequency and power, as a dynamical probe to measure the dipolar coupling between two spin-torque vortex oscillators. When the microwave field phase-locks one oscillator, an obvious frequency pulling is measured on the second oscillator. By including the coupling to external source in Eq. (7.1), we show analytically that this frequency pulling is due to in-phase actions of source-oscillator and inter-oscillator couplings within the phase-locking bandwidths, beyond which it disappears. The model is tested upon varying the source-oscillator coupling by changing the microwave power, as well as the inter-oscillator coupling by changing the vortex polarity states. It allows to extract dipolar coupling strengths and phase shifts, with the former compatible with analytical calculations [148]. Our results provide a new way to directly reveal and characterize the mutual coupling between oscillators through their attraction to a third reference oscillator, which can be applied to various oscillator systems.

In order to directly reveal and quantify the dipolar coupling, we fix both the biasing current and magnetic field and apply a weak microwave field, which couples to both

oscillators. The current is set to 95 mA, i.e., 1.5 times as the critical current to drive the auto-oscillations of the thick Py layers. The two oscillators are set to an unsynchronised state at $H = 319$ Oe, shown in Fig. 7.10(a). This figure was already introduced as figure 7.7(f). Fig. 7.10(b) shows the evolution of auto-oscillation peaks of the two oscillators as a function of the external microwave field frequency $\omega_e$. When $\omega_e$ crosses the peak of oscillator 1 around 460 MHz, the disappearance of the peak reflects the phase locking to the external RF source [115]. In addition, we also detect a significant frequency pulling on oscillator 2. This is a striking observation, because the frequency mismatch between oscillators, $(\omega_2 - \omega_1)/2\pi = 35$ MHz, is five times larger than the phase-locking bandwidths, around 7 MHz, of the two oscillators to the external source. The remote frequency pulling is a strong indication of coupling between the two oscillators as it is bound to the phase-locking bandwidth. It is important to note that no obvious frequency shift is observed when $\omega_e$ lies between the two auto-oscillation peaks. Reciprocally, a similar effect is also observed on oscillator 1 when oscillator 2 is phase-locked to the microwave field around 495 MHz.

### 7.4.2 Interpretation

The simulations in figure 7.11 were performed on a code based on the Thiele equations, where the exact solution is approached with high term orders of a Taylor development. The terms used in this development are extracted from micromagnetic simulations [158]. The convenient point about simulations is that one can set parameters arbitrarily. This is what is done in figure 7.11 where the dipolar coupling is switched on and off, thereby confirming that dipolar coupling is responsible for the observed features. We have thus acquired the certainty that these features originate from the dipolar coupling.

To understand these phenomena, we develop a simplified analytical formalism based on general oscillator equations [21]. For two dipolarly coupled vortex oscillators experiencing a linearly polarized microwave field, the phase equations can be formulated from the Thiele equation which describes the vortex core dynamics in a magnetic dot (*confere* chapter 5).

We show how to obtain those oscillator phase equations starting from the Thiele equation for STVO 1:

$$(-G_1\mathbf{e}_z) \times \dot{\mathbf{X}}_1 - \kappa_1\mathbf{X}_1 - D_1\dot{\mathbf{X}}_1 + \mathbf{F}_{1,\mathrm{STT}} + \mathbf{F}_{1e} + \mathbf{F}_{1d} = 0 \tag{7.2}$$

where $\mathbf{X_1}$ is the position of the vortex core, $G_1 = 2\pi p_1 M_{1s} h/\gamma$ is the amplitude of gyrovector, $\kappa_1$ denotes the stiffness of the vortex confining force, $D_1$ is the damping term proportional to the Gilbert damping, $\mathbf{F}_{1,\mathrm{STT}} = \sigma_1 J(\mathbf{e}_z \times \mathbf{X}_1)$ is the anti-damping term from spin-transfer torque, $\mathbf{F}_{1e}$ is the force from microwave field coupling and $\mathbf{F}_{1d}$ is the force from dipolar coupling. In the expression of $G_1$ the vortex polarity $p_1$ determines the sign of angular frequency, *i. e.* the direction of vortex core gyration. Here we set both chiralities of the two STVOs to be counter-clockwise from top view ($C_{1,2} = +1$). Because the two STVOs are patterned from the same film stack, we take $|G_1| = |G_2| = G$ for the two STVOs so that $G_{1,2} = p_{1,2}G$. The coordinate system is defined in Fig. 7.10.

In Eq. (7.2) $\mathbf{F}_{1e}$ and $\mathbf{F}_{1d}$ can be calculated from the energy expression as $\mathbf{F}_{1e,d} = -\partial W_{1e,d}/\partial \mathbf{X_1}$. In vortex state, the coupling energy to the microwave field can be expressed as $W_{1e} = -\mathbf{h}_{rf} \cdot (m_1\mathbf{X_1} \times C_1\mathbf{e}_z)$, where $\mathbf{h}_{rf}$ is the RF field, $C_1$ is the chirality

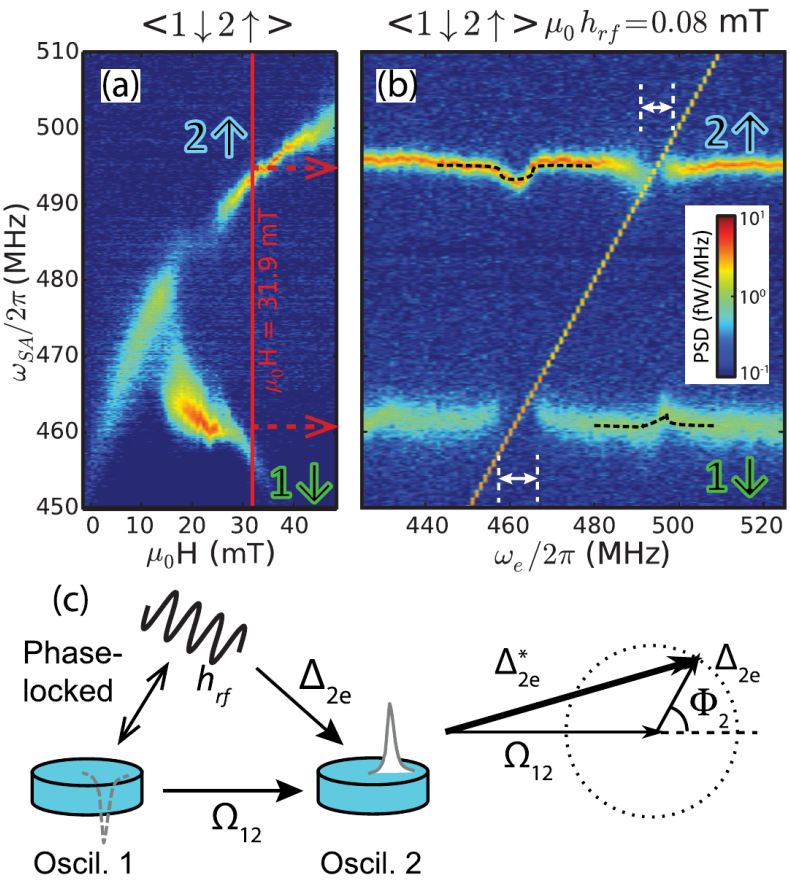


Fig. 7.10 *Sample #6C. (a) Working point in the* $< 1 \downarrow 2 \uparrow >$ *state for the microwave study (red vertical line). (b) Auto-oscillation spectra as a function of microwave field frequency for* $H = 319$ *Oe, indicated in (a). Signal from the source appears as the oblique narrow line. The microwave power is* $-23$ *dBm, corresponding to* $h_{rf} = 0.8$ *Oe. White arrows show the phase-locking bandwidths. Black dashed curves are the fits to Eq. (7.8). (c) Vector diagram of* $\Omega_{12}$ *and* $\Delta_{2e}$ *when oscillator 1 is phase-locked to the microwave field.*

($C_1 = +1$ denotes counter-clockwise) and $m_1 \sim (2/3)M_{1s}V_1/R_1$ is the effective dynamic magnetization divided by the disc radius [127], $V_1$ being the dot volume. This yields:

$$\mathbf{F}_{1e} = C_1 m_1 (\mathbf{e}_z \times \mathbf{h}_{rf}) \tag{7.3}$$

The dipolar coupling energy can be expressed as[148] $W_{1d} = -\mu^{\mathrm{P}}\mathbf{X_1}\cdot\mathbf{X_2} + \mu^{\mathrm{AP}}\mathbf{X_1}\cdot\mathbf{X_2^*}$, with $\mu^{\mathrm{AP}} = 3\mu^{\mathrm{P}}$. Here $\mathbf{X_2^*}$ is the conjugate of $\mathbf{X_2}$ (figure 7.10). Thus the dipolar coupling force can be expressed as:

$$\mathbf{F}_{1d} = \mu^{\mathrm{P}}\mathbf{X_2} - \mu^{\mathrm{AP}}\mathbf{X_2^*} \tag{7.4}$$

In polar coordinates we assume that the amplitudes and phases of $\mathbf{X}_{1,2}$ to be $X_{1,2}$ and $\varphi_{1,2}$. If we consider only the steady-orbit solution, by setting $dX_{1,2}/dt = 0$ and taking

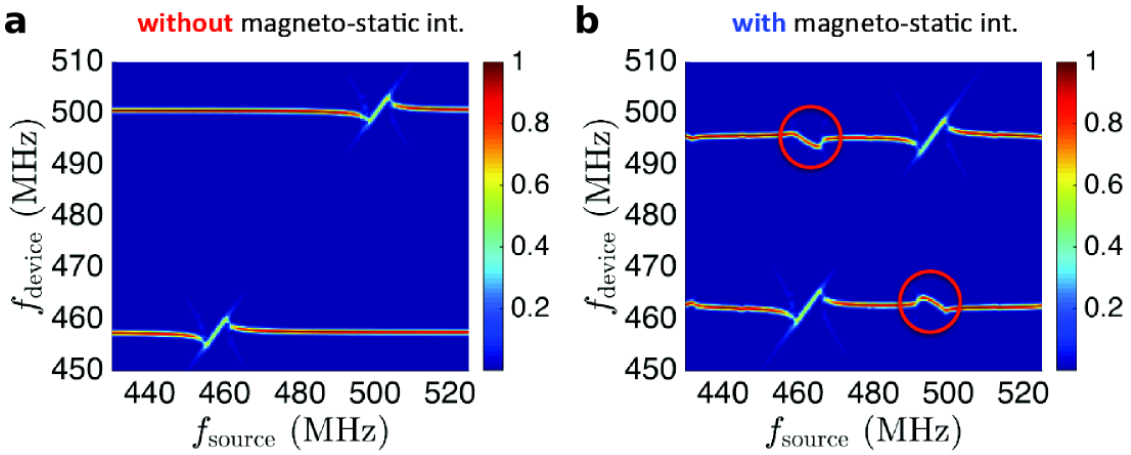


Fig. 7.11 *Simulations by solving the Thiele equation with: (a) zero dipolar coupling, $h_{rf} = 0.2Oe$ and (b) dipolar coupling, $h_{rf} = 0.2Oe$. Courtesy of Flavio Abreu Araujo.*

the dot product of Eq. (7.2) and $\mathbf{e}_r$, we obtain:

$$(p_1 \frac{d\varphi_1}{dt} - \omega_{1g})GX_1 + \mathbf{F}_{1e} \cdot \mathbf{e}_r + \mathbf{F}_{1d} \cdot \mathbf{e}_r = 0 \tag{7.5}$$

with $\omega_{1g} = \kappa_1/G$. We will show below that Eq. (7.5) can be written in a generalized form:

$$-\frac{d\theta_i}{dt} + \delta_i + \Omega_{ji}\cos(\theta_i + \gamma_i^{NL} - \theta_j) - \Delta_{ie}\sin(\theta_i + \gamma_i^{NL} + \gamma_i^{rf}) = 0 \tag{7.6}$$

where $\theta_i = \omega_e t - p_i\varphi_i$ is the phase difference between the microwave field and the position of the vortex core, $p_i = \pm 1$ is the vortex polarity, $\omega_{ig}$ is the free-running frequency of oscillator $i$, $\Omega_{ji} = \Omega(X_j/X_i)$ is the dipolar coupling strength $\Omega$ normalized by the ratio of vortex gyration amplitudes $X_j/X_i$ and $\Delta_{ie}$ is the coupling strength to the external microwave source. The index is defined as $(i, j) = (1,2)$ or $(2,1)$. In Eq. (7.6) two additional phases are present: $\gamma_i^{NL}$ is the intrinsic phase shift introduced by the nonlinearity of the oscillators [21, 159]; $\gamma_i^{rf}$ is the microwave coupling phase, determined by the geometric alignment of the microwave field to each oscillator (see Fig. 7.7(a)). We highlight that Eq. (7.6) describes the general behaviors of self-sustained oscillators: for $\Delta_{ie} = 0$, it is reduced to Kuramoto equations Eq. (7.1) with $\beta_i = \pi/2 - \gamma_i^{NL}$, where the $\pi/2$ phase originates from the conservative nature of dipolar coupling [21]; for $\Omega = 0$, it is reduced to the Adler equation responsible for one oscillator phase-locking to an external source [88].

In the general case, the phase dynamics of oscillator 2 evolves in a complex way due to the uncorrelated forces exerted by the microwave field and oscillator 1. However, when oscillator 1 phase-locks to the microwave field, the situation simplifies: its relative phase with respect to the microwave field, $\theta_1$, becomes a constant. In that case, we can rewrite the phase dynamics of oscillator 2 in Eq. (7.6) as driven solely by the action of the microwave field, but with a modified effective coupling strength $\Delta_{2e}^*$ that takes into

account both the microwave couplings, and the dipolar attraction to oscillator 1:

$$\Delta_{2e}^{*} = \sqrt{\Delta_{2e}^{2} + \Omega_{12}^{2} - 2\Delta_{2e}\Omega_{12}\cos\Phi_{2}} \tag{7.7}$$

From Eq. (7.7), we find $\Delta_{2e}^{*}$ is the vector sum of the effective dipolar coupling strength $\Omega_{12}$ and the microwave coupling strength $\Delta_{2e}$ with a phase difference $\Phi_2 = \theta_1 + \gamma_2^{rf} + \pi/2$ (Fig. 7.10c). The frequency of oscillator 2 is then determined by the frequency of the microwave field, and the strength of this new effective coupling $\Delta_{2e}$ through:

$$\omega_2 = \omega_e \pm \sqrt{(\omega_e - \omega_{2g})^2 - (\Delta_{2e}^{*})^2} \tag{7.8}$$

where "$\pm$" depends on the sign of $\omega_e - \omega_{2g}$. Eq. (7.8) indicates that when oscillator 1 is phase locked to the microwave field, it can help pulling the frequency of oscillator 2 towards the frequency of the source, as observed in Fig. 7.10(b).

### 7.4.3 Quantitative analysis

Full analytical solutions to our model can be obtained in the limit of weak microwave coupling. In Fig. 7.12 we use them to extract the coupling parameters under different conditions. First, the microwave power is varied, which sets the phase-locking bandwidths and associated remote frequency pullings. Second, both antiparallel (Figs. 7.12a,b) and parallel (Figs. 7.12c,d) vortex polarity alignments are examined, for which the strength of dipolar coupling is expected to change by a factor close to three [148, 119]. The data are fitted to Eq. (7.6) with $\Omega$ and $\gamma_i^{NL}$ as the fit parameters. Positive and negative signs of $\Omega$ are expected for parallel and antiparallel polarity alignments, respectively [148], which is taken into account. The fitting curves are shown in Fig. 7.12 and Fig. 7.10(b).

#### Pure phase oscillators, $\gamma_i^{NL} = 0$

If the angular frequency $\omega_{1g}$ does not depend on $X_1$, the nonlinearity of the STVO is zero and the nonlinear phase shift $\gamma_i^{NL} = 0$ in Eq. (7.6).

*Parallel polarity alignment:* We take the polarities as $p_1 = p_2 = +1$. For $\mathbf{F}_{1e}$ we assume an in-plane linearly polarized microwave field with an arbitrary direction $\mathbf{h}_{rf} = h_{rf}(\cos\phi^{rf}\mathbf{e}_x + \sin\phi^{rf}\mathbf{e}_y)\cos(\omega_e t)$, as shown in Fig. 7.10. Using Eq. (7.3), the microwave term $\mathbf{F}_{1e}\cdot\mathbf{e}_r$ in Eq. (7.5) can be expressed as:

$$\begin{aligned}\mathbf{F}_{1e}\cdot\mathbf{e}_r &= f_{1e}(\cos\phi^{rf}\mathbf{e}_y\cdot\mathbf{e}_r - \sin\phi^{rf}\mathbf{e}_x\cdot\mathbf{e}_r)\cos(\omega_e t)\\ &= f_{1e}\sin(\varphi_1 - \phi^{rf})\cos(\omega_e t)\\ &= (f_{1e}/2)[\sin(\omega_e t + \varphi_1 - \phi^{rf}) - \sin(\omega_e t - \varphi_1 + \phi^{rf})]\end{aligned} \tag{7.9}$$

with $f_{1e} = C_1 m_1 h_{rf}$. The two terms in Eq. (7.9) are the clockwise and counter-clockwise polarized components. In positive polarity state, the first term serves as a high frequency component with zero time average so we will neglect it.

For the dipolar coupling term, we have:

$$\begin{aligned}\mathbf{F}_{1d}\cdot\mathbf{e}_r &= \mu^{\mathrm{P}}(\mathbf{X_2}\cdot\mathbf{e}_r) - \mu^{\mathrm{AP}}(\mathbf{X_2^{*}}\cdot\mathbf{e}_r)\\ &= \mu^{\mathrm{P}}X_2\cos(\varphi_2 - \varphi_1) - \mu^{\mathrm{AP}}X_2\cos(\varphi_2 + \varphi_1)\end{aligned} \tag{7.10}$$

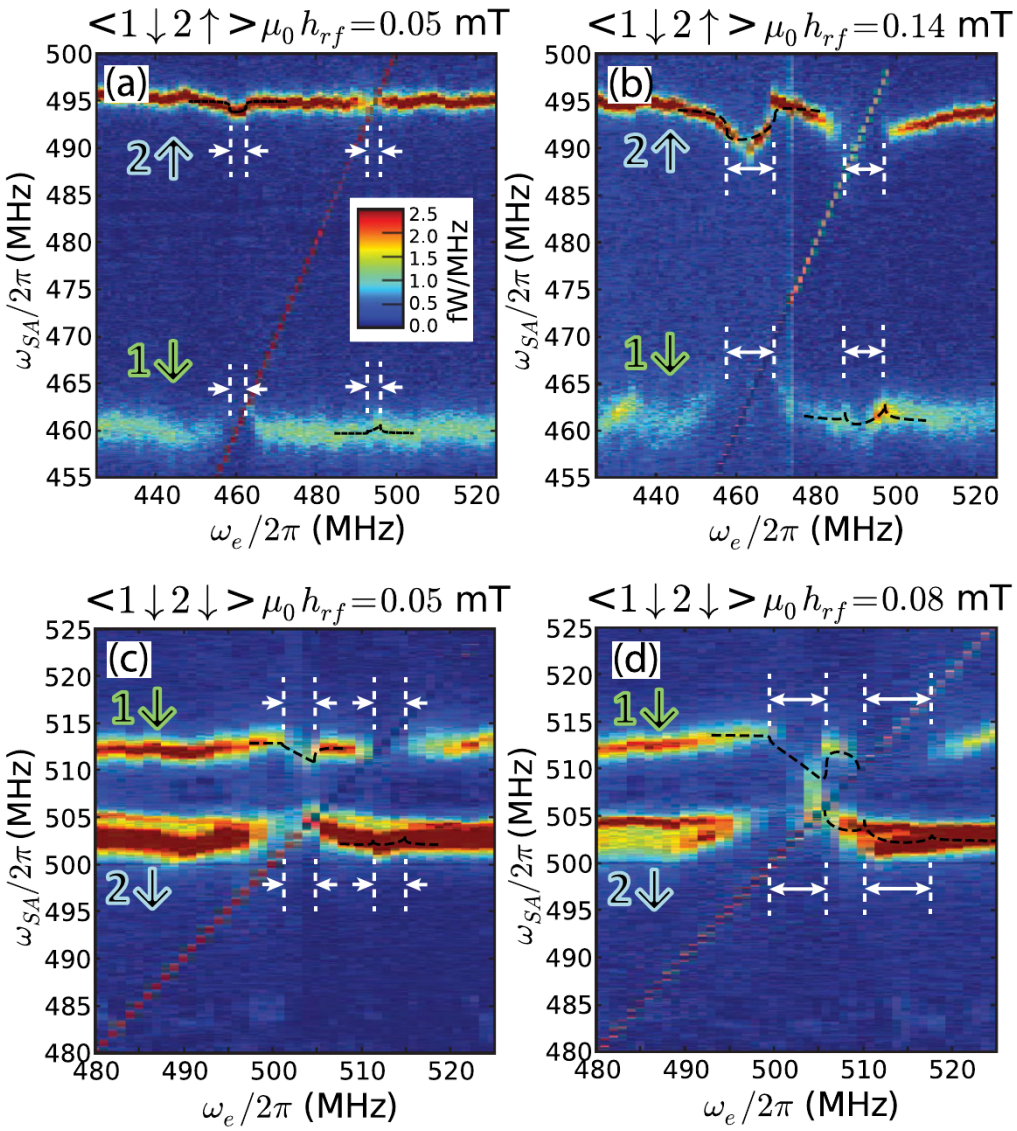


Fig. 7.12 *Sample #6C. Probing dipolar coupling in various conditions. (a),(b) The* $\langle 1\downarrow 2\uparrow\rangle$ *state for* $H = 319$ *Oe, with microwave powers of (a) 28 dBm and (b) 18 dBm. (c),(d) The* $\langle 1\downarrow 2\uparrow\rangle$ *state for* $H = 616$ *Oe with microwave power of (c) 28 dBm and (d) 23 dBm. White arrows show the phase-locking bandwidths. Black dashed curves are the fits to equation (7.8). The fit parameters are listed in Table 7.3.*

In the parallel polarity state the first term mainly contributes to Eq. (7.5) and the second term is a high-frequency term with an average of zero. As a result, Eq. (7.5) becomes:

$$\frac{d\varphi_1}{dt} - \omega_{1g} + \frac{\mu^{\mathrm{P}}}{G}\frac{X_2}{X_1}\cos(\varphi_2 - \varphi_1) - \frac{f_{1e}}{2GX_1}\sin(\omega_e t - \varphi_1 + \phi^{rf}) = 0 \tag{7.11}$$

Comparing with Eq. (7.6), we find $\Omega = \frac{\mu^{\mathrm{P}}}{G}$, $\Delta_{1e} = \frac{f_{1e}}{2GX_1}$ and $\gamma_1^{rf} = \phi^{rf}$. The equation for STVO 2 is the same except that the indices 1 and 2 are exchanged.

*Antiparallel polarity alignment:* We take the polarities as $p_1 = +1$ and $p_2 = -1$. This time $\varphi_1$ will increase but $\varphi_2$ will decrease with time. In Eq. (7.9) we still take the second term for STVO 1. In Eq. (7.10), however, the $\cos(\varphi_2 + \varphi_1)$ term mainly contributes to the phase interaction and the first term is a high frequency term. Eq. (7.5) becomes:

$$\frac{d\varphi_1}{dt} - \omega_{1g} - \frac{\mu^{\mathrm{AP}}}{G}\frac{X_2}{X_1}\cos(\varphi_2 + \varphi_1) - \frac{f_{1e}}{2GX_1}\sin(\omega_e t - \varphi_1 + \phi^{rf}) = 0 \tag{7.12}$$

Comparing with Eq. (7.6), we find $\Omega = -\frac{\mu^{\mathrm{AP}}}{G}$, $\Delta_{1e} = \frac{f_{1e}}{2GX_1}$ and $\gamma_1^{rf} = \phi^{rf}$.

For STVO 2, the active term in Eq. (7.9) is changed to the first term. Along with the negative polarity, the oscillator equation is:

$$-\frac{d\varphi_2}{dt} - \omega_{2g} - \frac{\mu^{\mathrm{AP}}}{G}\frac{X_1}{X_2}\cos(\varphi_2 + \varphi_1) + \frac{f_{2e}}{2GX_2}\sin(\omega_e t + \varphi_2 - \phi^{rf}) = 0 \tag{7.13}$$

Comparing with Eq. (7.6), we find $\Omega = -\frac{\mu^{\mathrm{AP}}}{G}$, $\Delta_{2e} = \frac{f_{2e}}{2GX_2}$ and $\gamma_2^{rf} = \pi - \phi^{rf}$.

For $\gamma_i^{rf}$ the different sign in $\phi^{rf}$ is due to the polarity change, with which the vortex gyrates along different circular directions. The vortex dynamics thus couples to different polarizations of the linearly polarized microwave field, as shown in Eq. (7.9)

The additional phase of $\pi$ in $\gamma_2^{rf}$ is due to the cross product in Eq. (7.3), adding a relative phase of $\pi/2$ to $\gamma_1^{rf}$ and $-\pi/2$ to $\gamma_2^{rf}$.

### Coupled phase-amplitude oscillators, $\gamma_i^{NL} \neq 0$

Here we include finite nonlinearity, which couples the phase equation to the amplitude equation derived from Eq. (7.2). Two effects are considered[21]. First, the auto-oscillation frequency depends on the precession amplitude, as $\omega = \omega_0 + Np$ where $p = |\mathbf{X}|^2$ and $N$ is the nonlinear frequency shift. Second, the relaxation rates also depend on the precession amplitude, with the first-order deviations defined as $G_\pm = \partial\Gamma_\pm/\partial p$ where $\Gamma_+ = D\omega_g/G$ and $\Gamma_- = \sigma J/G$ from Eq. (7.2). This allows to define a dimensionless nonlinearity coefficient $\nu = N/(G_+ - G_-)$. As a result, a factor of $\sqrt{1+\nu^2}$ will be multiplied to all the coupling coefficients, and a phase shift of $\gamma_i^{NL} = \tan^{-1}\nu$ will be added as shown in Eq. (7.6).

We emphasize that in Eq. (7.6), the finite phase shift $\gamma_i^{NL}$ of the dipolar coupling term has the same value as the phase shift $\gamma_i^{NL}$ of the microwave coupling term, because they both come from the nonlinearity of the $i$th STVO.

Table I lists the fitting results along with the microwave field amplitude $h_{rf}$. As expected the mean of phase-locking strengths $(\Delta_{1e} + \Delta_{2e})/2$ is proportional to the microwave field. For the antiparallel polarity alignment, the extracted dipolar coupling $\Omega$

| | antiparallel | | | parallel | |
|---|---|---|---|---|---|
| $h_{rf}$ (Oe) | 0.5 | 0.8 | 1.4 | 0.5 | 0.8 |
| $\frac{\Delta_{1e}+\Delta_{2e}}{2\cdot 2\pi}$ (MHz) | 1.8 | 3.2 | 5.5 | 1.8 | 3.5 |
| $\Omega/2\pi$ (MHz) | -6.7 | -7.9 | -9.3 | 3.6 | 4.2 |
| $\gamma_1^{NL}$ (rad) | -2.7 | -2.8 | -2.0 | 2.6 | 2.1 |
| $\gamma_2^{NL}$ (rad) | 1.1 | 1.1 | 0.7 | -2.1 | -1.4 |

Table 7.3: Fit parameters of Figs. 7.10(b) and 7.12. The values of $h_{rf}$ are calculated from the antenna geometry. The signs of $\Omega$ are fixed to the predictions in Ref. [148].

slightly increases with $h_{rf}$. One reason is that the vortex gyration amplitude $X_i$ might be increased as oscillator $i$ is phase-locked to the microwave field, resulting in an enhancement of $\Omega_{ij}$ on oscillator $j$. Another possibility is the incomplete phase locking at small $h_{rf}$ (observed in Fig. 7.12a for oscillator 2) due to thermal fluctuations, which are likely to reduce the effective coupling [160, 115]. Owing to these two counteracting effects, we take the average of the three experiments, $\Omega_{\mathrm{AP}}/2\pi = -8.0$ MHz, as the extracted value of $\Omega$. For the parallel polarity state, we take the value extracted from Fig. 7.12(c), $\Omega_{\mathrm{P}}/2\pi = 3.6$ MHz, as the strength of the dipolar coupling. In fact, the limit of weak microwave coupling does not hold in Fig. 7.12(d) due to the large microwave power in comparison to the small frequency mismatch between oscillators, which results in a more complex dynamics. It is interesting to note that the two values compare favorably with the ones obtained from macrodipole approximation taking into account solely the thick Py layers [147, 148]. In that case $\Omega_{\mathrm{AP(P)}}/2\pi = -3(+1)\cdot\xi^2\gamma M_s R^2 h/32\pi d^3 = -6.9(2.3)$ MHz (see equation (5.27)), where $\xi = 2/3$ from the two-vortex ansatz [127], $\gamma/2\pi = 29.7$ GHz/T is the gyromagnetic ratio, $M_s = 0.96$ T the saturation magnetization of the Py vortex layers [153], $h$ their thickness, and $d = 2R + L$ the center-to-center distance between oscillators. We also point out that the ratio $\Omega_{\mathrm{AP}}/\Omega_{\mathrm{P}}$ in our experiment agrees with the ratio of critical frequency mismatch, $\Delta f_{\mathrm{AP}}/\Delta f_{\mathrm{P}} = 2.4$ in our prior work [119], and depends on the exact geometry of the oscillator pair [148].

The phase shift $\gamma_i^{NL}$ is linked to the position of the largest remote frequency pulling in Fig. 7.12. In the antiparallel polarity alignment the values of $\gamma_i^{NL}$ are reproducible at various microwave fields but differ from that in the parallel alignment, indicating large variations of parameters in magnetic dynamics upon polarity change. From the model, $\tan\gamma_i^{NL}$ is the reduced nonlinear coefficient $\nu_i$ of oscillator $i$ [21]. However we note that the fitting results with negative values of $\gamma_i^{NL}$ point towards either additional extrinsic phase due, *e.g.*, to parasitic RF couplings between the antenna and sample circuits, or more complex dynamics than assumed in the simple analytical model.

### 7.4.4 Discussion

One interesting finding is that the extracted $\Omega$ in the antiparallel polarity alignment is much smaller than the phase-locking frequency mismatch of 28 MHz found in Fig. 7.7(g). In our experiments the amplitude ratio $X_2/X_1$ is close to one. In the phase-locking solution derived by Slavin and Tiberkevich [161], the maximal frequency mismatch for mutual synchronisation is then $\Omega(\nu_1 + \nu_2)$. Thus we confirm the role of nonlinearities, with $\nu_1 + \nu_2$ around 3.5, in the large phase-locking frequency mismatch. The fact that the synchronised mode is closer to the peak branch of oscillator 1 likely indicates that $\nu_2$ is greater than $\nu_1$, making it easier for oscillator 2 to adapt its frequency to oscillator 1.

In the theoretical derivation presented above, the limit of weak microwave coupling (i.e. microwave field) is required in order to obtain a simple expression for $\theta_1$ when oscillator 1 is phase-locked to the microwave field. In this situation, because the frequency difference between the microwave field and oscillator 2 is much greater than the coupling strength $\Delta_{2e}$, the phase of oscillator 2 will act as if there is no frequency pulling from the microwave field. The time evolution of the term $\omega_{1g} - \Omega_{21}\cos(\theta_1 + \gamma_1^{NL} - \theta_2)$ in Eq. (7.7) can be replaced by its time average, $\omega_{1g}^c$, the frequency of oscillator 1 in the presence of dipolar coupling only which corresponds to the experimentally measured auto-oscillation peak. The phase-locked state of $\theta_1$ can be analytically described by:

$$\sin(\theta_1 + \gamma_1^{NL} + \gamma_1^{rf}) = \frac{\omega_e - \omega_{1g}^c}{\Delta_{1e}} \tag{7.14}$$

Another point of view for the approximation of weak microwave coupling is that the remote frequency pullings in Figs. 7.10 and 7.12 are much smaller than the frequency mismatch of the two oscillators.

However, if the microwave coupling is not weak, the term $\omega_{1g}^c$ will be a function of $\theta_2$, which again depends on $\theta_1$. Thus it will be impossible to obtain an analytical expression of $\theta_1$ unless solved via numerical simulations. Another issue introduced from a strong microwave coupling is that the term $\Omega_{21}\cos(\theta_1 + \gamma_1^{NL} - \theta_2)$ in Eq. (7.7) may not be treated as a "time-averaged" constant, because the term $\omega_{1g}^c$ in Eq. (7.14) strongly varies with time. In this situation we cannot even reach a "phase-locked" state, but instead a complicated beating state between the two oscillators and the microwave field.

The results in this section show that two dipolarly coupled spin-torque vortex oscillators follow ideal oscillator systems described by Eq. (7.2), a pre-assumption for studies based on the Kuramoto model [90]. We confirm that the dipolar coupling strength can be tuned by a factor greater than two with bistable polarity states [148, 119], providing a unique freedom to manipulate the collective dynamics. For instance, a new propagating wave mode has been predicted in oscillator arrays with both attracting and repulsive interactions [162], which can be realized with the two different polarity alignments. In addition we learn about the nonlinearities in spin-torque nano-oscillators. Finite phase shifts $\gamma_i^{NL}$ are measured, as predicted in theory [163, 21] and identified in similar systems [51, 120]. This indicates that practical oscillator networks fall into the Sakaguchi-Kuramoto regime (Eq. 7.1 with nonzero $\beta_i$), in which synchronisation can be destroyed by the phase detunings at medium $\Omega$ [164].

In summary, we have developed a novel approach to study coupled oscillators with an external ac drive. By controlling the relative phases between the ac source and one

phase-locked oscillator, we acquire not only the strength but also the phase information of the inter-oscillator coupling. This probing technique is not restricted to spin-torque oscillators and microwave field, but applicable to all coupled oscillator systems and ac drives.

## 7.5 Resonant destruction of synchronisation

In this section the results are presented for measurements performed on sample #7H.

We have probed the coupling in a pair of mutually coupled but unsynchronised STVOs. As the frequencies get closer, the coupling does not change but a qualitative change occurs as the two oscillators synchronise. Since we have demonstrated we have an efficient probing tool with that external source, it could be used to probe this new situation. Now let us perform again the measurement described hereabove, for a working point of the system where the two oscillators are mutually synchronised. The evidence of mutual synchronisation at this working point is provided in figure 7.8.

### 7.5.1 Main experimental results

Now let us consider the measurement presented in figure 7.13. Actually it might be easier to read the figure from right to left. We are starting from a working point of the system where the two STVOs are mutually synchronised. Then we sweep the frequency $f_e$ of the external source visible as the thin red line crossing the graph along its diagonal, and labelled on the x-axis.

- Indeed when the frequency of the external source matches or gets very close to that of the auto-oscillating signal $f_0$ at 647MHz, then the signal behaves like one single oscillator and phase-locks to the external frequency.

- Now there is an unexpected phenomenon centered around a frequency of 618MHz, which has *a priori* no specific property for the system. This event is characterised by a spreading of the auto-oscillating signal in the frequency domain. This effect seems to be local, as the synchronous signal recovers before it later phase-locks to the external signal. Moreover it should be noted that although the source has little effect on the signal at the auto-oscillation frequency, the frequency-spreading event occurs on a significantly larger bandwidth. As the synchronised auto-oscillations peak vanishes during this event, the event will be described as a *Destruction of Synchronisation* (DoS).

- Then when the external signal frequency $f_e$ is around 580MHz, there is a feature appearing around 618MHz, that is, roughly half-way between the external signal and the auto-oscillation signal.

The smallness of the phase-locking bandwidth characterises the weak power of the RF field. Namely the locking bandwidth to the source does not seem to exceed 10MHz on the entire matrix, making the direct effect of the source on the signal relatively weak compared to the 50MHz locking bandwidth in figure 7.8. Additionally the mutual coupling makes the auto-oscillation signal more resilient to external perturbations. This makes

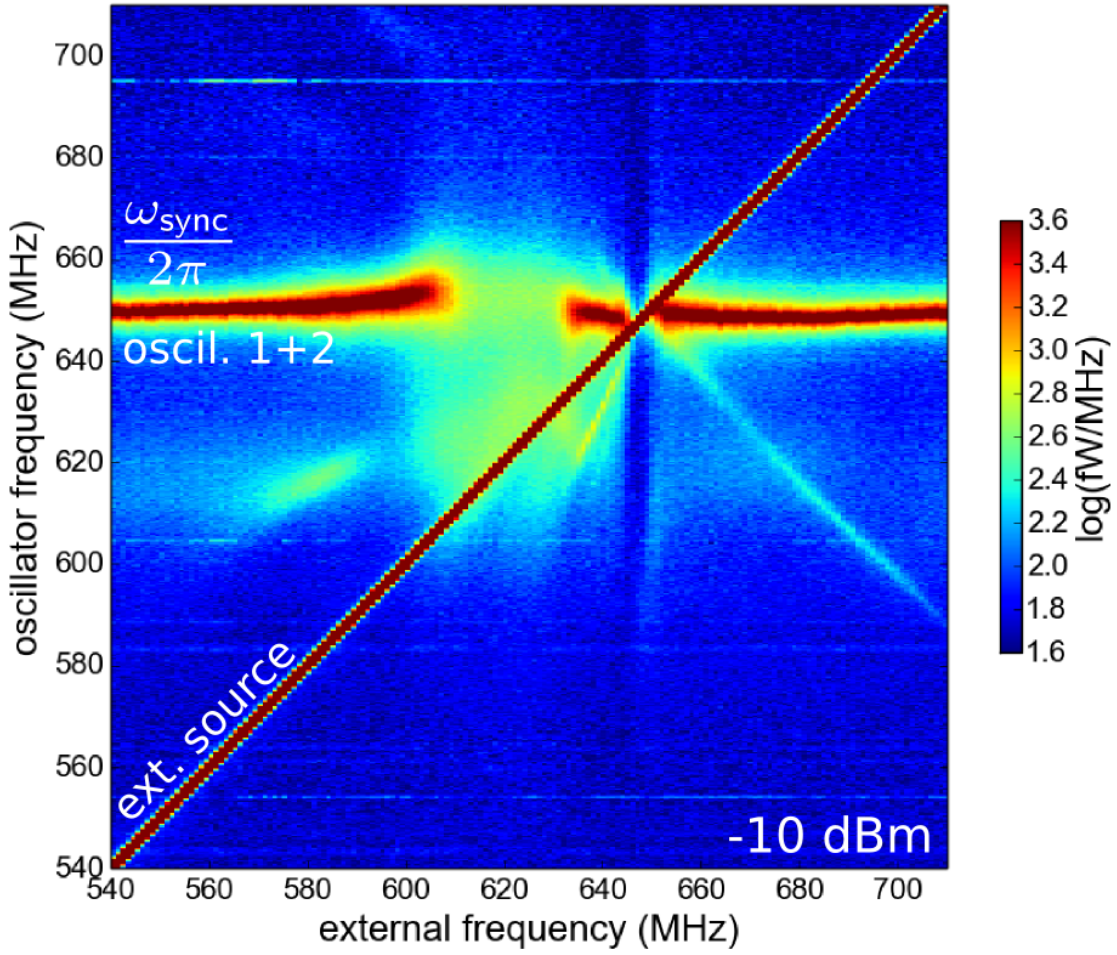


Fig. 7.13 *The two STVOs are mutually synchronised so only one auto-oscillating signal is visible at 647MHz. The external source frequency is swept in the vicinity of the auto-oscillating signal with an input power of -10dBm. The external signal is clearly visible on the diagonal of the plot, as well as its beating frequency resulting from the mix with the auto-oscillating signal. The external signal is rather weak since the locking range is rather small. The surprising feature is the effect of the source localised around 618MHz, which strongly reduces the power of the auto-oscillating signal at 647MHz. Here* $I_{dc} = 40mA$ *and* $H_{dc} = 644Oe$.

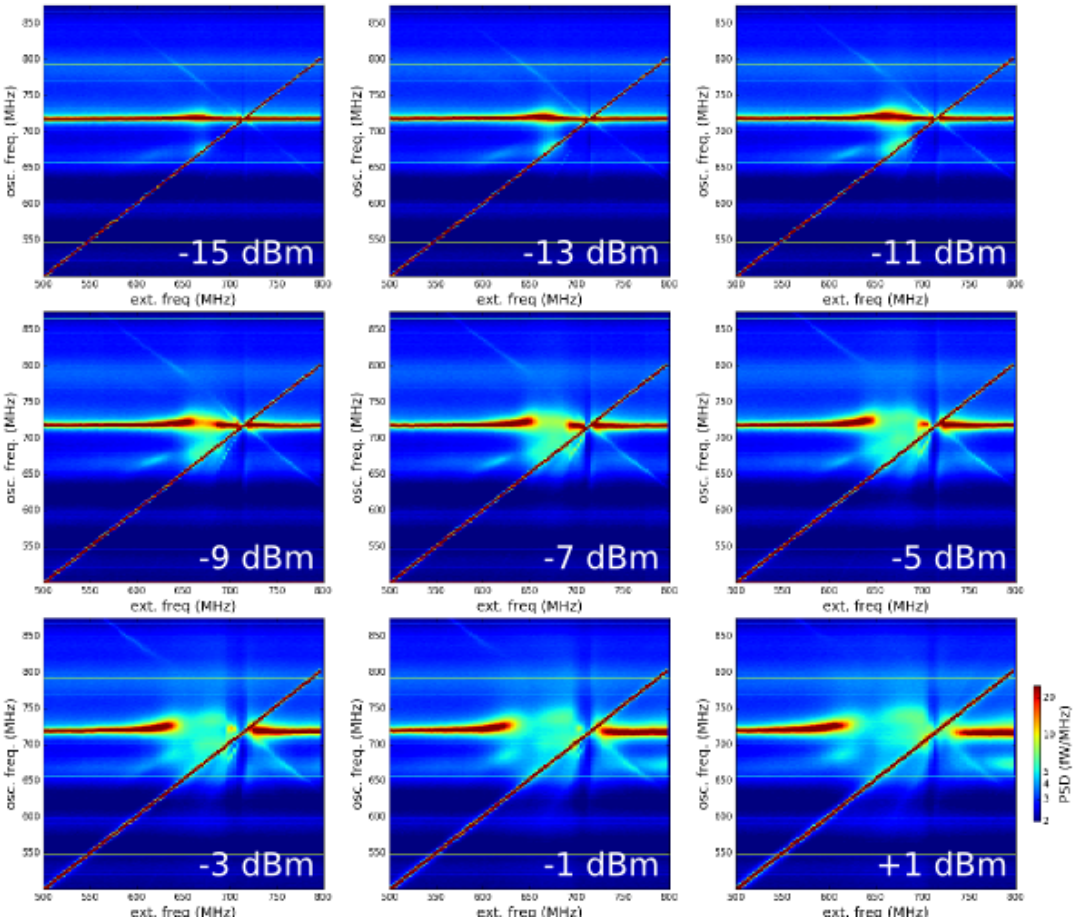


Fig. 7.14 *Dependence on source power. As the same experiment is reproduced at $I_{dc} = 41mA$, $H_{dc} = 714Oe$ with increasing power of the external source, the two main features (destruction on synchronisation at 670MHz an phase-locking at 710MHz) widen until they overlap.*

the strength of this effect is remarkable since even a small amplitude of the external perturbation may have a large impact on the synchronised signal at the aforementionned seldom frequency. In figure 7.14 the experiment is reproduced for several amplitudes of the external source. Even at extremely small power of the external source there seems to be a specific frequency whose excitation affects the coherence of the signal. This is characterised by an increase in the linewidth. It is not clear at this stage whether there is a threshold to the destruction of synchronisation, or the linewidth widens and ultimately spreads over the entire spectrum. Nevertheless it appears that the measured power reaches a minimum value at -7dBm external power. Indeed the phenomenon is local since it occurs on a larger bandwidth as the power of the external source increases, until it overlaps with the phase-locking of the auto-oscillation signal to the external source, but the effect is still centered around 618MHz.

In figure 7.15(a) the complementary experiment to 7.13 is performed. Having noticed

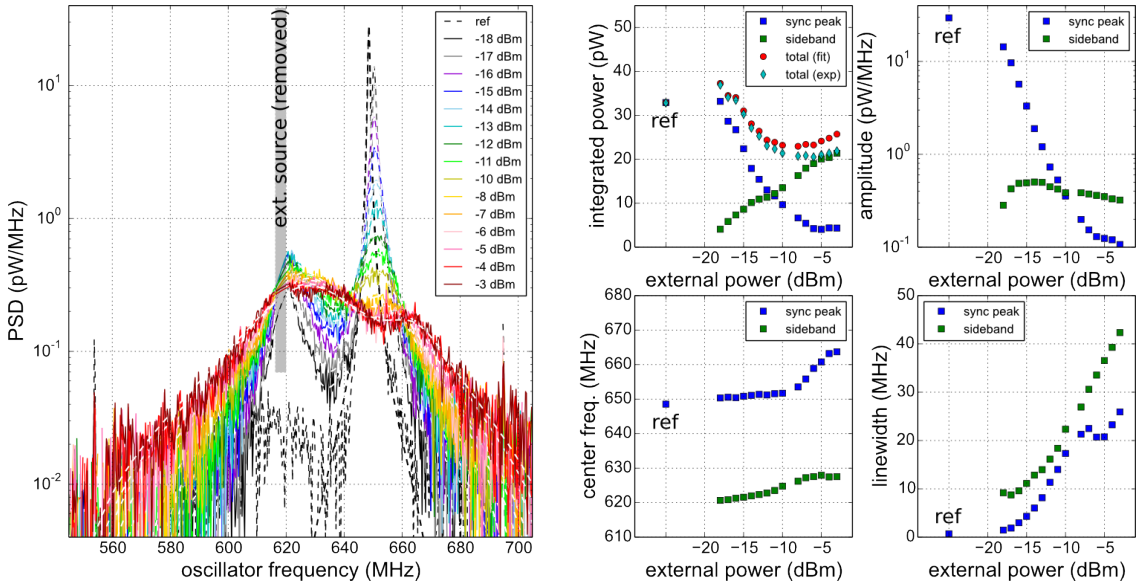


Fig. 7.15 *The data from figure 7.14 is fitted with two lorentzians after the spectrum under the external signal has been removed. The data at -25dBm corresponds to the external signal being absent.*

that the most novel effect in figures 7.13 and 7.14 occurs around 618MHz, we take a closer look of what is happening by sweeping the power of the source at this frequency. The frequency of the external source is fixed at 618MHz, and the RF power is increased. It appears that the main peak is not significantly displaced, as for the pulling effect near a synchronisation region, but as the power of the external source is increased the energy is sucked out of the auto-oscillation peak, and the peak decreases proportionally to the increasing power of the external source. At the same time the linewidth of the peak increases. The spreading of the signal over the spectrum can be clearly seen as the signal power decreases roughly linearly with the increasing source power. The peak due to the direct effects of the external source is removed, so the peaks of the spectrum can be fitted by lorentzians. The fits are presented in figure 7.15(b). The total power is estimated from the fits from the peak power times linewidth product, and is compared to the integrated power spectrum. The difference appearing at low peak amplitudes should be accounted for the fact that only a small part of the real spectrum is measured, while the peak spreads over the entire spectrum. It is not clear though whether we observe a threshold. Nontheless if any, it might be as well hidden by the noise.

### 7.5.2 Interpretation

The explanation of this phenomenon stems from a dynamical aspect. Actually the system can no longer be approximated to the weak coupling limit, since the system of oscillators changes from a synchronised state to a potentially desynchronised state. The phase equations provided in the nonlinear oscillator theory chapter are in fact equilibrium solutions, which can correctly predict the intrinsic phase shift of a nonlinear oscillator [163][165]. Clearly from the data the hypothesis of a constant amplitude may be questionned. More-

over in this complex situation with several competing mechanisms, the transient regime can no longer be neglected.

The first explanation that comes to mind is that we should be at the edge of the bandwidth for mutual synchronisation, so when the frequency of the external source matches the natural frequency of one of the oscillators then this ocillator phase-locks to the source and releases the second one. In this new state the two oscillators auto-oscillate at different frequencies, and the mutual synchronisation state becomes again more attractive, so basically one oscillator is undecided between the source and the other oscillator, what would explain the spreading of the signal frequency. However this mechanism should leave a trace of the natural frequency of the second oscillator, and would only be possible for a fine tuning of the parameters, while the observed effect is robust as it is observed over the full range of perpendicular bias field, when mutual synchronisation occurs. Here we propose an alternative explanation, which will be supported by theoretical arguments in the following chapter.

We propose that the synchronisation is broken by the resonant excitation of a frequency intrinsic to the synchronised system. The existence of such an intrinsic frequency $\Lambda$ has been numerically demonstrated from the Thiele equation and from micromagnetic simulations in [147] in the transient to synchronisation, as is displayed in figure 7.16(b). That is, when the pair of oscillators are kicked out of synchronisation by either noise or an external excitation, they will resynchronise with an oscillatory behaviour at an intrinsic frequency, which should appear as sidebands in the frequency domain. In [147] the authors created the transient by initiating their system with zero amplitude. An analytical expression for the mass of the system can be derived in the limit case of a weak coupling. The intrinsic phase oscillations of a nonlinear oscillator were predicted theoretically in [166]. It was even shown that these oscillations are responsible for resonant behaviour of a phase-locked spin-torque oscillator under modulation of bias current and may even lead to unlocking [167], which is visible as the small resonance peaks on figure 7.16(a), thus the designation of *resonant destruction of synchronisation*. This resonant behaviour would allow to continuously kick the system out-of-synchronisation for a small amplitude of the perturbation at this specific frequency.

This qualitative change in equations is introduced in [147]. The authors maintained the hypothesis of small amplitude variations, but allowed fast amplitude motion, by introducing a second derivative to the system of coupled equations. This can be physically interpreted as inertia, as for a harmonic oscillator characterised by a second-order differential equation. Inertia is indeed present in the dynamics of the amplitude of the nonlinear auto-oscillator. Then they deduce the coupling between oscillators from the transient to synchronisation, which displays an oscillatory behaviour.

There are several way to understand the implications of this inertia. If we take again the analogy of the massless particle sliding along a potential as in figure 7.17, then it should stop whenever it meets a potential hill. Now if we add inertia to the particle, it might accumulate enough energy during its descent to overcome the local potential hills. Now since the system is damped, the particle might as well loose too much energy and remain trapped in a potential well. The particle trapped in a potential well is a typical textbook problem, and it has the possibility to oscillate at an intrinsic frequency which will depend on the particle inertia and the potential shape (a parabolic potential will have a linear frequency, other shapes might be more complex). This is the resonant frequency

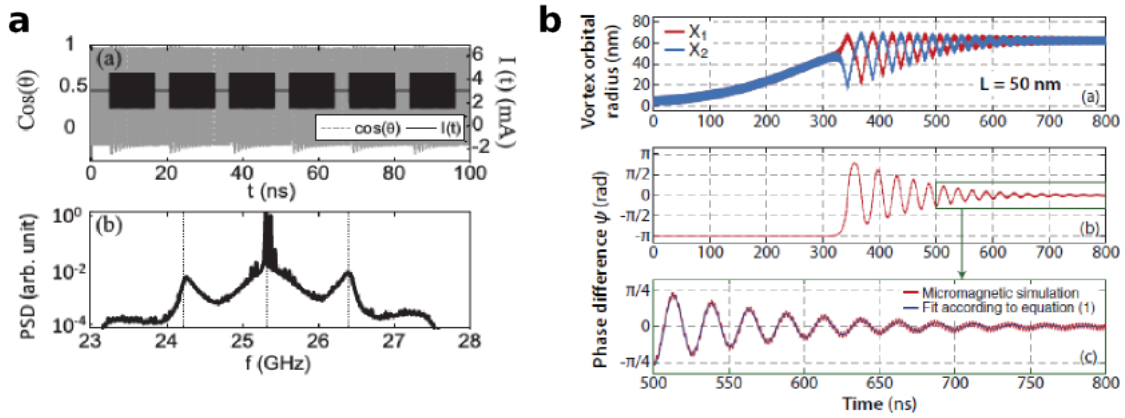


Fig. 7.16 **a** *Micromagnetic simulation of the apparition of sidebands for repeated perturbation pulses of a STNO synchronised to an external source.(a) Time trace of the numerical integration. A transient may be observed simultaneous to the chirps of the external source. (b) Corresponding FFT with two sidebands visible. Extracted from [166].* **b** *Micromagnetic simulations of the phase locking dynamics for a pair of 200nm-diameter STVOs with an out-of-plane polariser and 50nm STVO separation. Evolution as a function of time t of the vortex core orbital positions $X_1$ and $X_2$ (a) and the phase difference $\psi$ (b). In (c), a zoom of the phase difference $\psi$ is presented. Extracted from [147].*

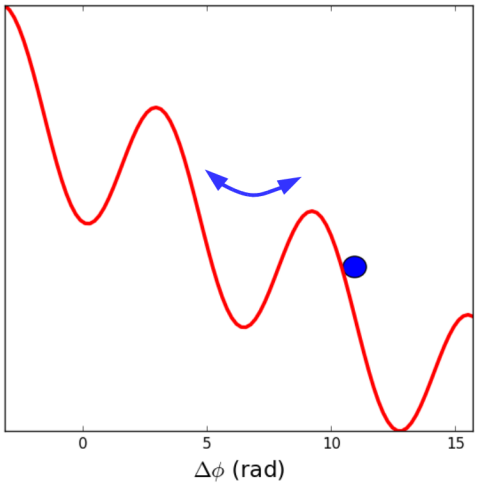


Fig. 7.17 *Particle sliding along a potential with regular potential hills. The nonlinearities add inertia to the model, so the particle can oscillate in a well or overcome the hills with the accumulated energy.*

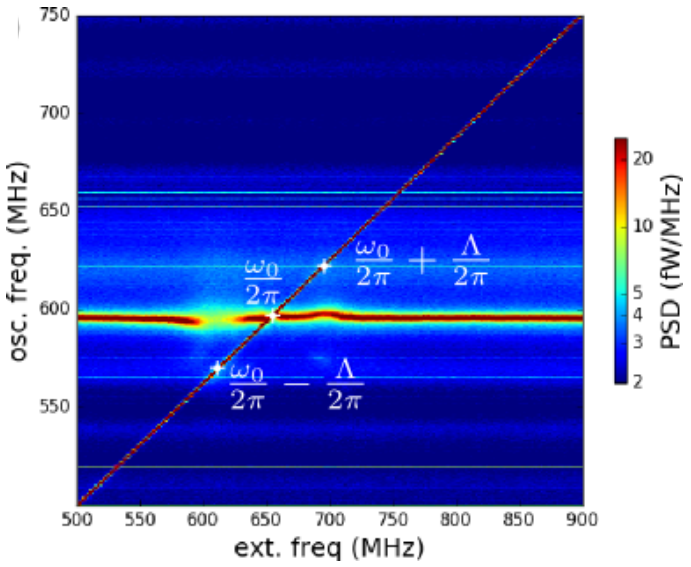


Fig. 7.18 *Measurement at bias field $H_{dc} = 961Oe$ and bias current $I_{dc} = 41mA$ with the frequency of the external source swept at a power of -9dBm. Two sidebands of symmetric frequencies and antisymmetric amplitudes are visible.*

of the system. Now if we provide energy to the particle through an external excitation, it might be able to leave the potential well and reach the next one *et cetera*.

To support this interpretation, we present additional experimental data. The measurement presented in figure 7.18 is similar to that of figure 7.13, but it is produced at a different field $H_{dc} = 961$Oe. Figure 7.18(a) supports this explanation of intrinsic frequency excitation by displaying 2 symmetric local effects on both sides of the crossing between external frequency and auto-oscillation signal, but with different amplitudes. Namely at the lower frequency of the two, the auto-oscillation signal decreases a lot in amplitude and may be considered as a destruction of synchronisation, but is much less affected at the upper frequency. This dyssymmetry is expected from a model developed by Vasyl Tiberkevich in a case where one STNO is phase-locked to an external signal, and perturbed by a weak other one.

These sidebands can also be observed experimentally in figure 7.19. In figure 7.19(a) a pattern appears at 618MHz for $1.4GHz < f_e < 1.5GHz$. Considering the central frequency, $f_e/2 \approx 725$MHz does not seem to be any remarkable to the system. The upper sideband being symmetric to the lower sideband, it should be located around 676MHz. When looking at panel 7.19, which compares the spectra for $f_e = 1{,}420$MHz (red) and $f_e = 1{,}800$MHz (green) and $f_e = 1{,}000$MHz (black), two sidebands are visible on either sides of the main peak. This time the system is excited around $2f_0$, so the leakage from the external source to the measuring circuit does not hide any the spectrum. This is fractional synchronisation: namely the harmonics of the source are more than 40dB smaller than the main signal, so the oscillators actually parametrically synchronise to half the frequency of the excitation. We cannot provide a definite explanantion for the observation of the phenomenon at $f_e = 1{,}420$MHz, but this is probably related to higher order nonlinear efffects.

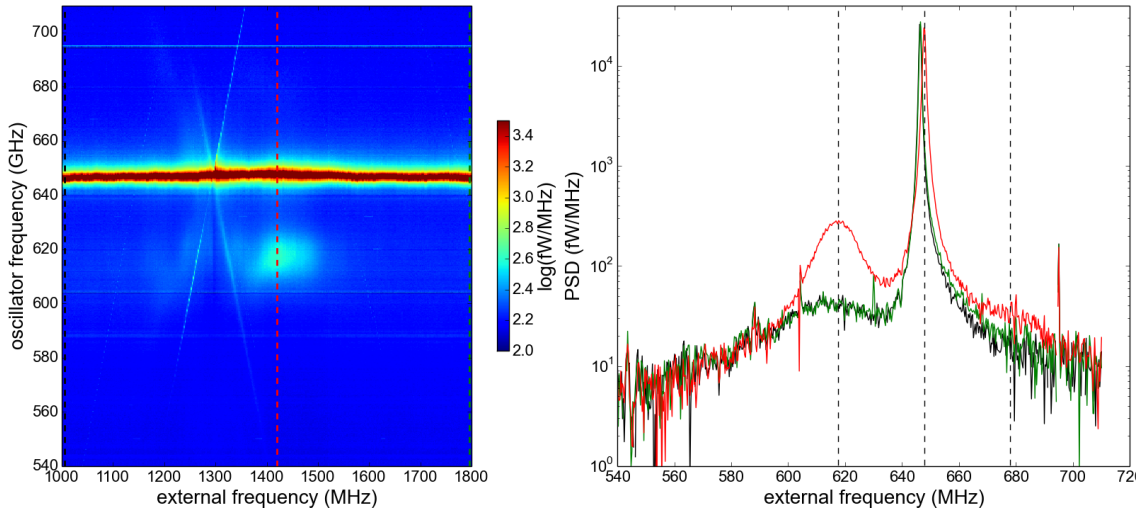


Fig. 7.19 *(a) Similar to figure 7.13 but the frequency of the external source is swept around twice that of the auto-oscillating signal, so the leakage from the antenna does not hide the spectrum of the STVOs. An interesting feature is the resurgence of the lowest sideband, although the cause for that latter excitation remains unclear. (b) Spectrum extracted from figure (a) at* $f_e = 1420MHz$ *(red),* $f_e = 1000MHz$ *(black) and* $f_e = 1800MHz$ *(green). The existence of sidebands centered on 618MHz and 676MHz can be noted on the blue curve by contrast with the green and black ones.*

### 7.5.3 Analytical derivation of the intrinsic frequency

To describe the dynamics of the phase difference in the pair of dipolarly coupled vortex oscillators, we follow the approach presented in the supplementary information of reference [119] and in references [2, 147]. To simplify the discussion below, we consider that the vortex core polarities in each oscillator are parallel to the applied field, i.e., $P_1 = P_2 = 1$, as well as their chiralities, i.e., $C_1 = C_2 = 1$ (similar equations as those written below will be found in other cases, [119, 148]). As shown in section 5.5 there is an equivalence between the Thiele approach and the universal model of nonlinear auto-oscillator. Deviations of the vortex gyration amplitudes $X_i$ in each oscillator can therefore be taken into account by considering deviations of the oscillations powers: $p_i = X_i^2 = p_{i0} + \delta p_i$, which yield deviations of the instantaneous gyration frequencies $\frac{d\phi_i}{dt} = \omega_i + N_i \delta p_i$, with $N_i$ the nonlinear frequency shift. By using the definitions of $\Gamma_p$ and $\nu$ defined in equations (4.4) and (4.7), respectively, and considering that both oscillators are quasi-identical, i.e., they differ only by their frequencies (in particular, $p_{10} = p_{20} = p_0$, $N_1 = N_2 = N$, $\Gamma_{p1} = \Gamma_{p2} = \Gamma_p$, $\nu_1 = \nu_2 = \nu$), the coupled equations of oscillators' power deviations $\delta p_i$ and phases $\phi_i$ can be recast in the following form:

$$\frac{d\delta p_i}{dt} = -2\Gamma_p \delta p_i + 2\Omega p_0 \left(\sin(\phi_j - \phi_i) + \alpha\eta \cos(\phi_j - \phi_i)\right) \tag{7.15a}$$

$$\frac{d\phi_i}{dt} = \omega_i + N\delta p_i + \Omega \left(\alpha\eta \sin(\phi_j - \phi_i) - \cos(\phi_j - \phi_i)\right) \tag{7.15b}$$

where the dipolar coupling is treated as a perturbation (its strength $\Omega$ being defined in equation (5.27)) and $\alpha\eta$ is the damping coefficient of the gyrotropic mode (see equation (5.19)). By subtracting these equations for each oscillator, and calling $\epsilon = \delta p_1 - \delta p_2$ and $\psi = \phi_1 - \phi_2$, respectively the difference in power deviation and the phase difference between both oscillators, one obtains:

$$\frac{d\epsilon}{dt} = -2\Gamma_p\epsilon - 4\Omega p_0 \sin\psi \tag{7.16a}$$

$$\frac{d\psi}{dt} = (\omega_1 - \omega_2) + N\epsilon - 2\alpha\eta\Omega \sin\psi \tag{7.16b}$$

In passing, we remind that by setting $\frac{d\epsilon}{dt} = 0$ and injecting the solution of the first equation of this system in the second one, one obtains the typical Adler equation,

$$\frac{d\psi}{dt} = (\omega_1 - \omega_2) - 2\Omega\,(\nu + \alpha\eta)\sin\psi\,, \tag{7.17}$$

which sets the conditions for mutual synchronisation (see reference [119] and the end of section 5.4.3).

But here, we are interested in the nonlinear dynamics of the phase difference close to equilibrium, without the constraint of vanishing power deviation. Therefore, we linearize the previous system of equations for small phase differences ($\sin\psi \simeq \psi$) and substitute the second equation into the first one to get the second order differential equation on the phase difference, which we are looking for:

$$\frac{d^2\psi}{dt^2} + 2\,(\Gamma_p + \alpha\eta\Omega)\,\frac{d\psi}{dt} + 4\Gamma_p\Omega\,(\nu + \alpha\eta)\,\psi = 2\Gamma_p(\omega_1 - \omega_2) \tag{7.18}$$

For typical STNOs, the damping parameter ($\alpha\eta \simeq 0.01$) is much smaller than the dimensionless nonlinear parameter ($\nu > 1$), therefore, the characterstic frequency of oscillations of the phase difference reads:

$$\Lambda \simeq 2\sqrt{\Gamma_p\Omega\nu}\,, \tag{7.19}$$

and the damping rate of these phase oscillations is mainly governed by $\Gamma_p$.

The above derivation holds in the very specific case of quasi-identical oscillators, and under simplified assumptions, in particular the dipolar coupling is treated as a perturbation, and the power deviations are limited to small values. Still, it enables to exhibit the important physical parameters governing the dynamics of phase oscillations, namely the nonlinear parameters $\Gamma_p$ and $\nu$, and of course the strengh of the mutual coupling $\Omega$. To take into account the full dynamics without the constraints noted above, one should rely on numerical simulations of the coupled amplitude and phase equations, which will be performed in chapter 8. In particular, the simulations will also take explicitely into account the external source.

We are very grateful to Vasyl Tiberkevich (Oakland University), who first pointed out the mechanism of resonant destruction of synchronisation when looking at our data, and provided a complete analytical treatment of one STNO phase-locked to one external source, and disturbed by a second, weaker external source, with some semi-quantitative estimate of the threshold yielding to destruction of synchronisation.

In this section we have experimentally demonstrated the existence of the sidebands at the intrinsic frequency of a system of mutually synchronised nonlinear spin torque

oscillators. We have additionally demonstrated that this intrinsic frequency could be resonantly excited, leading to the destruction of mutual synchronisation. These results are in principle valid for any pair of nonlinear oscillators. In the next chapter we will support this view using numerical simulations based on a minimalistic theoretical model.

## Summary

**We have been able to demonstrate the existence of a vortex in both magnetic layers of our STVOs and the possibility to control their chirality by measuring the magnetoresistance while sweeping the bias current. We focus on four specific devices most representative of the results obtained. In the case of single STVOs, we use voltage-FMR and transport measurements to demonstrate that under our bias conditions, the dynamics of STVOs is dominated by the thick layers, so we describe the STVOs using the vortex in the thick layer, and validate the bias field and current dependence introduced previously. Auto-oscillation signals are visible only when the polarities of the vortices in the two layers are opposite, and the observations corroborate the results from [101] and [108] as for the tunability, linewidth and power dependence versus bias parameters. As for synchronisation to the microwave field, we confirm a synchonisation bandwidth of 10 percent of the auto-oscillation frequency for an amplitude of the microwave field of 0.4mT [115].**

**In samples containing pairs of oscillators, we first observe the hybridisation of two modes dominated by the two thick layers using FMR, when the polarities are antiparallel. We unambiguously demonstrate mutual synchronisation in different device geometries and relative polarity states of adjacent oscillators, which confirms the first results reported in [119]. In particular, we show that the microwave characteristics are improving thanks to synchronisation, and that the synchronised state is more robust against external perturbations.**

**Then we introduce two original results. We demonstrate that in a situation where the two STVOs are not synchronised the microwave field can be used to reveal the mutual coupling, and provide quantitative data on the coupling. We provide an analytical model and our analysis is supported by simulations. In a situation where the two oscillators are mutually synchronised with parallel polarities, we experimentally demonstrate the existence of an intrinsic frequency, which can be resonantly excited by the microwave field, and eventually lead to the destruction of synchronisation.**

# Chapter 8

# Numerical modeling

In this chapter we try to reproduce the experimental data by integrating the coupled differential equations derived from the Thiele equations, and retrieve the main qualitative features. First we introduce the basic principle of the numerical integration, along with the equations used in the numerical model. We then discuss the validity of approximations and the values of the parameters used in the numerical integrations. In a second part we present the results of the integration where we reproduce the experimental results presented in sections 7.3 to 7.5. We conclude with a stability analysis using a software serving this purpose.

## 8.1 Derivations

### 8.1.1 Principle

The analysis of Ordinary Differential Equations (ODE) is something very general in solving physics problems. In the case of a system of linear differential equations, the problem can even be solved by determining the eigenvalues of the system as to determine the possible equilibrium states of the system and their stability.

In the present case we are dealing with systems of nonlinear equations: two phase equations or four equations if we add the amplitude equations. Finding an analytical solution to this problem, assuming such a solution exists, is not an easy task. An alternative is to solve these equations numerically by integrating them over time. The basic principle of the algorithm is relatively simple: starting from a system of equations $dX(t)/dt = f(X,t)$, where $X$ is a time variable which describes the state of the system, the state at $t_0 + dt$ is deduced from the state at $t_0$ by computing $X(t_0 + dt) = X(t_0) + dX/dt(t_0)dt = X(t_0) + f(X(t_0),t_0)dt$. This method has the advantage that it can be implemented quite easily on a standard computing machine, but has this weakness that some solutions may depend on the initial conditions.

Our strategy was to integrate the equations over time to produce timelines of the variables, and then rebuilt the corresponding signal and generate its Fourier Transform. The results could then be directly compared to the experimental data. During a first quick run the timelines are produced sequentially as one parameter is swept, on a time long enough so that the equilibrium state is reached, but short enough so this calculation step does not take too much time. The variables values are stored at the end of each run,

and reinjected as the initial state for the following run after the swept parameter was changed. Then timelines are integrated in parallel for the set of parameter values and starting from the corresponding equilibria, on longer times so that their FFT contains enough information for our purposes. This way the transient regime does not appear on the spectrum. The integration times in the first step can be kept very brief as the main parameter does usually not undergo large changes.

The following was produced using a code developped under Python, using the general-purpose Scipy, Numpy, Pylab... libraries since the Scipy library already includes a function for integrating ODEs. Adding noise is slightly more complex as it involves a stochastic process which is usually not provided by standard ODE functions. The equation is now $dX(t) = f(X,t)dt + g(X,t)dW$ where $W$ is a Wiener process, so $dW$ is a white Gaussian process. We use the sdeint Python library for integrating Stochastic Differential Equations (SDE), which conveniently provides a interface similar to odeint, and can be parallelised using the nsim Python library [168].

The objective is not necessarily to fit the data, given the great variability from one sample to the other on the same wafer and the complexity of the system, but rather to reproduce them qualitatively to validate our understanding of the data. However it is striking that even with such a simple model we can reproduce the main results with such fidelity.

### 8.1.2 Analytics

The equations we integrate in this chapter are the following. The variables ($X_1$,$X_2$,$\theta_1$,$\theta_2$) are respectively the relative amplitudes of oscillators 1 and 2 ($X = 1$ at the edge of the disk) and the instantaneous phases of oscillators 1 and 2 in the rotating frame of the external source. This formalism allows us to get rid of terms with direct expression of the time variable.

$$\begin{cases} \dot{\theta_1} & = \omega_e - \omega_1(X_1^2) & +\Omega\frac{X_2}{X_1}(\cos(\Delta\theta) + d(X_1^2)\sin(\Delta\theta)) & -\frac{\Delta_e}{X_1}(\sin\theta_1 - d(X_1^2)\cos\theta_1) \\ \dot{\theta_2} & = \omega_e - \omega_2(X_2^2) & +\Omega\frac{X_1}{X_2}(\cos(\Delta\theta) - d(X_2^2)\sin(\Delta\theta)) & -\frac{\Delta_e}{X_2}(\sin\theta_2 - d(X_2^2)\cos\theta_2) \\ \dot{X_1} & = \kappa_1(X_1^2)X_1 & +\Omega X_2(\sin(\Delta\theta) - d(X_1^2)\cos(\Delta\theta)) & +\Delta_e(\cos\theta_1 + d(X_1^2)\sin\theta_1) \\ \dot{X_2} & = \kappa_2(X_2^2)X_2 & -\Omega X_1(\sin(\Delta\theta) - d(X_2^2)\cos(\Delta\theta)) & +\Delta_e(\cos\theta_2 + d(X_2^2)\sin\theta_2) \end{cases} \tag{8.1}$$

where

$$\begin{aligned} \omega_i(X_i^2) &= \omega_{i,g} \times (1 + \zeta X_i^2) \\ d(X_i^2) &= \alpha\eta \times (1 + \xi X_i^2) \\ \kappa_i(X_i^2) &= \alpha\eta\omega_{i,g}\frac{I}{I_c}(1 - \beta X_i^2) - \omega_i(X_i^2)d(X_i^2) \\ \Delta\theta &= \theta_1 - \theta_2 \end{aligned} \tag{8.2}$$

$\omega_e$ is the pulsation of the external source, $\omega_1$ and $\omega_2$ are the natural pulsations of oscillators 1 and 2, with $\omega_{1,g}$ and $\omega_{2,g}$ their respective ground frequencies, that is, resonant frequency at zero power, $d$ is the damping with $\alpha\eta$ set to 0.02 in the following [101], $I/I_c$ is the supercriticality with $I_c$ the critical current for auto-oscillations, $\Omega$ the intensity of the mutual coupling, $\Delta_e$ the intensity of the external signal, and $\zeta$, $\xi$, $\beta$ the relative nonlinear

factors of respectively the nonlinear frequencies (or equally of the pulsations), the damping and the negative damping. $\kappa_i(X_i^2)$ describes the "balance" between the STT and the damping.

With 9 parameters the problem is indeed complex and it is not easy to perform fine tuning of the parameters to reproduce the experimental data, assuming it is possible with this very simple model. Instead we keep the parameters within a reasonable range according to the litterature [2, 155, 5], given that the qualitative results presented in this work should be very general.

The hereabove listed parameters can be arranged to a smaller set of parameters, which might be easier to interprete by directly referring to the parameters used in the chapters 4 and 5

$$N = \zeta\omega_0 \tag{8.3}$$

$$p_0 = \frac{\frac{I}{I_c} - 1}{\beta\frac{I}{I_c} + \xi + \zeta} \tag{8.4}$$

$$\Gamma_0 = \alpha\eta\omega_0 \left(\beta\frac{I}{I_c} + \xi + \zeta\right) p_0 \tag{8.5}$$

$$= \alpha\eta\omega_0 \left(\frac{I}{I_c} - 1\right) \tag{8.6}$$

$$\nu = \frac{Np_0}{\Gamma_0} = \frac{1}{\alpha\eta}\frac{\zeta}{\beta\frac{I}{I_c} + \xi + \zeta} \tag{8.7}$$

$$\tag{8.8}$$

where $p_0$ is the auto-oscillations power, $N$ is the nonlinear frequency shift, $\Gamma_0$ the damping and $\nu$ the adimensionalised nonlinearity.

Obviously it is not a simple task to tune one of these last four parameters individually by adjusting the previous nine. In the following we keep the parameters below as standard values

$$\begin{aligned}
\frac{\Omega}{2\pi} &= 10\text{MHz} \\
\alpha\eta &= 0.02 \\
\zeta &= 10\% \\
\xi &= 70\% \\
\beta &= 100\% \\
\frac{I}{I_c} &= 2
\end{aligned}$$

$\omega_1$, $\omega_2$, $\Delta_e = 2\pi F_e$, $\omega_e$ are the parameters which are varied from one plot to the other. A value may be printed by default for the swept parameter, but is then insignificant. The noise figure is defined by the standard deviation.

In principle all parameters could have different values for each STNO. However the objective was to use a minimal model, so as to identify the physical mechanisms underlying

the observed effects, rather than trying to reproduce the data quantitatively. In addition given the number of parameters, this would have uselessly complexified the system. We chose not to introduce too much asymmetry in the system, so the oscillators differ by their frequency only. Nevertheless as the two STNOs are very similar in the real-world experiment, this symmetry assumption is not an abberration.

### 8.1.3 Validity of approximations

The simple phase model failed to explain the data in part 7.5. Thus in order to explain these data, we need to use a more complete model. In particular as STNOs are highly nonlinear, it might be necessary to include equations on the dynamics of the amplitudes.

Actually in the framework of the phase model used in section 7.4 we have made several approximations which may be questionned:

- small amplitude variations what forbids the hysteresis in the synchronisation
- slow amplitude variations which sets the oscillator's inertia to zero

The validity of the first hypothesis can be evaluated from the ratio of the frequency adaptation involved in a synchronisation measurement to the estimated nonlinear frequency. The implications of the second hypothesis have been studied by Belanovski *et al.* [147] in the limit case of a weak coupling, and by Zhou *et al.* in a more general situation [166] where an STNO synchronised to an external source is kicked out of synchronisation by a pulse train.

In this chapter we make use of a the full Thiele model, with a 4 equations system taking into account the dynamics of the amplitudes, see equation (8.1). A comparison of the Adler equation, Thiele equations and micromagnetic simulations is illustrated with the shapes of the Arnold tongues for mutual synchronisation of two vortex oscillators which differ by their diameters. This has been performed in [169] in a figure reproduced as figure 8.1. The full Thiele equation indeed still does not model the synchronisation area perfectly compared to micromagnetic simulations, but it does a much better job than a simple phase model such as Adler's one. Still the subsequent modeling errors have to be put into perspective with the uncertainty of the fabrication process, the complicated mapping of the local magnetic field, the uncertainty on the current distribution...

## 8.2 Results

Starting from this model, we now try to reproduce at least qualitatively the experimental results from the previous chapter.

### 8.2.1 Mutual synchronisation

In this subsection we simulate a few measurements from section 7.3.

In the plots presented here, the timelines are calculated for the set of four variables by integrating the previously introduced set of equations. The signal of each oscillator is then reconstructed from the amplitudes and phases, and then Fourier-tranformed to produce the corresponding power spectrum density, with a Kaiser windowing to lower the

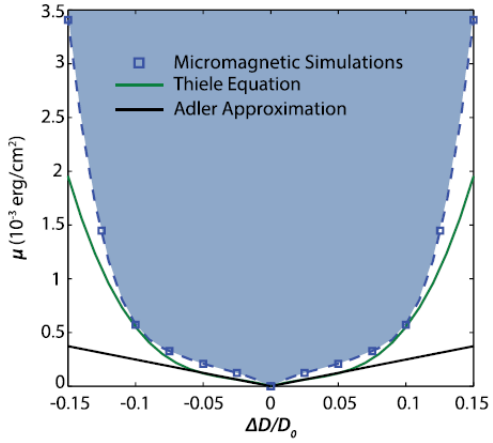


Fig. 8.1 *The synchronisation areas or Arnold tongues calculated according to the Adler equation, the Thiele equation and micromagnetic simulations. Taken from [169]*

sidelobs. The equations are integrated over typically 5μs what corresponds to a resolution bandwidth of 200kHz, and with a sampling frequency of 2100MHz. This permits a sufficient time resolution without excessive calculation time and resource consumption.

In figure 8.2 the external source is switched off, so only the two oscillators are present as we sweep the ground frequency of oscillator 1, which is visible on the x-axis. The frequency on the y-axis is the actual frequency from the Fast Fourier Transform (FFT) output. The signal from oscillator 1 is crossing the plot on its diagonal, while the signal of oscillator 2 is visible as a horizontal line since its parameters are kept constant. The two oscillators can be identified as the two most brightest modes on panels (a) and (b), while the other signals are beating modes.

We are able to extract from our simulations the power spectra for each oscillator, and their sum is the signal we measure in our experiments. The plotted data are, successively: the total power spectrum in linear and logarithmic scale respectively, and the individual power spectra of oscillators 1 and 2 respectively in logarithmic scale. With the logarithmic scale we are able to observe several harmonics corresponding to the beating frequencies resulting from the mixing of the several signals present in the system. Additionnaly from the individual spectra one can see that although the individual oscillator is mainly present in one mode, it distributes energy in other modes, in particular it is present at the main mode of the other oscillator.

We are able to reproduce qualitatively the data of the previous chapter in figure 7.7(f). There is a frequency jump as the two signals merge into one when the two oscillators synchronise, with a jump of on signal to join the other one corresponding to the nonlinear coupling. The system here jumps to the accoustic mode. Note that the simulated system is very symmetric as the two oscillators differ by their ground frequencies only.

The oscillators adapt their power to reach the frequency of the synchronised mode. The relative power variation can be far from negligible. This is visible from the integrated power spectra plotted as magenta lines on the 2D plots. Now let us consider the phase

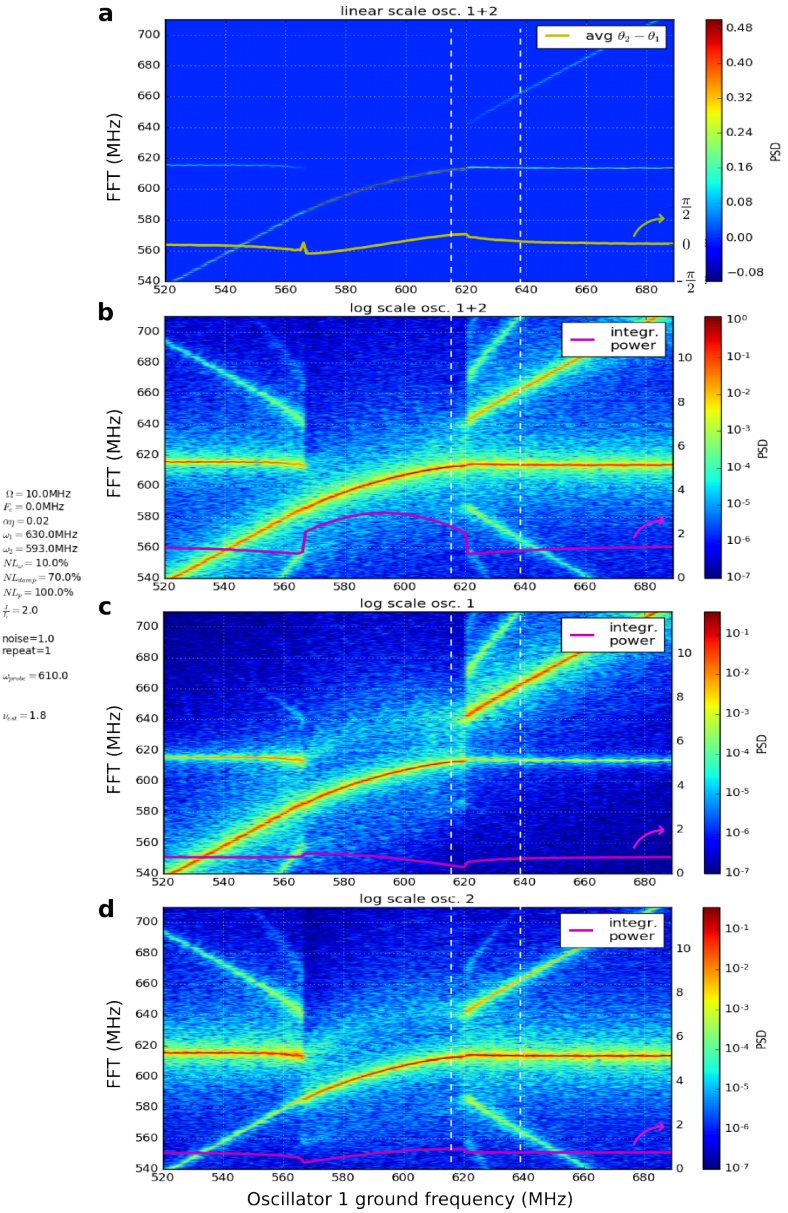


Fig. 8.2 *The ground frequency of STNO1 is swept while STNO2 is kept constant. When the two are close enough (compared to the mutual coupling) the upper one jumps to the lower one. From top to bottom are plotted: the total spectrum in linear scale, the total spectrum in logarithmic scale, the spectrum of oscillator 1 in logarithmic scale, the spectrum of oscillator 2 in logarithmic scale. The yellow line plots the average phase difference between the two oscillators, and the magenta lines the integrated power, and the values should be read from the right-hand-side y-axis. The two vertical lines indicate the working points where the external source probes the unsynchronised and synchronised mode (see sections 8.2.2 and 8.2.3 respectively).*

difference between the two oscillators, plotted as a yellow line on the linear scale spectrum plot. Actually the quantity plotted is the average phase difference, which takes non-zero values outside the mutual synchronisation window as during the frequency pulling the phase difference is constant for finite time slots with occasional $2\pi$ phase shifts. According to the phase model, the phase difference increases from $-\pi/2$ to $+\pi/2$ (or alternatively decreases from $+\pi/2$ to $-\pi/2$ depending on the convention selected) over the mutual synchronisation window. In the simulations presented this range is restrained. Namely by allowing the oscillators' amplitude to vary, we relax the constraints on the phase difference since with this extra degree of liberty, now two variables can adapt so that the system reaches synchronisation.

The magenta lines are the power density integrated over the entire spectrum for each value of the swept parameter. At the beginning of the simulation two PSD signals are visible, as the frequencies are too far apart from each other for the oscillators to mutually synchronise. As the frequency of oscillator 1 is linearly increased, it eventully gets close enough to oscillator 2 so they can mutually synchronise, and the frequency of oscillator 2 jumps to match that of oscillator 1. More precisely the magenta line plotting the integrated power on the power spectrum of oscillator 2 (plot (d)) shows that oscillator 2 adapts its frequency by adapting its amplitude. At the other edge of the synchronisation bandwidth, oscillator 1 is decreasing its amplitude to adapt its frequency, and recovers when synchronisation is broken (panel (c)). The total integrated power is maximum when the two oscillators are identical (panel (b)).

As explained higher, our calculation takes the final state of the simulation with the old parameter values as the initial state with the new parameter values. Therefore it is possible to observe whether the observed phenomena are hysteretic, by sweeping the parameter value in either way. From figure 8.3 it is confirmed that the synchronisation phenomenon is hysteretic [170, 171] since as we sweep the frequency of one of the oscillators in either way, the synchonisation bandwidth is shifted towards upper of lower frequencies. Namely the strength of the coupling depends on the amplitude ratio between the two oscillators, and this amplitude ratio changes when the two oscillators mutually synchronise.

### 8.2.2 Probing the dipolar coupling with an external signal

This part aims at reproducing the results in section 7.4 with the same model (equation (8.1)).

In figure 8.4 we reproduce the measurement in figure 7.10(b). The parameters are selected so that the system remains outside the synchronisation bandwidth, as indicated by the rightmost dotted line on figure 8.2. Oscillators 1 and 2 are mutually coupled via dipolar coupling, but not synchronised, so two distinct auto-oscillation signals can be observed. Then as we sweep the frequency of the external source at a reasonable power, it first phase-locks oscillator 2, what affects the dynamics of oscillator 1, and *vice-versa*. This is clearly visible on the linear scale plot in panel (a), which is very similar to figure 7.10(b). Now if we consider the logarithmic scale plots in figure 8.4(b) it is possible to observe all the harmonics and beating frequencies, which would be hidden under the noise level in the experimental measurements.

In addition we note that the two modes are not individual oscillators modes but rather

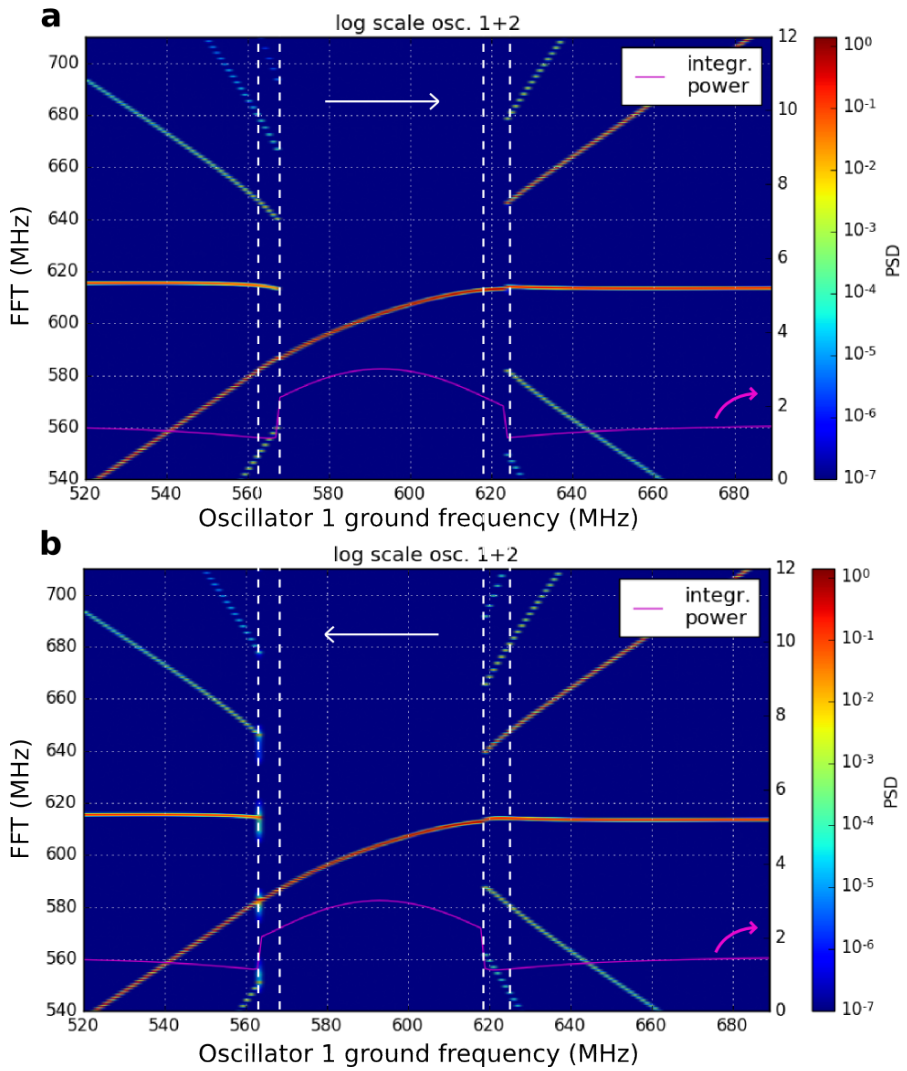


Fig. 8.3 *The ground frequency of STNO1 is swept up and down respectively. A small shift in the synchronisation bandwidth reveals the hysteretic behaviour. The vertical lines are guides to the eye. The arrows indicate the sweep direction.*

hybridised modes, and that the lower frequency mode gathers more energy than the higher frequency mode. This is visible both from the signal intensity, and from the phase-locking bandwidth to the source. It is similar to the previous plots in figure 8.2 where when the two oscillators are mutually synchronised, the lowest energy mode, gathers all the energy.

There is a small variation in the average phase difference and the individual integrated powers at the phase-locking events. Namely the phase of the phase-locked oscillator is affected by the external source, and the oscillator adapts its frequency to follow the source by adapting its power.

### 8.2.3 Resonant destruction of synchronisation

In this section we try to reproduce the experimental data in section 7.5.

#### Evidence of the intrinsic frequency for phase oscillations in the simulations

In figure 8.2 we reproduce the thermally induced sidebands [172] by adding a white Gaussian noise. This way the system is constantly perturbed from its equilibrium state, so statistically it spends time in the transient to synchronisation, what makes the intrinsic frequency introduced in section 7.5 visible through the sidebands. Surprisingly the sidebands are visible on the individual spectra of the oscillators but not on the sum of the two signals, which we measure in our experiments. So the intrinsic frequency is indeed present and can be resonantly excited, but the system we simulate might be too symmetrical and the two oscillators oscillate at the intrinsic frequency in antiphase. Lastly it seems that this intrinsic frequency is roughly independent from the natural frequencies mismatch, provided the two oscillators are mutually synchronised. One is even tempted to say that the sidebands look slightly more intense at the edges of the synchronisation bandwidth, indicating that it would be easier to excite resonant Destruction of Synchronisation (DoS) away from the center of the synchronisation bandwidth, or to put it differently, when the two oscillators are different enough.

This is described in figure 8.5. In panel (a), the mutual coupling is set to zero, and the STT is switched on at $t = 0$. The frequencies of both oscillators increase until they reach their equilibrium value, and the instantaneous frequencies calculated as the instantaneous phase derivatives adapt subsequently. At this point the mutual coupling is switched on (b) with an amplitude strong enough so they can mutually synchronise. In order to reach the same frequency, the two oscillators adapt their amplitudes with a transient, and this transient is followed by the instantaneous frequencies. In this transient a characteristic damping appears from the exponential behaviour, and a characteristic frequency appears from the oscillatory behaviour, exactly as for a damped harmonic oscillator reaching its equilibrium. Note that in this figure we are looking at the instantaneous frequency, whereas in figure 8.6(a) and (c) we will be looking at the phase difference.

To understand the DoS data in the previous chapter we choose to look directly at the phase difference temporal evolution between the two oscillators. These results are gathered in figure 8.6, which introduces three ways to put into evidence this intrinsic resonant frequency, which behaves as $2\sqrt{\nu\Omega\Gamma_p}$ where $\nu$ is the nonlinear parameter, $\Omega$ the coupling strength and $\Gamma_p$ the power damping (see equation (7.19)).

First let us consider the pair of oscillators with an arbitrary phase difference in panel 8.6(a). Then we switch on the mutual coupling, and look at the time evolution of the

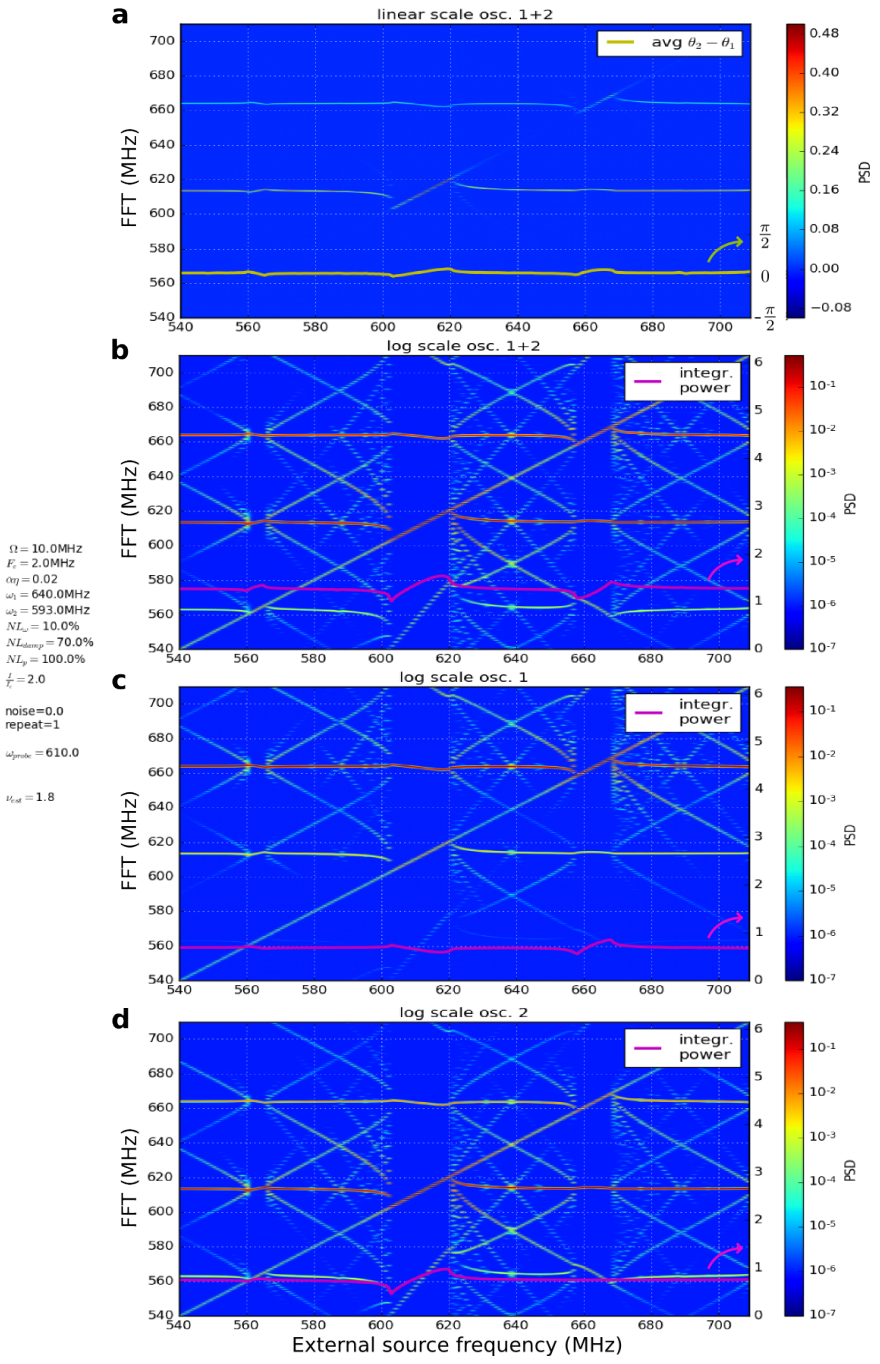


Fig. 8.4 *The frequency of the external source is swept across two mutually coupled but unsynchronised STNOs. As can be seen each STNO contains several frequencies from the beating frequencies. The yellow curve is the average phase difference between the two oscillators. (a) Total power spectrum in linear scale. (b) Total power spectrum in logarithmic scale. (c) Power spectrum for oscillator 1 in logarithmic scale. (d) Power spectrum of oscillator 2 in logarithmic scale. The magenta curves are the corresponding integrated powers.*

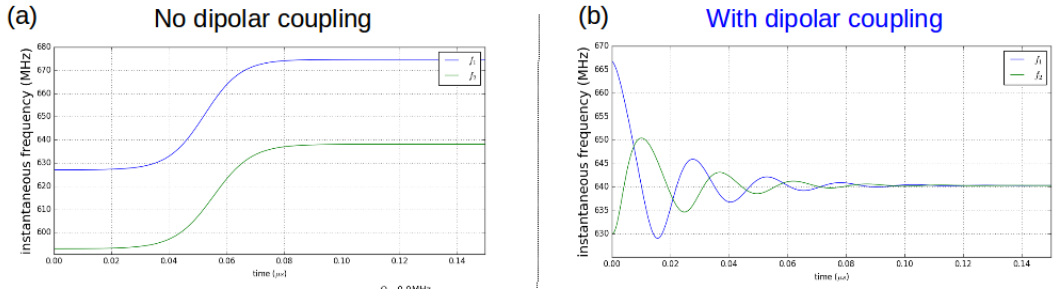


Fig. 8.5 *Instantaneous frequencies of the two oscillators: (a) Zero coupling. The frequencies of each oscillator adapt as the amplitudes of each oscillator increases from zero to their equilibrium value. (b) The coupling is switched on at the end of plot (a). The two oscillators reach the same frequency by adapting their amplitudes. There is a transient to synchronisation with an oscillatory behaviour.*

phase difference. We observe a transient to mutual synchronisation and constant phase difference, with an oscillatory behaviour, and an exponential decay towards an equilibrium value, as for the typical damped harmonic oscillator. This is the first evidence of this intrinsic frequency $\Lambda$. It can be put directly in relation with the particle sliding along a potential hill presented in the previous chapter. Figure 7.17 is reproduced in the inset of figure 8.6(a). The intrinsic frequency is characteristic of the shape of each potential well, and of the mass of the particle.

### Evidence of a threshold to the destruction of synchronisation

Now let us introduce the external source. The calculation in figure 8.6(b) reproduces the measurement undertaken in figure 7.13. Starting from a state where the two oscillators are mutually synchronised, we sweep the frequency of the external source at very low power. Here we register the signal from the pair of oscillators at the frequency of excitation of the external source, that is, the part of the signal that is located on the diagonal of figure 7.13. In some way, figure 8.6(b) is the power frequency response of the oscillators pair, as to use the vocabulary of automation. Of course we observe a large response at the auto-oscillation frequency, but we also observe two smaller resonant peaks on either side of the main peak, and these are separated from the main peak by the exact intrinsic frequency measured in plot 8.6(a). This is an evidence that this frequency can be resonantly excited.

From the sidebands positions in figures 8.2 and 8.6(b), we know where to expect the resonant DoS to occur. In figure 8.6(c) we excite the system with an external signal at three different powers (increasing from bottom to top) and three different frequencies labeled by three different colors on figure 8.6(b): one at the resonant frequency (magenta), one at a slightly lower frequency (blue), and one at a slightly higher frequency (green) but still keeping the exciting frequency far enough from the synchronised mode.

As the oscillators are mutually synchronised, their phase difference is constant. Now if one switches on the external signal at a small power, then the phase difference oscillates at the beating frequency, the frequency difference between those of the auto-oscillations and the external signal, but with a very small amplitude (lower three panels of figure

8.6(c)). As the power of the external frequency is increased (middle three panels of figure 8.6(c)), the amplitude of the oscillations in the phase difference increases. On both sides of the resonance frequency (blue and green traces), the phase difference remains bounded between $-\pi$ and $\pi$. At the resonant frequency however (magenta trace), one can see from the red traces in the inset graphs that the phase difference is no longer bounded. The corresponding magenta traces are the exact same time traces plotted modulo $2\pi$. One can clearly see occasional $2\pi$ jumps with no apparent periodicity. The center panel is produced for an external power right above the threshold for DoS, and the top panel at an even higher external power. It is important to note that the threshold power for DoS at this frequency is roughly three times as small as the coupling strength. The threshold power of the source for mutual synchronisation is calculated to be $\Delta_e$ =3.7MHz, while the mutual synchronisation was set at $\Omega$ =10MHz. The fact that the $2\pi$ jumps seem to appear at irregular times, although the system here is fully deterministic (no noise was involved in this very simulation), is taken as a signature of a chaotic behaviour. However we did not attempt to quantify the latter. As the power of the source keeps increasing, the $2\pi$-jumps at the resonant frequency are more and more frequent. However for the other two frequencies, no qualitative change is observed and the phase difference remains bounded.

**Stability diagram**

This criterion on the phase difference enables us to produce the stability diagram of figure 8.7. There are three signals in the system: those of the two oscillators, and the external signal, each having a phase. Then integrating the ODE system for a set of parameters, if after a transient time of 2µs the phase difference between two signals remains bounded for at least 5µs, then the two signals are considered to be synchronised. So starting from a state where the two oscillators are mutually synchronised, for each value of the frequency of the external source, we determine by dichotomy the threshold power of the external source at which synchronisation is broken. This enables us to detemine five areas corresponding to five distinct situations:

- oscillators 1 and 2 are mutually synchronised but not synchronised to the source (white)
- oscillator 1 is synchronised to the source (green)
- oscillator 2 is synchronised to the source (red)
- and the overlap of the two previous areas when oscillators 1 and 2 are synchronised to the source
- no synchronisation is stable, or equivalently all phase differences are unbounded (blue)

The initial state always is oscillators 1 and 2 mutually synchronised, so the diagram does not display the possible hysteresic behaviours.

The dashed lines in figure 8.7 define the synchronisation area for a single oscillator to the source and should be compared to the Arnold tongues in figure 8.1. This is not surprising as the equations we used are derived from the Thiele equation. The overlap

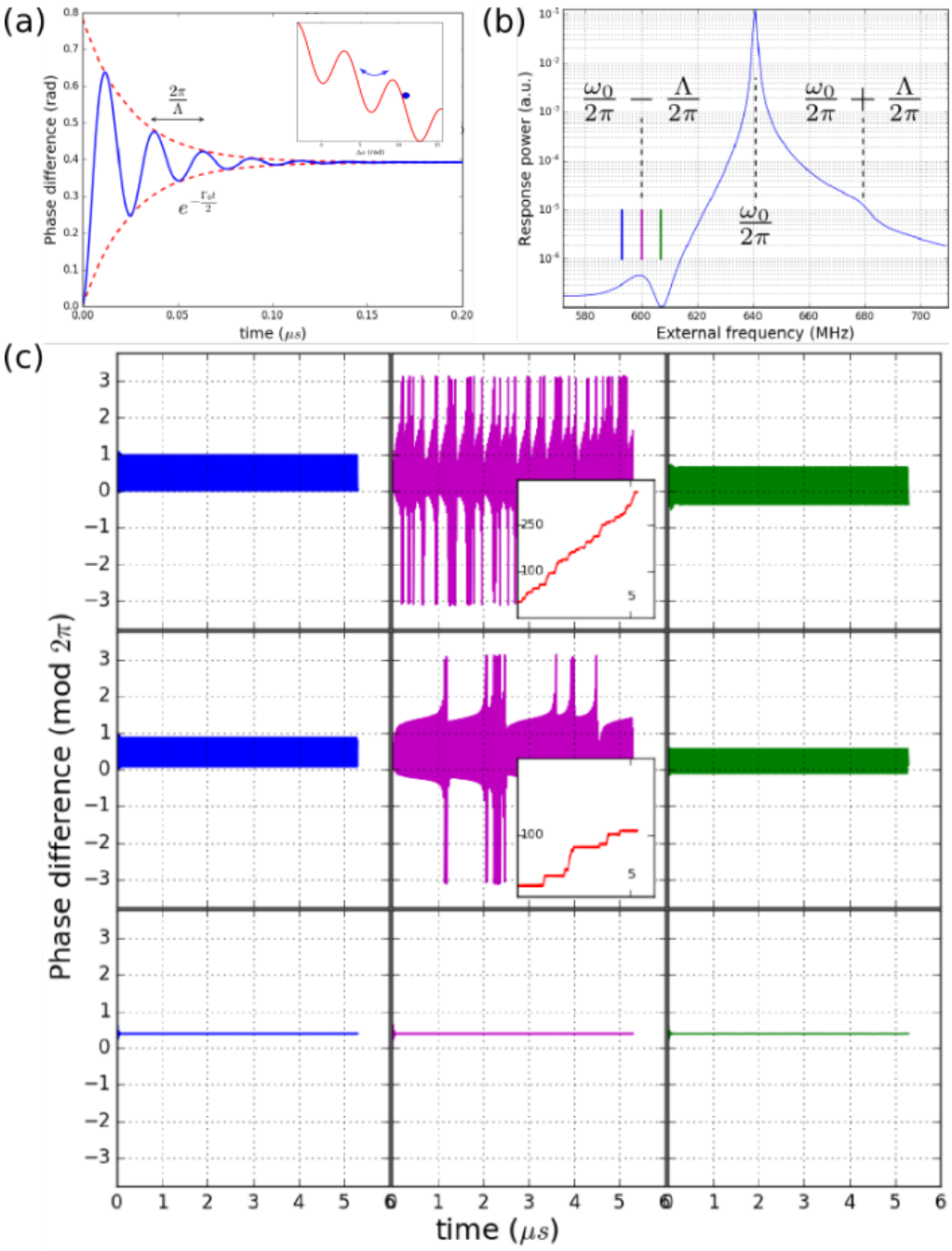


Fig. 8.6 *(a) Phase difference in the transient to the synchronisation. Figure 7.17 is plotted in the inset. (b) Response of the pair of oscillators at the frequency of the external source. Two small peaks ar visible on either side of the main peak. (c) Time traces of the phase difference for the three frequencies of the external source indicated by the colour labels on plot (b) and for three different amplitudes of the external source. The phase difference is plotted modulo $2\pi$. The red curve in the insets of the middle center and upper centre graphs plot the same data as the magenta curve without applying a modulo.*

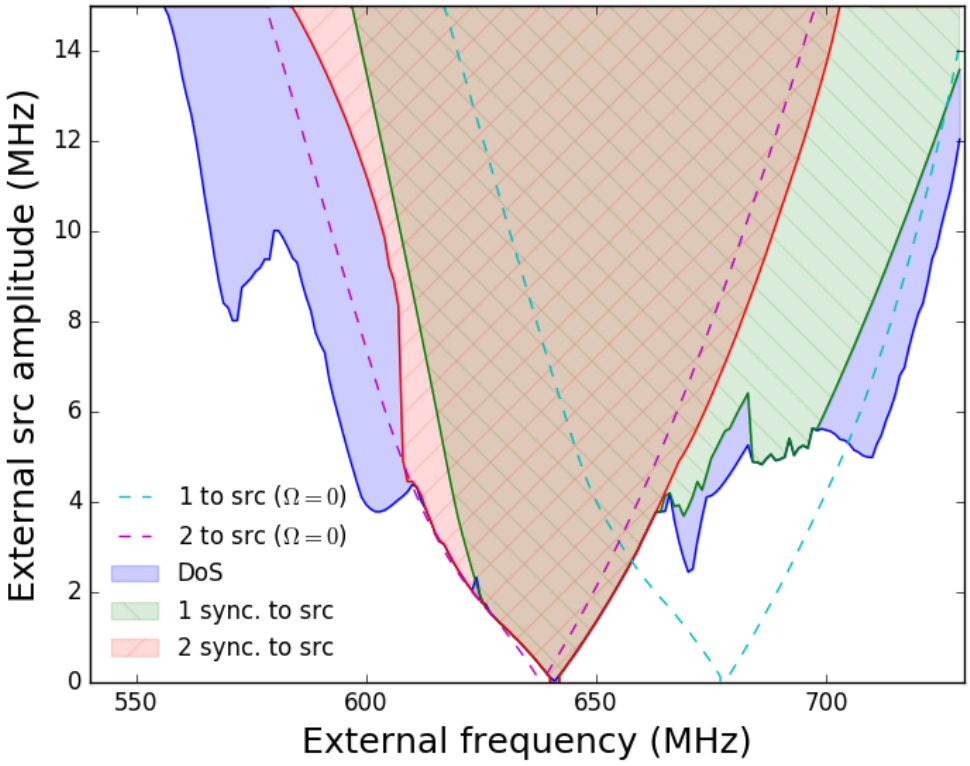


Fig. 8.7 *Stability diagram reporting the stable synchronisation patterns of the two mutually coupled nonlinear auto-oscillators excited by an external source, in a plane parametrised by the frequency and strength of the external excitation.*

area where both oscillators synchronise to the external source like one single oscillator has a very similar shape.

Now let us examine the DoS experiment by considering the stability diagram in figure 8.7. We set the external source power at, say, 3.8MHz, and sweep its ground frequency from 540 to 730MHz (see figure C.1). First the source does not affect the mutual synchronisation. Then around 603MHz, the two oscillators display a chaotic behaviour and mutual synchronisation is broken, but quickly recovers as soon as we keep increasing the frequency. Then oscillator 2 detaches from oscillator 1 to phase-lock to the external source. Then oscillator 1 joins as well and both are phase-locked to the source, until a frequency where they both detach from the source but remain mutually synchronised. For a small bandwidth mutual synchronisation is broken again and the power of the two oscillators is spread over a broad sprectrum, until they can mutually synchronise again.

Alternatively let us consider the case where we set the frequency of the external source at 603MHz, and sweep the source amplitude starting from zero power. At first the external source does not affect the mutual synchronisation, then as we pass the 3.7MHz threshold the auto-oscillations spectrum starts spreading. As could be seen from the three magenta plots in figure 8.6(c) (from the bottom plot to the upper plot), as the power of the external

excitation is increased $2\pi$ phase jumps occur more often and the auto-oscillations become more chaotic. However from figure 8.7 it can be seen that the power of the external signal may be increased a lot before we cross the border to the red area, where oscillator 2 phase-locks to the external source and the system loses its chaotic properties.

Several peaks can be seen pointing downwards in the blue surface. The parabolic-shaped peak centered at 603MHz corresponds to the resonant DoS mechanism introduced above. The symmetric peak however is more complicated. Namely as can be seen from the Arnold tongues, the chosen working point of the system is quite close to one edge of the synchronisation bandwidth (see the vertical lines in figure 8.2). So looking back at the sidebands in figure 8.2, we notice that the upper sideband is very close to the natural frequency of the highest frequency auto-oscillator. Thus for this point two mechanisms are competing for the destruction of synchronisation: the resonant excitation of an intrinsic frequency, and the seemingly equivalent opportunity for oscillator 1 to either mutually synchronise with oscillator 2 or to leave oscillator 2 to phase-lock to the external signal alone. The competition of those two mechanisms complexifies the stability diagram in the range around 660 to 700MHz.

A naive guess would be that the two extra peaks of the blue surface are related to harmonics of the intrinsic frequencies, that would be responsible for the local resurgences of the sidebands as in figure 7.13 when the external source frequency is at 580 MHz, and which might be easier to excite in our experimental system than our model permits to simulate. Nevertheless we will take this hypothesis with distance, as we have no argument to verify it, and leave it as an opening.

### 8.2.4 XPP-AUTO bifurcations and stability analysis

Our first approach to be able to predict the evolution of the system towards an equilibrium, and potentially describing the stability of this equilibrium, or a bistability between two equilibria, was to built by ourselves these stabiltiy diagrams or convergence diagrams. Namely for a system of two first-order differential equations with two variables, it is easy to map in the plane of those two variables the time derivative vectors of those two variables. Then one observes sink, well and saddle nodes, which behave as wells along one axis and as sinks along the other. As one parameter is swept, it is even possible to observe two nodes merging into one or diverging from one another, and the system qualitatively changes. However for a 4-dimensional system, the situation is more complex to represent. This is when we were introduced to XPP.

XPP is a free software (distributed under the GNU public license) for solving differential equations, boundary value problems, and stochastic equations (among others) [173]. XPP contains the code for AUTO, a popular software for continuation and bifurcation problems in ordinary differential equations [174]. These softwares are powerful bifurcation analysis tools. In our special case we have only a limited use of the resources they can provide. Still we can extract some useful information. Notably it is possible to determine the equilibrium states for a system of nonlinear ODEs, along with the corresponding eigenvalues.

This system is a nonlinear system with 4 equations and 4 variables. From the system presented at the beginning of the chapter, one can see that the problem can be restrained to 3 dimensions if we get rid of the source, since only the phase difference between the

two oscillators matters then. This means that we consider the intrinsic properties of the pair of oscillators, and the external source is just an external tool to excite the dynamical properties of the pair of oscillators, but does not add any physical property. This choice of variables allows us to describe the mutually synchonised state simply as an equilibrium point, since when the two oscillators are mutually synchronised, their phase difference and their respective amplitudes are fixed. Yet an equilibrium is not necessarily a point but may be an equilibrium cycle.

The stability of an equilibrium is determined from the eigenvalues of the jacobian matrix (that is, the multidimensional first derivative of the system) for the equilibrium point. This basically consists in linearising the equation system around the equilibrium. The system close to a stable equilibrium can thus be compared to a damped harmonic oscillator at first order, the real part of the eigenvalue describing the damping, and the imaginary part of the frequency of the oscillatory component. This latter component describes what we referred to as the intrinsic frequency of the system earlier. Of course for a stable equilibrium the real part has to be strictly negative, else the system is not damped and does not converge to the equilibrium. These two parts of the eigenvalues of the stable non-zero points of the system are represented in figure 8.8b, for the range where mutual synchronisation is possible. From this plot one can deduce that the intrinsic frequency around 30-35 MHz does not change much within the synchronisation bandwidth and seems similar to the frequencies of the sidebands present in figure 8.2. In addition the corresponding damping is lesser on the edges of the synchronisation bandwidth than at its center, so the resonant behaviour should be easier to excite at the edges of the synchronisation bandwidth than at its center. This provides an important piece of information. Namely as the power of the external excitation is increased, the intrinsic frequency gets more easily excited, but the system also phase-locks to the external signal on a larger bandwidth, which might overlap the sidebands. So it will probably be easier to observe the resonant destruction of synchronisation close to the edges of the synchronisation bandwidth, and more diffficult to observe it at the center of the synchronisation bandwidth, even though the phenomenon still exists. This is the case in section 7.5 and 8.2.3. Namely, it can be seen from figure 7.8 that the frequencies of the "isolated" STNOs are well-separated. For the simulation in section 8.2.3, the leftmost dotted line indicate the working point location.

In figure 8.8a we plot the equilibria for each variable as the ground frequency of oscillator 1 is swept. An equilibrium point can be read for each value of the parameter swept. Yet two branches can be distinguished, one for which the equilibrium is stable and one for which it is unstable. The stability of the equilibrium is determined from the sign of the real part of the eigenvalues of the jacobian matrix at this very point. For each variable of the system we have plotted the stable equilibria with a colour line (corresponding eigenvalue has a negative real part), the unstable equilibria (eigenvalue has a positive real part) with a thin black line and the limit cycles with colour circles (eigenvalue is purely imaginary). Let us consider for instance the line corresponding to the phase difference $\delta\phi$ (red on the plot). This red line is continued by two black lines at each edge. Indeed there exists an equilibrium value for the phase difference for all the parameters tested in this plot, but there is a stable equilibrium only within the synchronisation bandwidth. This analysis is also valid for the two other valiables of the system ($X_1$ and $X_2$).

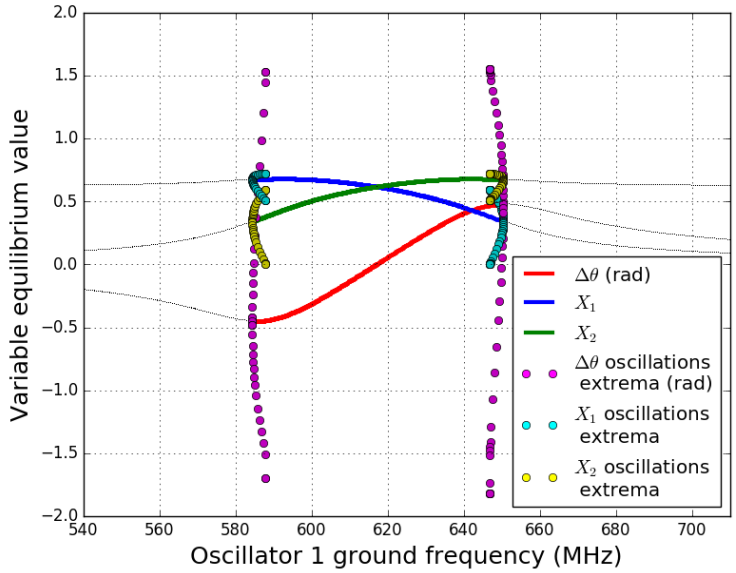


(a) *Equilibrium values of the several variable of the system for stable (colored) and unstable (black) equilibrium points. The circles correspond to the extremal values of the variables oscillationg on a limit cycle.*

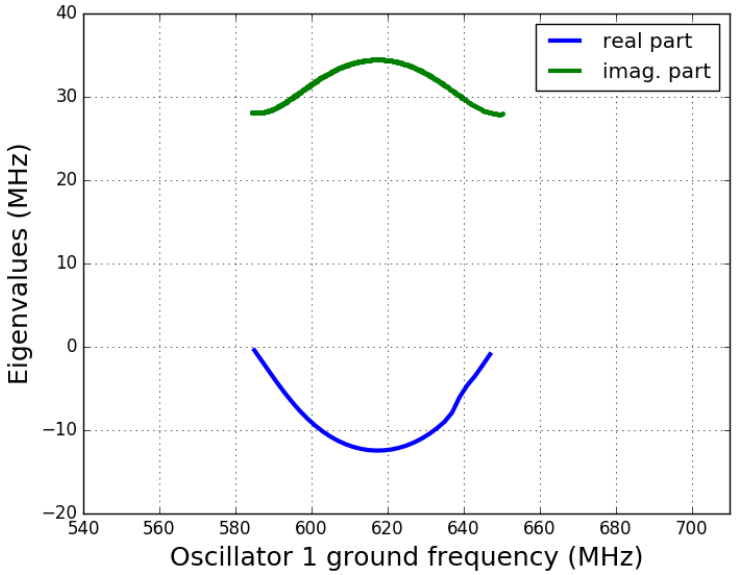


(b) *Real and imaginary parts of the eigenvalues of the jacobian of the system for the stable equilibrium point.*

Fig. 8.8 *Results of the analysis by XPP.*

At the edges of the synchronisation bandwidth (when the black line turns red or vice-versa) two dotted lines (plotted as magenta ($\Delta\theta$), cyan ($X_1$) and yellow ($X_2$) circles) depart from the point where the equilibrium changes from unstable to stable. In fact there is a small range of parameter values for which the system is bistable, and two equilibria exist with different corresponding eigenvalues. The circle lines describe the case where the eigenvalue of the equilibrium is purely imaginary, so the variable oscillates at a constant amplitude, and is neither damped nor explosive. This is a stable limit cycle. In this plot, for each parameter value of the x-axis where they exist, each pair of circles plot the maximum and minimum values between which the variable will oscillate during its oscillations.

A bifurcation is a qualitative change in the system's equilibria. For instance when the frequency difference between the two oscillators gets smaller than the synchronisation bandwidth, the synchronised state becomes a stable state, so this event corresponds to a bifurcation. The transition from stable to unstable of the equilibrium point describing the mutual synchronisation state is identified by AUTO as a Hopf bifurcation. An Andronov-Hopf bifurcation is the birth of a limit cycle from an equilibrium in dynamical systems generated by ODEs, when the equilibrium changes stability via a pair of purely imaginary eigenvalues. This is visible on the plot as the two branches (plotted with unconnected magenta ($\Delta\theta$), cyan ($X_1$), yellow ($X_2$) circles in our case) departing from the bifurcation point, which decribe the maximum and minimum values of the variable gyrating on the stable limit cycle. The limit cycle becomes unstable when the amplitude of oscillations of the phase difference exceeds $\pi$, or one of the amplitudes $X_1$ and $X_2$ reaches the zero-axis (so beyond this limit one vortex would cross the centre of the disk). Hopf bifurcations in STNOs have already been described by [175].

The stable/unstable equilibrium point for the phase difference should be compared to the average phase difference between the two oscillators plotted as the yellow line on the first plot of figure 8.2. In figure 8.2 the non-zero average value for the phase difference was interpreted as the constant phase difference for a finite time between consecutive $2\pi$ jumps.

## Summary

**In conclusion we have been able to reproduce qualitatively the two phenomena, revealing the dipolar coupling in the unsynchronised state and the destruction of synchronisation in the synchronised state. The power spectrum density plots can be compared to the experimental data and enable a deeper analysis, since we are not affected by noise. In the case of the destruction of synchronisation, we are able to reproduce mutual synchronisation data, and the addition of noise reveals the existence of the intrisic frequency. The timelines of the phase resulting from the numerical integration enable us to interprete the destruction of synchronisation phenomenon as a chaotic behaviour spreading the signal spectrum. The analysis from XPP-Auto provides additional information by revealing that the synchronisation is easier to destabilise at the edges of the synchronisation bandwidth, and is an opening to other ways of studying the problem.**

# Conclusions and perspectives

**General summary**

My thesis work has explored two similar elementary GMR structures in two geometries optimised for two different applications: one for field sensing, where the orientation of the free layer magnetisation by an external field is measured electrically via the magnetoresistance, and one for STNOs, where the STT is maximised to electrically destabilise the free layer by compensating the damping and obtaining self-sustained oscillations of the magnetisation.

In both situations, the problem has required both simulations and theoretical considerations in addition to the experimental measurements.

In the sensor study we demonstrate the feasability of a proximity sensor, which uses a GMR as an RF magnetic field detector, with frequencies in the 10kHz-100MHz range, and its applicability to pressure sensing and velocity sensing in two specific realisations. The questions answered here are more performance-related due to the applicative aspect. Namely the technology is mature, and the concerns are more related to the achievability of the targeted performances. The physical principles of this proximity sensor are similar to that of non-destructive testing, that is, measuring the magnetic field reflected by a conductive element. For the pressure sensor, the strategy consists in measuring the elastic deformation of a metallic membrane under the stress of a pressure. We demonstrate that with several coil designs, and the choice of an adapted material for the membrane, with sufficient deformation while staying in the elastic range, so the membrane does not deform over time, it was possible to realise a pressure sensor covering the 0-250bar range with a 0.5bar sensitivity, with the dedictated electronics. This will be used in automotive applications for measuring oil pressures. As the coil and sensor are deposited together to be encapsulated, and a GMR sensor is sensitive only in one direction, this direction has to be in the plane of the coil. Using analytical calculations and COMSOL simulations, we find a $1/z^4$ dependence of this component of the field. For the same surface occupation, two planar coils side-by-side generate a higher field at ranges comparable with the coil lateral dimension.

The studied samples for the STNO study were single STNOs and pairs of dipolarly coupled STNOs with various geometries. We were able to demonstrate that the magnetic distribution in both magnetic layer of each STNO was a vortex, and that we were able to control the topological charges of each vortex. The originality of this work is the presence of a microstrip antenna on top of the device, able to generate a microwave magnetic field to act on the STVOs. In this work, we fully characterise the dynamic properties of the single, and more interestingly of the pairs of STVOs using both spectrum analyser and voltage FMR measurements. We were able to reproduce the main results demonstrated in [108], [115] and [101] on single STVOs. We could also observe the auto oscillation signal for a pair of STVOs in the four combinations of polarities, and clearly observe mutual synchronisation for parallel and antiparallel relative polarities alignment [119]. In particular it was possible to spectroscopically observe the anticrossing in the hybridised modes in the case of antiparallel polarities.

The most original results are those involving the microwave field generated by the antenna.

First, we clearly observe that the mutual synchronisation strengenths the auto-oscillation signal against external perturbation, as the signal resulting from mutual synchronisation

is more resilient to phase-locking to the RF field than the signals of the isolated STVOs, and has narrower bandwidth.

Second, in a situation where the two auto-oscillators are not synchronised, but remain mutually coupled through the dipolar interaction, the microwave field frequency is swept across the two visible auto-oscillation signals. It is demonstrated that the microwave field can be used as a probe to reveal the mutual coupling as the phase-locking of one oscillator to the microwave field affects the dynamics and therefore the frequency of the second oscillator. Additionally we demonstrate that we can quantitatively extract the coupling parameters, namely its amplitude and phase, by fitting coupled phase equations taking into account the nonlinearity. The extracted data fall within the range of values expected from a macrodipole interaction model.

Third, in the situation where the two oscillators are already mutually synchronised, we observe a destruction of the auto-oscillation signal for a certain frequency. The approach developped in the previous paragraph is valid in the limit of the weak microwave coupling only, but the phase model is no longer sufficient to explain the observed features. We demonstrate that by taking into account the dynamical amplitude equations and thereby leveraging the hypothesis of slow, small variations of the amplitude, we introduce inertia to the system. This introduces an intrinsic resonant frequency for the phase oscillations, similarly as for the damped harmonic oscillator, which can be resonantly excited by an external signal and lead to the destruction of mutual synchronisation. This is quite different from the results reported in [176], where a nonresonant destruction of the synchronisation was observed at much lower frequency, for the modulation of a parametrically phase-locked STNO.

Lastly, we integrate the coupled differential equations on the phase and amplitude to reproduce the experimental results. In the case of mutual synchronisation, we reproduce the jump in frequency of one oscillator to the other one as they mutually synchronise, which is experimentally observed, while with only coupled phase equations the transition to synchronisation would occur with continuous adaptation of both frequenies. In the case where the STVOs are not synchronised, we reproduce the experimental data and make several features appear, as we are not affected by noise. In the case where they are synchronised, the numerical calculations back our explanation by revealing the intrinsic frequency in the oscillatory transient to mutual synchronisation, and by a resonant response to an external microwave field at this specific frequency. In addition by analysing the timelines of the phase we explain the destruction of synchronisation as a chaotic behaviour, leading to the spreading of the auto-oscillation frequency over the spectrum.

We complete this study by a stability analysis, based on the free software XPP, which demonstrates in particular that this phenomenon of resonant destruction of synchronisation will be easier to observe as we get closer to the edges of the mutual synchronisaton bandwidth. This is rather an opening to the implications of our results, which make STNOs a unique platform to experimentally study nonlinear auto-oscillators, which are seldom in physics.

### Perspectives

These results arrive simultaneously to first demonstrations of bio inspired computing architectures based on spin torque oscillators. Let us mention the works in [69] which

demonstrated pattern recognition using reservoir computing, and spoken digits recognition [177, 178] with four mutually coupled STVOs and two external sources. This puts into perspective our work, which reveal features specific to networks of mutually coupled nonlinear auto-oscillators, which are the basis for the hardware for bio-inspired computing architectures. For instance, the mechanism of resonant destruction of synchronization of nonlinear oscillators by a weak external force should happen in oscillatory systems of any nature provided the coupling and nonlinearity are strong enough. It could also be used in practice as a way to selectively destroy undesirable synchronized states, which may be important for oscillator-based neuromorphic computing.

In this work we use "first-generation" vortex-based STNOs in GMR structures, but other structures are now developped, notably the spin-Hall nano oscillators, with which the record number of nine oscillators were synchronised [97]. This type of spin torque oscillators use a new, simpler geometry, and opens the way to the magnetic equivalent of electronic devices, as it was demonstrated that it is possible to induce auto-oscillations of the magnetisation in an insulator [98].

As for the mutual synchronisation of STNOs, which was one of the main focus in this thesis, three types of coupling are efficient, which all have their own characteristics and assets. The electrical coupling makes it easier to connect STNOs and define the topology of the oscillators network [120]. With the spin wave coupling was reached the highest number of mutually synchronised STNOs [97]. The dipolar coupling used in this thesis is local, and tunable, as the relative vortex core polarities can change the intensity of the coupling by a ratio about three [119, 179]. So up to date there is no definite argument in favor of one or the other coupling, which might be as well combined together to achieve novel functionalities.

Let us emphasize one more time the fact that these results are not limited to magnetic oscillators but can in principle be generalised to every nonlinear oscillator. Actually the model used in this chapter is very similar to the well-known Landau Ginzburgh model which has already been applied to the description of STO dynamics [102].

Finally our results also suggest the existence of chaotic dynamics in mutually coupled STNOs, which can be controlled by an external source. An other situation with chaotic behaviour has been reported in STNOs [180] where chaos originates from incommensurate core reversal rate with respect to vortex gyration velocity, and in [181], with a feedback with a well-chosen delay. This latter reference outlines the role of nonlinearity, which adds one degree of liberty to the oscillator system, and proposes potential applications of chaos multiplexing for cryptography and chaos-based computing.

# Appendix A

# Magnetic static configuration in a STVO pair

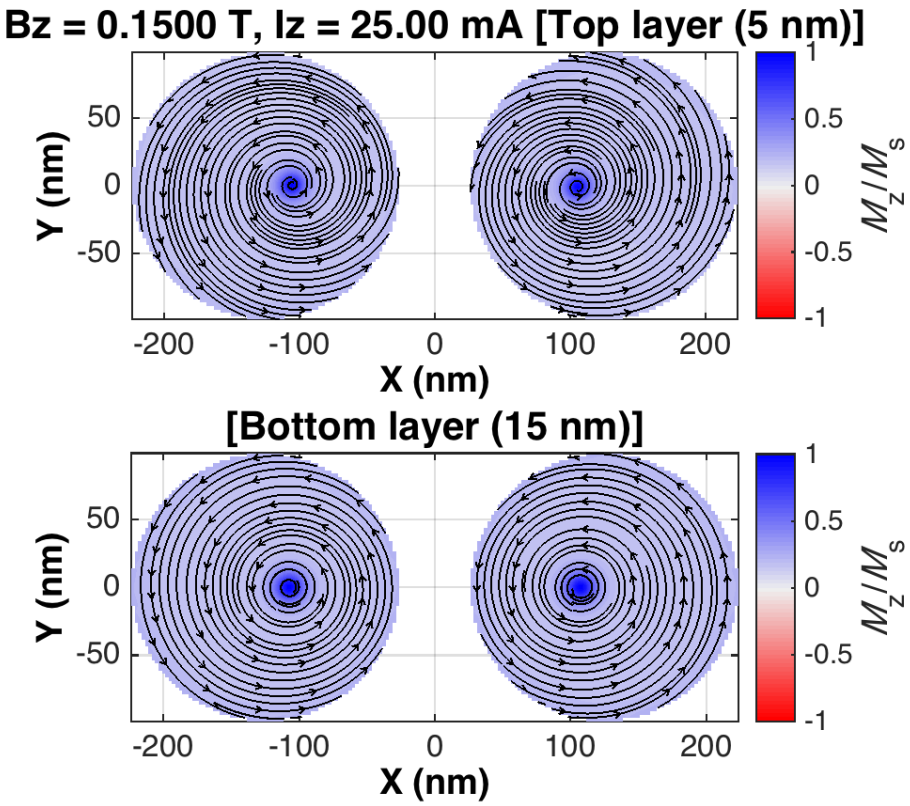


Fig. A.1 *Micromagnetic simulations displaying the equilibrium magnetisation distribution in two coupled nanopillars at 25mA dc current after a 10ns transient. Courtesy of Flavio Abreu Araujo.*

The simulations presented in figure A.1 were produced using micromagnetic simulations with the SpinPM package ([147, 158].

From the simulations presented in this figure it can be observed that the vortex equilibrium position is shifted from the center of the disk, although the current and dc field conditions are symmetrical for each pillar. This shift or asymmetry should be interpreted as the effect of the Oersted field caused by the dc current flowing through one pillar on the other one. This Oersted field is in-plane and favors the alignment of in-plane spins in one direction preferentially.

# Appendix B

# Selective polarity reversal in a pair of coupled STVOs

In this part we demonstrate the microwave-assisted polarity switching of either oscillator in a pair of mutually coupled vortex oscillators, by applying an external signal at the proper frequency and power. These measurements should be compared to those of [182]. Yet there are a few essential differences with our work:

- we are working on spin torque vortex oscillators instead of simple magnetic nanotdots in the vortex state
- the signals we are using to switch the polarities are characterised by their frequencies and amplitudes only, but not the pulse duration. The pulse duration used here is 3 seconds, which is long enough for the reversal to happen.

In our measurements the four polarity combination states are read by comparing the FMR signal at a reference field, where the four polarity combination states can exist, and be discriminated by four different signals which can be easily distinguished. Then the protocol consists in

- preparing a state where the polarities of both STVOs are parallel by applying a saturating field,
- then decrease the field intensity to a value where the four polarity combinations are stable
- apply the external signal at a set power and frequency
- measure the FMR signal at the calibration field and compare it to the previously calibrated signals

In fact it is possible to prepare all four polarity combination states by initialising the system at a well-chosen bias field, as mentionned in figure B.1, since the two nanopillars are slightly different. From figure B.1(d) it seems that the threshold for microwave-assisted switching is relatively independent from the initial state. This is of interest as two different relative polarity alignments lead to different coupling intensities [119], so the microwave-assisted switching would be coupling-insensitive.

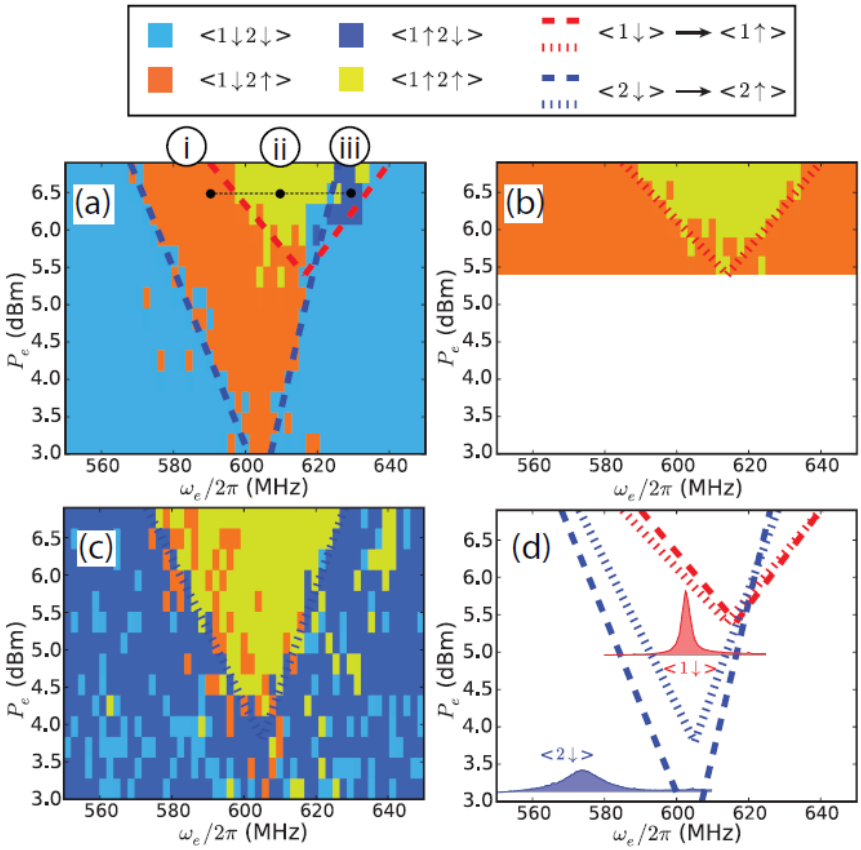


Fig. B.1 *Selective switching of the polarity in a pair of STVOs by an external signal at a chosen power (y-axis) and frequency (x-axis), starting from a (a)*$< 1 \downarrow 2 \downarrow >$*, (b)*$< 1 \downarrow 2 \uparrow >$*, (c)*$< 1 \uparrow 2 \downarrow >$ *polarity state. Each colour corresponds to a different combination of the two polarities in the final state. (d) plots the switching boundaries for the previous figures. The blue and red cones correspond to the switching of STVO 1 and 2, respectively.*

The microwave-assisted polarity switching of one single vortex oscillators is well understood, where the vortex reaches a critical gyration velocity which can be calculated from [128], resulting in a new vortex with an opposite polarity. The results for mutually coupled STNOs is particularly interesting as is suggest a way to selectively address individual devices in an array of STNOs.

Thanks to these results we are able to control selectively the states of the oscillators, whether they are synchonised or not, using an RF pulse, which is more convenient than a dc field.

# Appendix C

# Simulation of a PSD map with destruction of synchronisation

The power spectrum density in figure C.1 corresponds to a cut of figure 8.7 where the frequency of the source is swept at constant amplitude of the source.

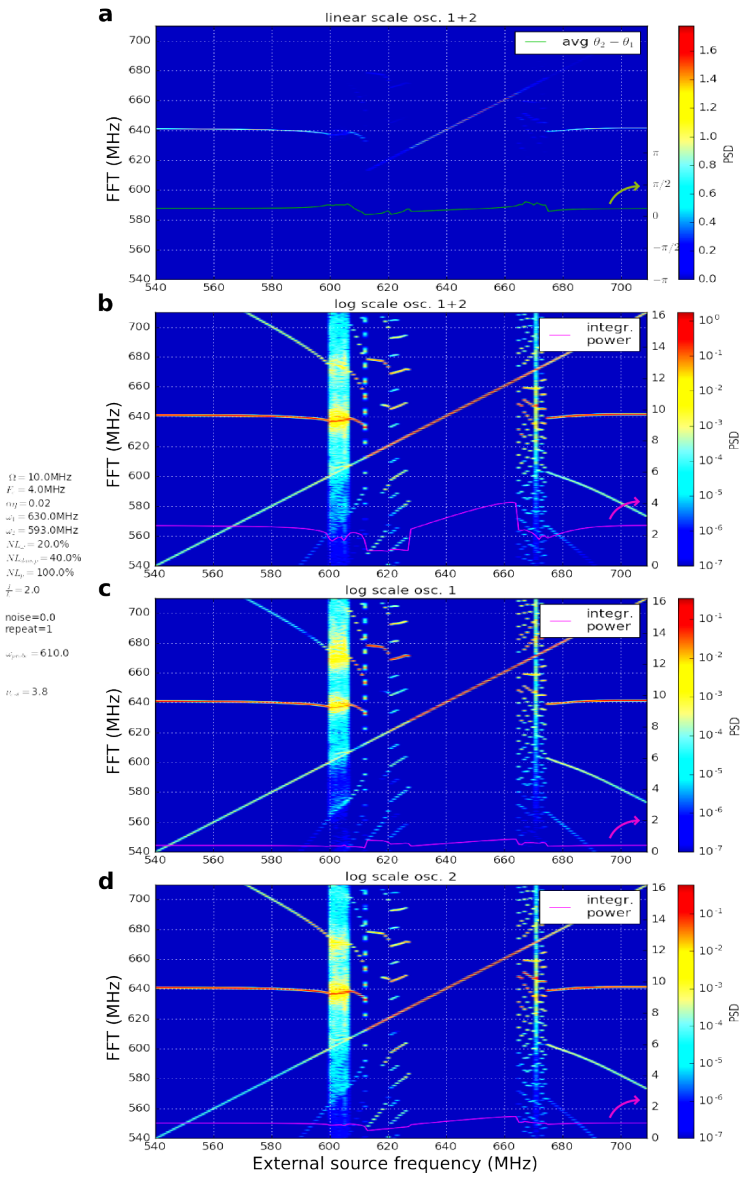


Fig. C.1 *PSD map while the frequency of the external source is varied at constant power. A spreading of the spectrum is visible around 603MHz, over a small range of frequencies because we are right above the threshold for destruction of synchronisation. At 610 MHz oscillator 1 synchronises to the source while oscillator 2 goes back to its isolated frequency, and is phase-locked as well at 620 MHz. (a) Total power spectrum in linear scale. The yellow curve is the average phase difference between the two oscillators. (b) Total power spectrum in logarithmic scale. (c) Power spectrum for oscillator 1 in logarithmic scale. (d) Power spectrum of oscillator 2 in logarithmic scale. The magenta curves are the corresponding integrated powers.*

# Appendix D

# Softwares fiability and noise in sensors

We have compared the results of three softwares of the field dependence on the distance to the coil plane for three different softwares that are Comsol, Civa and Maxwell, in logarithmic scale. The results are plotted in figure D.1 for the three softwares solving the exact same problem. The three softwares seem to agree on the power dependence over the distance of the in-plane component of the field at long distance, but the qualitative mismatches at short range are quite significant. Up to date we still lack the arguments to decide in favor of one or the other software.

In the problem simulated the single coil is square with an outer length of 2.2mm and the inner square is 1mm. This leaves a 600 microns width for the loop. The loop contains 30 wires and a 10mA current flows in the wires. In figure D.2 the noisy GMR signal is compared to the LASER signal, which is very stable.

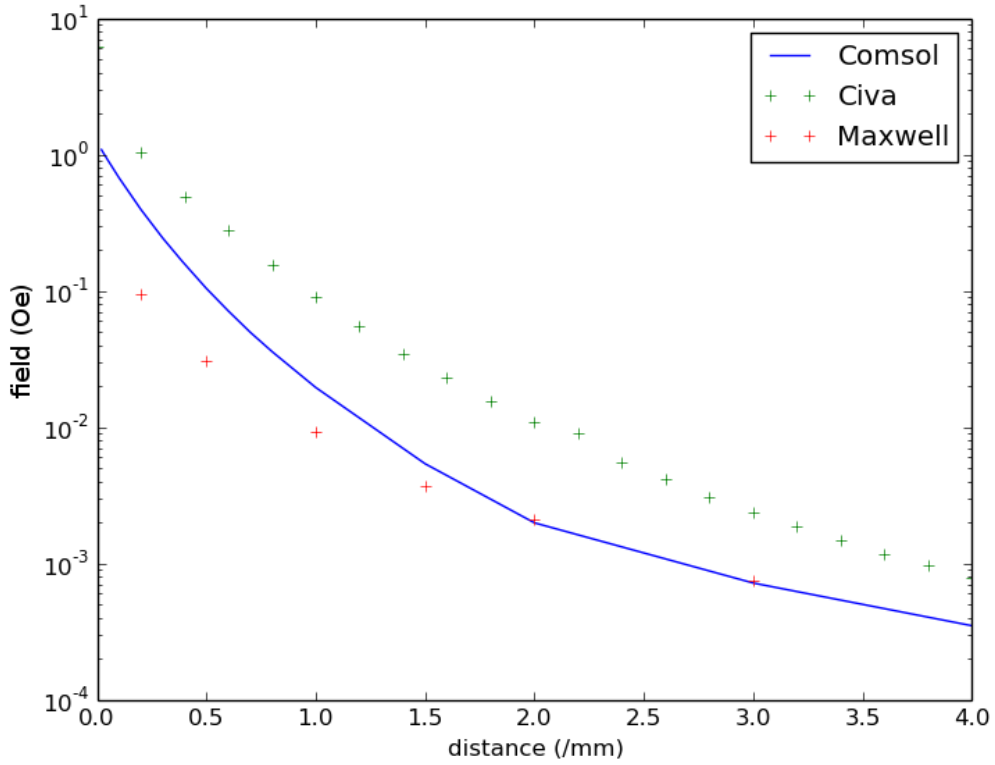


Fig. D.1 *Comparison of the simulation of our problem by three different softwares that are Comsol, Civa and Maxwell.*

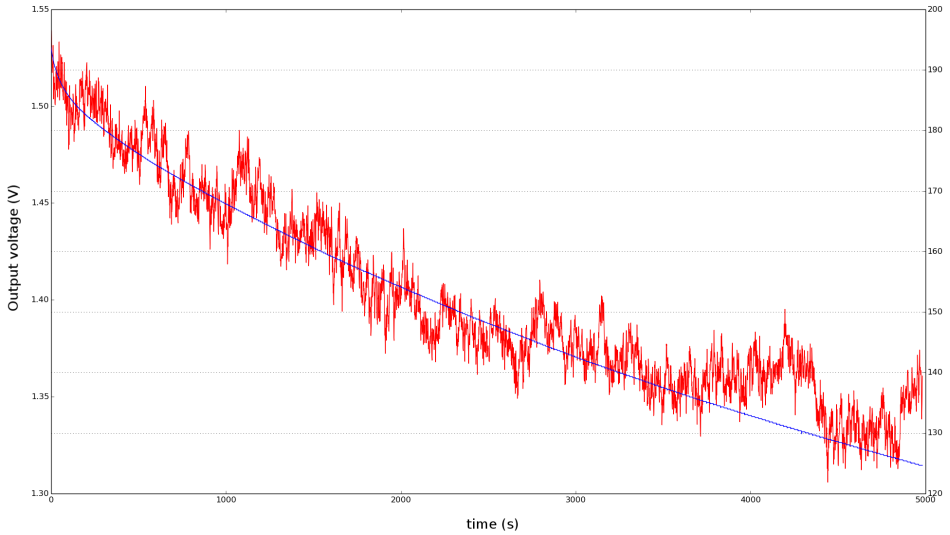


Fig. D.2 *Comparison of the LASER signal (blue) and the GMR signal (red) for the first batch of sensors.*

# Appendix E

# Résumé substantiel en français

## Introduction

Bien que la naissance de la spintronique, la branche de la physique qui utilise le degré de liberté de l'électron, remonte aux années 70, celle-ci n'a connu son véritable essor qu'à partir de 1988 avec la découverte de l'effet de magnétorésistance géante [3, 4]. Cet effet se traduit par une dépendence de la résistance d'un empilement de couches magnétiques et non magnétiques par rapport à l'orientation relative de leurs aimantations. La magnétorésistance géante a rapidement pu être mise à profit dans la réalisation de capteurs de champs magnétiques locaux, par opposition aux capteurs de flux tels que les bobines et SQUIDs, et dont on peut donc réduire les dimensions sans perdre en sensibilité, avec des sensibilités mille fois plus élevées que les capteurs à effet Hall de spin. Il trouvait des applications à l'échelle industrielle dès 1996 dans les têtes de lectures de disque durs, permettant d'augmenter de façon drastique la densité de stockage.

La magnétorésistance géante (ou GMR) permet par une mesure électrique de connaître la direction de l'aimantation d'une couche magnétique perturbée par un champ magnétique externe, par rapport à une couche magnétique de référence. Il existe un effet réciproque appelé couple de transfert de spin (STT pour Spin Transfer Torque), qui permet de manipuler l'orientation relative de ces couches en compensant l'amortissement par un signal électrique, en apportant du moment angulaire depuis un courant polarisé en spin pour compenser l'amortissement [19]. Ceci déstabilise la couche libre, ce qui conduit à lorsque l'amortissement est compensé exactement à des précessions entretenues voire un retournement de son aimantation. Cet effet est exploité dans les RAM magnétiques (MRAMs), dans lesquelles l'information binaire est stockée dans l'orientation relative des couches. L'information est alors lue par une mesure GMR/TMR. L'écriture se fait par retournement de l'aimantation de la couche la plus sensible. Ceci peut se faire par plusieurs techniques, telles que l'application d'un champ via un fil électrique proche, mais l'utilisation du STT pour retourner la couche libre présente cet avantage que l'écriture et la lecture se font par le même effet. Ces structures de RAM trouvent déjà des applications à l'échelle industrielle pour des applications niches, et visent à remplacer les DRAMs et SRAMs. En effet bien que le gain en performances qu'elles apportent face aux RAMs actuelles ne semble pas justifier l'investissement technologique requis par leur

complexité, car ces structures impliquent le dépôt et la gravure d'un nombre relativement élevé de couches, elles présentent d'autres avantages telles que leur résistance aux radiations et leur non-volatilité[66][70]. Dans le cas des nano-oscillateurs à transfert de spin (STNOs), l'amortissement est compensé exactement afin d'obtenir des précessions entretenues de l'aimantation, comme un composant actif joue un rôle de résistance négative dans un circuit RLC. Ces précessions entretenues de l'aimantation sont converties en un signal électrique oscillant via l'effet de GMR. Ces oscillateurs sont particulièrement intéressants pour leurs propriétés non linéaires, leur compacité face aux oscillateurs électroniques classiques, leur intégrabilité aux technologies CMOS, leur accordabilité et leur agilité en fréquence; mais la faible puissance du signal émis due à leurs dimensions intrinsèquement nanoscopiques, ainsi que la largeur de raie, qui se voit augmentée par la nonlinéarité, limitent les applications à l'état de prototypes. Une des stratégies pour améliorer ces propriétés consiste à synchroniser plusieurs tels oscillateurs pour augmenter le volume oscillant, et par là même augmenter la puissance du signal émis et réduire la sensibilité au bruit thermique. Une application plus prospective est celle des architectures de calcul bioinspirées que sont les mémoires associatives. En effet ces dernières bénéficient de la capacité accrue qu'ont les STNOs, de par leur non-linéarité, à se synchroniser entre eux, pour reproduire au niveau de la couche matérielle, plutôt que la couche logicielle, une architecture s'inspirant de l'architecture hautement interconnectée des neurones dans le cerveau.

Cette thèse aborde ces deux aspects, à savoir un aspect appliqué basé sur l'effet GMR uniquement, avec le développement d'un prototype de capteur magnétique de position, et visant à la réalisation d'un produit fini obéissant à un cahier des charges précis; et un aspect plus prospectif avec l'étude de la synchronisation de STNOs, qui utilisent l'effet complémentaire de la GMR, à savoir le couple de transfert de spin. Ces deux volets sont basés sur une même structure de vanne de spin.

## Capteurs magnétiques

Les capteurs magnétiques basés sur l'effet de GMR sont bien établis sur le marché dans une grande variété d'applications [23]. L'application la plus spectaculaire est pour le stockage d'information avec les têtes de lecture de disque durs. Mais on les trouve également dans d'autres applications, qu'il s'agisse de mesure de courant électrique, de contrôle non destructif, de magnétœncéphalographie...

L'application qui est développée dans cette thèse est celle d'un capteur de proximité utilisé pour des mesures de pression via la déformation d'une membrane élastique. Le champ magnétique basse fréquence émis par une bobine est réfléchi par la membrane conductrice, avec une amplitude dépendant de leur séparation. Cette membrane se déforme linéairement sous l'effet d'une pression uniforme, et la mesure de ce déplacement fournit une mesure de la pression. Les dispositifs expérimentaux permettent d'évaluer la dépendance du signal mesuré par rapport à la séparation entre le capteur et la surface métallique réfléchissante, avec une précision micrométrique, grâce à un positionneur 3 axes; de mesurer directement à l'aide d'un capteur laser et d'une jauge de pression com-

merciale, la déformation de la membrane métallique soumise à une pression grâce à un système hydraulique, pour des pressions allant jusqu'à 250 bars; enfin d'évaluer directement un prototype du capteur. Le choix du matériau de la membrane est crucial, car il doit autoriser une déformation pour permettre une sensibilité suffisante sur une gamme de mesure étendue, mais les déformations doivent rester dans le domaine élastique du matériau pour assurer une répétabilité de la mesure. L'endurance de la membrane a donc été évaluée pour chaque matériau testé pour un grand nombre de cycles de déformation, et à différentes températures.

Comme le capteur GMR est déposé en même temps que la bobine, les couches magnétiques sont nécessairement déposées parallèles au plan de la bobine. Le capteur est donc sensible à la composante du champ contenue dans le plan de la bobine. Cette composante est maximale à proximité des nappes de courant qui constituent la bobine. Les bobines ont été choisies carrées, afin d'occuper un maximum de surface disponible et augmenter la valeur du champ créé. Des calculs analytiques basés sur la loi de Biot et Savart et des simulations sous COMSOL permettent de confirmer la dépendance spatiale en $1/d^4$ de la composante planaire du champ à une distance $d$ de la nappe de courant, lorsque cette distance est supérieures aux dimensions de la bobine, permettant de valider en partie les résultats de COMSOL. Le comportement de la membrane est pour l'instant assimilé à celui de son point le plus proche du capteur.

Les GMR sont montées en ponts de Wheatstone. Chaque GMR a une structure de joug, ce qui est une stratégie classique pour confiner les parois de domaines aux extrémités de la structure et réduire l'hystérèse du cycle de magnétorésistance. La bobine et le capteur sont alimentés par des courants alternatifs à deux fréquences différentes, et le signal est directement démodulé dans la GMR pour amener à la tension de sortie à une troisième fréquence. Cette méthode permet de s'affranchir du bruit en $1/f$. Les premières mesures expérimentales sur un système complet ont permis de déterminer une résolution de 2 bars en l'absence de traitement des signaux, et qui doit être améliorée par une mesure en gradiomètre pour annuler l'effet des vibrations mécaniques qui affectent actuellement le capteur. Celle-ci peut être réalisée en comparant alors les mesures entre plusieurs capteurs situés en des points différents de la bobine. On devrait alors atteindre une résolution de 0,5 bar sur la gamme de mesure allant de 0 à 250 bars.

## Oscillateurs à transfert de spin

Les STNOs ont donné lieu à des prototypes pour l'émission de signal hyperfréquences [39], sa détection notamment grâce à l'effet de diode de spin [63], et son traitement [57][58][42].

Les STNOs sont un exemple particulier d'oscillateurs non-linéaires, ou non-isochrones, c'est-à-dire dont la fréquence des oscillations dépend de leur puissance. Les équations décrivant l'évolution temporelle de la phase, sont alors couplées à des équations sur la dynamique de la puissance des oscillations, décrivant le retour de l'amplitude vers le cycle limite. Le cycle limite est déterminé par l'équilibre entre les amortissements positif (dû à la dissipation) et négatif dû à un élément actif. Ce couplage entre phase et amplitude

(ou de façon équivalente, entre fréquence et puissance) est caractérisé par un paramètre adimensionné $\nu$, qui permet de restreindre le système de deux équations sur la phase et l'amplitude de l'oscillateur à une seule équation sur la phase, selon le modèle développé dans [21]. Ce modèle permet de décrire l'élargissement dû aux non-linéarité de la bande de synchronisation d'un oscillateur à un signal externe, ou de deux oscillateurs entre eux, ainsi que la sensibilité accrue au bruit.

Depuis la première mesure directe d'un signal électrique oscillant dans une vanne de spin en 2003 [14], il a été démontré expérimentalement qu'il était possible de synchroniser efficacement un STNO à un signal externe, qu'il s'agisse d'un courant [111] ou d'un champ [114] hyperfréquence. Il a également été démontré qu'il était possible de synchroniser mutuellement plusieurs STNOs via des ondes de spin [116, 117] dans un matériau commun, via un couplage électrique [121] et via le champ dipolaire rayonné [119]. Il a récemment été démontré qu'il était possible de synchroniser mutuellement jusqu'à 9 STNOs [97]. A présent certaines équipes commencent à envisager des structures plus complexes, notamment dans le cadre d'architectures de calcul bio-inspirées. Dans notre étude nous faisons appel aux deux mécanismes, celui de synchronisation à un signal externe et celui de synchronisation mutuelle [69, 68].

Les STNOs se déclinent en fait en plusieurs familles. Dans le cas d'une vanne de spin le moment angulaire permettant de compenser les pertes est apporté par un courant électrique polarisé en spin; dans le cas d'un courant à effet Hall de spin cela se fait par un courant de spin pur créé dans un matériau à fort angle de spin. Dans le cas des STVO (Spin Torque Vortex Oscillators), la distribution de l'aimantation au sein de la même couche magnétique n'est pas homogène mais forme un vortex, c'est-à-dire une circulation des spins individuels dans le plan autour d'une singularité hors du plan qu'est le cœur de vortex. Ces STVOs présentent l'avantage d'avoir une largeur de raie relativement faible, du fait de leur plus faible nonlinéarité, et le gain en puissance d'émission et cohérence spectrale résultant de la synchronisation mutuelle de plusieurs STVOs ne se fait ni au prix de la nonlinéarité ni de l'agilité en fréquence, du fait de la forte dépendence en courant de la fréquence d'émission. Le mode d'intérêt ici est le mode gyrotropique, pour lequel le cœur de vortex se déplace autour de sa position d'équilibre. La dynamique du cœur de vortex est alors décrite par l'équation de Thiele. Il peut être démontré que ce modèle entre dans le cadre du modèle de l'oscillateur non-linéaire [150]. L'interaction entre oscillateurs peut être modélisée par une interaction dipôle-dipôle [119].

### Dispositif expérimental

Nous étudions donc des paires de nanopilliers Py (15nm)/Cu (10nm)/Py (4nm) circulaires de diamètres égaux (200nm ou 400nm) et pour des séparations variées. La géométrie de l'échantillon impose un état vortex dans les couches magnétiques. L'originalité de ce travail réside dans la présence d'une antenne microondes au-dessus de la paire de STVO, capable de générer un champ magnétique hautes fréquences, ce qui permet de simuler l'action d'un troisième oscillateur "idéal". Alternativement ce champ hyperfréquence peut être utilisé pour des caractérisations de résonnance ferromagnétique en tension. Le champ

magnétique hyperfréquence excite la dynamique de l'aimantation des couches magnétiques à une certaine fréquence, et le signal se mesure par un changement de résistance qui se mesure par une variation de tension. Comme le signal demeure très faible, car les ratios GMR sont typiquement de quelques pourcent, ce signal est amplifié et est observé directement sur un analyseur de spectre pour un signal auto-oscillant, ou sur un lock-in pour des mesures de résonance ferromagnétique.

**Résultats expérimentaux**

Un vortex magnétique est caractérisé par sa polarité, qui indique l'orientation du cœur par rapport au champ extérieur, et sa chiralité. La chiralité peut être manipulée en jouant sur le signe du courant de polarisation, qui impose le sens de rotation du champ d'Oersted-Ampère, ce que nous mettons en évidence par des mesures de magnétorésistance en balayant l'intensité du courant de polarisation continu. À fort courant, la chiralité du vortex est imposée par les paramètres extérieurs. Lorsque le courant change de polarisation, il impose sa chiralité plus facilement au vortex de la couche fine qu'à celui de la couche épaisse. Les deux retournements de chiralité ont lieu à des courants différents, ce qui donne lieu à deux sauts de résistance. En effet lorsque les chiralités deviennent antiparallèles, la résistance augmente brusquement, puis retrouve une valeur plus basse tout aussi soudainement lorsque les deux chiralités sont à nouveau parallèles. Cette mesure permet de nous assurer de l'existence d'un vortex dans chacune des couches magnétiques.

Étant donné qu'il n'est possible d'observer un signal d'auto-oscillations que si les vortex de la couche épaisse et de la couche fine sont opposées, et que la dynamique du STVO est dominée par celle du vortex de la couche épaisse, du fait de son volume et de la polarisation du courant, dans la suite on fera référence uniquement à la polarité du vortex de la couche épaisse. D'autre part les intensités utilisées dans les mesures dynamiques imposent la chiralité des deux vortex, comme observé dans les mesures du paragraphe précédent. Ainsi on distingue les polarités parallèles et antiparallèles au champ magnétique externe dans le cas d'un STVO unique.

Dans le cas d'un STVO unique, l'observation du signal d'auto-oscillations permet de vérifier les lois de dépendence de la fréquence en champ, en courant et selon le diamètre du pilier. Une analyse plus complète de l'évolution de la largeur de raie et de la puissance intégrée permet de reproduire les observations de [101], qui décrit une puissance intégrée constante du signal et explique les oscillations de la largeur de raie à mesure que le champ de polarisation augmente par des transferts d'énergie entre modes, conduisant à une perte de cohérence dea auto-oscillations. Cette même analyse de dépendence en courant de la fréquence permet d'observer une augmentation de la puissance du signal d'auto-oscillations au-delà de la densité de courant seuil, jusqu'à ce qu'elle sature. La dépendence en courant de la fréquence reste quand à elle linéaire. L'observation par résonance ferromagnétique (FMR) en tension des mêmes échantillons permet de suivre les modes d'oscillations même lorsqu'ils sont amortis, sans se limiter aux modes auto-oscillants. De cette façon on peut observer la dépendence en champ et en courant du mode dominé par la couche épaisse sur une gamme plus étendue, et observer le retourne-

ment hystérétique de la polarité de la couche épaisse.

Quant à la synchronisation d'un STVO individuel à un champ magnétique radiofréquence externe, nous reproduisons sur un nanopilier de 400nm de diamètre les mesures effectuées sur un pilier de 200nm de diamètre dans [115]. On observe une bande de synchronisation de 50MHz pour une amplitude du champ radiofréquences de 0.4mT, soit 10% de la fréquence d'auto-oscillations. En outre on observe des événements de synchronisation lorsque la fréquence $f_e$ du signal externe vaut un multiple entier de la fréquence d'auto-oscillations $f_0$ [114] .

Dans le cas d'une paire de STVOs, on peut en jouant sur les paramètres de champ externe et de courant de polarisation préparer un état où les deux STVOs on des polarités opposées. Leurs dépendences en champs ont alors des pentes opposées. Il est donc possible de faire se croiser les deux signaux en balayant le champ continu. Lorsque les fréquences des deux STVOs sont suffisamment proches, l'un des deux STVOs effectue un saut en fréquence pour se synchroniser à l'autre STVO (voir figure E.2.a). Dans le régime passif (pas d'auto-oscillations), la même procédure permet d'observer par résonance ferromagnétique un anticroisement des signaux en lieu de croisement. Cet anticroisement permet d'identifier un mode optique et un mode accoustique (voir figure E.1). Cette mesure reproduit les résultats obtenus pour une paire de disques magnétiques dans l'état saturé, mesurés par une technique MRFM. Les fréquences des modes de chaque disques étaient alors modifiés par le champ rayonné par la bille magnétique à l'extrémité de la pointe MRFM. Ce même champ rayonné rendait impossible la mesure d'un anticroisement dans l'état vortex.

Lorsque la paire de STVOs est préparée dans un état où les fréquences naturelles d'auto-oscillations sont trop éloignées pour qu'ils puissent se synchroniser mutuellement, ils n'en restent pas moins couplés via le champ magnéto-dipolaire du fait de leur proximité. Ce couplage est révélé lorsqu'on balaie la fréquence d'un signal externe à proximité des fréquences d'auto-oscillations (voir figure E.2). En effet si cette fréquence est suffisamment proche de celle d'un des deux oscillateurs, ce dernier se verrouille en phase au signal externe, mais cet événement affecte la dynamique de l'autre STVO via leur couplage mutuel. En outre en intégrant numériquement un modèle analytique similaire au modèle d'Adler développé dans [21], on peut reproduire ces événements et extraire quantitativement les paramètres du couplage en amplitude et en phase, ainsi que les paramètres non-linéaires. En particulier on note que dans la configuration où les cœurs de vortex sont antiparallèles, le couplage est typiquement deux à trois fois plus intense par rapport à la configuration parallèle.

Lorsque les deux STVOs sont mutuellement synchronisés, un seul signal d'auto-oscillations est visible. D'après le modèle précédent, les deux STVOs se comportent alors comme un seul STVO. On peut observer la signature de la synchronisation mutuelle en isolant fréquentiellement chaque STVO, ce qui peut se faire en jouant sur leurs polarités individuelles, et en comparant ces signaux au signal unique qu'on observe lorsqu'on met les deux en présence. Le signal est alors beaucoup plus étroit fréquentiellement que ceux des STVOs isolés, et la puissance intégrée est strictement supérieure à la somme des signaux

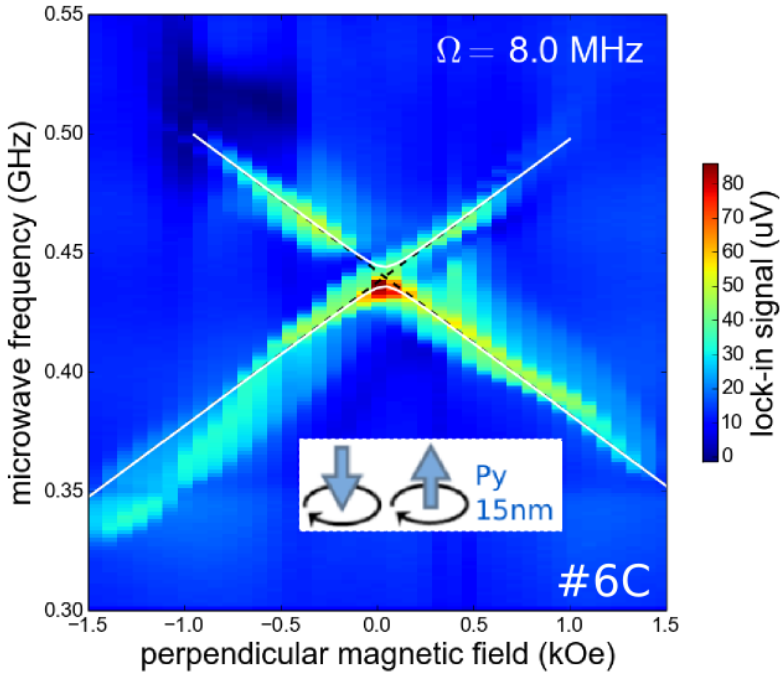


Fig. E.1 *Anticroisement mesuré par résonance ferromagnétique pour une paire de STVOs adjacents (nanopiliers de 400nm de diamètre séparés de 200nm, échantillon 6C) dont les fréquences se rapprochent linéairement l'une de l'autre à mesure que l'on varie le champ magnétique externe. La courbe théorique blanche est calculée à partir des formules d'hybridation (équations (5.22)) en supposant la dépendence linéaire en champ de la fréquence.*

isolés.

À mesure que l'on balaye la fréquence de la source externe à des fréquences proches du signal observé, il apparaît que le signal d'auto-oscillations s'étale sur le spectre localement pour une fréquence particulière de la source externe (see figure E.3), et ce sur une bande de fréquences qui augmente avec la puissance de la source externe. Cet effet est local puisque le signal d'auto-oscillations est restauré avant de se synchroniser à la source externe. Pour expliquer ces effets il est nécessaire d'inclure les équations sur la dynamique de l'amplitude issues du modèle de Thiele, pour tenir compte de l'évolution des amplitudes, ce que ne permet pas le modèle de phases dérivé dans [21]. On démontre que ceci équivaut à introduire de l'inertie dans le système. La différence de phase entre les deux oscillateurs peut dans cette mesure être décrite comme une bille dans un puit de potentiel. Il est alors possible de mettre en évidence l'existence d'une fréquence itrinsèque pour de petites déviations du système autour de l'équilibre, prédite dans [147, 166, 167], qui peut s'écrire comme $\Lambda = 2\sqrt{\nu\Omega\Gamma_p}$ dans une première approximation, où $\nu$ est la non-linéarité, $\Omega$ l'amplitude du couplage et $\Gamma_p$ le taux de relaxation des fluctuations d'amplitude. Cette fréquence peut être excitée de façon résonante, conduisant à la destruction de la synchronisation au-delà d'un certain seuil, qui reste faible devant l'amplitude du couplage. Cet explication est soutenue par l'existence d'un effet symmétrique observable sur certaines

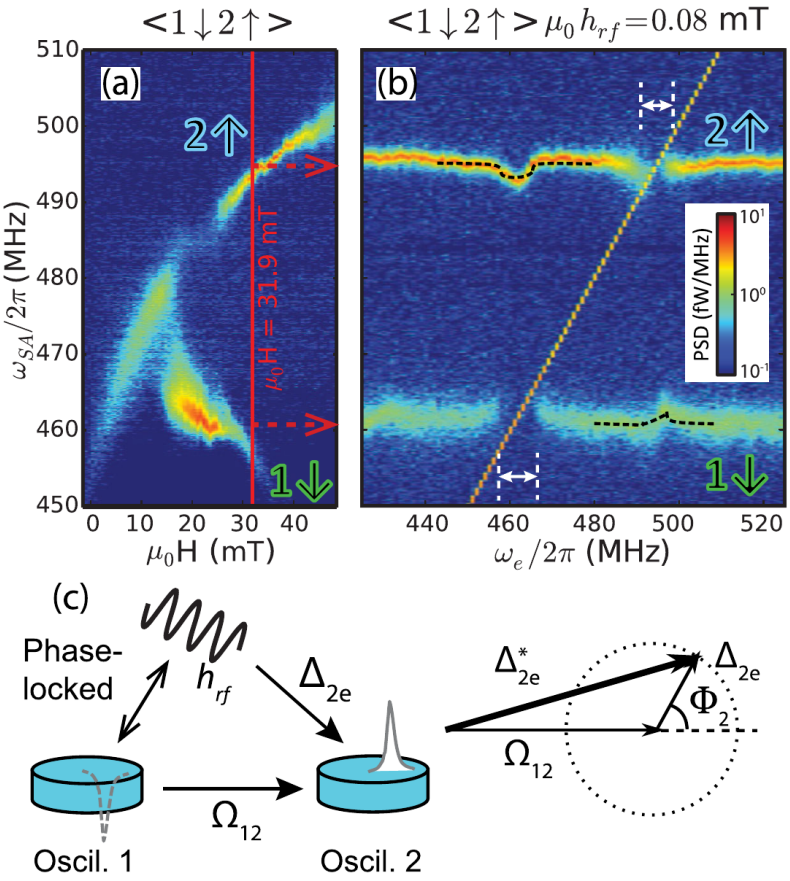


Fig. E.2 *Échantillon #6C. (a) Point de fonctionnement dans l'état* $<1\downarrow 2\uparrow>$ *pour l'étude microondes (ligne rouge verticale). (b) Spectres d'auto-oscillations en fonction de la fréquence du champ microondes pour* $H = 319$ *Oe, comme indiqué en (a). Le signal de la source est visible sous la forme d'un étroit trait oblique. La puissance du signal micro-ondes est de* $-23$ *dBm, ce qui correspond à un champ* $h_{rf} = 0.8$ *Oe. Les flèches blanches indiquent les bande de verrouillage de phase. Les coubes en pointillés noirs sont les résultats de l'éq. (7.8) ajustée aux données expérimentales. (c) Diagramme vecteur de* $\Omega_{12}$ *et* $\Delta_{2e}$ *quand l'oscillateur 1 est verouillé en phase au champ micro-ondes.*

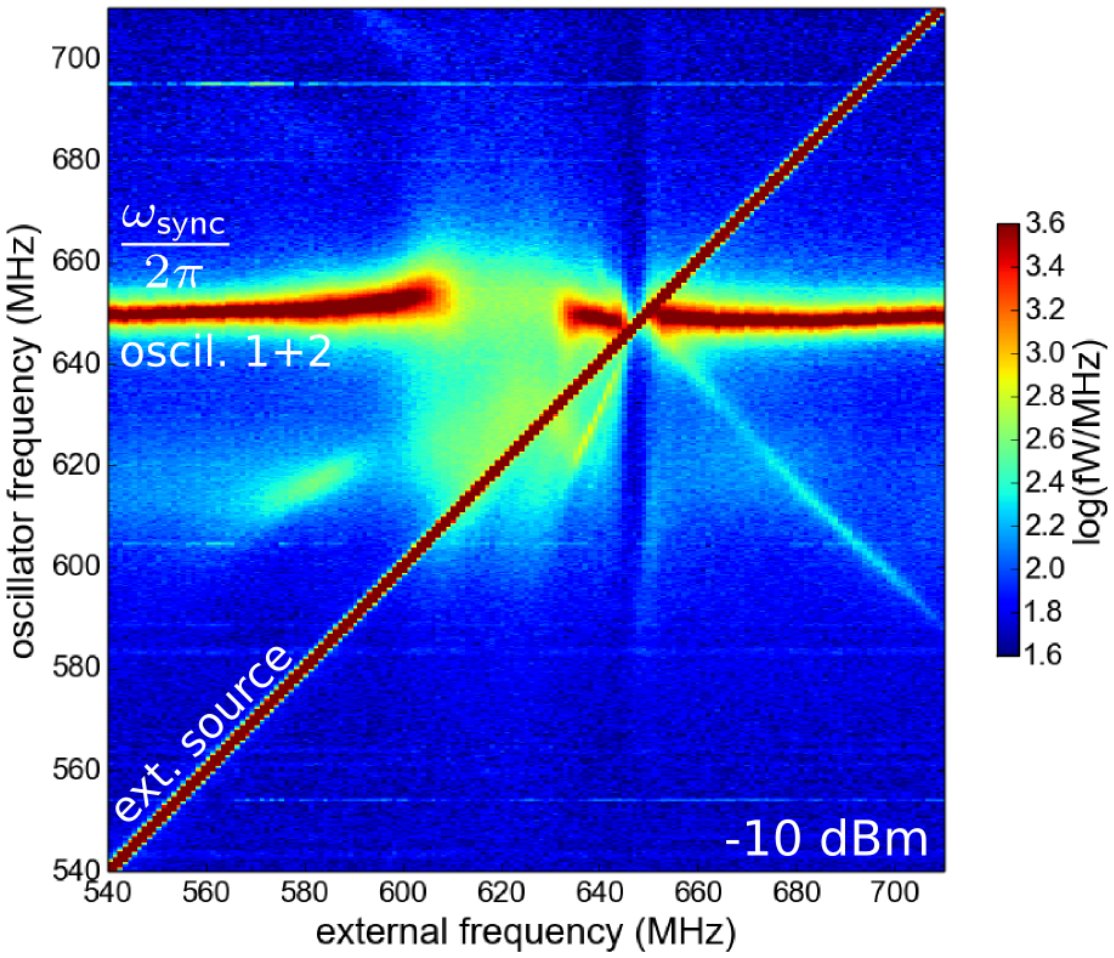


Fig. E.3 *Les deux STVOs sont mutuellement synchronisés, de sorte qu'un seul signal d'auto-oscillations es visible à 647MHz. La fréquence de la source externe est balayée dans le voisinage du signal d'auto-oscillation avec une puissance d'entrée de -10dBm. Le signal externe est clairement visible sur la diagonale montante du diagramme, ainsi que la fréquence de battement résultant du mélange avec le signal d'auto-oscillation. Le signal externe peut être considéré comme relativement faible étant donné que la bande de verrouillage de phase est assez étroite. La particularité remarquable est l'effet de la source lorsqu'elle est située autour de 618MHz, qui diminue fortement le signal d'auto-oscillation qui se trouve quant à lui à 647MHz. Ici* $I_{dc} = 40mA$ *et* $H_{dc} = 644Oe$.

données.

### Simulations

Pour mieux comprendre les implications de ces non-linéarités, nous avons entrepris de simuler ce système en intégrant numériquement les équations de Thiele couplées. Dans un premier temps nous reproduisons les résultats expérimentaux. En particulier dans le cas de deux oscillateurs synchronisés, nous démontrons l'existence et le caractère résonant de cette fréquence intrinsèque par l'apparition de deux bandes latérales en présence de bruit, et par l'apparition de deux pics de résonance de part et d'autre du pic d'auto-oscillations lorsque le système est excité par un signal externe de très faible amplitude. Lorsque la synchronisation est détruite et que le signal d'auto-oscillations s'étale spectralement, les variables ont un comportement chaotique. Par ailleurs étant donné que l'on a accès directement aux variables, il est possible de s'intéresser à des considérations de stabilité. Ainsi deux oscillateurs sont synchronisés si leur différence de phase est bornée dans le temps. À partir de ce critère il est possible de construire un diagramme de stabilité, qui permet de définir des zones où les deux oscillateurs sont mutuellement synchronisés, sont individuellement synchronisés au signal externe, et où le chaos prédomine. Dans des considérations de stabilité, l'analyse matricielle du système permet de déterminer numériquement les états stables du système, et l'évolution de cette fréquence intrinsèque à mesure qu'on varie un des paramètres.

Ces derniers résultats sont représentés dans le diagramme de stabilité en figure E.4. À chaque fois les deux auto-oscillateurs sont mutuellement synchronisés, puis on allume la source externe au début de la simulation. Deux éléments (dans l'ensemble formé par les trois éléments que sont les auto-oscillateurs 1 et 2 et la source externe) sont considérés comme synchronisés si après un régime transitoire de leur différence de phase reste bornée.

Ces travaux sont plus une ouverture vers d'autres manières d'appréhender le problème qu'une conclusion, en introduisant les analyses de stabilité, la théorie des bifurcations... Un des intérêts de ces derniers résultats est qu'ils sont généralisables à n'importe que système d'oscillateurs non-linéaires, et ne se limitent pas aux oscillateurs magnétiques. Ces résultats sont donc transférables aux STNOs en général, mais en font également une plate-forme permettant de vérifier expérimentalement les prédiction théoriques sur les propriétés des oscillateurs non-linéaires.

## Conclusion

En conclusion, nous avons exploré toute la gamme d'applications qu'offre la spintronique, à l'image du slogan du CEA: "De la recherche fondamentale à l'industrie". Notre étude démontre que la synchronisation entre deux oscillateurs à transfert de spin donne lieu à une dynamique très riche, et ces résultats ne se limitent pas aux oscillateurs magnétiques.

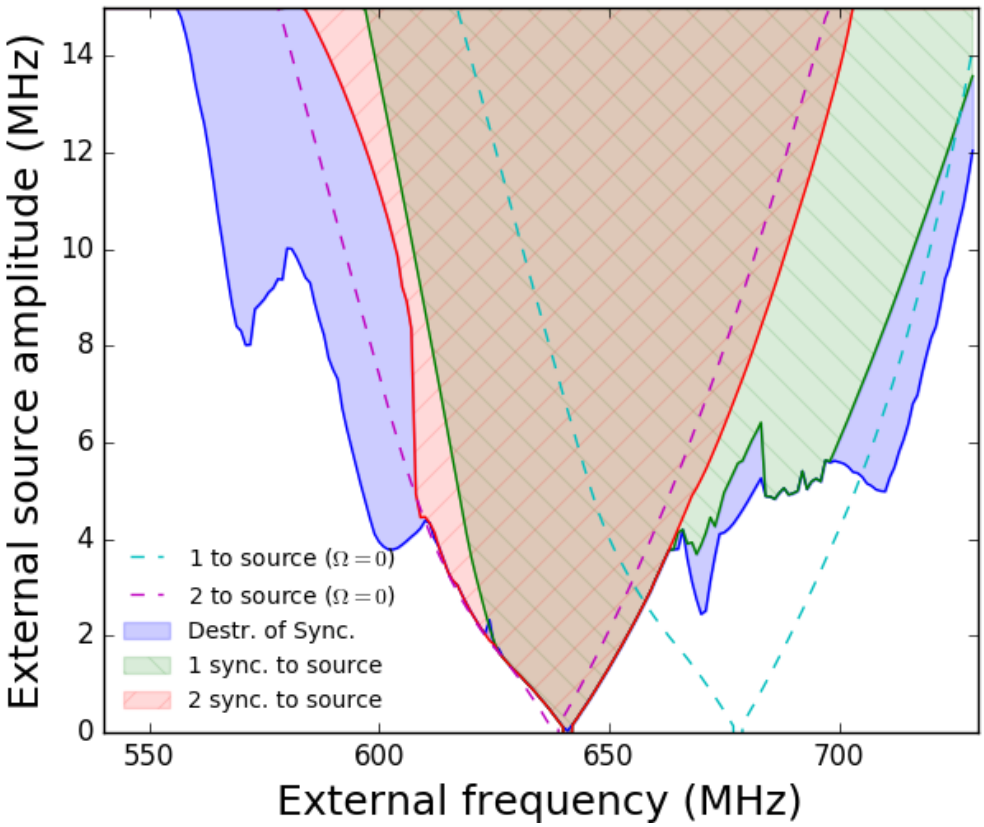


Fig. E.4 *Diagramme de stabilité reportant les motifs de synchronisation stables des deux auto-oscillateurs non-linéaires mutuellement couplés et excités par une source externe, dans un plan paramétré par la fréquence de la source externe en abscisses et son amplitude en ordonnées. "src" se lit "source" et "DoS" se lit "destruction de synchronisation" (en anglais "Destruction of Synchronisation")*

# Bibliography

[1] Nevill Francis Mott. The electrical conductivity of transition metals. In *Proceedings of the Royal Society of London A: Mathematical, Physical and Engineering Sciences*, volume 153, pages 699–717. The Royal Society, 1936.

[2] Nicolas Locatelli. *Dynamique par transfert de spin et synchronisation d'oscillateurs couplés à base de vortex magnétiques*. PhD thesis, Paris 11, 2012.

[3] Mario Norberto Baibich, Jean Marc Broto, Albert Fert, F Nguyen Van Dau, Frédéric Petroff, P Etienne, G Creuzet, A Friederich, and J Chazelas. Giant magnetoresistance of (001) fe/(001) cr magnetic superlattices. *Physical review letters*, 61(21):2472, 1988.

[4] Grünberg Binasch, Peter Grünberg, F Saurenbach, and W Zinn. Enhanced magnetoresistance in layered magnetic structures with antiferromagnetic interlayer exchange. *Physical review B*, 39(7):4828, 1989.

[5] Romain Lebrun. *Vortex magnétiques couplés dans des oscillateurs à transfert de spin: de l'excitation résonante à la synchronisation mutuelle*. PhD thesis, Université Paris-Saclay, 2015.

[6] T Valet and A Fert. Theory of the perpendicular magnetoresistance in magnetic multilayers. *Physical Review B*, 48(10):7099, 1993.

[7] B Dieny, VS Speriosu, BA Gurney, SSP Parkin, DR Wilhoit, KP Roche, S Metin, DT Peterson, and S Nadimi. Spin-valve effect in soft ferromagnetic sandwiches. *Journal of Magnetism and Magnetic Materials*, 93:101–104, 1991.

[8] Robert Meservey and PM Tedrow. Spin-polarized electron tunneling. *Physics reports*, 238(4):173–243, 1994.

[9] M. Julliere. Tunneling between ferromagnetic films. *Physics Letters A*, 54(3):225 – 226, 1975.

[10] Jagadeesh Subbaiah Moodera, Lisa R Kinder, Terrilyn M Wong, and R Meservey. Large magnetoresistance at room temperature in ferromagnetic thin film tunnel junctions. *Physical review letters*, 74(16):3273, 1995.

[11] Terunobu Miyazaki and N Tezuka. Giant magnetic tunneling effect in fe/al2o3/fe junction. *Journal of Magnetism and Magnetic Materials*, 139(3):L231–L234, 1995.

[12] Daniel C Ralph and Mark D Stiles. Spin transfer torques. *Journal of Magnetism and Magnetic Materials*, 320(7):1190–1216, 2008.

[13] Arne Brataas, Andrew D Kent, and Hideo Ohno. Current-induced torques in magnetic materials. *Nature materials*, 11(5):372, 2012.

[14] S Il Kiselev, JC Sankey, IN Krivorotov, NC Emley, RJ Schoelkopf, RA Buhrman, and DC Ralph. Microwave oscillations of a nanomagnet driven by a spin-polarized current. *Nature*, 425(6956):380–383, 2003.

[15] Lev Landau and Evgeny Lifshitz. On the theory of the dispersion of magnetic permeability in ferromagnetic bodies. *Phys. Z. Sowjetunion*, 8(153):101–114, 1935.

[16] TL Gilbert. A lagrangian formulation of the gyromagnetic equation of the magnetization field. *Phys. Rev.*, 100:1243, 1955.

[17] Alexander G Gurevich and Gennadii A Melkov. *Magnetization oscillations and waves*. CRC press, 1996.

[18] John C Slonczewski. Current-driven excitation of magnetic multilayers. *Journal of Magnetism and Magnetic Materials*, 159(1-2):L1–L7, 1996.

[19] L Berger. Emission of spin waves by a magnetic multilayer traversed by a current. *Physical Review B*, 54(13):9353, 1996.

[20] AV Khvalkovskiy, KA Zvezdin, Ya V Gorbunov, V Cros, J Grollier, A Fert, and AK Zvezdin. High domain wall velocities due to spin currents perpendicular to the plane. *Physical review letters*, 102(6):067206, 2009.

[21] Andrei Slavin and Vasil Tiberkevich. Nonlinear auto-oscillator theory of microwave generation by spin-polarized current. *Magnetics, IEEE Transactions on*, 45(4):1875–1918, 2009.

[22] T. Chen, R. K. Dumas, A. Eklund, P. K. Muduli, A. Houshang, A. A. Awad, P. Dürrenfeld, B. G. Malm, A. Rusu, and J. Åkerman. Spin-torque and spin-hall nano-oscillators. *Proceedings of the IEEE*, 104(10):1919–1945, Oct 2016.

[23] Paolo Campiglio and Claude Fermon. Large-volume applications of spin electronics-based sensors. *Nanomagnetism: Applications and Perspectives*, 2016.

[24] Candid Reig, Susana Cardoso, and Subhas Chandra Mukhopadhyay. Giant magnetoresistance (gmr) sensors. *SSMI6*, pages 157–180, 2013.

[25] Myriam Pannetier, Claude Fermon, Gerald Le Goff, Juha Simola, and Emma Kerr. Femtotesla magnetic field measurement with magnetoresistive sensors. *Science*, 304(5677):1648–1650, 2004.

[26] Claude Fermon and Marcel Van de Voorde. *Nanomagnetism: Applications and Perspectives*. John Wiley & Sons, 2016.

[27] Myriam Pannetier-Lecoeur, C Fermon, Paolo Campiglio, Quentin Herreros, and Guenaelle Jasmin-Lebras. Spin electronics based magnetic sensors for biomagnetic measurements. In *Magnetoencephalography*, pages 1001–1005. Springer, 2014.

[28] Francesca Barbieri, Vincent Trauchessec, Laure Caruso, Josué Trejo-Rosillo, Bartosz Telenczuk, Elodie Paul, Thierry Bal, Alain Destexhe, Claude Fermon, Myriam Pannetier-Lecoeur, et al. Local recording of biological magnetic fields using giant magneto resistance-based micro-probes. *Scientific reports*, 6:39330, 2016.

[29] J Loureiro, R Ferreira, S Cardoso, PP Freitas, J Germano, C Fermon, G Arrias, M Pannetier-Lecoeur, F Rivadulla, and J Rivas. Toward a magnetoresistive chip cytometer: Integrated detection of magnetic beads flowing at cm/s velocities in microfluidic channels. *Applied Physics Letters*, 95(3):034104, 2009.

[30] S. X. Wang and G. Li. Advances in giant magnetoresistance biosensors with magnetic nanoparticle tags: Review and outlook. *IEEE Transactions on Magnetics*, 44(7):1687–1702, July 2008.

[31] R. Wood. The feasibility of magnetic recording at 1 terabit per square inch. *IEEE Transactions on Magnetics*, 36(1):36–42, Jan 2000.

[32] ©2017 Seagate Technology LLC. Seagate continues to lead as hamr technology advances. web. last accessed August 21st, 2017.

[33] Mark H Kryder, Edward C Gage, Terry W McDaniel, William A Challener, Robert E Rottmayer, Ganping Ju, Yiao-Tee Hsia, and M Fatih Erden. Heat assisted magnetic recording. *Proceedings of the IEEE*, 96(11):1810–1835, 2008.

[34] R. Wood, M. Williams, A. Kavcic, and J. Miles. The feasibility of magnetic recording at 10 terabits per square inch on conventional media. *IEEE Transactions on Magnetics*, 45(2):917–923, Feb 2009.

[35] BD Terris, T Thomson, and G Hu. Patterned media for future magnetic data storage. *Microsystem technologies*, 13(2):189–196, 2007.

[36] Rie Sato, Kiwamu Kudo, Tazumi Nagasawa, Hirofumi Suto, and Koichi Mizushima. Simulations and experiments toward high-data-transfer-rate readers composed of a spin-torque oscillator. *IEEE Transactions on magnetics*, 48(5):1758–1764, 2012.

[37] Jian-Gang Zhu and Yiming Wang. Microwave assisted magnetic recording utilizing perpendicular spin torque oscillator with switchable perpendicular electrodes. *IEEE Transactions on Magnetics*, 46(3):751–757, 2010.

[38] PM Braganca, BA Gurney, BA Wilson, JA Katine, S Maat, and JR Childress. Nanoscale magnetic field detection using a spin torque oscillator. *Nanotechnology*, 21(23):235202, 2010.

[39] Patrick Villard, Ursula Ebels, Dimitri Houssameddine, Jordan Katine, Daniele Mauri, Bertrand Delaet, Pierre Vincent, Marie-Claire Cyrille, Bernard Viala, Jean-Philippe Michel, et al. A ghz spintronic-based rf oscillator. *IEEE Journal of solid-state circuits*, 45(1):214–223, 2010.

[40] M Quinsat, Daria Gusakova, JF Sierra, JP Michel, Dimitri Houssameddine, B Delaet, M-C Cyrille, Ursula Ebels, Bernard Dieny, LD Buda-Prejbeanu, et al. Amplitude and phase noise of magnetic tunnel junction oscillators. *Applied Physics Letters*, 97(18):182507, 2010.

[41] E Grimaldi, R Lebrun, A Jenkins, A Dussaux, J Grollier, V Cros, A Fert, H Kubota, K Yakushiji, A Fukushima, et al. Spintronic nano-oscillators: Towards nanoscale

and tunable frequency devices. In *Frequency Control Symposium (FCS), 2014 IEEE International*, pages 1–6. IEEE, 2014.

[42] B Georges, J Grollier, V Cros, A Fert, A Fukushima, H Kubota, K Yakushijin, S Yuasa, and K Ando. Origin of the spectral linewidth in nonlinear spin-transfer oscillators based on mgo tunnel junctions. *Physical Review B*, 80(6):060404, 2009.

[43] D Houssameddine, SH Florez, JA Katine, J-P Michel, U Ebels, D Mauri, O Ozatay, B Delaet, B Viala, L Folks, et al. Spin transfer induced coherent microwave emission with large power from nanoscale mgo tunnel junctions. *Applied Physics Letters*, 93(2):022505, 2008.

[44] D Houssameddine, U Ebels, B Delaët, B Rodmacq, I Firastrau, F Ponthenier, M Brunet, C Thirion, J-P Michel, L Prejbeanu-Buda, et al. Spin-torque oscillator using a perpendicular polarizer and a planar free layer. *Nature materials*, 6(6):441, 2007.

[45] Stefano Bonetti, Pranaba Muduli, Fred Mancoff, and Johan Åkerman. Spin torque oscillator frequency versus magnetic field angle: The prospect of operation beyond 65 ghz. *Applied Physics Letters*, 94(10):102507, 2009.

[46] Ran Cheng, Di Xiao, and Arne Brataas. Terahertz antiferromagnetic spin hall nano-oscillator. *Physical review letters*, 116(20):207603, 2016.

[47] V Baltz, A Manchon, M Tsoi, T Moriyama, T Ono, and Y Tserkovnyak. Antiferromagnetism: the next flagship magnetic order for spintronics? *arXiv preprint arXiv:1606.04284*, 2016.

[48] A Dussaux, B Georges, J Grollier, V Cros, AV Khvalkovskiy, A Fukushima, M Konoto, H Kubota, K Yakushiji, S Yuasa, et al. Large microwave generation from current-driven magnetic vortex oscillators in magnetic tunnel junctions. *Nature communications*, 1:8, 2010.

[49] Mark W Keller, Anthony B Kos, Thomas J Silva, William H Rippard, and Matthew R Pufall. Time domain measurement of phase noise in a spin torque oscillator. *Applied Physics Letters*, 94(19):193105, 2009.

[50] Shingo Tamaru, Hitoshi Kubota, Kay Yakushiji, Shinji Yuasa, and Akio Fukushima. Extremely coherent microwave emission from spin torque oscillator stabilized by phase locked loop. *Scientific reports*, 5, 2015.

[51] R Lebrun, A Jenkins, A Dussaux, N Locatelli, S Tsunegi, E Grimaldi, H Kubota, P Bortolotti, K Yakushiji, J Grollier, et al. Understanding of phase noise squeezing under fractional synchronization of a nonlinear spin transfer vortex oscillator. *Physical review letters*, 115(1):017201, 2015.

[52] T. A. Gosavi and S. A. Bhave. Magneto-acoustic oscillator. In *2017 19th International Conference on Solid-State Sensors, Actuators and Microsystems (TRANSDUCERS)*, pages 448–451, June 2017.

[53] Mustafa Mert Torunbalci, Tanay A Gosavi, Kerem Y Camsari, and Sunil A Bhave. Magneto acoustic spin hall oscillators. *arXiv preprint arXiv:1708.04735*, 2017.

[54] Mauricio Manfrini, Thibaut Devolder, Joo-Von Kim, Paul Crozat, N Zerounian, Claude Chappert, Wim Van Roy, Liesbet Lagae, G Hrkac, and T Schrefl. Agility of vortex-based nanocontact spin torque oscillators. *Applied Physics Letters*, 95(19):192507, 2009.

[55] Mauricio Manfrini, Thibaut Devolder, Joo-Von Kim, Paul Crozat, Claude Chappert, Wim Van Roy, and Liesbet Lagae. Frequency shift keying in vortex-based spin torque oscillators. *Journal of Applied Physics*, 109(8):083940, 2011.

[56] M Quinsat, F Garcia-Sanchez, AS Jenkins, VS Tiberkevich, AN Slavin, LD Buda-Prejbeanu, A Zeltser, JA Katine, B Dieny, M-C Cyrille, et al. Modulation bandwidth of spin torque oscillators under current modulation. *Applied Physics Letters*, 105(15):152401, 2014.

[57] A Ruiz-Calaforra, A Purbawati, T Brächer, J Hem, C Murapaka, E Jiménez, D Mauri, A Zeltser, JA Katine, M-C Cyrille, et al. Frequency shift keying by current modulation in a mtj-based stno with high data rate. *arXiv preprint arXiv:1707.04467*, 2017.

[58] Hyun Seok Choi, Sun Yool Kang, Seong Jun Cho, Inn-Yeal Oh, Mincheol Shin, Hyuncheol Park, Chaun Jang, Byoung-Chul Min, Sang-Il Kim, Seung-Young Park, et al. Spin nano–oscillator–based wireless communication. *Scientific reports*, 4, 2014.

[59] JC Sankey, PM Braganca, AGF Garcia, IN Krivorotov, RA Buhrman, and DC Ralph. Spin-transfer-driven ferromagnetic resonance of individual nanomagnets. *Physical review letters*, 96(22):227601, 2006.

[60] AA Tulapurkar, Y Suzuki, A Fukushima, H Kubota, et al. Spin-torque diode effect in magnetic tunnel junctions. *Nature*, 438(7066):339, 2005.

[61] Jian Zhu, JA Katine, Graham E Rowlands, Yu-Jin Chen, Zheng Duan, Juan G Alzate, Pramey Upadhyaya, Juergen Langer, Pedram Khalili Amiri, Kang L Wang, et al. Voltage-induced ferromagnetic resonance in magnetic tunnel junctions. *Physical review letters*, 108(19):197203, 2012.

[62] S Miwa, S Ishibashi, H Tomita, T Nozaki, E Tamura, K Ando, N Mizuochi, T Saruya, H Kubota, K Yakushiji, et al. Highly sensitive nanoscale spin-torque diode. *Nature materials*, 13(1):50, 2014.

[63] AS Jenkins, E Grimaldi, P Bortolotti, R Lebrun, H Kubota, K Yakushiji, A Fukushima, G De Loubens, O Klein, S Yuasa, et al. Controlling the chirality and polarity of vortices in magnetic tunnel junctions. *Applied Physics Letters*, 105(17):172403, 2014.

[64] AS Jenkins, R Lebrun, E Grimaldi, S Tsunegi, P Bortolotti, H Kubota, K Yakushiji, A Fukushima, G de Loubens, O Klein, et al. Spin-torque resonant expulsion of the

vortex core for an efficient radiofrequency detection scheme. *Nature Nanotechnology*, 11(4):360–360, 2016.

[65] Dmitri E Nikonov, Gyorgy Csaba, Wolfgang Porod, Tadashi Shibata, Danny Voils, Dan Hammerstrom, Ian A Young, and George I Bourianoff. Coupled-oscillator associative memory array operation for pattern recognition. *IEEE Journal on Exploratory Solid-State Computational Devices and Circuits*, 1:85–93, 2015.

[66] Nicolas Locatelli, Vincent Cros, and Julie Grollier. Spin-torque building blocks. *Nature materials*, 13(1):11–20, 2014.

[67] Julie Grollier, Damien Querlioz, and Mark D Stiles. Spintronic nanodevices for bioinspired computing. *Proceedings of the IEEE*, 104(10):2024–2039, 2016.

[68] Damir Vodenicarevic, Nicolas Locatelli, Flavio Abreu Araujo, Julie Grollier, and Damien Querlioz. A nanotechnology-ready computing scheme based on a weakly coupled oscillator network. *Scientific Reports*, 7, 2017.

[69] Jacob Torrejon, Mathieu Riou, Flavio Abreu Araujo, Sumito Tsunegi, Guru Khalsa, Damien Querlioz, Paolo Bortolotti, Vincent Cros, Akio Fukushima, Hitoshi Kubota, et al. Neuromorphic computing with nanoscale spintronic oscillators. *Nature*, 547(7664):428–431, July 26 2017.

[70] Sabpreet Bhatti, Rachid Sbiaa, Atsufumi Hirohata, Hideo Ohno, Shunsuke Fukami, and SN Piramanayagam. Spintronics based random access memory: a review. *Materials Today*, 2017.

[71] AV Khvalkovskiy, D Apalkov, S Watts, R Chepulskii, RS Beach, A Ong, X Tang, A Driskill-Smith, WH Butler, PB Visscher, et al. Basic principles of stt-mram cell operation in memory arrays. *Journal of Physics D: Applied Physics*, 46(7):074001, 2013.

[72] Tom Andre, Syed M Alam, Dietmar Gogl, Javed Barkatullah, Jieming Qi, Halbert Lin, Xiaohu Zhang, William Meadows, Frederick Neumeyer, Greg Viot, et al. St-mram fundamentals, challenges, and outlook. In *Memory Workshop (IMW), 2017 IEEE International*, pages 1–4. IEEE, 2017.

[73] Everspin. Everspin readies industry's first 256mb perpendicular spin torque mram for production and is now sampling customers. Technical report, 2016.

[74] Luqiao Liu, Chi-Feng Pai, Y. Li, H. W. Tseng, D. C. Ralph, and R. A. Buhrman. Spin-torque switching with the giant spin hall effect of tantalum. *Science*, 336(6081):555–558, 2012.

[75] Ioan Mihai Miron, Kevin Garello, Gilles Gaudin, Pierre-Jean Zermatten, Marius V Costache, Stéphane Auffret, Sébastien Bandiera, Bernard Rodmacq, Alain Schuhl, and Pietro Gambardella. Perpendicular switching of a single ferromagnetic layer induced by in-plane current injection. *Nature*, 476(7359):189, 2011.

[76] Claude Chappert, Albert Fert, and Frédéric Nguyen Van Dau. The emergence of spin electronics in data storage. *Nature materials*, 6(11):813, 2007.

[77] C Fermon and Myriam Pannetier-Lecoeur. Noise in gmr and tmr sensors. In *Giant Magnetoresistance (GMR) Sensors*, pages 47–70. Springer, 2013.

[78] FN Hooge. 1/f noise. *Physica B+ C*, 83(1):14–23, 1976.

[79] Quentin Herreros. *Very low field magnetic resonance imaging*. PhD thesis, Paris 5, 2013.

[80] Yong Ouyang, Jinliang He, Jun Hu, and Shan X Wang. A current sensor based on the giant magnetoresistance effect: Design and potential smart grid applications. *Sensors*, 12(11):15520–15541, 2012.

[81] Javier García-Martín, Jaime Gómez-Gil, and Ernesto Vázquez-Sánchez. Non-destructive techniques based on eddy current testing. *Sensors*, 11(3):2525–2565, 2011.

[82] Norman E Dowling. *Mechanical behavior of materials: engineering methods for deformation, fracture, and fatigue*. Pearson, 2012.

[83] Andrew YC Nee. *Handbook of manufacturing engineering and technology*, chapter Compliant Manipulators, pages 1–64. Springer London: Imprint: Springer,, 2015.

[84] Arkady Pikovsky, Michael Rosenblum, and Jürgen Kurths. *Synchronization: a universal concept in nonlinear sciences*, volume 12. Cambridge university press, 2003.

[85] Vasil S Tiberkevich, Roman S Khymyn, Hong X Tang, and Andrei N Slavin. Sensitivity to external signals and synchronization properties of a non-isochronous auto-oscillator with delayed feedback. *Scientific reports*, 4, 2014.

[86] Joo-Von Kim. Spin-torque oscillators. *Solid State Physics*, 63:217 – 294, 2012.

[87] Kyle CA Wedgwood, Kevin K Lin, Ruediger Thul, and Stephen Coombes. Phase-amplitude descriptions of neural oscillator models. *The Journal of Mathematical Neuroscience*, 3(1):2, 2013.

[88] R. Adler. A study of locking phenomena in oscillators. *Proceedings of the IRE*, 34(6):351–357, June 1946.

[89] Juan A Acebrón, Luis L Bonilla, Conrad J Pérez Vicente, Félix Ritort, and Renato Spigler. The kuramoto model: A simple paradigm for synchronization phenomena. *Reviews of modern physics*, 77(1):137, 2005.

[90] Vegard Flovik, Ferran Macià, and Erik Wahlström. Describing synchronization and topological excitations in arrays of magnetic spin torque oscillators through the kuramoto model. *Scientific reports*, 6:32528, 2016.

[91] Joo-Von Kim, Vasil Tiberkevich, and Andrei N. Slavin. Generation linewidth of an auto-oscillator with a nonlinear frequency shift: Spin-torque nano-oscillator. *PHYSICAL REVIEW LETTERS*, 100(1), JAN 11 2008.

[92] Steven H Strogatz. *Nonlinear dynamics and chaos: with applications to physics, biology, chemistry, and engineering*. 2014.

[93] M Tsoi, AGM Jansen, J Bass, W-C Chiang, M Seck, V Tsoi, and P Wyder. Excitation of a magnetic multilayer by an electric current. *Physical Review Letters*, 80(19):4281, 1998.

[94] MI D'yakonov and VI Perel. Possibility of orienting electron spins with current. *Soviet Journal of Experimental and Theoretical Physics Letters*, 13:467, 1971.

[95] Vladislav E Demidov, Sergei Urazhdin, Henning Ulrichs, Vasyl Tiberkevich, Andrei Slavin, Dietmar Baither, Guido Schmitz, and Sergej O Demokritov. Magnetic nano-oscillator driven by pure spin current. *Nature materials*, 11(12):1028, 2012.

[96] VE Demidov, S Urazhdin, A Zholud, AV Sadovnikov, and SO Demokritov. Nanoconstriction-based spin-hall nano-oscillator. *Applied Physics Letters*, 105(17):172410, 2014.

[97] AA Awad, P Dürrenfeld, A Houshang, M Dvornik, E Iacocca, RK Dumas, and Johan Åkerman. Long-range mutual synchronization of spin hall nano-oscillators. *Nature Physics*, 2016.

[98] Martin Collet, Xavier De Milly, O d'Allivy Kelly, Vladimir V Naletov, Rozenn Bernard, Paolo Bortolotti, J Ben Youssef, VE Demidov, SO Demokritov, JL Prieto, et al. Generation of coherent spin-wave modes in yttrium iron garnet microdiscs by spin–orbit torque. *Nature communications*, 7:10377, 2016.

[99] P. K. Muduli, O. G. Heinonen, and Johan Åkerman. Decoherence and mode hopping in a magnetic tunnel junction based spin torque oscillator. *Phys. Rev. Lett.*, 108:207203, May 2012.

[100] Sumito Tsunegi, Hitoshi Kubota, Kay Yakushiji, Makoto Konoto, Shingo Tamaru, Akio Fukushima, Hiroko Arai, Hiroshi Imamura, Eva Grimaldi, Romain Lebrun, Julie Grollier, Vincent Cros, and Shinji Yuasa. High emission power and q factor in spin torque vortex oscillator consisting of feb free layer. *Applied Physics Express*, 7(6):063009, 2014.

[101] A Hamadeh, N Locatelli, VV Naletov, R Lebrun, G De Loubens, J Grollier, O Klein, and Vincent Cros. Origin of spectral purity and tuning sensitivity in a spin transfer vortex nano-oscillator. *Physical review letters*, 112(25):257201, 2014.

[102] MA Hoefer, Mark J Ablowitz, Boaz Ilan, Matthew R Pufall, and Thomas J Silva. Theory of magnetodynamics induced by spin torque in perpendicularly magnetized thin films. *Physical review letters*, 95(26):267206, 2005.

[103] S Mizukami, F Wu, A Sakuma, J Walowski, D Watanabe, T Kubota, X Zhang, H Naganuma, M Oogane, Y Ando, et al. Long-lived ultrafast spin precession in manganese alloys films with a large perpendicular magnetic anisotropy. *Physical review letters*, 106(11):117201, 2011.

[104] Hiroki Maehara, Hitoshi Kubota, Yoshishige Suzuki, Takayuki Seki, Kazumasa Nishimura, Yoshinori Nagamine, Koji Tsunekawa, Akio Fukushima, Alina M. Deac, Koji Ando, and Shinji Yuasa. Large emission power over 2 w with high q factor obtained from nanocontact magnetic-tunnel-junction-based spin torque oscillator. *Applied Physics Express*, 6(11):113005, 2013.

[105] VS Pribiag, IN Krivorotov, GD Fuchs, PM Braganca, O Ozatay, JC Sankey, DC Ralph, and RA Buhrman. Magnetic vortex oscillator driven by dc spin-polarized current. *Nature Physics*, 3(7):498, 2007.

[106] R. Lebrun, J. Grollier, F. Abreu Araujo, P. Bortolotti, V. Cros, A. Hamadeh, X. de Milly, Y. Li, G. de Loubens, O. Klein, S. Tsunegi, H. Kubota, K. Yakushiji, A. Fukushima, and S. Yuasa. Driven energy transfer between coupled modes in spin-torque oscillators. *Phys. Rev. B*, 95:134444, Apr 2017.

[107] A Dussaux, E Grimaldi, B Rache Salles, AS Jenkins, AV Khvalkovskiy, P Bortolotti, J Grollier, H Kubota, A Fukushima, K Yakushiji, et al. Large amplitude spin torque vortex oscillations at zero external field using a perpendicular spin polarizer. *Applied Physics Letters*, 105(2):022404, 2014.

[108] Nicolas Locatelli, VV Naletov, Julie Grollier, Grégoire De Loubens, Vincent Cros, Cyrile Deranlot, C Ulysse, G Faini, Olivier Klein, and Albert Fert. Dynamics of two coupled vortices in a spin valve nanopillar excited by spin transfer torque. *Applied Physics Letters*, 98(6):062501, 2011.

[109] Q Mistral, Maarten van Kampen, G Hrkac, Joo-Von Kim, T Devolder, P Crozat, C Chappert, Liesbet Lagae, and T Schrefl. Current-driven vortex oscillations in metallic nanocontacts. *Physical review letters*, 100(25):257201, 2008.

[110] T Yamamoto, T Seki, T Kubota, H Yako, and K Takanashi. Zero-field spin torque oscillation in co2 (fe, mn) si with a point contact geometry. *Applied Physics Letters*, 106(9):092406, 2015.

[111] W. H. Rippard, M. R. Pufall, S. Kaka, T. J. Silva, S. E. Russek, and J. A. Katine. Injection locking and phase control of spin transfer nano-oscillators. *Phys. Rev. Lett.*, 95:067203, Aug 2005.

[112] M Quinsat, JF Sierra, I Firastrau, V Tiberkevich, A Slavin, D Gusakova, LD Buda-Prejbeanu, M Zarudniev, J-P Michel, U Ebels, et al. Injection locking of tunnel junction oscillators to a microwave current. *Applied Physics Letters*, 98(18):182503, 2011.

[113] A Dussaux, AV Khvalkovskiy, J Grollier, V Cros, A Fukushima, M Konoto, H Kubota, K Yakushiji, S Yuasa, K Ando, et al. Phase locking of vortex based spin transfer oscillators to a microwave current. *Applied Physics Letters*, 98(13):132506, 2011.

[114] Sergei Urazhdin, Phillip Tabor, Vasil Tiberkevich, and Andrei Slavin. Fractional synchronization of spin-torque nano-oscillators. *Physical review letters*, 105(10):104101, 2010.

[115] A Hamadeh, Nicolas Locatelli, VV Naletov, Romain Lebrun, Grégoire De Loubens, Julie Grollier, Olivier Klein, and V Cros. Perfect and robust phase-locking of a spin transfer vortex nano-oscillator to an external microwave source. *Applied Physics Letters*, 104(2):022408, 2014.

[116] Shehzaad Kaka, Matthew R Pufall, William H Rippard, Thomas J Silva, Stephen E Russek, and Jordan A Katine. Mutual phase-locking of microwave spin torque nano-oscillators. *Nature*, 437(7057):389–392, 2005.

[117] FB Mancoff, ND Rizzo, BN Engel, and S Tehrani. Phase-locking in double-point-contact spin-transfer devices. *NATURE*, 437(7057):393–395, SEP 15 2005.

[118] Antonio Ruotolo, V Cros, B Georges, A Dussaux, J Grollier, C Deranlot, R Guillemet, K Bouzehouane, S Fusil, and A Fert. Phase-locking of magnetic vortices mediated by antivortices. *Nature Nanotechnology*, 4(8):528–532, 2009.

[119] Nicolas Locatelli, Abbass Hamadeh, Flavio Abreu Araujo, Anatoly D Belanovsky, Petr N Skirdkov, Romain Lebrun, Vladimir V Naletov, Konstantin A Zvezdin, Manuel Muñoz, Julie Grollier, et al. Efficient synchronization of dipolarly coupled vortex-based spin transfer nano-oscillators. *Scientific reports*, 5, 2015.

[120] R Lebrun, S Tsunegi, P Bortolotti, H Kubota, AS Jenkins, M Romera, K Yakushiji, A Fukushima, J Grollier, S Yuasa, et al. Mutual synchronization of spin torque nano-oscillators through a long-range and tunable electrical coupling scheme. *Nature Communications*, 8, 2017.

[121] J. Grollier, V. Cros, and A. Fert. Synchronization of spin-transfer oscillators driven by stimulated microwave currents. *Phys. Rev. B*, 73:060409, Feb 2006.

[122] Sergey Erokhin and Dmitry Berkov. Robust synchronization of an arbitrary number of spin-torque-driven vortex nano-oscillators. *Physical Review B*, 89(14):144421, 2014.

[123] Ernst Feldtkeller and Harry Thomas. Struktur und energie von blochlinien in dünnen ferromagnetischen schichten. *Physik der kondensierten Materie*, 4(1):8–14, Jul 1965.

[124] NA Usov and SE Peschany. Magnetization curling in a fine cylindrical particle. *Journal of Magnetism and Magnetic Materials*, 118(3):L290–L294, 1993.

[125] K Yu Guslienko, V Novosad, Y Otani, H Shima, and K Fukamichi. Magnetization reversal due to vortex nucleation, displacement, and annihilation in submicron ferromagnetic dot arrays. *Physical Review B*, 65(2):024414, 2001.

[126] Konstantin L Metlov and Konstantin Yu Guslienko. Stability of magnetic vortex in soft magnetic nano-sized circular cylinder. *Journal of magnetism and magnetic materials*, 242:1015–1017, 2002.

[127] K Yu Guslienko, BA Ivanov, V Novosad, Y Otani, H Shima, and K Fukamichi. Eigenfrequencies of vortex state excitations in magnetic submicron-size disks. *Journal of Applied Physics*, 91(10):8037–8039, 2002.

[128] K Yu Guslienko. Magnetic vortex state stability, reversal and dynamics in restricted geometries. *Journal of nanoscience and nanotechnology*, 8(6):2745–2760, 2008.

[129] A. Dussaux, A. V. Khvalkovskiy, P. Bortolotti, J. Grollier, V. Cros, and A. Fert. Field dependence of spin-transfer-induced vortex dynamics in the nonlinear regime. *Phys. Rev. B*, 86:014402, Jul 2012.

[130] Grégoire De Loubens, A Riegler, Benjamin Pigeau, F Lochner, F Boust, Konstantin Yu Guslienko, H Hurdequint, LW Molenkamp, G Schmidt, Andrei N Slavin, et al. Bistability of vortex core dynamics in a single perpendicularly magnetized nanodisk. *Physical review letters*, 102(17):177602, 2009.

[131] B. A. Ivanov and G. M. Wysin. Magnon modes for a circular two-dimensional easy-plane ferromagnet in the cone state. *Phys. Rev. B*, 65:134434, Mar 2002.

[132] André Thiaville, José Miguel García, Rok Dittrich, Jacques Miltat, and Thomas Schrefl. Micromagnetic study of bloch-point-mediated vortex core reversal. *Phys. Rev. B*, 67:094410, Mar 2003.

[133] S. Urazhdin, C. L. Chien, K. Y. Guslienko, and L. Novozhilova. Effects of current on the magnetic states of permalloy nanodiscs. *Phys. Rev. B*, 73:054416, Feb 2006.

[134] A. A. Thiele. Steady-state motion of magnetic domains. *Phys. Rev. Lett.*, 30:230–233, Feb 1973.

[135] Yuri Gaididei, Volodymyr P Kravchuk, and Denis D Sheka. Magnetic vortex dynamics induced by an electrical current. *International Journal of Quantum Chemistry*, 110(1):83–97, 2010.

[136] Konstantin L Metlov. Vortex precession frequency and its amplitude-dependent shift in cylindrical nanomagnets. *Journal of Applied Physics*, 114(22):223908, 2013.

[137] O. V. Sukhostavets, B. Pigeau, S. Sangiao, G. de Loubens, V. V. Naletov, O. Klein, K. Mitsuzuka, S. Andrieu, F. Montaigne, and K. Y. Guslienko. Probing the anharmonicity of the potential well for a magnetic vortex core in a nanodot. *Phys. Rev. Lett.*, 111:247601, Dec 2013.

[138] Youn-Seok Choi, Sang-Koog Kim, Ki-Suk Lee, and Young-Sang Yu. Understanding eigenfrequency shifts observed in vortex gyrotropic motions in a magnetic nanodot driven by spin-polarized out-of-plane dc current. *Applied Physics Letters*, 93(18):182508, 2008.

[139] AV Khvalkovskiy, J Grollier, A Dussaux, Konstantin A Zvezdin, and V Cros. Vortex oscillations induced by spin-polarized current in a magnetic nanopillar: Analytical versus micromagnetic calculations. *Physical Review B*, 80(14):140401, 2009.

[140] K Yu Guslienko. Low-frequency vortex dynamic susceptibility and relaxation in mesoscopic ferromagnetic dots. *Applied physics letters*, 89(2):022510, 2006.

[141] AV Khvalkovskiy, J Grollier, N Locatelli, Ya V Gorbunov, KA Zvezdin, and V Cros. Nonuniformity of a planar polarizer for spin-transfer-induced vortex oscillations at zero field. *Applied Physics Letters*, 96(21):212507, 2010.

[142] Volker Sluka, Attila Kákay, Alina M Deac, Daniel E Bürgler, Riccardo Hertel, and Claus M Schneider. Quenched slonczewski windmill in spin-torque vortex oscillators. *Physical Review B*, 86(21):214422, 2012.

[143] Konstantin Yu. Guslienko, Ki-Suk Lee, and Sang-Koog Kim. Dynamic origin of vortex core switching in soft magnetic nanodots. *Phys. Rev. Lett.*, 100:027203, Jan 2008.

[144] Bartel Van Waeyenberge, A Puzic, H Stoll, KW Chou, T Tyliszczak, R Hertel, M Fähnle, H Brückl, Karsten Rott, Günter Reiss, et al. Magnetic vortex core reversal by excitation with short bursts of an alternating field. *Nature*, 444(7118):461, 2006.

[145] Benjamin Pigeau. *Magnetic vortex dynamics nanostructures.* PhD thesis, Paris 11, 2012.

[146] N Locatelli, AE Ekomasov, AV Khvalkovskiy, Sh A Azamatov, KA Zvezdin, J Grollier, EG Ekomasov, and V Cros. Reversal process of a magnetic vortex core under the combined action of a perpendicular field and spin transfer torque. *Applied Physics Letters*, 102(6):062401, 2013.

[147] A. D. Belanovsky, N. Locatelli, P. N. Skirdkov, F. Abreu Araujo, J. Grollier, K. A. Zvezdin, V. Cros, and A. K. Zvezdin. Phase locking dynamics of dipolarly coupled vortex-based spin transfer oscillators. *Phys. Rev. B*, 85:100409, Mar 2012.

[148] F Abreu Araujo, AD Belanovsky, PN Skirdkov, KA Zvezdin, AK Zvezdin, N Locatelli, R Lebrun, J Grollier, V Cros, G de Loubens, et al. Optimizing magnetodipolar interactions for synchronizing vortex based spin-torque nano-oscillators. *Physical Review B*, 92(4):045419, 2015.

[149] Junya Shibata, Kunji Shigeto, and Yoshichika Otani. Dynamics of magnetostatically coupled vortices in magnetic nanodisks. *Phys. Rev. B*, 67:224404, Jun 2003.

[150] Eva Grimaldi. *Étude des propriétés non-linéaires et de l'origine du bruit d'oscillateurs à transfert de spin à base de vortex: vers le développement de nano-dispositifs radiofréquences spintroniques.* PhD thesis, Université Paris Sud-Paris XI, 2015.

[151] GM Wysin. Magnetic vortex mass in two-dimensional easy-plane magnets. *Physical Review B*, 54(21):15156, 1996.

[152] KY Guslienko, GN Kakazei, J Ding, XM Liu, and AO Adeyeye. Giant moving vortex mass in thick magnetic nanodots. *Scientific reports*, 5, 2015.

[153] V. V. Naletov, G. de Loubens, G. Albuquerque, S. Borlenghi, V. Cros, G. Faini, J. Grollier, H. Hurdequint, N. Locatelli, B. Pigeau, A. N. Slavin, V. S. Tiberkevich,

C. Ulysse, T. Valet, and O. Klein. Identification and selection rules of the spin-wave eigenmodes in a normally magnetized nanopillar. *Phys. Rev. B*, 84:224423, Dec 2011.

[154] Joern N. Kupferschmidt, Shaffique Adam, and Piet W. Brouwer. Theory of the spin-torque-driven ferromagnetic resonance in a ferromagnet/normal-metal/ferromagnet structure. *Phys. Rev. B*, 74:134416, Oct 2006.

[155] Abbass Hamadeh. *Synchronization of spin trasnsfer nano-oscillators*. PhD thesis, Université Paris Sud-Paris XI, 2014.

[156] K Yu Guslienko, Kristen S Buchanan, SD Bader, and V Novosad. Dynamics of coupled vortices in layered magnetic nanodots. *Applied Physics Letters*, 86(22):223112, 2005.

[157] Benjamin Pigeau, Christian Hahn, Grégoire De Loubens, VV Naletov, Olivier Klein, Kaname Mitsuzuka, D Lacour, M Hehn, S Andrieu, and F Montaigne. Measurement of the dynamical dipolar coupling in a pair of magnetic nanodisks using a ferromagnetic resonance force microscope. *Physical review letters*, 109(24):247602, 2012.

[158] Flavio Abreu Araujo et al. *Dynamical and synchronization properties of vortex based spin-torque nano-oscillators*. PhD thesis, UCL, 2015.

[159] Vasil Tiberkevich, Andrei Slavin, Elena Bankowski, and Grant Gerhart. Phase-locking and frustration in an array of nonlinear spin-torque nano-oscillators. *Applied Physics Letters*, 95(26):262505, 2009.

[160] B. Georges, J. Grollier, M. Darques, V. Cros, C. Deranlot, B. Marcilhac, G. Faini, and A. Fert. Coupling efficiency for phase locking of a spin transfer nano-oscillator to a microwave current. *Phys. Rev. Lett.*, 101:017201, Jul 2008.

[161] AN Slavin and VS Tiberkevich. Theory of mutual phase locking of spin-torque nanosized oscillators. *Physical review B*, 74(10):104401, 2006.

[162] Hyunsuk Hong and Steven H. Strogatz. Kuramoto model of coupled oscillators with positive and negative coupling parameters: An example of conformist and contrarian oscillators. *Phys. Rev. Lett.*, 106:054102, Feb 2011.

[163] Yan Zhou, Johan Persson, and Johan Åkerman. Intrinsic phase shift between a spin torque oscillator and an alternating current. *Journal of applied Physics*, 101(9):09A510, 2007.

[164] Oleh E. Omel'chenko and Matthias Wolfrum. Nonuniversal transitions to synchrony in the sakaguchi-kuramoto model. *Phys. Rev. Lett.*, 109:164101, Oct 2012.

[165] Yan Zhou, Johan Persson, Stefano Bonetti, and Johan Åkerman. Tunable intrinsic phase of a spin torque oscillator. *Applied Physics Letters*, 92(9):092505, 2008.

[166] Yan Zhou, Vasil Tiberkevich, Giancarlo Consolo, Ezio Iacocca, Bruno Azzerboni, Andrei Slavin, and Johan Åkerman. Oscillatory transient regime in the forced dynamics of a nonlinear auto oscillator. *Physical Review B*, 82(1):012408, 2010.

[167] Ezio Iacocca and Johan Åkerman. Resonant excitation of injection-locked spin-torque oscillators. *Physical Review B*, 87(21):214428, 2013.

[168] Matthew J Aburn. Critical fluctuations and coupling of stochastic neural mass models. 2017.

[169] A. D. Belanovsky, N. Locatelli, P. N. Skirdkov, F. Abreu Araujo, K. A. Zvezdin, J. Grollier, V. Cros, and A. K. Zvezdin. Numerical and analytical investigation of the synchronization of dipolarly coupled vortex spin-torque nano-oscillators. *Applied Physics Letters*, 103(12):–, 2013.

[170] Phillip Tabor, Vasil Tiberkevich, Andrei Slavin, and Sergei Urazhdin. Hysteretic synchronization of nonlinear spin-torque oscillators. *Phys. Rev. B*, 82:020407, Jul 2010.

[171] M. d'Aquino, S. Perna, A. Quercia, V. Scalera, and C. Serpico. Current-driven hysteretic synchronization in vortex nanopillar spin-transfer oscillators. *IEEE Magnetics Letters*, PP(99):1–1, 2017.

[172] M d'Aquino, C Serpico, R Bonin, G Bertotti, and ID Mayergoyz. Micromagnetic analysis of injection locking in spin-transfer nano-oscillators. *Physical Review B*, 82(6):064415, 2010.

[173] Bard Ermentrout. *Simulating, analyzing, and animating dynamical systems: a guide to XPPAUT for researchers and students*. SIAM, 2002.

[174] Eusebius J Doedel, Thomas F Fairgrieve, Björn Sandstede, Alan R Champneys, Yuri A Kuznetsov, and Xianjun Wang. Auto-07p: Continuation and bifurcation software for ordinary differential equations. 2007.

[175] G. Bertotti, A. Magni, R. Bonin, I.D. Mayergoyz, and C. Serpico. Bifurcation analysis of magnetization dynamics driven by spin transfer. *Journal of Magnetism and Magnetic Materials*, 290(Part 1):522 – 525, 2005. Proceedings of the Joint European Magnetic Symposia (JEMS' 04).

[176] P Dürrenfeld, E Iacocca, Johan Åkerman, and PK Muduli. Modulation-mediated unlocking of a parametrically phase-locked spin torque oscillator. *Applied Physics Letters*, 105(25):252404, 2014.

[177] Damir Vodenicarevic, Nicolas Locatelli, Julie Grollier, and Damien Querlioz. Synchronization detection in networks of coupled oscillators for pattern recognition. pages 2015–2022, 2016.

[178] Damir Vodenicarevic, Nicolas Locatelli, and Damien Querlioz. A neural network based on synchronized pairs of nano-oscillators. *arXiv preprint arXiv:1709.02274*, 2017.

[179] Yi Li, Xavier De Milly, Flavio Abreu Araujo, Olivier Klein, Vincent Cros, Julie Grollier, and Grégoire De Loubens. Probing phase coupling between two spin-torque nano-oscillators with an external source. *Physical Review Letters*, 118(24):247202, 2017.

[180] Sebastien Petit-Watelot, Joo-Von Kim, Antonio Ruotolo, Ruben M Otxoa, Karim Bouzehouane, Julie Grollier, Arne Vansteenkiste, Ben Van de Wiele, Vincent Cros, and Thibaut Devolder. Commensurability and chaos in magnetic vortex oscillations. *Nature Physics*, 8(9):682–687, 2012.

[181] Jérôme Williame, Artur Difini Accioly, and Joo-Von Kim. Chaotic dynamics in a macrospin spin-torque nano-oscillator with time-delayed feedback. *arXiv preprint arXiv:1709.04310*, 2017.

[182] Benjamin Pigeau, G De Loubens, Klein Olivier, Andreas Riegler, Florian Lochner, Georg Schmidt, and Laurens W Molenkamp. Optimal control of vortex core polarity by resonant microwave pulses. *Nature Physics*, 7:26–31, 2011.

université PARIS-SACLAY

ÉCOLE DOCTORALE
Physique en île-de-France (EDPIF)

**Titre:** Manipulation de la synchronisation mutuelle dans une paire d'oscillateurs à transfert de spin

**Mots clés:** spintronique, magnétisme, hyperfréquences, capteur, simulation

**Résumé** Les oscillateurs à transfert de spin se distinguent des autres oscillateurs électroniques hyperfréquences notamment par leurs grandes non-linéarité et agilité en fréquence. Cependant quoi que les principes fondamentaux de ces systèmes soient bien compris, leurs performances en termes de puissance de sortie et de largeur de raie en limitent les applications au stade de prototype. Pour y remédier, une des stratégies est celle de la synchronisation mutuelle, qui devrait améliorer les caractéristiques de ces systèmes en augmentant le volume oscillant, mais aussi permettre la réalisation de structures plus complexes. Bien que le mécanisme fondamental a été démontré, toutes ses implications ne sont pas encore parfaitement comprises. C'est dans cette perspective que nous étudions le réseau minimal d'oscillateurs non-linéaires constitué par une paire d'oscillateurs à transfert de spin mutuellement couplés via leur rayonnement dipolaire. L'originalité de ce travail réside dans l'introduction d'une antenne, qui peut générer un signal hyperfréquence et agir comme troisième oscillateur "idéal" pour explorer la riche dynamique du système, qui présente des intérêts aussi bien fondamentaux qu'applicatifs.

**Title:** Manipulation of the mutual synchronisation in a pair of spin torque oscillators

**Keywords:** spintronics, magnetism, microwaves, sensor, modeling

**Abstract** Spin torque oscillators have driven interest among other electronic microwave oscillators notably for their high nonlinearity and agility. However although the fundamental principles of those systems are well-understood, these are limited to the realisation of prototypes due to their poor performances in terms of emitted power and linewidth. One strategy to deal with those limitations consists in mutually synchronising several such oscillators, which would increase the oscillating volume, thereby improving these characteristics and allowing the realisation of more complex structures. Despite the fact that the fundamental principle has been demonstrated, its implication are still far from being perfectly understood. In this perspective we study the minimalistic network consisting in a pair of spin torque oscillators mutually coupled via their magneto-dipolar interaction. The originality of this work lies in the introduction of a microstrip antenna, which enables the generation a microwave signal and acts as a third "ideal" oscillator to probe the rich dynamics of this system, which displays fundamental as well as applicative interests.

**Université Paris-Saclay**
Espace Technologique / Immeuble Discovery
Route de l'Orme aux Merisiers RD 128 / 91190 Saint-Aubin, France